

**UNIVERSITÄT
BAYREUTH**

**Developing Functional Layered Materials:
From Synthesis and Characterization towards
Applications**

DISSERTATION

zur Erlangung des akademischen Grades eines
Doktors der Naturwissenschaften (Dr. rer. nat.)
an der Fakultät für Biologie, Chemie und Geowissenschaften
der Universität Bayreuth

vorgelegt von

Patrick Loch

geboren in Bamberg

Bayreuth, 2021

Die vorliegende Arbeit wurde in der Zeit von November 2018 bis Dezember 2021 in Bayreuth am Lehrstuhl für Anorganische Chemie I unter Betreuung von Prof. Dr. Josef Breu angefertigt.

Vollständiger Abdruck der von der Fakultät für Biologie, Chemie und Geowissenschaften der Universität Bayreuth genehmigten Dissertation zur Erlangung des akademischen Grades eines Doktors der Naturwissenschaften (Dr. rer. nat.).

Dissertation eingereicht am: 22.12.2021

Zulassung durch die Promotionskommission: 26.01.2022

Wissenschaftliches Kolloquium: 26.07.2022

Amtierender Dekan: Prof. Dr. Benedikt Westermann

Prüfungsausschuss:

Prof. Dr. Josef Breu (Gutachter)

Prof. Dr. Jürgen Senker (Gutachter)

Prof. Dr. Markus Retsch (Vorsitz)

Prof. Dr. Andreas Greiner

„Obstacles don't have to stop you. If you run into a wall, don't turn around and give up. Figure out how to climb it, go through it, or work around it.“

- Michael Jordan -

Gewidmet meiner Familie

Content

List of Abbreviations	XI
1. Summary	1
2. Zusammenfassung	5
3. Introduction.....	9
3.1. Challenges in material science	9
3.2. Fundamentals of layered materials.....	10
3.3. Properties of layered materials	16
3.4. Selected applications of layered materials	22
3.5. Scope of this thesis	25
4. Synopsis.....	27
4.1. Structural investigation of Ni-hectorites	29
4.2. Insights into the CO ₂ swelling mechanism of Ni-hectorites.....	33
4.3. Delamination of layered zeolites into aqueous dispersions of nanosheets..	36
4.4. Egyptian blue as colored substrate for pearlescent pigments	39
5. Literature	43
6. Results	51
6.1. Structure of Ni-hectorites	51
6.2. Insights into the CO ₂ swelling mechanism of Ni-Hectorites	69
6.3. Delamination of layered zeolites into aqueous dispersions of nanosheets..	93
6.4. Egyptian blue as colored substrates for pearlescent pigments.....	115
7. List of Publications and Patents	127
7.1. Publications included in this thesis	127
7.2. Additional publications.....	127
7.3. Patents	128
8. Acknowledgements	129
9. Erklärung des Verfassers	131

List of Abbreviations

2D	2-dimensional
3D	3-dimensional
AAS	Atomic absorption spectroscopy
AFM	Atomic force microscopy
<i>c</i>	Crystallographic <i>c</i> -axis
CCS	Carbon Capture and Storage
CEC	Cation exchange capacity
CHN-analysis	CHN elemental analysis
DFT	Density Functional Theory
d^{01}	Basal spacing of an ordered interstratification
EDX	Energy dispersive X-ray spectroscopy
EXAFS	Extended X-ray absorption fine structure
ICP-OES	Inductively coupled plasma atomic emission spectroscopy
INS	Inelastic Neutron Scattering
IZA	International Zeolite Association
LDH	Layered Double Hydroxide
Meglumine	<i>N</i> -Methyl- <i>D</i> -glucamonium
Mo	Octahedral coordinated cation
MOF	Metal Organic Framework
MRs	Membered rings
M _t	Tetrahedral coordinated cation
φ	Volume fraction
p.f.u.	per formula unit
PXRD	Powder X-ray diffraction
r.h.	Relative humidity

List of Abbreviations

SAXS	Small angle X-ray scattering
SDA	Structure-directing agent
SEM	Scanning electron microscopy
SLS	Static light scattering
vol.%	Volume percentage
ω	Relative weighting of interlayer occupation
WL	Water layer
XPS	X-ray photoelectron spectroscopy

1. Summary

The present thesis deals with structural features of layered compounds, resulting properties and their use for the systematic design of functional materials with regard to potential industrial applications. The focus is set on two main classes of layered structures. In particular, in the first part of the thesis, the structure and properties of 2:1 layered silicates are discussed (e.g., Na-hectorite, $\text{Na}^{+0.5}[\text{Mg}^{2+2.5}\text{Li}^{+0.5}]<\text{Si}^{4+}>\text{O}_{10}\text{F}_2$), while the layered zeolite llerite, also known as NaRUB-18 or octosilicate ($\text{Na}_8[\text{Si}_{32}\text{O}_{64}(\text{OH})_8]\cdot 32 \text{H}_2\text{O}$), was used for the design of functional materials in the second part.

For negatively charged layered compounds like Na-hectorite or llerite, ion exchange of interlayer cations represents an easy approach to functionalize the interlayer space. For example, simple Ni-exchange of synthetic Na-hectorite could be used to obtain Ni-hectorites, which show significant crystalline swelling upon exposure to high pressures of CO_2 . This leads to high volumetric CCS (Carbon Capture and Storage) capacities, making Ni-hectorites attractive for the capture of anthropogenic CO_2 . While the swelling of 2:1 layered silicates in response to water is well understood, the swelling mechanism with CO_2 still lacks explanations. To explain the swelling capability and optimize the adsorption properties concerning a potential industrial feasibility, the structure of the intercalation compound was analyzed in detail. In some cases of intercalation, ordered or random interstratified structures may be formed. Therefore, the focus was set on the identification of such potential structures. Due to the high tendency of Ni to condensate to oligocations, an ordered interstratified structure was formed during ion exchange in Ni-hectorite, consisting of interlayers of uncondensed, smectite-like, hydrated $[\text{Ni}(\text{H}_2\text{O})_6]^{2+}$, and condensed, chlorite-like $[\text{Ni}(\text{OH})_{0.83}(\text{H}_2\text{O})_{1.17}]_{0.37}^{1.17+}$ interlayers. Despite the presence of such an ordered interstratification, electron densities of the two interlayer species are too similar, and no typical superstructure reflection could be observed. Therefore, the electron contrast of both interlayers was improved by ion exchange with an alkylammonium cation and by thermal annealing, increasing the intensity of the superstructure reflection and helping to identify the ordered interstratification. In the next step, the obtained structure of Ni-hectorite was used to identify the underlying swelling mechanism with CO_2 . Combining a combination of analytical tools, the interactions of CO_2 and thus the swelling could be entirely attributed to the intercalated

Summary

$[\text{Ni}(\text{OH})_{0.83}(\text{H}_2\text{O})_{1.17}]_{0.37}^{1.17+}$ interlayer species. The mechanism was ascribed to the reversible formation of a carbonate species at the edges of the chlorite-like interlayer species, binding CO_2 in the interlayers and leading to the observed swelling. DFT calculations supported this mechanism. Consequently, the CCS capacity of Ni-hectorite can be optimized by increasing the amount of condensed chlorite-like interlayers, rendering Ni-hectorite competitive to other adsorption materials.

The second part of the thesis deals with the systematic design of functional materials, applying established mechanisms to the layered zeolite Ilerite. The production of dispersions consisting of single-layer nanosheets via repulsive osmotic swelling represents an established procedure for selected classes of layered compounds, like 2:1 layered silicates, layered titanates, or niobates. Despite the potential of their porous and catalytically active layers, nanosheet production of layered zeolites is still difficult and limited to certain examples. Contrary to 2:1 layered silicates, where the layer charge is independent of the pH, exposed OH groups at the basal surfaces of layered zeolites lead to a variation of the layer charge with pH and complicate delamination. However, the conditions to trigger osmotic swelling for 2:1 layered silicates were recently identified. Applying the appropriate conditions for osmotic swelling, the mechanism could be adapted to the layered zeolite Ilerite. Ilerite can be crystallized in a scalable and mild sol-gel process in appealing, large, square-shaped platelets. By ion exchange of interlayer sodium with the sterically demanding, hydrophilic amino sugar *N*-methyl-*D*-glucamonium, functional, large aspect ratio nanosheets were obtained in a scalable and environmentally friendly process. The functionality of the zeolite nanosheets was demonstrated by doctor blading of a nematic suspension into thin, inorganic films. Due to the high aspect ratio, these films showed excellent gas barrier properties, relevant for industrial application.

Moreover, the layered, square-shaped morphology makes Ilerite attractive for the application as a pearlescent pigment. Extending the color range of pearlescent pigments is still a challenge and may be achieved by using colored substrates. Therefore, Ilerite was used as starting material to synthesize one of the first synthetic blue pigments, the layered compound Egyptian blue ($\text{CaCuSi}_4\text{O}_{10}$), to maintain the appealing morphology of Ilerite. This pseudomorphosis was achieved in a two-step procedure, by cation exchange of Ilerite with Cu, followed by the addition of missing stoichiometric amounts of Ca and Cu, allowing the synthesis of Egyptian blue at relatively low temperatures of

1000°C. Being technically benign and allowing control of the morphology, this process is advantageous over existing hydrothermal, solid-state or melt flux synthesis routes.

This work is a cumulative thesis. A detailed description of the results can be found in the attached manuscripts.

2. Zusammenfassung

Die vorliegende Arbeit beschäftigt sich mit den strukturellen Merkmalen von Schichtverbindungen, den daraus resultierenden Eigenschaften und der Nutzung dieser für das systematische Design von Funktionsmaterialien im Hinblick auf potentielle industrielle Anwendungen. Der Fokus liegt hierbei auf zwei prominenten Vertretern von Schichtstrukturen. Während im ersten Teil die Struktur und Eigenschaften von 2:1-Schichtsilikaten (wie z.B. Na-Hectorit, $\text{Na}^{+0.5}[\text{Mg}^{2+2.5}\text{Li}^{+0.5}]<\text{Si}^{4+}>\text{O}_{10}\text{F}_2$) behandelt werden, wird im zweiten Teil der Arbeit der schichtartige Zeolith Ilerit, auch bekannt als NaRUB-18 oder Oktosilikat ($\text{Na}_8[\text{Si}_{32}\text{O}_{64}(\text{OH})_8]\cdot 32 \text{H}_2\text{O}$) verwendet.

Für negativ geladene Schichtverbindungen wie Na-Hectorit oder Ilerit stellt der Ionenaustausch von Zwischenschichtkationen eine einfache Möglichkeit dar den Zwischenschichtraum zu funktionalisieren. Durch einfachen Ni-Austausch von synthetischem Na-Hectorit wurden beispielsweise Ni-Hectorite erhalten, die bei hohem CO_2 -Drücken kristalline Quellung zeigen. Dies führt zu hohen volumetrischen CO_2 Kapazitäten (CO_2 -Abscheidung und Speicherung, engl. *Carbon Capture and Storage*) und macht Ni-Hectorite daher attraktiv für die Entfernung von anthropogenem CO_2 . Während die Quellung von 2:1-Schichtsilikaten mit Wasser weitgehend verstanden ist, gibt es für den Quellungsmechanismus mit CO_2 noch keine Erklärung. Um die Quellfähigkeit zu erklären und schließlich die Adsorptionseigenschaften im Hinblick auf eine mögliche industrielle Nutzung zu optimieren, wurde die Struktur der Interkalationsverbindung im Detail analysiert. In einigen Fällen der Interkalation können geordnete oder statistische Wechsellagerungen gebildet werden, daher wurde der Schwerpunkt auf die Identifizierung solcher, potenziell vorliegender Strukturen gelegt. Aufgrund der hohen Kondensationsneigung von Ni zur Bildung von Oligokationen, kommt es während des Ionenaustausches zur Ausbildung einer geordneten Wechsellagerung, bestehend aus alternierend besetzten Smectit-artigen, hydratisierten $[\text{Ni}(\text{H}_2\text{O})_6]^{2+}$ Zwischenschichten und kondensierten, Chlorit-artigen $[\text{Ni}(\text{OH})_{0.83}(\text{H}_2\text{O})_{1.17}]_{0.37}^{1.17+}$ Zwischenschichten. Trotz des Vorliegens einer solchen Heterostruktur sind die Elektronendichten der beiden Zwischenschichtspezies zu ähnlich, sodass die für geordnete Wechsellagerungen üblichen Überstrukturreflexe nicht beobachtet werden konnten. Der Elektronenkontrast beider Zwischenschichten konnte dennoch durch selektiven Ionenaustausch der smectischen Zwischenschichten

Zusammenfassung

mit einem Alkylammoniumkation oder alternativ durch Tempern verbessert werden. Dadurch konnte die Intensität der Überstrukturreflexe erhöht und die geordnete Wechsellagerung identifiziert werden.

Im nächsten Schritt wurde die erhaltene Struktur von Ni-Hectorit verwendet um den zugrunde liegenden Quellungsmechanismus mit CO₂ zu identifizieren. Durch eine Kombination verschiedener Charakterisierungsmethoden konnten die Wechselwirkungen von CO₂ und damit die Quellung vollständig auf die interkalierte $[\text{Ni}(\text{OH})_{0.83}(\text{H}_2\text{O})_{1.17}]_{0.37}^{1.17+}$ -Zwischenschichtspezies zurückgeführt werden. Der Mechanismus wurde als reversible Bildung einer Carbonatspezies an den Kanten der Chlorit-artigen Zwischenschichtspezies beschrieben, wodurch CO₂ in den Zwischenschichten gebunden wird und folglich eine kristalline Quellung beobachtet werden kann. DFT-Berechnungen bestätigten zudem diesen Mechanismus. Folglich kann die CCS-Kapazität von Ni-Hectorit durch Erhöhung der Menge an kondensierten Chlorit-artigen Zwischenschichten optimiert werden, wodurch Ni-Hectorit gegenüber anderen Adsorptionsmaterialien wettbewerbsfähig wird.

Der zweite Teil der Arbeit befasst sich mit dem systematischen Design von Funktionsmaterialien, wobei etablierte Mechanismen wie die osmotische Quellung auf den schichtartigen Zeolith Ilerit angewendet werden. Die Herstellung von Dispersionen bestehend aus einzelnen Nanoschichten durch repulsive osmotische Quellung ist ein etabliertes Verfahren für ausgewählte Klassen von Schichtverbindungen, wie 2:1 Schichtsilikate, schichtartige Titanate oder Niobate. Trotz des Potenzials schichtartiger Zeolithe, mit ihren porösen und katalytisch aktiven Schichten, ist die Herstellung von Nanoschichten immer noch schwierig und auf ausgewählte Beispiele beschränkt. Im Gegensatz zu 2:1 Schichtsilikaten, bei denen die Schichtladung unabhängig vom pH-Wert ist, führen OH-Gruppen an den basalen Oberflächen der Schichten zu einer Variation der Schichtladung mit dem pH-Wert und erschweren dadurch die Delaminierung. Die Voraussetzungen für das Einsetzen osmotischer Quellung wurden jedoch kürzlich für 2:1 Schichtsilikate identifiziert. Bei Anwendung geeigneter Bedingungen konnte so der Mechanismus auf den schichtartigen Zeolith Ilerit übertragen werden. Ilerit kann in einem skalierbaren, milden Sol-Gel Prozess in Form von ansprechenden, großen, quadratischen Plättchen kristallisiert werden. Durch Ionenaustausch der Zwischenschichtkationen mit einem sterisch anspruchsvollen, hydrophilen Aminozucker *N*-Methyl-*D*-glucammonium wurden funktionelle Zeolith-Nanoschichten mit außerordentlich großen

Aspektverhältnis in einem skalierbaren und umweltfreundlichen Prozess hergestellt. Die Funktionalität der erhaltenen Nanoschichten wurde durch Rakeln einer nematischen Suspension in dünne Filme demonstriert. Aufgrund des hohen Aspektverhältnisses der Nanoschichten zeigten diese ausgezeichnete Gas-Barriereigenschaften, die darüber hinaus von industrieller Relevanz sind.

Die schichtartige und quadratische Morphologie macht Ilerit außerdem interessant für die Anwendung als Perlglanzpigment. Die Erweiterung des Farbspektrums von Perlglanzpigmenten ist nach wie vor eine Herausforderung und kann durch die Verwendung farbiger Substrate erreicht werden. Daher wurde Ilerit als Ausgangsmaterial für die Synthese eines der ersten synthetischen Blaupigmente verwendet, der Schichtverbindung Ägyptisch Blau ($\text{CaCuSi}_4\text{O}_{10}$), mit dem Ziel die attraktive Morphologie des Ilerits zu erhalten. Diese Pseudomorphose wurde in einem zweistufigen Verfahren erreicht, das technisch günstig ist, die Kontrolle der Morphologie ermöglicht und somit Vorteile gegenüber bestehenden Hydrothermal-, Festkörper- und Schmelzfluss-Synthesen aufweist. Der Ionenaustausch von Ilerit mit Cu, gefolgt von der Zugabe fehlender stöchiometrischer Mengen von Cu und Ca, ermöglichte die Synthese von Ägyptisch Blau bei relativ niedrigen Temperaturen von 1000°C , wobei die quadratische Morphologie von Ilerit erhalten blieb.

Diese Arbeit ist eine kumulative Dissertation. Eine detaillierte Beschreibung der Ergebnisse befindet sich in den angehängten Manuskripten.

3. Introduction

3.1. Challenges in material science

Climate change, growing global industry, and an increasing energy demand possess new challenges to material science. In this term, research and development of new materials and technologies is necessary to increase energy production while reducing greenhouse gas emissions.¹ However, limitations of available resources restrict this development. For example, increasing electro-mobility will lead to an increasing demand of lithium for battery technologies, reducing its availability.^{1, 2} Consequently, a sustainable production of materials is desired, overcoming energetic issues and giving opportunity for the development of materials for innovative applications and technologies.

Despite the growing significance of renewable energies, the number of non-carbon-emitting energy sources is still limited.³ More than 85 % of the global energy consumption are still obtained from non-renewable origin, whereas CO₂ is responsible for more than 60 % of the greenhouse gas emissions.^{4, 5} Therefore, it is a major challenge to achieve a significant reduction of anthropogenic CO₂. To reduce the long-run risks of climate change, it is necessary to utilize or store CO₂.^{6, 7} Utilization can be achieved, for example, in the synthesis of functional polymers and products.⁸ Alternatively, capture and storage of CO₂ (CCS) gives new opportunities for the permanent or temporary removal of CO₂ with the opportunity for a subsequent usage.⁹

Besides a reduction of ongoing CO₂ emissions, the search for alternative carbon-free energy sources is essential. To overcome the increasing energy demand, development of green technologies and alternative energy sources are necessary. Regenerative energy sources such as wind, solar, geothermal, and hydrothermal are gaining in significance and becoming more competitive with fossil fuels.¹⁰ Hydrogen, which can be produced by using renewable energies, may be considered as one of the most promising candidates for a future high efficiency and zero-emission fuel.^{11, 12} However, production of hydrogen still lacks broad application and often requires purification steps for its final use as fuel.¹³ Therefore, development of efficient permselective hydrogen membranes is of high interest.¹⁴

Introduction

3.2. Fundamentals of layered materials

Depending on the potential application, materials with individual and adjusted properties are required. Due to the variety of different compositions, structures, and properties, layered materials are a versatile toolbox for the design of functional materials.¹⁵⁻¹⁸ Contrary to 3-dimensional (3D) materials, layered or 2-dimensional (2D) materials are characterized by anisotropic bonding conditions.¹⁸ This is reflected in a structure, where individual layers show strong in-plane interactions, which are stacked to crystals with weaker interactions in a third dimension. Due to crystallographic reasons, stacks of these layers cannot be referred as a crystal anymore and are called tactoids.¹⁹ The height of the individual layers is typically in the range of nanometers, while the lateral extension of the layers can exceed micrometer to centimeter. Consequently, a single layer can be referred as a nanosheet.²⁰

The characteristic structure of 2D materials allows the transformation of tactoids through exfoliation into thinner stacks and ultimately through delamination into single nanosheets.²¹ Upon delamination, the physical properties of 2D materials change drastically compared to the bulk material, which results in differences in e.g., electronic, magnetic, or mechanical properties.²² Moreover, the surface area and the aspect ratio (ratio between lateral size and height) increases, which is maximized in the case of a single nanosheet.¹⁹

Due to the variety of 2D materials and the different properties, a subdivision into groups is necessary and can be conducted, for example, depending on the chemical composition, the crystal structure, or physical properties. The layer charge of the 2D material represents the most common method for a subdivision into groups. A single layer can be neutral, carry a negative or a positive charge.¹⁵ Introduction of a layer charge requires a charge balance mechanism. This can be ensured by incorporating counter ions of opposite charges into the interlayer space of the nanosheets.²³ Whereas in the case of neutral layers, adjacent layers are held together by relatively weak interactions, like van der Waals or hydrogen bonds, stronger coulomb interactions are present in charged layered materials.¹⁹

One of the most famous examples of neutral 2D materials is graphite. As a material consisting only of carbon atoms, graphite is built from stacked atomically thin single carbon layers, known as graphene. Differences in the physical behavior of 2D materials are clearly observable in the case of graphite and graphene. While the bulk material

is a semi-metal,²⁴ a single graphene layer is a 2D topological insulator,²⁵ showing a remarkably high in-plane thermal conductivity²⁶ and mechanical stability²⁷.

Layer charges can be introduced with isomorphic substitution,²⁸ chemical modification of the layers²⁹ or redox reaction³⁰. For example, oxidation of graphite was used to obtain graphene oxide, having a negative layer charge.³⁰ The direct synthesis of charged layered materials using isomorphic substitution is an established procedure to obtain materials with either positive or negative layer charges. Typically, layered double hydroxides (LDHs) possess a positive layer charge,^{31, 32} while layered silicates^{33, 34} are negatively charged. Contrary to the permanent layer charge due to isomorphic substitution, chemical modification or redox reactions may be reversible.

Focus of the present thesis is set on selected examples of layered materials, taking advantage of the characteristic properties. Therefore, the structure of layered silicates will be discussed on the example of Na-hectorite in **Chapter 3.2.1**, while more complex layered materials with variable layer charges, are specified in **Chapter 3.2.2** on the example of the layered zeolite Ilerite.

3.2.1. Structure of Na-Hectorite

Layered silicates are widely known and typically used for ceramics,³⁵ in rheology³⁶ or as filler in polymers to improve flame retardancy,^{37, 38} mechanical³⁹ or gas barrier properties^{40, 41}. Layered silicates, also referred to as clay minerals, are part of the phyllosilicate group having a layered structure.⁴² Depending on several characteristics like linkage, type, or charge of the silicate layers, classification into groups is possible, leading to significant differences in the chemical properties.⁴³ In the following, the focus is set on 2:1-layered silicates, particularly on Na-hectorite, which was used in the present thesis.

In general, 2:1-layered silicates consist of tetrahedral and octahedral sheets, connected to layers. The tetrahedral sheets are built from $\langle M_t^{z+}O_4 \rangle$ tetrahedra, which are connected through the basal oxygen atoms to form a 2D hexagonal network. Typical tetrahedral coordinated cations can be Si^{4+} , Al^{3+} , Fe^{3+} or Ge^{4+} . The octahedral layer is formed by condensed, edge-shared $[M_o^{y+}O_4X_2]$ octahedra ($X = \text{e.g. } OH^-, F^-$), which can be occupied by a variety of different M_o cations like Mg^{2+} , Fe^{2+} , Fe^{3+} , Mn^{2+} , Al^{3+} or Li^+ . Two tetrahedral layers are connected via the apical oxygen atoms of the tetrahedra to one octahedral layer, forming a sandwich-like structure with a thickness of approximately 0.96 nm. A permanent negative layer charge can be generated by isomorphic

Introduction

substitution of higher valent cations with lower charged cations in the octahedral, the tetrahedral, or both layers. The generated layer charge is compensated by incorporation of interlayer cations like Li^+ , Na^+ , Cs^+ or Ba^{2+} . This leads to a general composition of $\text{Z}^{x+}[\text{M}_o^y\text{+}_a]\langle\text{M}_t^z\text{+}_b\rangle\text{O}_{10}\text{X}_2$ for 2:1-layered silicates. The resulting layer charge is typically given by charges x *per formula unit* (p.f.u.) O_{10}X_2 .⁴²

The structure of layered silicates is illustrated on the example of Na-hectorite with a layer charge of 0.5 p.f.u. and a composition of $\text{Na}^{+0.5}[\text{Mg}^{2+2.5}\text{Li}^{+0.5}]\langle\text{Si}^{4+}\rangle\text{O}_{10}(\text{OH}/\text{F})_2$ (**Figure 1**). Na-Hectorite is a member of the smectite group, whereas all octahedral cations are occupied, which is typical for trioctahedral layered silicates. Starting from the non-charged talc, with an ideal composition of $[\text{Mg}^{2+3}]\langle\text{Si}^{4+}\rangle\text{O}_{10}(\text{OH}/\text{F})_2$,⁴⁴ Na-hectorite can be obtained upon partial isomorphous substitution of octahedral Mg^{2+} with lower charged Li^+ . Charge balance is ensured by the additional incorporation of Na^+ in the interlayer space.^{45, 46}

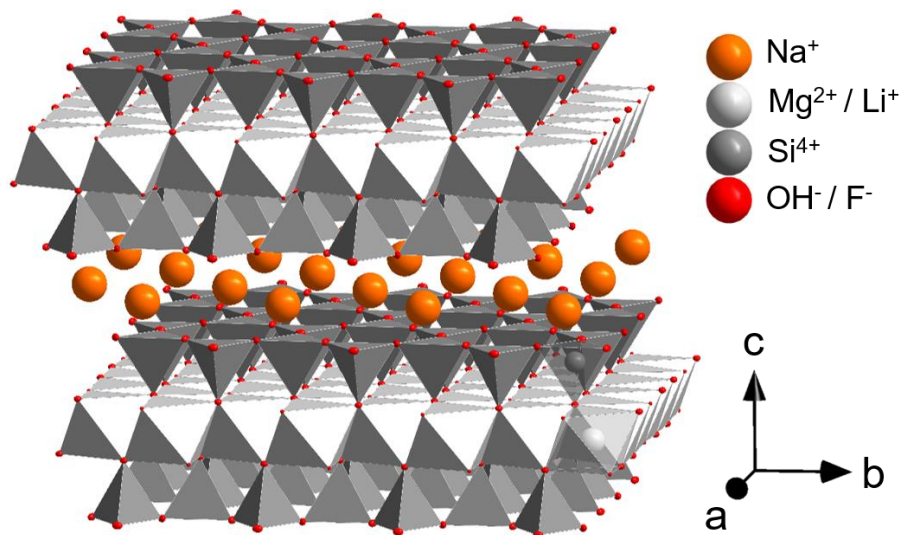


Figure 1: Schematic representation of the crystal structure of Na-hectorite: Two layers of SiO_4 -tetrahedra are connected to a hexagonal network, forming 2:1-layers with one octahedral layer, in which Mg^{2+} is partially substituted by Li^+ . The permanent layer charge resulting from this substitution is compensated by incorporation of interlayer Na^+ ions.^{46, 47}

Isomorphous substitution has a significant impact on the properties of the layered silicate. For example, substitution with transition metals like $\text{Fe}^{2+/3+}$ can increase the electrical conductivity, leading to semiconductive materials.^{48, 49} Moreover, the type of interlayer cation, the layer charge and the charge homogeneity have a crucial influence on the swelling behavior (**Chapter 3.3.1**). A statistical isomorphous substitution is necessary to obtain charge homogenous materials, which are capable to swell osmotically in water. For Na^+ as interlayer cation, osmotic swelling in water can be observed if

charge homogeneity is sufficiently high and the layer charge low enough (< 0.55 p.f.u.).³³

Even though the usage of naturally occurring layered silicates is possible, undefined compositions, impurities, layer charge inhomogeneities, low lateral extensions, and limited aspect ratios cannot fulfill the requirements for an efficient design for a wide range of applications.^{41, 46} Furthermore, the presence of OH^- limits the thermal stability in natural layered silicates to $300\text{ }^\circ\text{C}$.⁵⁰ Synthetic layered silicates offer the opportunity to solve these problems, giving phase pure, charge homogenous materials with large lateral extensions and a high thermal stability. Several synthesis protocols were developed to achieve these goals, using for example solid-state⁵¹ or hydrothermal synthesis⁵². However, simulations proved that temperatures above 1000 K are necessary to achieve a statistical isomorphic substitution.⁵³ Melt synthesis can overcome these disadvantages and charge homogenous, high aspect ratio material with a uniform intracrystalline reactivity can be obtained. Using this procedure, the synthesis of a phase pure Na-hectorite with a composition of $\text{Na}^{+0.5}[\text{Mg}^{2+2.5}\text{Li}^{+0.5}]<\text{Si}^{4+}>\text{O}_{10}\text{F}_2$ is possible.^{33, 46} F^- substitution of OH^- increases the thermal stability contrary to natural silicates from 300 to $750\text{ }^\circ\text{C}$.⁵⁰ The high charge homogeneity results in a uniform intracrystalline reactivity, allowing the spontaneous delamination into single nanosheets via repulsive osmotic swelling (**Chapter 3.3.1**). The large lateral extensions of the particles (approx. $20\text{ }\mu\text{m}$) result in nanosheets with exceptional aspect ratio of more than 20000 , making Na-hectorite a promising candidate for applications, e.g. as polymer filler, where a high aspect ratio is crucial.⁴⁰

3.2.2. Structure of Ilerite

While layered silicates like Na-hectorite are famous 2D materials used in various applications, layered zeolites are far less common. Conventional 3D zeolites are established materials in industry with variable compositions and structures, which are used, for example, as cracking catalysts.⁵⁴ Despite being per definition a 3D crystalline material,^{55, 56} under certain circumstances, zeolite structures with anisotropic bonding conditions forming layers, can be accessed.⁵⁷ Layered zeolites can either be synthesized directly, e.g. by using a suitable structure-directing agent (SDA)⁵⁸⁻⁶⁰ or via a top-down approach upon decomposition of 3D zeolites^{61, 62}. An overview of current accessible layered zeolites and their potential applications is presented in several recent reviews.^{15, 56, 57}

Introduction

In general, zeolites are formed from primary building units of $\langle M_i^{z+}O_4 \rangle$ tetrahedra, which are connected via their corners to more complex secondary building units, forming crystalline structures. Typical tetrahedral coordinated cations are Si^{4+} , Al^{3+} , Ge^{4+} or Fe^{3+} .^{55, 56} Due to the variety of possible structures, zeolites are classified according to their framework by the International Zeolite Association (IZA). This variety makes a detailed discussion of all zeolite structures nearly impossible. Therefore, the focus is set in the following on a specific layered zeolite precursor Ilerite, which was used in the present thesis.⁶³⁻⁶⁵

Ilerite, also known as NaRUB-18 or Octosilicate, is besides Kanemite and Magadiite a member of the group of layered sodium silicates.⁶⁶ The layered structure is built from corner-sharing SiO_4 tetrahedra, forming $[5^4]$ cages similar to MFI and MOR type zeolites, which are connected to crystallographic polar layers with a thickness of 0.74 nm.^{63, 66} The single-layer exhibits a pore system of 4 and 6 membered rings (4 and 6 MRs) across the layers. The negative layer charge, originating from the half protonated terminal Si-O-bonds, is balanced by chains of edge sharing $[Na(H_2O)_6]$ -octahedra in the interlayer space, resulting in a composition of $Na_8[Si_{32}O_{64}(OH)_8] \cdot 32 H_2O$ (**Figure 2**).⁶³

While for clay minerals like Na-hectorite, the layer charge is permanent and independent of pH, acidic OH-groups are exposed at the basal surfaces of layered zeolites^{55, 57} and thus, the layer charge will consequently alter with pH. The layers are stacked in a centrosymmetric fashion along *c*-direction, forming crystals with a characteristic square-shaped morphology. Unlike typical layered zeolites (e. g. MFI,⁵⁹ MCM-56,⁶⁰ or MCM-22⁶⁷), the synthesis of Ilerite requires no SDA and can be performed under mild conditions applying a water-based sol-gel route.⁶⁸⁻⁷⁰ This easy, scalable, and environmentally friendly process combined with unique properties like the intrinsic porosity and the appealing square-shaped morphology make Ilerite a promising material for different applications like for the fabrication of permselective hydrogen membranes.

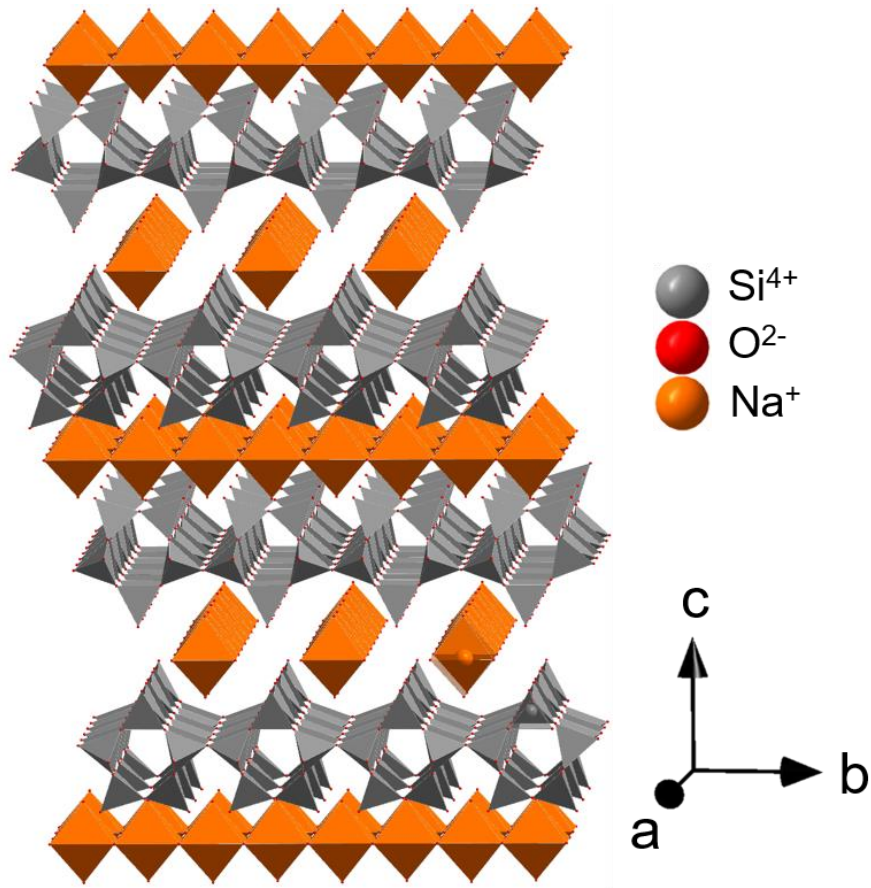


Figure 2: Schematic representation of the crystal structure of Illerite: SiO_4 tetrahedra are connected to $[5^4]$ cages, forming layers, where half of the Si-O bonds are unsaturated. Chains of hydrated interlayer Na^+ ions compensate the resulting layer charge. The layers are themselves stacked in a centrosymmetric fashion in stacking direction along the c -axis.⁶³

3.3. Properties of layered materials

The unique layered structure of layered materials can be exploited, applying several approaches, to influence their features. One possibility represents changes in the chemical composition and/or the crystal structure of the layers. By simply modifying the composition and the structure of transition metal dichalcogenides, for example, physical properties can be tuned and materials with metallic, semimetallic, or semiconductive properties can be obtained.⁷¹ Alternatively, exfoliation and delamination²¹ can be used to adjust the properties, interlayer ions can be exchanged against another species (intercalation),⁷² interlayer ions can be complexed by suitable ligands (complexation)⁷³ or non-charged molecules can be additionally incorporated into the interlayer space (swelling)¹⁹. Even though, some of these reactions are also possible for neutral layered materials, focus is hereinafter on charged layered compounds.

3.3.1. Swelling and delamination

Swelling is an often-observed phenomenon for charged layered compounds, leading to an expansion of the interlayer space and thus affecting the attractive interactions between the nanosheets. This results in a lowered attraction of adjacent layers and to different physical and chemical properties of the materials.¹⁹ In order to swelling occur, the incorporation of molecules, and in consequence the swelling itself must be thermodynamically favored.¹⁹ The process depends on several factors: the type of interlayer species,⁷⁴⁻⁷⁶ its enthalpy of hydration,⁷⁷ the layer charge,^{76, 78} temperature,⁷⁹ pressure,⁸⁰ ionic background in solvents,⁸¹ and humidity^{82, 83}. For isolating layered materials such as Na-hectorite, where electron reshuffling is limited, contrary to electrical conductive materials like graphite, layer charge homogeneity is crucial.⁸⁴ Due to the high charge homogeneity and the capability to swell spontaneously in water and humid air, synthetic Na-hectorite can be used as an example for other charged layered materials to explain the swelling process in detail.^{33, 85} The swelling process can be subdivided into two main regimes (**Figure 3**):

In the first stage, known as crystalline swelling, swelling occurs in discrete steps. For synthetic Na-hectorite for example, this depends on the relative humidity (defined as the relative amount of water in air, r.h.). Starting from the fully dried material containing no interlayer water (0 WL), Na-hectorite swells at 22 % r.h. and 64 % r.h. to a swollen structure containing one water layer (1 WL) and two water layers (2 WL) following a hysteresis behavior. In the course of the swelling process, the layers are separated by

the size of atoms or molecules. For water, this leads to an increasing basal spacing from 9.6 to 12.2 Å and 15.1 Å, respectively.^{33, 47, 85} If charge homogeneity is limited like in the case of natural layered silicates, a continuous increase of the basal spacing might be observed, which is an artefact of random interstratifications (see **Chapter 3.3.2**).⁸⁶ Crystalline swelling is not only limited to water but can also occur in organic solvents,⁸⁷⁻⁸⁹ mixtures of solvents and water^{90, 91} or under exposure to gases⁹²⁻⁹⁴. The swelling process depends on several factors like, for example, the interlayer species due to different sizes and/or hydration enthalpies. This can be used to tune the properties of the material. For example, at 40 % r.h., Na⁺ intercalated hectorite swells to its 1 WL state, while K⁺ intercalated hectorite shows no crystalline swelling.⁷⁷ In this line, specific materials can be developed, which swell in response to CO₂ and can be used for CCS (**Chapter 3.4.1**).

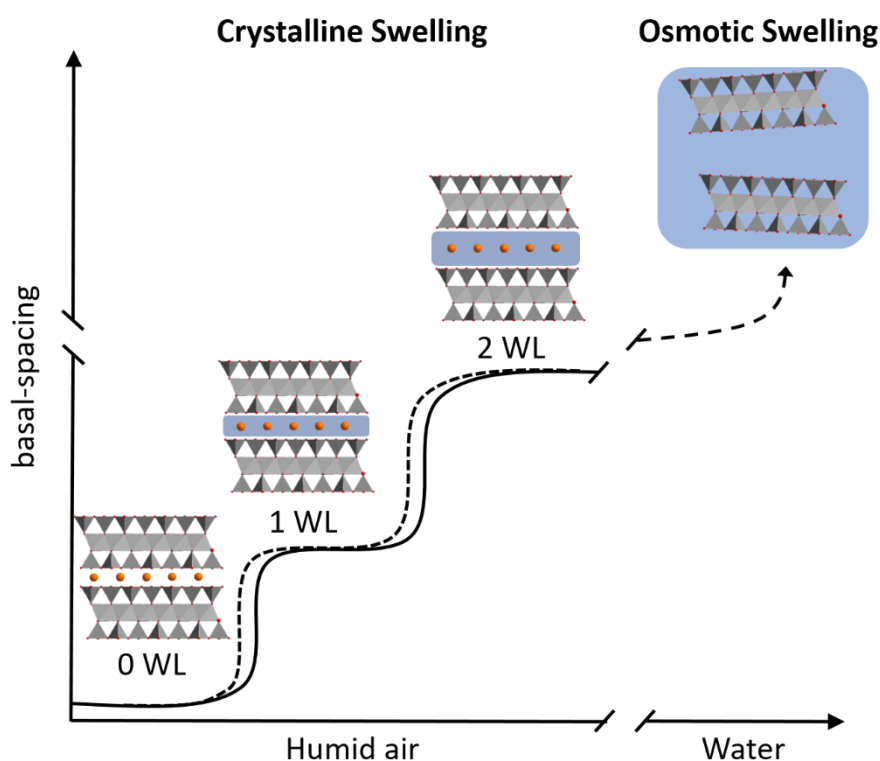


Figure 3: Swelling process of melt synthesized Na-hectorite, starting from the completely dried state (0 WL) with increasing humidity crystalline swelling can be observed with a step-wise increase of the basal-spacing upon hydration of interlayer cations from 0 WL to 2 WL (solid line), while dehydration occurs at slightly lower relative humidities within a hysteresis. At sufficiently high water activities further incorporation of water takes place, ending in a complete disintegration of the tactoids (osmotic swelling).⁸⁵

Introduction

In some cases, repulsive osmotic swelling follows crystalline swelling.^{85, 95-99} This process is characterized by a progressive incorporation of solvent molecules, leading to a continuous separation of the layers and ultimately to a disintegration of the tactoids into single nanosheets, comparable to a dissolution of an ionic crystal limited to one dimension. Thermodynamically allowed delamination by repulsive osmotic swelling represents the most gentle way to quantitatively produce nanosheets with uniform thickness. Contrary to mechanical exfoliation,¹⁰⁰ no mechanical impact is required and the lateral extension, as well as the structure of the parent crystal, are preserved, while the aspect ratio is maximized.⁸⁵

Melt synthesized Na-hectorite is one example of a charged compound, which swells spontaneously in water into nanosheets of approximately 1 nm thickness.³³ In a first stage at highly concentrated suspensions (more than 2.5 vol.%), called the Gouy-Chapman regime, Na-hectorite forms a Wigner crystal. Due to the strong repulsive forces, the nanosheets try to maximize their distance, and therefore, every additional solvent molecule is used to maximize the distance between the nanosheets. Due to the large lateral extensions of Na-hectorite, the nanosheets align parallel towards each other.^{85, 101} This behavior can be used to confirm the completeness of osmotic swelling, as the basal spacing scales to the volume fraction ϕ with ϕ^{-1} . For higher dilutions and larger distances of the nanosheets towards each other, partial screening of the repulsive forces leads to a slightly lower scaling of the basal spacing with the volume fraction of $\phi^{-0.66}$. However, the negatively charged nanosheets still adopt a co-facial arrangement, forming a nematic liquid crystalline phase, as the rotation of the nanosheets is still hindered, due to the large diameter of the nanosheets.^{85, 101} Further dilution to sufficiently small concentrations leads to isotropic suspensions.⁸⁵

In general, the occurrence of osmotic swelling depends on certain main criteria, which were evaluated for synthetic 2:1 layered silicates in detail.^{76, 102} To trigger osmotic swelling, adjacent charged layers need to be separated by incorporation of solvent to a certain threshold value. If the separation can be achieved, the translational entropy of the interlayer species is dominating over the electrostatic attraction between interlayer cations and adjacent layers. Adjacent layers in the ionic crystal will consequently repel each other. The threshold separation can be obtained by a sufficiently high solvation enthalpy of the interlayer ion, supported by a steric pressure arising from the interlayer species. Therefore, the charge equivalent area of the interlayer cation needs to exceed the charge equivalent area of the underlying anionic layer.⁷⁶ For Na-hectorite

with a layer charge of 0.5 *p.f.u.*, the hydration enthalpy of the Na⁺ interlayer cations is sufficient to reach the threshold separation.³³ At higher charge densities, osmotic swelling can be still achieved by supplementing hydration forces of bulky interlayer organo cations.^{76, 99} A typical example for such a hydrophilic and sterically demanding organo cation is the cationic amino sugar *N*-methyl-*D*-glucamonium (meglumine).¹⁰²

Osmotic swelling is not only limited to clay minerals^{85, 99} like Na-hectorite but was also observed for other charged layered compounds like layered titanates^{95, 96} or layered niobates^{97, 98}. However, delamination of layered zeolites via repulsive osmotic swelling to produce functional high-quality nanosheets is still a major challenge. First efforts on selected zeolite structures showed only minor success.^{103, 104} Therefore, the layered zeolite Ilerite was successfully delaminated into single nanosheets to open new opportunities for material science, making layered zeolite nanosheets easily accessible (**Chapter 6.3**).

3.3.2. Heterostructures

Moreover, the layered structure of 2D materials allows the stacking of two or more different types of nanosheets into heterostructures. In that way, the properties of layered compounds can be changed drastically compared to the bulk material and the single layer case, taking advantage of synergistic effects of chemical and physical properties of different layered materials.¹⁰⁵

These heterostructures can be produced in various ways, for example by bottom up approaches via direct growth of nanosheets by using vapor-phase deposition. Alternatively, a combined top-down and bottom-up approach using exfoliation or delamination, followed by re-assembly into alternating stacked structures, can be used.¹⁰⁶ For neutral layered materials, stepwise mechanical exfoliation and subsequent transfer onto substrates is an established procedure for high-quality van der Waals heterostructures.¹⁶ Charged layered compounds, which can be delaminated or exfoliated into single nanosheets, can be easily assembled into heterostructures using flocculation, layer-by-layer assembly or Langmuir-Blodgett assembly and offer a wide range of possibilities.¹⁰⁶ Using the Langmuir-Blodgett technique for example, heterostructures consisting from alternating delaminated perovskite-type LaNb₂O₇⁻ and Ca₂Nb₃O₁₀⁻ nanosheets were produced and the physical properties of the material could be tuned. While both nanosheets are paraelectric, the heterostructure of both shows a ferroelectric behavior.¹⁰⁷

Introduction

Even though the assembly of delaminated or exfoliated nanosheets into respective heterostructures is an attractive approach for the production of materials with unique properties, large-scale industrial production is a challenge. The big advantage of charged layered compounds is the possibility of delamination and the capability of intercalation. Therefore, ion exchange, for example of layered silicates, can be used as an easy and scalable top-down approach to form heterostructures, while the interlayer space is concomitantly functionalized. Starting from the bulk material, upon partial ion exchange, ordered interstratified structures are thermodynamically favored under certain conditions.^{83, 108-110} In such an ordered interstratification two different interlayer species alternating occupy the interlayer space along the stacking direction (**Figure 4**). These heterostructures can be seen as two types of nanoreactors separated by a single nanosheet.

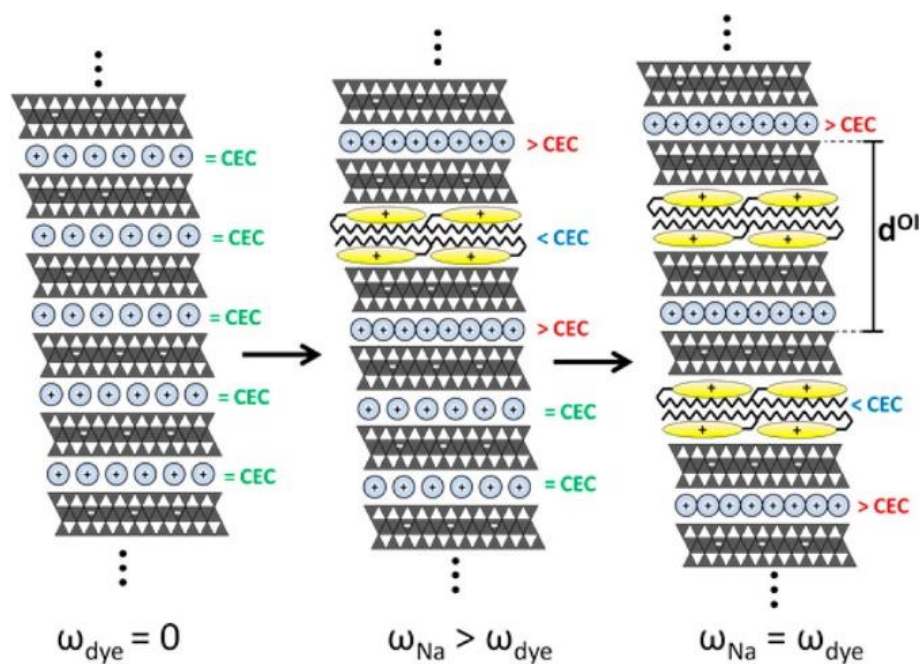


Figure 4: Formation of ordered interstratified heterostructures by partial ion exchange of Na⁺ interlayer cations of Na-hectorite (blue) with dye cations (yellow). Starting from pure Na-hectorite and a relative weighting of dye interlayers $\omega_{\text{dye}} = 0$, first dye exchanged interlayers tend to segregate ($\omega_{\text{dye}} < \omega_{\text{Na}}$) influencing the CEC in adjacent layers. At a certain equilibrium stage an ordered interstratified structure of alternating dye and Na⁺ interlayers is formed ($\omega_{\text{dye}} = \omega_{\text{Na}}$), which results in the formation of a superstructure reflection in the powder X-ray diffraction pattern with a basal spacing d^{01} . The basal spacing corresponds to the sum of the basal spacing of Na⁺ intercalated interlayers and the basal spacing of dye-intercalated interlayers. Further ion exchange would lead to complete ion exchanged Na-hectorite.⁸³ (Reprinted with permission from reference⁸³. Copyright (2014) American Chemical Society)

In contrast to ordered heterostructures, random interstratified intercalation compounds may be formed, where two or more interlayer species occupy the interlayer space in a statistical fashion. Both types of heterostructures might lead to basal spacings in the powder X-ray diffraction pattern, which do not simply correspond to the size of atoms or molecules. Contrary to random interstratifications, the formation of such an ordered interstratification results often in the occurrence of a superstructure reflection in the powder X-ray diffraction (PXRD) pattern, which corresponds to sum of the basal spacing of the two interlayer species (d^{OI}). However, the intensity of the superstructure reflection might be low or is not clearly visible and can be easily overseen. This is especially the case if the electron contrast of the different interlayer species and/or the basal spacing is similar. However, a distinction between a random and an ordered interstratification is often possible applying PXRD. Contrary to an ordered interstratification, random interstratifications show an irrational $00l$ series of low intensity and broad reflections with a varying full width of half maximum.¹¹¹

Formation of such heterostructures is mainly driven by attractive coulomb interactions. This leads to the minimization of the basal spacing in the ionic crystal and to a segregation of the different types of interlayer species into separate interlayer spaces. The segregation results in a different occupation of the different interlayer spaces and consequently in a local charge modulation. As a result, the cation exchange capacity (CEC) of adjacent interlayer spaces is alternating, ensuring charge neutrality in the ionic crystal with a CEC higher and lower than average CEC in adjacent interlayer spaces.⁸³

For instance, by using a synthetic Na-hectorite, heterostructures of functional organic dyes and Na^+ interlayers were accessible, which could be converted into coatings with anisotropic optical properties.¹¹² The production of such heterostructures is not only limited to organic molecules, but is a general mechanism and can also be applied to nanoparticles,¹¹³ complexes¹¹⁴ or other inorganic cations¹⁰⁸. In some cases, the formation of ordered interstratifications is a spontaneous effect like in the case of Ni-exchanged Na-hectorites, as used for CCS (**Chapter 6.1**).

3.4. Selected applications of layered materials

3.4.1. Carbon capture and storage (CCS)

Temporary or permanent removal of CO₂ from the atmosphere is a major challenge to achieve a significant reduction of the anthropogenic CO₂. Materials and techniques for CCS are highly demanding but need to be cheap, environmentally friendly, stable, non-toxic, show a low energy consumption and a high CCS capacity at the same time. Several materials and techniques have been studied and were developed to design materials with a high CCS capacity in the last years. Up to now, the most applicable technology is proposed to use amine solutions, also known as amine scrubbing.¹¹⁵ Nevertheless, amine scrubbing is highly energy consuming and needs up to 40 % of the energy output for its regeneration.¹¹⁶ Alternative materials like zeolites,^{117, 118} metal organic frameworks (MOFs),¹¹⁹ functionalized porous polymers,^{120, 121} activated carbon,¹²² and hybrid solutions¹²³ have also been discussed in literature. However, challenging synthesis, high costs, environmental friendliness and scalability limit large-scale application.

As natural occurring and cheap materials with the capability to swell, layered silicates are promising candidates for CCS. Depending on the type of layered silicate, its layer charge, type of interlayer species and its hydration state, differences in the swelling behavior were observed in response to CO₂.^{93, 124-131} One of the highest volumetric CCS capacities was found for Ni-intercalated hectorites.^{93, 127} However, the reason for the superior behavior compared to other smectites is still unclear and is subject to be studied in **Chapter 6.1** and **Chapter 6.2**.

3.4.2. Permselective hydrogen membranes

CCS represents one possibility to reduce atmospheric CO₂. Alternatively low carbon emission fuels are required to reduce significantly greenhouse gas emissions. Hydrogen, as near-zero emission source with a high-energy conversion efficiency might be a promising alternative energy carrier.¹³² A critical issue that still needs to be solved is the purification of hydrogen from gas mixtures.¹³ Using steam reforming, for example, separation of hydrogen from CO₂, CH₄, and CO is necessary. Purification based on membranes is one of the most promising routes for the production of high purity hydrogen, as they can remove hydrogen selectively from the production cycle, while shifting the thermodynamic equilibrium to the product side for a higher conversion, allowing a continuous production of hydrogen.¹³³

Currently used polymeric membranes are admittedly cheap and can be produced in a large scale but suffer from chemical and thermal stability, durability, and most important, selectivity. However, the versatile structure and the characteristic anisotropic built-up of layered materials, consisting of nanosheets, opens new opportunities for the fabrication of membranes and overcome existing issues. Assembly of nanosheets with appropriate pore size, allowing the selective permeation of hydrogen, represents one possibility of membrane fabrication.¹³⁴ The high thermal and chemical stability of zeolites will allow the use even under harsh conditions and thus overcome the drawbacks of polymer-based membranes.¹³⁵⁻¹³⁹ For membranes built from exfoliated and assembled RUB-15 nanosheets, consisting of hydrogen-permeable 6-MRs of SiO₄-tetrahedra in the layers, H₂/CO₂ selectivities up to 100 could be already achieved.¹⁴⁰

Production of high-quality and high-aspect-ratio zeolite nanosheets is still limited, hindering a low-cost and highly scalable fabrication of perm-selective zeolite membranes. In **Chapter 6.3** a process for the production of such zeolite nanosheets of Illeite, based on delamination by repulsive osmotic swelling is presented, preserving the zeolitic structure and addressing one of the main issues in the preparation of zeolite membranes.

3.4.3. Pearlescent pigments

Layered materials can be moreover used to design materials with exceptional optical properties like, for example, pearlescent pigments. Contrary to pigments in general, which are simply defined as colored materials, insoluble in the medium for application, pearlescent pigments show an appealing interplay of iridescent colors, gloss, and brilliance, similar to natural pearls. This makes pearlescent pigments attractive for widespread of applications ranging from automotive paints to cosmetics.

To obtain this effect, reflection and interference from multiple thin layers with high and low refraction indexes are required. Therefore, sheets or layers with atomically flat surfaces perfectly parallel to the applied surface are necessary to prevent any diffuse reflection.¹⁴¹ For natural pearls, this is achieved by combining alternating layers of CaCO₃ and proteins.¹⁴² To obtain the perfect texture and the high reflectivity for synthetic pearlescent pigments, layered materials need to have an appreciable aspect ratio to ensure a parallel alignment parallel to the surface and giving the desired lustrous effect (**Figure 5**).¹⁴¹

Introduction

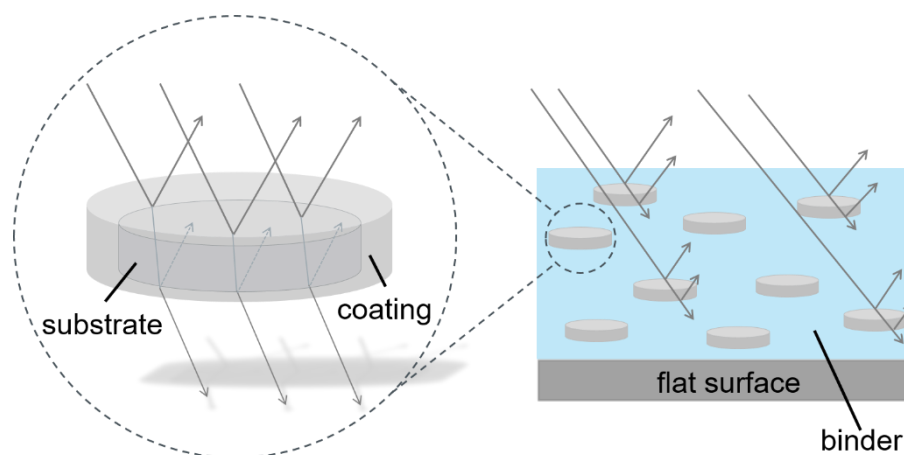


Figure 5: Schematic representation of synthetic pearlescent pigments coated on a flat surface, which are oriented parallel to the applied surface due to the high aspect ratio of the pigment. The pigment consists of a substrate with low refractive index and a coating with high refractive index, leading to reflection at the interfaces of substrate and coating, which then is responsible for the observed interference colors.¹⁴¹

Colors typically arise due to interference of reflected light at the interface between layers with different refractive indices and depend on the thickness of the layers.¹⁴¹ Common used pearlescent pigments are low refractive layered silicates (mica) coated with a highly refracting metal oxide.¹⁴³ The accessible color range by interference is limited and can be extended by coating absorption colors (e.g., iron oxide) or applying colorants on the surface of the pigment. However, such surface modification with colorant reduces the pearlescent effect. Additionally, the distribution of the colorant might be uneven over the surface resulting in insufficient color saturation. Using colored layered substrates represents a gentle and technically attractive way to obtain combined interference and absorption pigments. Such colored substrates were recently developed and can be produced by ion exchange of layered silicates with dye molecules.¹⁴⁴ In **Chapter 6.4**, an alternative approach is presented, based on the synthesis of colored layered substrates containing transition metal ions. Taking advantage of the appealing morphology of Illerite, square-like blue pigments of Egyptian blue can be produced following a topomorphological synthesis route.

3.5. Scope of this thesis

Layered materials offer various physical and chemical properties, which can be used for the development of functional materials. However, the design of materials for specific applications requires the comprehension of the structure and the resulting properties. Therefore, the relationship between the properties of a material and its structural features should be evaluated exemplarily on Ni-exchanged layered silicates, which show a high volumetric CCS capacity due to crystalline swelling when being exposed to CO₂ (**Chapter 3.4.1**).

Fundamental knowledge of one material class can then be transferred to other materials, tailoring their properties. Focus is set in this part on the layered zeolite Ilerite, which should be used to design functional compounds. Here, the delamination via repulsive osmotic swelling, which is well understood for layered silicates, should be transferred to layered zeolites, to produce zeolite nanosheets. These nanosheets allow the production of thin zeolite films, which can be used, for example, for gas barrier applications or as permselective hydrogen membranes. Moreover, the use of intercalation compounds to synthesize functional materials should be discussed exemplarily for colored effect pigments, like Egyptian blue. The concept of this work is based on the following steps:

- Structure-property relationship of Ni-hectorites
 - Synthesis of Ni-hectorite by using charge homogeneous, melt synthesized Na-hectorite and successive ion exchange
 - Structural analysis applying spectroscopic, diffraction and thermal analysis
 - Mechanistic study of the swelling process upon exposure to CO₂
- Systematic synthesis of functional materials based on Ilerite
 - Synthesis of large aspect ratio layered zeolite particles of Ilerite
 - Delamination into Ilerite nanosheets
 - Structural characterization of Ilerite nanosheets and processing into thin films
 - Topomorphological conversion of Ilerite into the blue pigment Egyptian blue by ion exchange

4. Synopsis

The presented cumulative thesis consists of four manuscripts, dealing with the investigation of layered compounds, their properties and their use for the design of materials for specific applications (graphical synopsis in **Figure 6**). Comprehension of the structure and the resulting properties of a material are the focus of the first part of this thesis, while the second part deals with the directed design of functional materials.

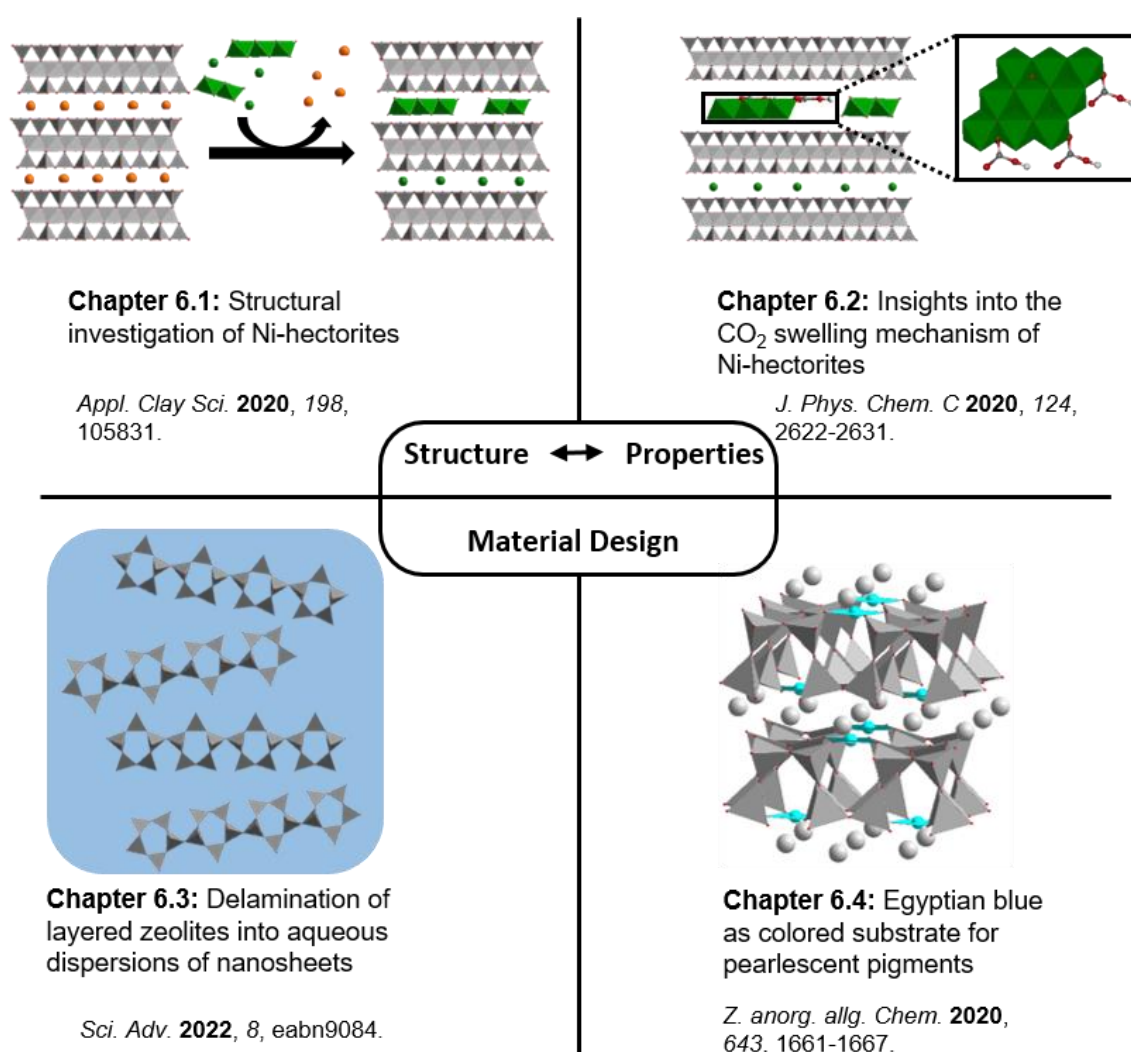


Figure 6: Graphical synopsis of this thesis, representing the main topics.

Synopsis

The first two manuscripts deal with Ni-hectorites as promising CCS materials and their structural features to understand the rather uninvestigated swelling mechanism under CO₂ pressure. In **Chapter 4.1** and the publication “Spontaneous formation of an ordered interstratification upon Ni-exchange of Na-fluorohectorite” (**Chapter 6.1**), the resulting structure of Ni-hectorite upon Ni-exchange of synthetic Na-hectorite was analyzed in respect to the potential formation of an ordered interstratifications that might have been overseen so far, considering the high condensation tendency of nickel, forming nickel hydroxides during the ion exchange.

In **Chapter 4.2** and the publication “CO₂ Capture by Nickel Hydroxide Interstratified in the Nanolayered Space of a Synthetic Clay Mineral” (**Chapter 6.2**), the swelling process of Ni-hectorite with CO₂ was investigated in detail and could be explained with the help of the previously solved structure from **Chapter 6.1**. Combining spectroscopic and diffraction methods, the interaction of CO₂ during swelling could be traced back to the intercalated nickel hydroxide species, which was formed during the Ni-exchange.

The last two manuscripts transfer known reactivities and properties of layered compounds to the layered zeolite Ilerite to design functional materials for potential later applications with regard to industrial scalability. In **Chapter 4.3** and the publication “Nematic suspension of a microporous layered silicate obtained by forceless spontaneous delamination via repulsive osmotic swelling for casting high-barrier all Inorganic Films” (**Chapter 6.3**), for the first time high aspect ratio, layered zeolite nanosheets of Ilerite were produced. Contrary to existing routes of zeolite nanosheet production, applying delamination via repulsive osmotic swelling, the sheet diameter of the parent compound Ilerite was preserved and nanosheets with exceptional aspect ratio could be obtained. The nanosheets were characterized and could be processed into thin inorganic zeolite films with excellent gas barrier properties to prove their functionality.

In **Chapter 4.4** and the publication “Synthesis of Large Platelets of Egyptian Blue via Pseudomorphosis after NaRUB-18” (**Chapter 6.4**), Ilerite was used as a starting material for the transformation into Egyptian blue. Advantageous, the morphology of Ilerite and consequently the high aspect ratio could be maintained in an industrially feasible process. Thus, the obtained Egyptian blue can act as absorption pigment and substrate for pearlescent pigments in one.

4.1. Structural investigation of Ni-hectorites

Intercalation chemistry is a widely observed phenomenon for charged layered compounds like smectite clay minerals and can be used to functionalize their interlayer space (**Chapter 3.3**). For example, Ni-exchange of interlayer cations of Na-hectorite was used to obtain materials, which are capable to swell in response to CO₂ at near ambient conditions.⁹³ This behavior makes these smectites highly attractive as CCS materials with a high volumetric CCS capacity for temporary or permanent removal of CO₂ (**Chapter 3.4.1**). However, the reason of this phenomenon remains unclear. In order to explain the high swelling tendency in response to CO₂ and maximize the CCS capacity regarding potential industrial application, the knowledge of the structure of Ni-hectorite is essential.

A first hint of Ni-hectorite not being a simple intercalation compound, only consisting from isolated ion-exchanged Ni²⁺ ions is given in the drying and hydration behavior, as swelling and drying follows a continuous behavior typical for random or ordered interstratified compounds.¹⁴⁵ Therefore, Ni-hectorite was prepared by Ni-exchange of charge homogeneous, melt synthesized Na-hectorite with a layer charge of 0.5 p.f.u. and was compared with structural characterized Ca-exchanged Na-hectorite (Ca-hectorite) and Na-hectorite itself. For these charge homogeneous hectorites, hydration and drying occur in discrete steps with the size of molecules or atoms (**Chapter 3.3.1**). This leads at 43 % r.h. to the formation of a 1 WL structure (12.3 Å) in the case of Na-hectorite and a 2 WL structure (15.2 Å) for the higher charged interlayer cation Ca²⁺. After careful drying at conditions used for CO₂ swelling, the basal spacing decreases to < 10 Å, corresponding to the thickness of the silicate layer due to the release of 1 or 2 WL water. Even after drying, Ni-hectorite remains at an atypical high basal spacing of 11.4 Å and an interlayer height of 1.8 Å, which is even smaller than the typical size of a water molecule. Consequently, the basal spacing is too high for the 0 WL structure and too low for a 2 WL hydrate. Moreover, the determined Ni/Si-ratio of Ni-hectorite, applying ICP-OES, exceeds the theoretical expected Ni-content required for charge balance significantly, indicating that the conducted Ni-exchange is not only a simple ion exchange reaction. Consequently, the structure can be only explained by an ordered or random interstratification (**Chapter 3.3.2**). These structures can be easily overseen, especially if superstructure reflections are not clearly visible.

Synopsis

Earlier published EXAFS studies already revealed the presence of a brucite-like $\text{Ni}(\text{OH})_2$ -species, which was proposed by the authors to be located at the external surfaces of the hectorite surfaces.¹⁴⁶ In this publication, we considered the high condensation tendency of $[\text{Ni}(\text{H}_2\text{O})_6]^{2+}$ cations above a pH of 4 to form brucite-type $\text{Ni}(\text{OH})_2$. At the pH of Ni-exchange of 6.9 and in the presence of negatively charged hectorite nanosheets, oligocations consisting of small positively charged $\text{Ni}(\text{OH})_2$ -structures are formed and may finally be intercalated into the interlayer space of hectorite. In this term, chlorite structures consisting of positively charged metal hydroxide layers in the interlayer space of smectites may form instead of an isolated $[\text{Ni}(\text{H}_2\text{O})_6]^{2+}$ interlayer species. Alternatively, intermediate structures of chlorite type interlayers and isolated Ni-cations in the form of ordered interstratifications can be formed, also known as corrensites.

The formation of such an intercalated positively charged $\text{Ni}(\text{OH})_2$ -structure was confirmed by UV/Vis-spectroscopy and XPS, clearly indicating the presence of a β - $\text{Ni}(\text{OH})_2$ species. According to XPS, an accessory $\text{Ni}(\text{OH})_2$ side phase on external surfaces could be ruled out and indicated a positivated Ni-species in the interlayer space of Ni-hectorite. Chrono amperometric measurements proved that a major amount of the Ni-species is present as Ni^{2+} . This indicates a charge compensation mechanism by protonation of the $\text{Ni}(\text{OH})_2$ -islands rather than oxidation of Ni^{2+} to Ni^{3+} , forming chlorite-like $[\text{Ni}(\text{OH})_{2-y}(\text{H}_2\text{O})_y]_x^{y+}$ interlayers. As the basal spacing of a fully condensed chlorite structure, even after careful drying is expected to be in the range of 14 to 15 Å, the observed basal spacing of dried Ni-hectorite of 11.4 Å is significantly lower. Consequently, the present structure consist of both, isolated Ni-interlayer species and condensed $\text{Ni}(\text{OH})_2$ interlayers. Thermal analyses was used to analyze the drying behavior of Ni-hectorite in detail and confirmed the presence of both species. It turned out that at the temperature of 150°C used for drying, coordinated water of a potentially uncondensed $[\text{Ni}(\text{H}_2\text{O})_6]^{2+}$ interlayer species and interlayer water is removed, while the $[\text{Ni}(\text{OH})_{2-y}(\text{H}_2\text{O})_y]_x^{y+}$ interlayers remain unaffected. Using inelastic neutron scattering (INS) confirmed their presence, only showing vibrations, which could be assigned to the $\text{Ni}(\text{OH})_2$ species.

The structure of Ni-hectorite can be explained either by an ordered or a random interstratification of condensed $[\text{Ni}(\text{OH})_{2-y}(\text{H}_2\text{O})_y]_x^{y+}$ and uncondensed $[\text{Ni}(\text{H}_2\text{O})_6]^{2+}$ interlayers. As the electron density of both species and the basal spacing of the hydrated phase is quite similar, distinction is difficult. However, changing the hydration state of the uncondensed smectite Ni-interlayers to the 1 WL structure, changed the electron density and the basal spacing so far, that a slightly visible superstructure reflection was already visible, indicating the presence of an ordered interstratified structure of both species. To confirm the postulated ordered interstratification, two approaches were conducted to change the basal spacing of the smectite interlayers and concomitantly the electron contrast (**Figure 7**).

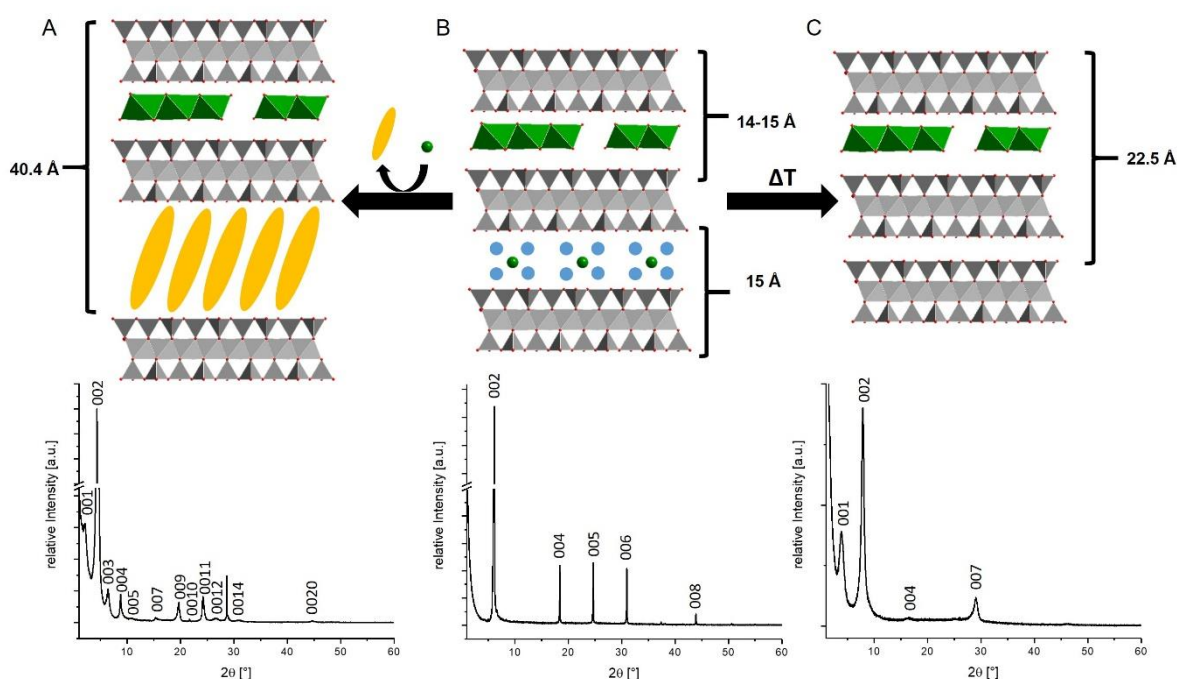
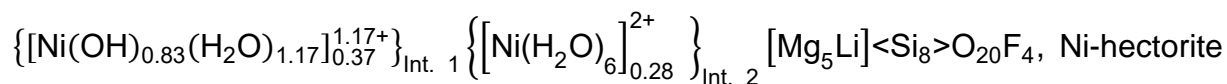


Figure 7: Two approaches to identify the proposed ordered interstratified structure of Ni-hectorite, starting from the as prepared material (B) either cation exchange with a long chain alkylammonium cation (A) or thermal annealing (C) can be used in the case of Ni-hectorite.¹⁴⁷ (Reprinted with permission from reference¹⁴⁷, Copyright (2020) with permission from Elsevier)

Selective cation exchange of the uncondensed Ni^{2+} interlayers of Ni-hectorite with a long-chained and bulky *n*-alkylammonium cation (C_{16} , $\text{C}_{16}\text{H}_{33}\text{NH}_3\text{Cl}$) led to clearly visible, highly crystalline superstructure of alternating arrangement of paraffin-like C_{16} interlayers and condensed $[\text{Ni}(\text{OH})_{2-y}(\text{H}_2\text{O})_y]_x^{y+}$ interlayers (**Figure 7A**). ICP-OES and CHN-analysis was used to determine the composition of the resulting structure, giving a composition of $\left\{ [\text{Ni}(\text{OH})_{2-y}(\text{H}_2\text{O})_y]_{0.37}^{y+} \right\}_{\text{Int. } 1} \left\{ \text{C}_{16}_{0.72} \right\}_{\text{Int. } 2} [\text{Mg}_5\text{Li}] < \text{Si}_8 > \text{O}_{20}\text{F}_4$ per unit cell. Comparison with the total Ni-content of the as-synthesized Ni-hectorite allows the determination of the structural formula of Ni-hectorite. With a composition of

Synopsis



forms spontaneously a corrensite-like structure, built from the alternation of $\left[\text{Ni}(\text{OH})_{0.83}(\text{H}_2\text{O})_{1.17} \right]_{0.37}^{1.17+}$ and $\left[\text{Ni}(\text{H}_2\text{O})_6 \right]_{0.28}^{2+}$ interlayers (**Figure 7B**). The driving force of the formation of such an ordered structure was assumed to be the higher selectivity of $\left[\text{Ni}(\text{OH})_{2-y}(\text{H}_2\text{O})_y \right]_x^{y+}$ oligocations, present in the exchange solution for the interlayer space compared to isolated Ni-ions. Alternatively, thermal annealing at 600°C, followed by rehydration at 43 % r.h. improved the visibility of the superstructure, leading to a collapsed smectite interlayer (**Figure 7C**). The collapsed talc-like interlayer remained collapsed even after rehydration, while the chlorite interlayers were partially rehydrated.

Simple ion exchange of charged layered compounds consequently produced complex structures consisting of different interlayer types. These structures can be easily overseen by simple analytical methods. However, such random or ordered interstratified structures might be the reason of the unique behavior of a material like Ni-hectorite. Only with the knowledge of these complex structural features of Ni-hectorite, which exceed the simple intercalation of isolated Ni^{2+} ions, comprehension of the CO_2 swelling mechanism is possible.

4.2. Insights into the CO₂ swelling mechanism of Ni-hectorites

The evaluated structure of Ni-hectorite in **Chapter 4.1**, consisting of a corrensite-like structure, formed by alternation of $[\text{Ni}(\text{OH})_{0.83}(\text{H}_2\text{O})_{1.17}]_{0.37}^{1.17+}$ and $[\text{Ni}(\text{H}_2\text{O})_6]_{0.28}^{2+}$ interlayers, was used to explain the swelling mechanism in response to CO₂. Therefore, Ni-hectorite was prepared analogous to **Chapter 4.1** and was analyzed under exposure to CO₂ in dried and at 43 % r.h. hydrated state, applying powder X-ray diffraction, Raman spectroscopy, and INS.

The swelling process of Ni-hectorite at 300 K with CO₂ can be traced by changes of the basal spacing in the PXRD pattern. For dried Ni-hectorite, with a collapsed smectite interlayer and chlorite type interlayers, the corresponding 002 reflection of the superstructure shifts from 11.40 Å to 12.29 Å upon increasing CO₂ pressure. Within this process, the number of swollen interlayers increases until the swelling process is complete. Gravimetric adsorption data demonstrate that the swelling is mainly caused by CO₂, as the changes in the PXRD pattern correlate closely with the gravimetric uptake of CO₂. Hydrated Ni-hectorite showed a minor swelling from 14.82 Å to 15.06 Å compared to dry Ni-hectorite.

Interaction of Ni-hectorite with CO₂ was analyzed in detail with *in situ* Raman spectroscopy. However, the high fluorescence of Ni²⁺ did not allow the measurement of dried Ni-hectorite. For fully hydrated Ni-hectorite only expected modes for hectorite, the two interlayer species and water were observed. After exposure to 40 bar CO₂, interactions of CO₂ with interlayer water result in a local modification of the water population in the interlayers, changing the shape of the spectra in the H₂O/OH-region. Moreover, changes of vibrations corresponding to the $[\text{Ni}(\text{OH})_{0.83}(\text{H}_2\text{O})_{1.17}]_{0.37}^{1.17+}$ interlayer species and vibrations of a potentially formed CO₃²⁻ species could be observed, already indicating interactions of CO₂ with the intercalated $[\text{Ni}(\text{OH})_{0.83}(\text{H}_2\text{O})_{1.17}]_{0.37}^{1.17+}$ species.

INS was then used to understand these interactions in detail. Dry Ni-hectorite showed, as mentioned earlier in **Chapter 4.1**, only vibrations associated with the intercalated $[\text{Ni}(\text{OH})_{0.83}(\text{H}_2\text{O})_{1.17}]_{0.37}^{1.17+}$ interlayer species. Exposing dry Ni-hectorite to CO₂ leads to significant changes in the INS spectrum. Most prominent changes correspond to vibrations associated with the intercalated $[\text{Ni}(\text{OH})_{0.83}(\text{H}_2\text{O})_{1.17}]_{0.37}^{1.17+}$ species, which are losing significantly intensity. Contrary to dried Ni-hectorite, Na-hectorite and other smectites, which contain only isolated, uncondensed interlayer cations, show no sign of swelling after being exposed to CO₂. This indicated that the smectite interlayers of

Synopsis

Ni-hectorite play no role for the CO₂ swelling in the dried state and only the condensed species is of relevance. In this term, the smectite interlayer remains unaffected and stays collapsed at a basal spacing of 9.6 Å, while the [Ni(OH)_{0.83}(H₂O)_{1.17}]_{0.37}^{1.17+} interlayer swell crystalline from 13-14 Å to 15-16 Å (**Figure 8**). The swelling process, as traced by PXRD, is reversible. After the release of CO₂, the 002 reflection returns to the initial position. Moreover, changes in the INS spectrum return mostly to the initial state. Permanent structural changes in the [Ni(OH)_{0.83}(H₂O)_{1.17}]_{0.37}^{1.17+} species could not be completely ruled out due to differences in the INS spectrum after CO₂ release compared to the initial spectrum but might be an artefact of a transient state during the return to the initial structure.

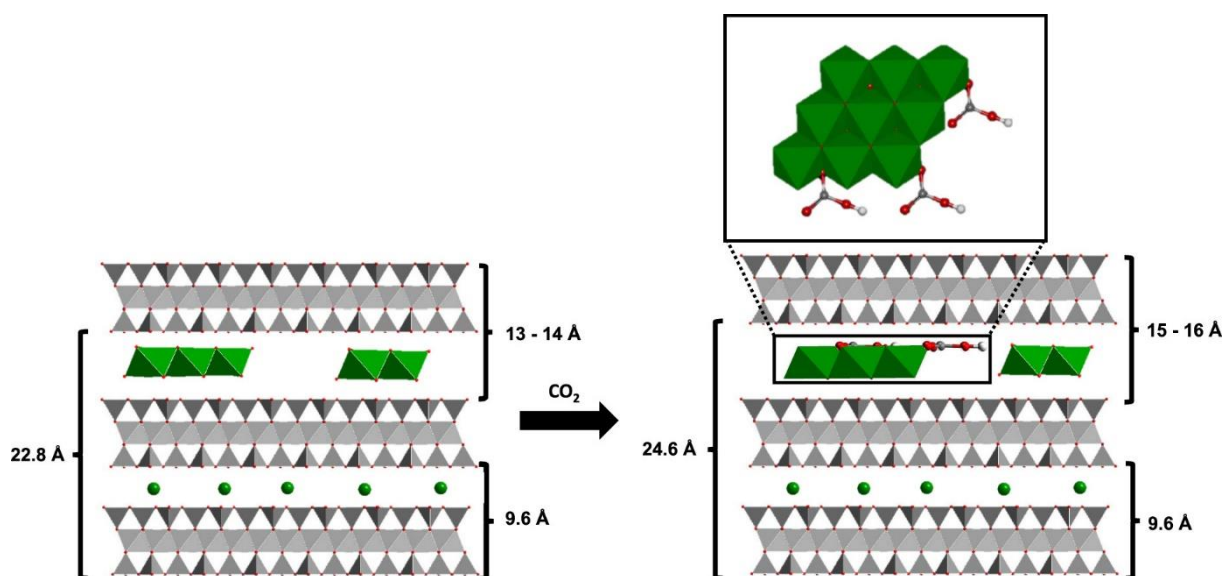


Figure 8: Schematic representation of the swelling mechanism in dried Ni-hectorite under exposure to CO₂, representing the proposed interactions of CO₂ with the intercalated [Ni(OH)_{0.83}(H₂O)_{1.17}]_{0.37}^{1.17+} interlayer species.⁹⁴ (Reprinted from reference⁹⁴)

In the case of hydrated Ni-hectorite, besides vibrations of the intercalated [Ni(OH)_{0.83}(H₂O)_{1.17}]_{0.37}^{1.17+} species, modes corresponding to different types of interlayer water were observed. Due to various hydrogenous species, changes upon exposure to CO₂ are less obvious than in the case of dried Ni-hectorite. However, observed changes in the Raman spectra and the INS spectrum, indicated a similar interaction of CO₂ with the Ni-hectorite structure as for the dried case. Thus, swelling occurs solely in the chlorite-like interlayers.

From Raman spectroscopy, the formation of a potential CO_3^{2-} species was already observed. Considering the formation of such a species combined with the observed changes in the INS spectra, a mechanism based on the reaction of goethite with CO_2 under anhydrous conditions was proposed.¹⁴⁸ Following the reaction mechanism of $\text{Ni-OH} + \text{CO}_2 \rightarrow \text{Ni-O}-(\text{HCO}_2)$, hydroxide groups at the edges of the $[\text{Ni}(\text{OH})_{0.83}(\text{H}_2\text{O})_{1.17}]_{0.37}^{1.17+}$ interlayer species, are converted into bicarbonates and CO_2 is chemisorbed as a bicarbonate leading to the macroscopically observed swelling. Although the formation of such a structure could not be verified directly by spectroscopy, the role of the $[\text{Ni}(\text{OH})_{0.83}(\text{H}_2\text{O})_{1.17}]_{0.37}^{1.17+}$ interlayer species is crucial for the swelling. Moreover, DFT simulations reinforce this proposed mechanism, as calculated basal spacings are in agreement with the observed experimental data.

Consequently, due to the formation of a CO_3^{2-} species, spontaneously formed $[\text{Ni}(\text{OH})_{0.83}(\text{H}_2\text{O})_{1.17}]_{0.37}^{1.17+}$ interlayers by Ni-exchange of Na-hectorite are responsible for the superior CCS behavior of Ni-hectorites. This can be used in future to optimize the volumetric CCS capacity of Ni-hectorites by simply increasing the amount of condensed chlorite-like interlayers. By adjusting the pH of the exchange solution, chlorites may be formed consisting only of condensed $\text{Ni}(\text{OH})_2$ interlayers, leading to a doubling of the CCS capacity and making Ni-hectorites to technologically competitive CCS materials.

4.3. Delamination of layered zeolites into aqueous dispersions of nanosheets

Comprehension of the properties of one material can be used to adapt specific mechanisms to a new class of material. For example, the swelling behavior of clay minerals in water like Na-hectorite, was analyzed in detail and is widely understood. Repulsive osmotic swelling of these layered silicates is the most gentle way to obtain nanosheets from the parent compound, which are potentially useful for a broad range of applications such as polymer filler for gas barrier films (**Chapter 3.3.1**). This delamination process is still limited to selected classes of charged layered materials. Despite the broad features of layered zeolites like intrinsic porosity or catalytic activity, examples of the delamination are limited and large-scale production is still challenging. Nanosheets of layered zeolites with pores of 6 MRs across the layers for instance, would allow the production of permselective hydrogen membranes (**Chapter 3.4.2**). To overcome these issues, nanosheets of Ilerite were produced in a scalable, economically friendly delamination process applying repulsive osmotic swelling.

Ilerite can be synthesized without any SDA under mild conditions and in large quantities applying a water-based sol-gel process, starting from NaOH, H₂O, and a colloidal SiO₂ dispersion, making Ilerite an attractive compound for industrial applications.⁶⁸⁻⁷⁰ Following this simple synthesis route, phase pure Ilerite in the form of large-square like platelets with an average diameter of 6.7 μm were obtained. Phase purity was checked with PXRD and the PXRD pattern could be completely indexed according to literature data. Contrary to the permanent layer charge of layered silicates, the layer charge of Ilerite originates from only half protonated Si-O⁻ groups at the basal surfaces and thus depends on the pH. The layer charge itself is compensated by interlayer Na⁺ (**Chapter 3.2.2**). For triggering osmotic swelling, the layers of the crystal need to be separated to a certain threshold value by incorporation of solvent molecules (for details see **Chapter 3.3.1**). Cation exchange of interlayer Na⁺ with a suitable hydrophilic and sterically demanding cationic amino sugar *N*-methyl-*D*-glucamonium (meglumine), followed by a reduction of the ionic background was used to trigger osmotic swelling, resulting in zeolite nanosheets (**Figure 9**).

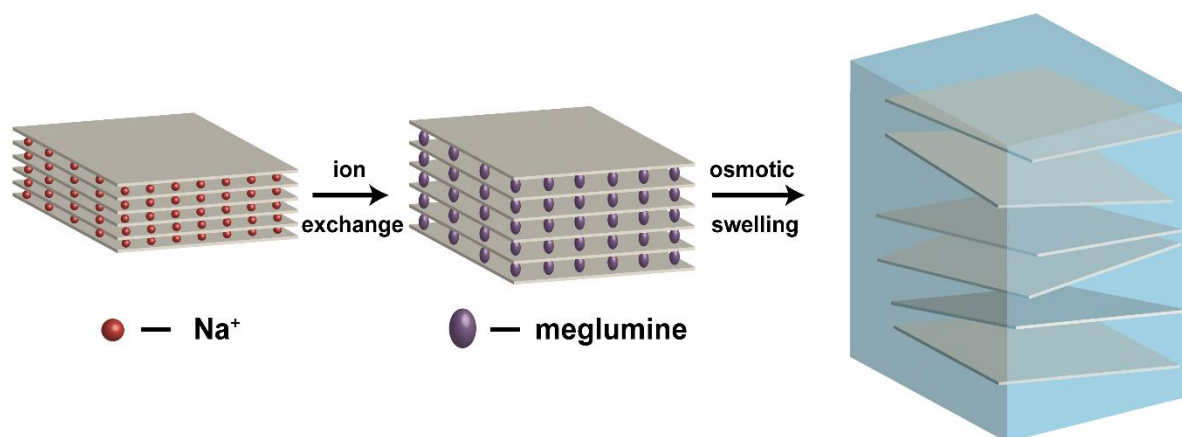


Figure 9: Delamination process of Illerite, starting with cation exchange of interlayer Na^+ , followed by reduction of the ionic strength to trigger osmotic swelling into dispersions of single nanosheets.¹⁴⁹ (Adapted from reference¹⁴⁹)

As the layer charge is highly dependent on the pH, the pH of the meglumine solution was adjusted to a pH of 9, where Illerite is stable and a permanent layer charge is ensured, while meglumine is still protonated. Completeness of the meglumine exchange of the obtained meglu-Illerite was checked with PXRD and EDX. With PXRD of a textured sample, an increase of the basal spacing from 11.0 Å to 14.9 Å was observed, while with EDX any residual interlayer Na^+ could be excluded. CHN-Analysis was used to confirm meglumine intercalation and was used to calculate the amount of intercalated meglumine as well as the charge equivalent area of meglu-Illerite. The calculated meglumine content of 2.16 mmol/g was slightly lower than the initial Na^+ content of 2.83 mmol/g, indicating a partial reduction of the layer charge due to protonation of the Si-O^- groups. However, the remaining layer charge and the corresponding charge equivalent area of 77 Å²/charge was still high enough to enable osmotic swelling with intercalated meglumine in water.

Reduction of the ion background was then used to trigger delamination of meglu-Illerite into the respective nanosheets and nematic suspensions were obtained. SAXS confirmed the uniform separation to large distances with a co-facial arrangement of the single nanosheets, leading to a rational $00l$ series with a basal spacing of 10.6 nm. Reflections of the basal spacing of restacked meglu-Illerite were not observed, confirming the complete delamination. As osmotic swelling is characterized by a progressive incorporation of solvent molecules, the obtained highly concentrated gel was further diluted with water. The continuous separation of the layers and ultimately the disintegration into single nanosheets could be also traced with SAXS.

Synopsis

Complete conversion of meglu-Ilerite into single nanosheets was furthermore confirmed with AFM. For highly diluted dispersions, only nanosheets of 1.5 nm thickness were found, in agreement with PXRD. During the delamination, the structure of the nanosheets was maintained. The integrity of the structure and the completeness of delamination could be verified by electron diffraction, comparing the experimental diffraction pattern with the simulated pattern of a single nanosheet and the one of the bulk material. During delamination, centrosymmetry is lost and absent reflections are observed. Moreover, the diffraction pattern of turbostratic restacked nanosheets showed significant differences, consisting of misoriented patterns of multiple single layers.

Due to the gentle delamination by thermodynamically allowed repulsive osmotic swelling, the lateral extensions of the parent compound are maintained and can be converted into the respective nanosheets. Thus, an aspect ratio of more than 9000 can be achieved for Ilerite nanosheets. This renders these nanosheets appropriate for gas barrier applications, where the performance significantly depends on the aspect ratio. Nematic suspensions of the zeolite nanosheets are easily processable. The processability was shown by casting functional films. Using doctor blading for example, thin functional zeolite films were produced. Permeation tests confirmed the excellent barrier properties of these films, showing their functionality.

In summary, simple ion exchange of layered zeolites with a bulky, cheap, hydrophilic organic cation like meglumine allows for the first time the quantitative delamination of layered zeolites like Ilerite into nanosheets via repulsive osmotic swelling. The obtained Ilerite nanosheets show an exceptional aspect ratio and are easy to process into functional thin films. Moreover, in the present work used Ilerite consists of layers with hydrogen permeable pores of 6 MRs across the layers, making the obtained nanosheets potentially suitable for the production of hydrogen membranes.

4.4. Egyptian blue as colored substrate for pearlescent pigments

Cation exchange of charged layered compounds is not limited to functionalize layered compounds directly, as shown specifically for Ni-hectorites. Moreover, intercalation compounds can be used as starting materials for further synthesis. The uniform square-shaped, platy morphology of Illerite is particularly attractive for applications as a pearlescent pigment (**Chapter 3.4.3**). To expand the accessible color range of pearlescent pigments and prevent the use of colorants, Illerite, also known as NaRUB-18, was used to synthesize the blue pigment Egyptian blue, preserving the attractive morphology and the aspect ratio of the starting compound (pseudomorphosis).

As one of the oldest synthetic blue pigments, Egyptian blue with a chemical composition of $\text{CaCuSi}_4\text{O}_{10}$ possesses a layered structure like Illerite, which consists of condensed SiO_4 tetrahedra forming corrugated layers. The color originates from Cu^{2+} , coordinated by the non-bridging oxygen atoms of the SiO_4 tetrahedra, while the layer charge is compensated by interlayer Ca^{2+} (**Figure 10**). With atomically flat surfaces and the layered structure, blue pearlescent pigments like Egyptian blue are sought after in industry and are therefore highly interesting for the use as a colored substrate.

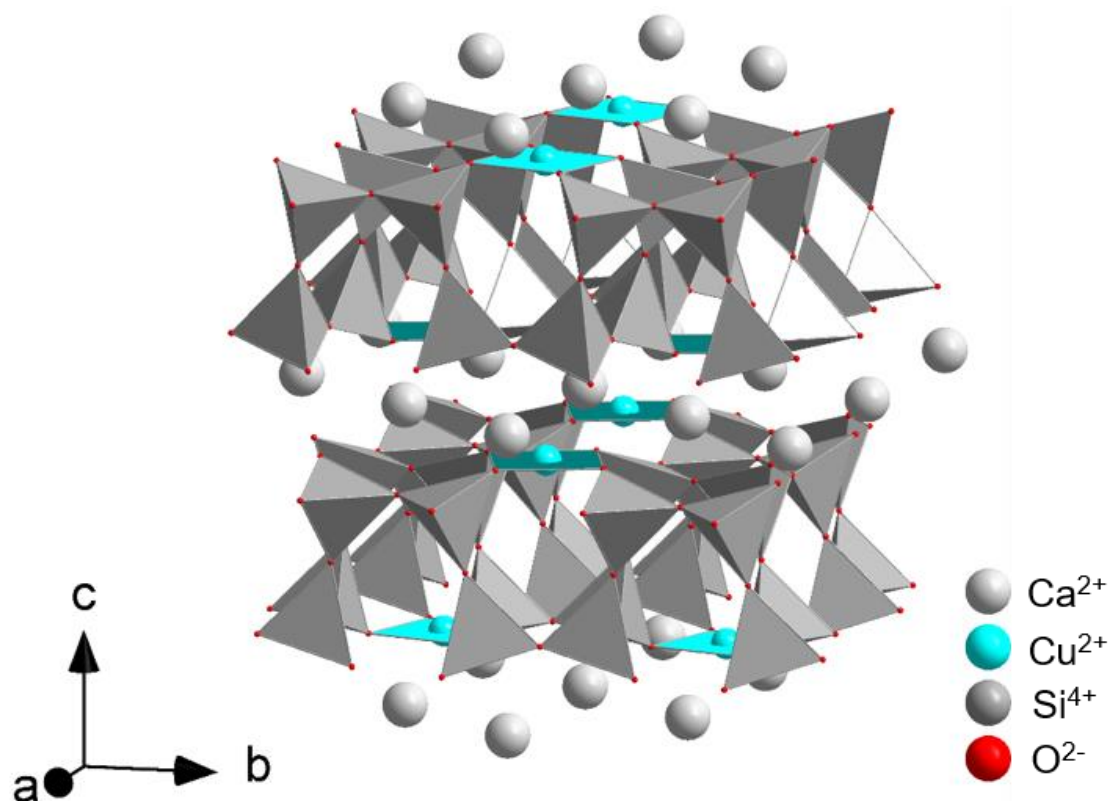


Figure 10: Crystal structure of Egyptian blue, solved by Pabst 1959¹⁵⁰ and later refined using neutron scattering¹⁵¹.

Synopsis

High costs or insufficient morphologies hinder the use of established synthesis routes like solid-state or hydrothermal synthesis in industry. Moreover, Cu^{2+} will be reduced at ambient oxygen fugacity at temperatures above 1150°C , preventing the use of melt synthesis, which would otherwise allow the growth of high aspect ratio crystals, necessary for the use as substrates for pearlescent pigments. The synthesis temperature can be reduced by using Ilerite as starting compound for the pseudomorphosis into Egyptian blue.

NaRUB-18 or Ilerite can be obtained phase pure as large, square platelets in a mild sol-gel synthesis in large quantities (**Chapter 3.2.2**), making it a cheap and environmentally friendly starting compound. Despite the structural differences, NaRUB-18 can be already converted at relatively low temperatures of 1000°C to Egyptian blue. Therefore, interlayer Na^{+} of NaRUB-18 was exchanged in the first step by Cu^{2+} , using Cu-acetate to obtain CuRUB-18. Completeness of this ion exchange was checked with EDX, excluding any remaining interlayer Na^{+} , while SEM images exclude any morphological changes as expected. As the Cu-content of CuRUB-18 is sub-stoichiometric compared to Egyptian blue, additional Ca^{2+} and Cu^{2+} were added in the form of CaCO_3 and CuSO_4 to obtain a Ca:Cu:Si-ratio of 1:1:4 as required for Egyptian blue. Therefore, ground CaCO_3 and powder of CuRUB-18 were mixed with the desired volume of CuSO_4 solution and evaporated, to obtain a gel. Egyptian blue was obtained after annealing the gel at 1000°C . However, CuO was formed as a side phase during the synthesis. The formation of CuO could not be prevented but could easily be removed by washing with concentrated HCl.

Rietveld refinement was conducted to confirm the formation of Egyptian blue after purification and was in good agreement with literature data. The determined Cu-content according to AAS of 1.69 mmol/g was lower than commercial available Egyptian blue (2.26 mmol/g), synthesized with a melt-flux procedure, which in turn was again lower compared to the theoretically expected Cu-content of the ideal Egyptian blue composition (2.66 mmol/g). The absorption spectrum of the synthesized and purified Egyptian blue, as well as the commercial available one, showed all expected transitions for the square-planar ligand field of Cu^{2+} in the crystal structure. Most likely, the lower Cu-content results most likely in a lower absorbance and consequently in a less intense blue color compared to the commercially available product. Despite the reconstruction during the synthesis, the morphology of NaRUB-18 could be conserved, as indicated by SEM and SLS, resulting in the desired square-shaped platelets of Egyptian blue.

Conversion of NaRUB-18 led to the fabrication of blue pigments of Egyptian blue, preserving the initial morphology of the starting material. Being technical benign, environmentally friendly, and allowing the control of the morphology this process is advantageous over existing hydrothermal, solid-state, or melt flux synthesis routes. Especially if the synthesis of compounds with desired particle sizes or morphologies applying classical synthetic methods is not possible or temperatures are limited, like in the case of Egyptian blue, alternative synthetic approaches may be used.

5. Literature

1. D. Gielen, F. Boshell and D. Saygin, *Nat. Mater.*, **2016**, *15*, 117-120.
2. M. Hofmann, H. Hofmann, C. Hagelüken and A. Hool, *Sustain. Mater. Technol.*, **2018**, *17*, e00074.
3. S. Chu and A. Majumdar, *Nature*, **2012**, *488*, 294-303.
4. A. M. Abdalla, S. Hossain, O. B. Nisfindy, A. T. Azad, M. Dawood and A. K. Azad, *Energy Convers. Manag.*, **2018**, *165*, 602-627.
5. C.-H. Yu, C.-H. Huang and C.-S. Tan, *Aerosol Air Qual. Res.*, **2012**, *12*, 745-769.
6. C. Hepburn, E. Adlen, J. Beddington, E. A. Carter, S. Fuss, N. Mac Dowell, J. C. Minx, P. Smith and C. K. Williams, *Nature*, **2019**, *575*, 87-97.
7. D. W. Keith, *Science*, **2009**, *325*, 1654-1655.
8. N. Yadav, F. Seidi, D. Crespy and V. D'Elia, *ChemSusChem*, **2019**, *12*, 724-754.
9. A. I. Osman, M. Hefny, M. I. A. Abdel Maksoud, A. M. Elgarahy and D. W. Rooney, *Environ. Chem. Lett.*, **2020**, *19*, 797-849.
10. G. A. Olah, T. Mathew, A. Goeppert and G. K. Surya Prakash, *Top. Catal.*, **2018**, *61*, 522-529.
11. R. F. Service, *Science*, **2009**, *324*, 1257-1259.
12. J. Tollefson, *Nature*, **2010**, *464*, 1262-1264.
13. G. Bernardo, T. Araújo, T. da Silva Lopes, J. Sousa and A. Mendes, *Int. J. Hydrog. Energy*, **2020**, *45*, 7313-7338.
14. S. Adhikari and S. Fernando, *Ind. Eng. Chem. Res.*, **2006**, *45*, 875-881.
15. W. J. Roth, B. Gil, W. Makowski, B. Marszalek and P. Eliášová, *Chem. Soc. Rev.*, **2016**, *45*, 3400-3438.
16. K. S. Novoselov, A. Mishchenko, A. Carvalho and A. H. Castro Neto, *Science*, **2016**, *353*, aac9439.
17. M. Chhowalla, H. S. Shin, G. Eda, L. J. Li, K. P. Loh and H. Zhang, *Nat. Chem.*, **2013**, *5*, 263-275.
18. V. Nicolosi, M. Chhowalla, M. G. Kanatzidis, M. S. Strano and J. N. Coleman, *Science*, **2013**, *340*, 1226419.
19. M. Stöter, S. Rosenfeldt and J. Breu, *Annu. Rev. Mater. Res.*, **2015**, *45*, 129-151.

Literature

20. T. Sasaki, M. Watanabe, H. Hashizume, H. Yamada and H. Nakazawa, *J. Am. Chem. Soc.*, **1996**, *118*, 8329-8335.
21. J. E. F. C. Gardolinski and G. Lagaly, *Clay Miner.*, **2005**, *40*, 547–556.
22. J. N. Coleman, M. Lotya, A. O'Neill, S. D. Bergin, P. J. King, U. Khan, K. Young, A. Gaucher, S. De, R. J. Smith, I. V. Shvets, S. K. Arora, G. Stanton, H.-Y. Kim, K. Lee, G. T. Kim, G. S. Duesberg, T. Hallam, J. J. Boland, J. J. Wang, J. F. Donegan, J. C. Grunlan, G. Moriarty, A. Shmeliov, R. J. Nicholls, J. M. Perkins, E. M. Grieveson, K. Theuwissen, D. W. McComb, P. D. Nellist and V. Nicolosi, *Science*, **2011**, *331*, 568–571.
23. R. Ma, Z. Liu, L. Li, N. Iyi and T. Sasaki, *J. Mater. Chem.*, **2006**, *16*, 3809.
24. D. D. L. Chung, *J. Mater. Sci.*, **2002**, *37*, 1475-1489.
25. C. L. Kane and E. J. Mele, *Phys. Rev. Lett.*, **2005**, *95*, 146802.
26. A. A. Balandin, *Nat. Mater.*, **2011**, *10*, 569-581.
27. C. Lee, J. Wei, J. W. Kysar and J. Hone, *Science*, **2008**, *231*, 385-388.
28. R. M. Hazen and D. R. Wones, *Am. Mineral.*, **1978**, 885–892.
29. Y. Ide, G. Ozaki and M. Ogawa, *Langmuir*, **2009**, *25*, 5276–5281.
30. D. R. Dreyer, S. Park, C. W. Bielawski and R. S. Ruoff, *Chem. Soc. Rev.*, **2010**, *39*, 228–240.
31. R. Ma, K. Takada, K. Fukuda, N. Iyi, Y. Bando and T. Sasaki, *Angew. Chem. Int. Ed.*, **2008**, *47*, 86–89.
32. Z. Liu, R. Ma, M. Osada, N. Iyi, Y. Ebina, K. Takada and T. Sasaki, *J. Am. Chem. Soc.*, **2006**, *128*, 4872–4880.
33. M. Stöter, D. A. Kunz, M. Schmidt, D. Hirsemann, H. Kalo, B. Putz, J. Senker and J. Breu, *Langmuir*, **2013**, *29*, 1280–1285.
34. G. Lagaly, *Clays Clay Miner.*, **1982**, *30*, 215–222.
35. J. F. Burst, *Appl. Clay Sci.*, **1991**, *5*, 421-443.
36. F. Bergaya, B. K. G. Theng and G. Lagaly, in *Handbook of clay science*, Elsevier, Amsterdam; London, 2006, pp. 501-540.
37. M. R. Schütz, H. Kalo, T. Lunkenbein, A. H. Gröschel, A. H. E. Müller, C. A. Wilkie and J. Breu, *J. Mater. Chem.*, **2011**, *21*, 12110.
38. J. Hausner, B. Fischer, M. Stöter, A. Edenharter, J. Schmid, R. Kunz, S. Rosenfeldt, V. Altstadt and J. Breu, *Polym. Degrad. Stab.*, **2016**, *128*, 141-148.
39. M. Ziadeh, S. Weiss, B. Fischer, S. Forster, V. Altstadt, A. H. Muller and J. Breu, *J. Colloid Interface Sci.*, **2014**, *425*, 143-151.

40. C. Habel, E. S. Tsurko, R. L. Timmins, J. Hutschreuther, R. Kunz, D. D. Schuchardt, S. Rosenfeldt, V. Altstadt and J. Breu, *ACS Nano*, **2020**, *14*, 7018-7024.
41. M. W. Moller, T. Lunkenbein, H. Kalo, M. Schieder, D. A. Kunz and J. Breu, *Adv. Mater.*, **2010**, *22*, 5245–5249.
42. F. Bergaya, B. K. G. Theng and G. Lagaly, in *Handbook of clay science*, Elsevier, Amsterdam; London, 2006, pp. 19-84.
43. S. Guggenheim, J. M. Adams, D. C. Bain, F. Bergaya, M. F. Brigatti, V. A. Drits, M. L. L. Formoso, E. Galán, T. Kogure and H. Stanjek, *Clays Clay Miner.*, **2006**, *54*, 761–772.
44. B. Perdikatsis and H. Burzlaff, *Z. Kristallogr.*, **1981**, *156*, 177-186.
45. W. F. Bleam, *Clays Clay Miner.*, **1990**, *38*, 527-536.
46. J. Breu, W. Seidl, A. J. Stoll, K. G. Lange and T. U. Probst, *Chem. Mater.*, **2001**, *13*, 4213–4220.
47. H. Kalo, W. Milius and J. Breu, *RSC Adv.*, **2012**, *2*, 8452.
48. R. Mariychuk, A. Baumgartner, F. E. Wagner, A. Lerf, A. Dubbe, R. Moos and J. Breu, *Chem. Mater.*, **2007**, *19*, 5377–5387.
49. M. Daab, P. Loch, W. Milius, D. Schönauer-Kamin, M. Schubert, A. Wunder, R. Moos, F. E. Wagner and J. Breu, *Z. anorg. allg. Chem.*, **2017**, *643*, 1661–1667.
50. R. Kunz, T. Martin, C. Callsen, J. Hutschreuther, V. Altstadt and J. Breu, *Polymer*, **2019**, *169*, 74-79.
51. H. Tateyama, S. Nishimura, K. Tsunematsu, K. Jinnai, Y. Adachi and M. Kimura, *Clays Clay Miner.*, **1992**, *40*, 180-185.
52. J. T. Klopogge, *Clays Clay Miner.*, **1990**, *38*, 409–414.
53. E. J. Palin, M. T. Dove, A. Hernández-Laguna and C. I. Sainz-Díaz, *Am. Mineral.*, **2004**, *89*, 164–175.
54. J. Weitkamp, *Solid State Ion.*, **2000**, *131*, 175-188.
55. L. Xu and P. Wu, *New J. Chem.*, **2016**, *40*, 3968–3981.
56. W. J. Roth, P. Nachtigall, R. E. Morris and J. Čejka, *Chem. Rev.*, **2014**, *114*, 4807–4837.
57. F. S. O. Ramos, M. K. d. Pietre and H. O. Pastore, *RSC Adv.*, **2013**, *3*, 2084-2111.
58. J. Grzybek, W. J. Roth, B. Gil, A. Korzeniowska, M. Mazur, J. Čejka and R. E. Morris, *J. Mater. Chem. A*, **2019**, *7*, 7701-7709.

Literature

59. M. Choi, K. Na, J. Kim, Y. Sakamoto, O. Terasaki and R. Ryoo, *Nature*, **2009**, *461*, 246-249.
60. B. Gil, W. Makowski, B. Marszalek, W. J. Roth, M. Kubu, J. Cejka and Z. Olejniczak, *Dalton Trans.*, **2014**, *43*, 10501-10511.
61. W. J. Roth, O. V. Shvets, M. Shamzhy, P. Chlubná, M. Kubů, P. Nachtigall and J. Čejka, *J. Am. Chem. Soc.*, **2011**, *133*, 6130–6133.
62. W. J. Roth, P. Nachtigall, R. E. Morris, P. S. Wheatley, V. R. Seymour, S. E. Ashbrook, P. Chlubná, L. Grajciar, M. Položij, A. Zukal, O. Shvets and J. Cejka, *Nat. Chem.*, **2013**, *5*, 628–633.
63. S. Vortmann, J. Rius, S. Siegmann and H. Gies, *J. Phys. Chem. B*, **1997**, *101*, 1292–1297.
64. M. Borowski, O. Kovalev and H. Gies, *Micropor. Mesopor. Mat.*, **2008**, *107*, 71–80.
65. R. K. Iler, *J. Colloid Sci.*, **1964**, *19*, 648-657.
66. T. Selvam, A. Inayat and W. Schwieger, *Dalton Trans.*, **2014**, *43*, 10365–10387.
67. V. V. Narkhede and H. Gies, *Chem. Mater.*, **2009**, *21*, 4339–4346.
68. G. Borbély, H. K. Beyer, H. G. Karge, W. Schwieger, A. Brandt and K. H. Bergk, *Clays Clay Miner.*, **1991**, *39*, 490–497.
69. W. Schwieger and K.-H. Bergk, *Z. Chem.*, **1985**, *25*, 228-230.
70. P. Loch, T. Martin, M. Grüner, G. Kaupp, W. Schwieger and J. Breu, *Z. anorg. allg. Chem.*, **2020**, *646*, 1570-1574.
71. J. A. Wilson and A. D. Yoffe, *Adv. Phys.*, **1969**, *18*, 193-335.
72. A. Lerf, *Dalton Trans.*, **2014**, *43*, 10276-10291.
73. G. W. Brindley, *Clay Miner.*, **1966**, *6*, 237-259.
74. T. Maluangnont, K. Matsuba, F. Geng, R. Ma, Y. Yamauchi and T. Sasaki, *Chem. Mater.*, **2013**, *25*, 3137–3146.
75. D. A. Young and D. E. Smith, *J. Phys. Chem. B*, **2000**, *104*, 9163-9170.
76. M. Daab, N. J. Eichstaedt, C. Habel, S. Rosenfeldt, H. Kalo, H. Schießling, S. Förster and J. Breu, *Langmuir*, **2018**, *34*, 8215–8222.
77. M. W. Möller, U. A. Handge, D. A. Kunz, T. Lunkenbein, V. Altstädt and J. Breu, *ACS Nano*, **2010**, *4*, 717–724.
78. H. Kalo, M. W. Moller, D. A. Kunz and J. Breu, *Nanoscale*, **2012**, *4*, 5633–5639.
79. E. L. Hansen, H. Hemmen, D. M. Fonseca, C. Coutant, K. D. Knudsen, T. S. Plielic, D. Bonn and J. O. Fossum, *Sci. Rep.*, **2012**, *2*, 618.

80. S. You, D. Kunz, M. Stöter, H. Kalo, B. Putz, J. Breu and A. V. Talyzin, *Angew. Chem. Int. Ed.*, **2013**, *52*, 3891–3895.
81. G. Lagaly and S. Ziesmer, *Adv. Colloid Interface Sci.*, **2003**, *100-102*, 105-128.
82. M. Schneider and K.-U. Goss, *Geoderma*, **2012**, *170*, 64–69.
83. M. Stöter, B. Biersack, N. Reimer, M. Herling, N. Stock, R. Schobert and J. Breu, *Chem. Mater.*, **2014**, *26*, 5412–5419.
84. E. Ferrage, B. Lanson, B. A. Sakharov, N. Geoffroy, E. Jacquot and V. A. Drits, *Am. Mineral.*, **2007**, *92*, 1731-1743.
85. S. Rosenfeldt, M. Stöter, M. Schlenk, T. Martin, R. Q. Albuquerque, S. Förster and J. Breu, *Langmuir*, **2016**, *32*, 10582-10588.
86. K. Devineau, I. Bihannic, L. Michot, F. Villiéras, F. Masrouri, O. Cuisinier, G. Fragneto and N. Michau, *Appl. Clay Sci.*, **2006**, *31*, 76-84.
87. A. Weiss, *Angew. Chem.*, **1963**, *75*, 113-122.
88. K. K. Bissada, W. D. Johns and F. S. Cheng, *Clay Miner.*, **1967**, *7*, 155-166.
89. S. Olejnik, A. M. Posner and J. P. Quirk, *Clays Clay Miner.*, **1974**, *22*, 361-365.
90. R. Kunz, S. Amschler, A. Edenharter, L. Mayr, S. Herlitz, S. Rosenfeldt and J. Breu, *Clays Clay Miner.*, **2019**, *67*, 481-487.
91. L. Mayr, S. Amschler, A. Edenharter, V. Dudko, R. Kunz, S. Rosenfeldt and J. Breu, *Langmuir*, **2020**, *36*, 3814-3820.
92. P. P. Ziemiański, A. Derkowski, M. Szczerba and S. Guggenheim, *J. Phys. Chem. C*, **2021**, *125*, 7598-7610.
93. L. P. Cavalcanti, G. N. Kalantzopoulos, J. Eckert, K. D. Knudsen and J. O. Fossum, *Sci. Rep.*, **2018**, *8*, 11827.
94. K. W. B. Hunvik, P. Loch, L. P. Cavalcanti, K. K. Seljelid, P. M. Røren, S. Rudić, D. Wallacher, A. Kirch, K. D. Knudsen, C. Rodrigues Miranda, J. Breu, H. N. Bordallo and J. O. Fossum, *J. Phys. Chem. C*, **2020**, *124*, 2622-2631.
95. T. Sasaki and M. Watanabe, *J. Am. Chem. Soc.*, **1998**, *120*, 4682–4689.
96. F. Geng, R. Ma, Y. Ebina, Y. Yamauchi, N. Miyamoto and T. Sasaki, *J. Am. Chem. Soc.*, **2014**, *136*, 5491–5500.
97. Y. Song, N. Iyi, T. Hoshida, T. C. Ozawa, Y. Ebina, R. Ma, S. Yamamoto, N. Miyamoto and T. Sasaki, *Dalton Trans.*, **2018**, *47*, 3022–3028.
98. N. Miyamoto and T. Nakato, *J. Phys. Chem. B*, **2004**, *108*, 6152-6159.
99. G. F. Walker, *Nature*, **1960**, *187*, 312–313.

Literature

100. K. S. Novoselov, D. Jiang, F. Schedin, T. J. Booth, V. V. Khotkevich, S. V. Morozov and A. K. Geim, *Proc. Natl. Acad. Sci. U.S.A.*, **2005**, *58*, 9.
101. K. Sano, Y. S. Kim, Y. Ishida, Y. Ebina, T. Sasaki, T. Hikima and T. Aida, *Nat. Commun.*, **2016**, *7*, 12559.
102. M. Daab, N. J. Eichstaedt, A. Edenharter, S. Rosenfeldt and J. Breu, *RSC Adv.*, **2018**, *8*, 28797–28803.
103. T. Maluangnont, Y. Yamauchi, T. Sasaki, W. J. Roth, J. Cejka and M. Kubu, *Chem. Commun.*, **2014**, *50*, 7378-7381.
104. W. J. Roth, T. Sasaki, K. Wolski, Y. Song, D.-M. Tang, Y. Ebina, R. Ma, J. Grzybek, K. Kalahurska, B. Gil, M. Mazur, S. Zapotoczny and J. Cejka, *Sci. Adv.*, **2020**, *6*, eaay8163.
105. A. K. Geim and I. V. Grigorieva, *Nature*, **2013**, *499*, 419–425.
106. B. V. Lotsch, *Annu. Rev. Mater. Res.*, **2015**, *45*, 85–109.
107. B.-W. Li, M. Osada, T. C. Ozawa, Y. Ebina, K. Akatsuka, R. Ma, H. Funakubo and T. Sasaki, *ACS Nano*, **2010**, *4*, 6673-6680.
108. M. W. Möller, D. Hirsemann, F. Haarmann, J. r. Senker and J. Breu, *Chem. Mater.*, **2010**, *22*, 186-196.
109. D. A. Kunz, M. J. Leitl, L. Schade, J. Schmid, B. Bojer, U. T. Schwarz, G. A. Ozin, H. Yersin and J. Breu, *Small*, **2015**, *11*, 792-796.
110. M. Rieß, R. Siegel, J. Senker and J. Breu, *Cell Rep. Phys. Sci.*, **2020**, *1*.
111. D. M. Moore and R. C. J. Reynolds, *X-Ray Diffraction and the Identification and Analysis of Clay Minerals*, Oxford University Press, New York, 2nd edn., 1997.
112. M. Stöter, B. Biersack, S. Rosenfeldt, M. J. Leitl, H. Kalo, R. Schobert, H. Yersin, G. A. Ozin, S. Förster and J. Breu, *Angew. Chem. Int. Ed.*, **2015**, *54*, 4963–4967.
113. O. Khoruzhenko, D. R. Wagner, S. Mangelsen, M. Dulle, S. Förster, S. Rosenfeldt, V. Dudko, K. Ottermann, G. Papastavrou, W. Bensch and J. Breu, *J. Mater. Chem. C*, **2021**, *9*, 12732-12740.
114. M. Matejdes, M. Stöter, R. Czerwieniec, M. Leitl, S. Rosenfeldt, T. Schumacher, J. Albert, M. Lippitz, H. Yersin and J. Breu, *Adv. Opt. Mater.*, **2021**, *9*, 2100516.
115. G. T. Rochelle, *Science*, **2009**, *325*, 1652-1654.
116. A. Schoedel, Z. Ji and O. M. Yaghi, *Nat. Energy*, **2016**, *1*.
117. R. Banerjee, A. Phan, B. Wang, C. Knobler, H. Furukawa, M. O'Keeffe and O. M. Yaghi, *Science*, **2008**, *319*, 939-943.

118. S. Cavenati, C. A. Grande and A. E. Rodrigues, *J. Chem. Eng. Data*, **2004**, *49*, 1095-1101.
119. H. Furukawa, N. Ko, Y. Bok Go, N. Aratani, S. B. Choi, E. Choi, A. Ö. Yazaydin, R. Q. Snurr, M. O'Keeffe, J. Kim and O. M. Yaghi, *Science*, **2010**, *329*, 424-428.
120. K. E. Hart and C. M. Colina, *Langmuir*, **2014**, *30*, 12039-12048.
121. M. G. Rabbani and H. M. El-Kaderi, *Chem. Mater.*, **2011**, *23*, 1650-1653.
122. M. Cox and R. Mokaya, *Sustain. Energy Fuels*, **2017**, *1*, 1414-1424.
123. A. Chakraborty, A. Achari, M. Eswaramoorthy and T. K. Maji, *Chem. Commun.*, **2016**, *52*, 11378-11381.
124. V. N. Romanov, *Int. J. Greenh. Gas. Con.*, **2013**, *14*, 220-226.
125. N. Loganathan, G. M. Bowers, A. O. Yazaydin, H. T. Schaefer, J. S. Loring, A. G. Kalinichev and R. J. Kirkpatrick, *J. Phys. Chem. C*, **2018**, *122*, 4391-4402.
126. N. Loganathan, A. O. Yazaydin, R. J. Kirkpatrick and G. M. Bowers, *J. Phys. Chem. C*, **2019**, *123*, 4848-4855.
127. L. Michels, J. O. Fossum, Z. Rozynek, H. Hemmen, K. Rustenberg, P. A. Sobas, G. N. Kalantzopoulos, K. D. Knudsen, M. Janek, T. S. Plivelic and G. J. da Silva, *Sci. Rep.*, **2015**, *5*, 8775.
128. N. Loganathan, G. M. Bowers, A. O. Yazaydin, A. G. Kalinichev and R. J. Kirkpatrick, *J. Phys. Chem. C*, **2018**, *122*, 23460-23469.
129. P. Giesting, S. Guggenheim, A. F. Koster van Groos and A. Busch, *Environ. Sci. Technol.*, **2012**, *46*, 5623-5630.
130. A. Busch, P. Bertier, Y. Gensterblum, G. Rother, C. J. Spiers, M. Zhang and H. M. Wentinck, *Geochem. Geophys. Geo.*, **2016**, *2*, 111-130.
131. K. W. Bo Hunvik, P. Loch, D. Wallacher, A. Kirch, L. P. Cavalcanti, M. Riess, M. Daab, V. Josvanger, S. Gratz, F. Yokaichiya, K. D. Knudsen, C. Rodrigues Miranda, J. Breu and J. O. Fossum, *Langmuir*, **2021**, *37*, 14491-14499.
132. I. Dincer and C. Acar, *Int. J. Hydrog. Energy*, **2015**, *40*, 11094-11111.
133. G. Q. Lu, J. C. Diniz da Costa, M. Duke, S. Giessler, R. Socolow, R. H. Williams and T. Kreutz, *J. Colloid Interface Sci.*, **2007**, *314*, 589-603.
134. E. Yang, A. B. Alayande, K. Goh, C.-M. Kim, K.-H. Chu, M.-H. Hwang, J.-H. Ahn and K.-J. Chae, *Int. J. Hydrog. Energy*, **2021**, *46*, 11389-11410.
135. N. Rangnekar, N. Mittal, B. Elyassi, J. Caro and M. Tsapatsis, *Chem. Soc. Rev.*, **2015**, *44*, 7128-7154.
136. J. Caro and M. Noack, *Micropor. Mesopor. Mat.*, **2008**, *115*, 215-233.

Literature

137. K. Varoon, X. Zhang, B. Elyassi, D. D. Brewer, M. Gettel, S. Kumar, A. Lee, S. Maheshwari, A. Mittal, C.-Y. Sung, M. Cococcioni, L. F. Francis, A. V. McCormick and K. A. T. Mkhoyan, M., *Science*, **2011**, *334*, 72–75.
138. M. Y. Jeon, D. Kim, P. Kumar, P. S. Lee, N. Rangnekar, P. Bai, M. Shete, B. Elyassi, H. S. Lee, K. Narasimharao, S. N. Basahel, S. Al-Thabaiti, W. Xu, H. J. Cho, E. O. Fetisov, R. Thyagarajan, R. F. DeJaco, W. Fan, K. A. Mkhoyan, J. I. Siepmann and M. Tsapatsis, *Nature*, **2017**, *543*, 690-694.
139. H. Wang, X. Dong and Y. S. Lin, *J. Membr. Sci.*, **2014**, *450*, 425-432.
140. M. Dakhchoune, L. F. Villalobos, R. Semino, L. Liu, M. Rezaei, P. Schouwink, C. E. Avalos, P. Baade, V. Wood, Y. Han, M. Ceriotti and K. V. Agrawal, *Nat. Mater.*, **2020**, *20*, 362-369.
141. G. Buxbaum and G. Pfaff, *Industrial Inorganic Pigments*, Wiley, 2006.
142. M. R. Snow, A. Pring, P. Self, D. Losic and J. Shapter, *Am. Mineral.*, **2004**, *89*, 1353-1358.
143. G. Pfaff and J. Weitzel, in *Coloring of Plastics*, 2003, pp. 226-241.
144. M. Matejdes, J. Hausner, M. Grüner, G. Kaupp and J. Breu, *Clays Clay Miner.*, **2020**, *68*, 428-435.
145. M. A. S. Altoé, L. Michels, E. C. d. Santos, R. Droppa, G. Grassi, L. Ribeiro, K. D. Knudsen, H. N. Bordallo, J. O. Fossum and G. J. da Silva, *Appl. Clay Sci.*, **2016**, *123*, 83-91.
146. L. Michels, L. Ribeiro, M. S. P. Mundim, M. H. Sousa, R. Droppa, J. O. Fossum, G. J. da Silva and K. C. Mundim, *Appl. Clay Sci.*, **2014**, *96*, 60-66.
147. P. Loch, K. W. B. Hunvik, F. Puchtler, S. Weiß, K. K. Seljelid, P. M. Roren, S. Rudic, S. Raaen, K. D. Knudsen, H. N. Bordallo, J. O. Fossum and J. Breu, *Appl. Clay Sci.*, **2020**, *198*, 105831.
148. M. Yeşilbaş, X. Song and J.-F. Boily, *Environ. Sci.: Nano*, **2020**, *7*, 437-442.
149. P. Loch, D. Schuchardt, G. Algara-Siller, P. Markus, K. Ottermann, S. Rosenfeldt, T. Lunkenbein, W. Schwieger, G. Papastavrou and J. Breu, *Sci. Adv.*, **2022**, *8*, eabn9084.
150. A. Pabst, *Acta Cryst.*, **1959**, *12*, 733–739.
151. B. C. Chakoumakos, J. A. Fernandez-Baca and L. A. Boatner, *J. Solid State Chem.*, **1993**, *103*, 105–113.

6. Results

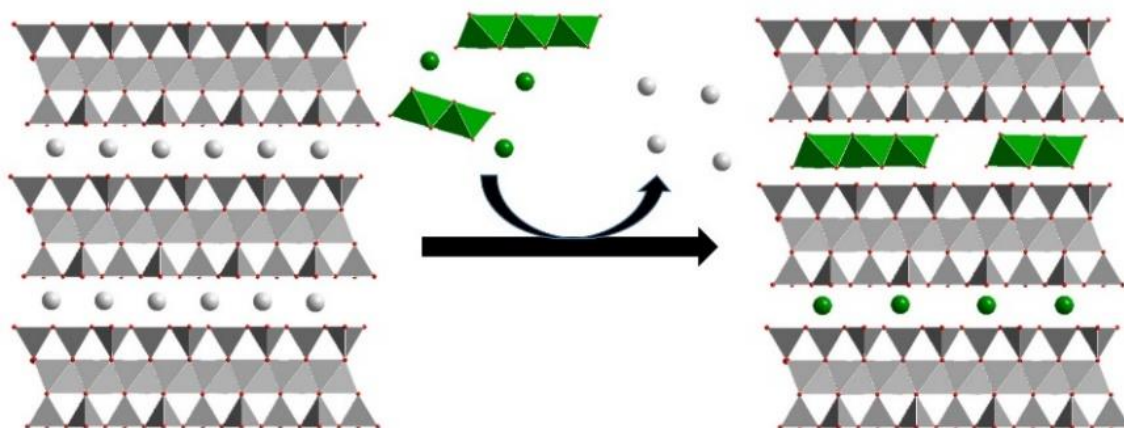
6.1. Structure of Ni-hectorites

Patrick Loch^a, Kristoffer William Bø Hunvik^b, Florian Puchtler^a, Sebastian Weiß^a, Konstanse Kvaem Seljelid^b, Paul Monceyron Røren^b, Svemir Rudić^c, Steinar Raaen^b, Kenneth Dahl Knudsen^{b, d}, Heloisa Nunes Bordallo^{e, f, *}, Jon Otto Fossum^{b, *} and Josef Breu^{a, *}

Spontaneous formation of an ordered interstratification upon Ni exchange of Na-fluorohectorite

Published in: *Applied Clay Science* **2020**, *198*, 105831.

Reprinted with permission, Copyright (2020) Elsevier.



^a Bavarian Polymer Institute and Department of Chemistry, University of Bayreuth, Universitätsstraße 30, D-95440 Bayreuth, Germany

^b Department of Physics, Norwegian University of Science and Technology, Høgskoleringen 5, NO 7495 Trondheim, Norway

^c ISIS Neutron and Muon Source, STFC Rutherford Appleton Laboratory, Chilton, Didcot OX11 0QX, United Kingdom

^d Institute for Energy Technology (IFE), POB 40, N-2027 Kjeller, Norway

^e Niels Bohr Institute-University of Copenhagen, Universitetsparken 5, 2100 Copenhagen, Denmark

^f European Spallation Source ESS ERIC, PO Box 176, SE-221 00 Lund, Sweden

* Corresponding authors

Results

Individual Contribution:

This publication is the result of a cooperation with the NTNU. I conceived and planned the experiments together with Prof. Breu, Prof. Fossum and K.W.B. Hunvik. The manuscript was written by Prof. J. Breu and me. K.W.B. Hunvik, Prof. J. Fossum and Prof. H.N. Bordallo commented on the manuscript. F. Puchtler conducted the ion exchange of the materials under my supervision. I characterized all the materials by PXRD, EDX, UV/Vis-spectroscopy and CHN-analysis. Together with K.W.B. Hunvik, K.K. Seljelid, Prof. K.D. Knudsen and Prof. J. Fossum, I conducted X-ray diffraction experiments at ALBA synchrotron. K.W.B. Hunvik measured TGA and XPS together with Prof. S. Raaen. K.W.B. Hunvik, S Rudić, P.M. Røren, Prof. K.D. Knudsen, Prof. H.N. Bordallo and Prof. J.O. Fossum carried out INS at the ISIS Pulsed Neutron and Muon Source. S. Weiß contributed with chrono amperometric measurements. Together with K.W.B. Hunvik I analyzed all the results.

My contribution to the publication is approx. 65 %

6.1.1. Spontaneous formation of an ordered interstratification upon Ni exchange of Na-fluorhectorite

Applied Clay Science 198 (2020) 105831



Contents lists available at ScienceDirect

Applied Clay Science

journal homepage: www.elsevier.com/locate/clay

Research Paper

Spontaneous formation of an ordered interstratification upon Ni-exchange of Na-fluorhectorite



Patrick Loch^a, Kristoffer William Bø Hunvik^b, Florian Puchtler^a, Sebastian Weiß^a,
Konstanse Kvaem Seljelid^b, Paul Monceyron Røren^b, Svemir Rudic^c, Steinar Raaen^b,
Kenneth Dahl Knudsen^{b,d}, Heloisa N. Bordallo^{e,f,*}, Jon Otto Fossum^{b,*}, Josef Breu^{a,*}

^a Bavarian Polymer Institute and Department of Chemistry, University of Bayreuth, Universitätsstraße 30, D-95440 Bayreuth, Germany

^b Department of Physics, Norwegian University of Science and Technology, Høgskoleringen 5, No. 7495 Trondheim, Norway

^c ISIS Neutron and Muon Source, STFC Rutherford Appleton Laboratory, Chilton, Didcot OX11 0QX, United Kingdom

^d Institute for Energy Technology (IFE), POB 40, N-2027 Kjeller, Norway

^e Niels Bohr Institute-University of Copenhagen, Universitetsparken 5, Copenhagen, Denmark

^f European Spallation Source ESS ERIC, PO Box 176, SE-221 00 Lund, Sweden

ARTICLE INFO

Keywords:

Ni-exchange
Smectite
Fluorhectorite
Ordered interstratification
Chlorite
Corrensites

ABSTRACT

Interstratified structures are a common phenomenon in layered silicates and the differentiation between random and ordered interstratifications might be in some cases difficult. Atypical basal spacings observed for Ni-exchanged fluorhectorites could be related to such an ordered interstratified structure. Applying powder X-ray diffraction, thermal gravimetric analysis, and various spectroscopic techniques, an ordered interstratification of smectite-like $[\text{Ni}(\text{H}_2\text{O})_6]^{2+}$ and condensed, chlorite-like $[\text{Ni}(\text{OH})_{2-y}(\text{H}_2\text{O})_y]_x^{y+}$ interlayers, where x refers to the degree of condensation, was observed. By simple ion exchange a corrensites-like structure was obtained with a structural formula of $\{[\text{Ni}(\text{OH})_{0.83}(\text{H}_2\text{O})_{1.17}]_{0.37}^{1.17+}\}_{\text{Int. 1}}\{[\text{Ni}(\text{H}_2\text{O})_6]_{0.23}^{2+}\}_{\text{Int. 2}}[\text{Mg}_5\text{Li}] < \text{Si}_8 > \text{O}_{20}\text{F}_4$. Improving the contrast between the two distinct d -spacings and between the electron densities of the interlayers by partial ion exchange with a long chain alkylammonium cation or thermal annealing, helped to increase the intensity of superstructure reflections rendering the ordered interstratified structures more clearly visible.

1. Introduction

A transcription of Dalton's law of multiple proportions into the world of intercalation chemistry restricts changes of interlayer heights in the course of swelling or ion exchange to multiple values of the real size of atoms or molecules. In this line, the basal spacing increases in discrete steps when going from 0 to 1 to 2 layer hydrates of Na-fluorhectorite (9.6 Å, 12.2 Å and 15.1 Å, respectively) (Kalo et al., 2012; Rosenfeldt et al., 2016; Stöter et al., 2013). The non-incremental increase of the basal spacing is slightly smaller than the van der Waals radius of oxygen since in a close-packed interlayer water molecules are partially penetrating the corrugated silicate surface.

For natural clays, these expectations frequently appear not to apply as water adsorption isotherms and the corresponding basal spacings seem to vary quasi-continuously (Devineau et al., 2006). This observation, however, is an artefact of random interstratification of different hydration states within a length scale corresponding to the

coherence length of the radiation used (Ferrage et al., 2005, 2010). In most cases such random interstratifications are easily identified by an irrational $00l$ series of low intensity and broad reflections and varying full widths of half maximum (FWHM) (Moore and Reynolds, 1997).

In recent years, smectites have been shown by several groups to swell with carbon dioxide (CO_2) (Busch et al., 2016). In particular, their volumetric adsorption capacity renders them potentially interesting for capture and storage of CO_2 (Cavalcanti et al., 2018; Giesting et al., 2012a, 2012b; Hemmen et al., 2012; Kadoura et al., 2016; Michels et al., 2015; Rother et al., 2013). Among the various smectites probed, Ni-fluorhectorites (Ni-Hec) showed the highest capacity (Cavalcanti et al., 2018; Michels et al., 2015). Crystalline swelling of dried Ni-Hec with CO_2 allows hereby the reversible and fast capture of CO_2 under nearly ambient conditions (typically, 25 °C, 10 bar CO_2). While the reason for the superior behavior of interlayer Ni remains unclear, the drying and hydration behavior of Ni-Hec indicated an unusual behavior (Altoé et al., 2016). Even careful drying (5 days, Ar flow at 150 °C), that for other interlayer

* Corresponding authors.

** Corresponding author at: Niels Bohr Institute-University of Copenhagen, Universitetsparken 5, 2100 Copenhagen, Denmark.

E-mail addresses: bordallo@nbi.ku.dk (H.N. Bordallo), jon.fossum@ntnu.no (J.O. Fossum), josef.breu@uni-bayreuth.de (J. Breu).

<https://doi.org/10.1016/j.clay.2020.105831>

Received 9 July 2020; Received in revised form 31 August 2020; Accepted 3 September 2020

Available online 22 September 2020

0169-1317/ © 2020 Elsevier B.V. All rights reserved.

cations results in a fully dehydrated state with a basal spacing $< 10 \text{ \AA}$, a basal spacing of 11.4 \AA is observed. Subtracting the thickness of a 2:1 silicate layer (9.6 \AA) a gallery height of 1.8 \AA , significantly smaller than the van der Waals radius of a water molecule, is observed.

A first hint regarding the singular structure of Ni-Hec came from EXAFS studies that suggested a brucite-like $\text{Ni}(\text{OH})_2$ species, which was hypothesized to be an accessory phase adsorbed on the external surfaces of the layered silicate particles (Michels et al., 2014). Applying similar ion exchange routines, several other authors have synthesized chlorites by ion exchanging Ni^{2+} at appropriate pH into natural and synthetic smectites (Ohtsuka et al., 1990; Uehara et al., 1999; Yamanaka and Brindley, 1978). Chlorites are so-called 2:1 layered silicates where the negative charge of smectites is compensated by condensed, positively charged metal hydroxide layers of Cd_2 -type, rather than by isolated hydrated interlayer cations.

Besides the two end-members smectite and chlorite, ordered interstratifications of the two are known, the natural mineral being named corrensite. For corrensites, basal spacings in the range of 22.8 \AA , depending on particular composition, have been reported (Vivaldi and MacEwan, 1960). This happens to be approximately double the value of the basal spacing of 11.4 \AA reported for dried Ni-Hec, which might indicate that the latter is actually the 002 of a so far overlooked ordered interstratification. Applying a melt synthesized Na-fluorohectorites (Na-Hec) we here verify the hypothesis of Ni-exchanged Na-Hec actually being a corrensite type ordered interstratification.

2. Materials and methods

2.1. Synthesis of fluorohectorites and cation-exchange

Na-fluorohectorite (Na-Hec) with a nominal layer charge of 1 per unit cell and a compositions of $\text{Na}[\text{Mg}_5\text{Li}] < \text{Si}_8 > \text{O}_{20}\text{F}_4$ was prepared via melt synthesis according to a published procedure (Daab et al., 2018), followed by annealing (6 weeks, $1045 \text{ }^\circ\text{C}$) to improve charge homogeneity and phase purity (Stöter et al., 2013). The cation exchange capacity (CEC) has been determined with BaCl_2 according to DIN ISO 11260.

Ca-fluorohectorite (Ca-Hec) and Ni-fluorohectorite (Ni-Hec) were obtained by cation exchange with CaCl_2 (1 M) and Ni-Acetate (0.2 M), respectively. Typically, 500 mg of the synthesized Na-Hec were exchanged with 40 mL CaCl_2 and Ni-Acetate solution (> 10 -fold excess of the CEC, 5 times), respectively. The ion-exchanged Ca- and Ni-Hec were washed 5 times with Millipore-water, equilibrated at 43% relative humidity (r. h.) over a saturated K_2CO_3 -solution. This r. h. corresponds to plateaus in the adsorption isotherms (Möller et al., 2010a, 2010b; Rosenfeldt et al., 2016) and defined hydration states were obtained. Additionally, Na-Hec, Ni-Hec and Ca-Hec were dried at $150 \text{ }^\circ\text{C}$ under Ar flow for 5 days to completely remove interlayer water.

Cation exchange of Ni-Hec with a long-chain *n*-alkylammonium solution (C_{16} , $\text{C}_{16}\text{H}_{33}\text{NH}_3\text{Cl}$) was performed at 10-fold excess of CEC ($80 \text{ }^\circ\text{C}$, 3 times) to ensure complete exchange. The obtained C_{16} exchanged Ni-Hec was washed 5 times with ethanol:water (1:1), once with ethanol (p. a.) and then dried at $80 \text{ }^\circ\text{C}$.

Finally, Ni-Hec was annealed at $600 \text{ }^\circ\text{C}$ in air to enable ion migration followed by equilibration at 43% r. h..

2.2. Powder X-ray diffraction (PXRD)

PXRD patterns of Na-, Ca- and Ni-Hec in transmission mode were recorded in sealed glass capillaries on a STOE Stadi P powder diffractometer using $\text{Cu K}\alpha_1$ radiation ($\lambda = 1.5406 \text{ \AA}$).

Synchrotron PXRD patterns of the partially dried Ni-Hec was recorded at the MSPD beamline at ALBA (Barcelona, Spain) using a microstrip MYTHEN-II detector ($\lambda = 0.61978 \text{ \AA}$), sealed in glass capillaries in a custom-made high-pressure sample cell, rotated ± 10 degrees per acquisition of 20 s. Prior to loading, the sample was prepared at 0%

r. h. in a desiccator over silica gel for 2 weeks. The obtained PXRD pattern of the beamline was finally converted to 2θ corresponding to $\text{Cu K}\alpha_1$ radiation ($\lambda = 1.5406 \text{ \AA}$).

Textured samples were measured in Bragg-Brentano geometry on a PANalytical Empyrean diffractometer with $\text{Cu K}\alpha_1$ radiation ($\lambda = 1.5406 \text{ \AA}$) equipped with a PixCel1D-Medipix3 detector.

2.3. Energy dispersive X-ray spectroscopy (EDX)

Completeness of the ion exchange was checked with EDX on a Zeiss 1530 equipped with an EDX INCA 400 unit (Oxford).

2.4. Inductive-coupled plasma atomic emission spectroscopy (ICP-OES)

The Ni-content of the Ni-Hec was determined by ICP-OES. About 20 mg equilibrated at 43% were weighed into clean Teflon flasks of 15 mL volume. After addition of 1.5 mL of 30 wt% HCl (Merck), 0.5 mL of 85 wt% H_3PO_4 (Merck), 0.5 mL of 65 wt% HNO_3 (Merck), and 1 mL of 48 wt% HBF_4 (Merck), the sample was digested in a MLS 1200 Mega microwave digestion apparatus for 6.5 min and heated at 600 W (MLS GmbH, Mikrowellen-Labor-Systeme, Leutkirch, Germany). The closed sample container was cooled to room temperature and the clear solution was diluted to 100 mL in a volumetric flask and analyzed on Perkin Elmer Avio 200 spectrometer.

2.5. UV/Vis-spectroscopy

The diffuse reflectance UV/Vis spectra were measured using a Varian Cary 5000 UV-Vis-NIR-Spectrophotometer (Agilent) with attached Diffuse Reflectance Accessory between 250 and 1300 nm. The obtained reflectance spectra were transformed into an absorption spectrum with the Kubelka-Munk function (Yang and Kruse, 2004). Teflon has been used as a white standard. $\beta\text{-Ni}(\text{OH})_2$ (Sigma-Aldrich) was chosen as reference material.

2.6. X-ray photoelectron spectroscopy (XPS)

XPS spectra were recorded using a SES2002 spectrometer (Scienta) in conjunction with a monochromatized Al $\text{K}\alpha$ source (Scienta). An energy resolution of about 1 eV was obtained at 500 eV pass energy. A flood gun (Prevac FS 40A1) was used for charge neutralization during the photoemission measurements. The sample powder was distributed on a conductive carbon tape. The spectrum was charge corrected by assuming the position of C 1s at 284.8 eV for adventitious carbon. For Ni-Hec, annealed at $600 \text{ }^\circ\text{C}$, adventitious carbon did not provide to be a good metric for charge correction and the Si 2p core level was used to charge correct.

2.7. Thermogravimetric analysis (TGA)

TGA was recorded on a Netzsch STA F3 448 Jupiter from 25 to $900 \text{ }^\circ\text{C}$ at a heating rate of 10 K/min under N_2 flow after equilibration at 43% r. h. of Ni- and Na-Hec.

2.8. Inelastic neutron scattering spectroscopy (INS spectroscopy)

INS spectra were recorded at the TOSCA spectrometer (Parker et al., 2014) at the ISIS facility (Rutherford Appleton Laboratory, UK), detecting the neutron energy loss up to a range of 4000 cm^{-1} . In order to minimize thermal effects, spectra were recorded at $T < 20 \text{ K}$. Powder samples, homogeneously distributed in a sachet prepared with aluminum foil, were placed in stainless steel cylinders and heated under vacuum (10^{-6} mbar) at $145 \pm 15 \text{ }^\circ\text{C}$ overnight prior to measurements. Data were reduced using the software package Mantid (Arnold et al., 2014). After subtracting the signal of the empty cell, the spectra were normalized by the sample mass.

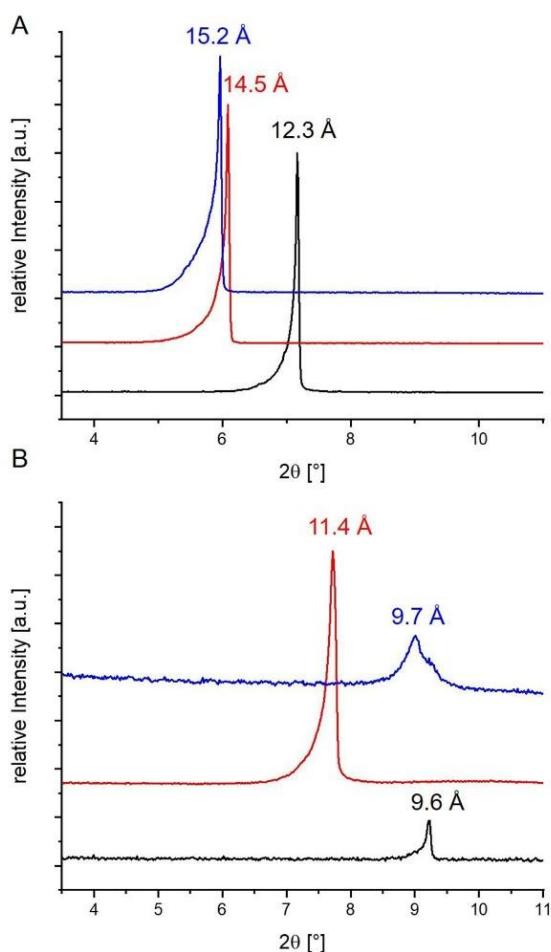


Fig. 1. PXRD pattern recorded in transmission mode of Na-Hec (black), Ni-Hec (red) and Ca-Hec (blue) at 43% r. h. and dried under Ar flow at 150 °C (B). (For interpretation of the references to colour in this figure legend, the reader is referred to the web version of this article.)

2.9. CHN-analysis

A Elemental Unicode equipped with a combustion tube filled with tungsten(VI)-oxide-granules was used at a combustion temperature of 1050 °C. Prior to the measurement, the sample was dried at 80 °C.

3. Results and discussion

3.1. Cation exchange

Phase pure and charge homogeneous Na-Hec with a nominal composition of $\text{Na}[\text{Mg}_5\text{Li}] < \text{Si}_8 > \text{O}_{20}\text{F}_4$ was obtained via melt synthesis followed by long-term annealing (Breu et al., 2001; Stöter et al., 2013). The material showed a homogeneous charge density and consequently a uniform intracrystalline reactivity as indicated by water vapor adsorption isotherms showing decisive steps separated by plateaus (Rosenfeldt et al., 2016). In line with published results, the PXRD pattern recorded in transmission mode of Na-Hec (Fig. 1A), equilibrated at 43% r. h., showed a crystalline swollen one water layer hydrate

(1WL) with a rational $00l$ -series and a d_{00l} -spacing of 12.3 Å (Stöter et al., 2013). Appearance of λ -shaped $02/11$ - and $20/13$ -bands (Fig. S1) in PXRD patterns recorded in transmission mode indicate a high concentration of planar defects (turbostratic stacking) (Breu et al., 2003). The determined CEC of 129 meq/100 g is in good agreement with the value of 130 meq/100 g expected from the composition. In the 1 WL hydrate of the Na-Hec, Na^+ is coordinated by three water molecules on the one side and six basal oxygen atoms of the silicate layer on the other side (Kalo et al., 2012). Upon drying (150 °C, Ar flow, 5 days) the basal spacing decreases uniformly to 9.6 Å, which is in agreement with the loss of the one water layer (≈ 3 Å). With a coefficient of variation (CV) (Bailey, 1982) of 0.12 and 0.15% for the 1 WL and 0 WL, respectively, both states show a nearly perfect rational $00l$ -series with well-defined interlayer distance.

Exchanging Na^+ by divalent cations like Ca^{2+} (Ca-Hec) and equilibration at 43% r. h. lead to a 2 WL structure with a basal spacing of 15.2 Å (CV = 0.32) because of the much higher hydration enthalpy as compared to monovalent cations (Möller et al., 2010a, 2010b). The Ni-exchanged fluorohectorite (Ni-Acetate, pH 6.9) showed a basal spacing of 14.5 Å (CV = 0.16), significantly different from Ca-Hec, which is a first indication of interlayer species in Ca-Hec and Ni-Hec being different.

Completeness of ion exchange with Ca-Hec and Ni-Hec was checked with EDX. For Ni-Hec additionally the Ni/Si ratio was determined by ICP analysis and the Ni-content per unit cell was derived to be 0.65 Ni atoms per unit cell. This significantly exceeded the CEC (0.496 for divalent cations), which was the second indication that Ni-exchange might not be a simple cation exchange reaction. The interlayer Ni^{2+} might not be a hexaqua complex as for instance in the 2 WL of Na-Hec (Kalo et al., 2012).

This was further corroborated when drying the different hectorites (Fig. 1B). While for Na-Hec and Ca-Hec basal spacings collapsed to < 10 Å (Na-Hec: 9.6 Å and Ca-Hec: 9.7 Å, CV = 0.29) as expected upon complete removal of interlayer water. The basal spacing of Ni-Hec decreased only to 11.4 Å upon drying as previously reported for various Ni-exchanged fluorohectorites (Michels et al., 2014, 2015). With the thickness of a 2:1 layer being 9.6 Å, the interlayer height amounts to only 1.8 Å, which clearly is too small to accommodate a water molecule with a van der Waals radius of > 3 Å and thus this basal spacing makes chemically no sense, stressing again the uniqueness of the Ni-Hec. The basal spacing of the dried Ni-Hec is too high for a fully dehydrated material and too low for the 1 WL hydrate (Möller et al., 2010a, 2010b; Stöter et al., 2013) and can only be explained with a random or ordered interstratified structure.

3.2. Structural characterization of Ni-fluorohectorite

At pH values above 4, $[\text{Ni}(\text{H}_2\text{O})_6]^{2+}$ shows a high condensation tendency, which is increasing with pH and reaches a maximum at 8.5 to 10 (Nam et al., 2015). Initially, oligocations are formed with $\text{Ni}(\text{OH})_2$ being the end product of condensation. For instance, at a pH of 6.9 as defined with Ni-Acetate, precipitation of a poorly crystalline $\text{Ni}(\text{OH})_2$ material was observed (Sato et al., 1975). Therefore, several authors have previously suggested that instead of a molecular $[\text{Ni}(\text{H}_2\text{O})_6]^{2+}$ moiety oligocationic domains or continuous cationic layers of CdI_2 -type structure are formed upon cation exchange with Ni^{2+} producing a 2:1 structure (synthetic chlorite) (Ohtsuka et al., 1990; Uehara et al., 1999; Yamanaka and Brindley, 1978). Since upon condensation protons are released the pH of the supernatant indeed continuously dropped with reaction time and progressing condensation (Fig. S2) (Purnell and Yun, 1993). $\text{Ni}(\text{OH})_2$ is a solid pH buffer with a point of zero charge (PZC) for the bulk compound of around 11 (Kosmulski, 2016). At the pH of the supernatant during Ni exchange, condensed species will therefore carry a positive charge. At the given concentrations of Ni^{2+} and $(\text{OH})^-$ in the exchange solution, $\text{Ni}(\text{OH})_2$ is expected to be fully condensed according to Nam et al. (Nam et al., 2015). The

Results

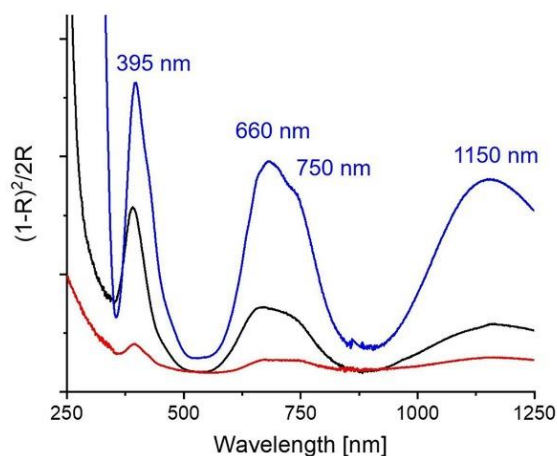


Fig. 2. Absorption spectrum of Ni-Hec equilibrated at 43% r. h. (black) in comparison with commercial available β -Ni(OH)₂ (blue) and annealed Ni-Hec at 600 °C after reequilibration at 43% r. h. (red). (For interpretation of the references to colour in this figure legend, the reader is referred to the web version of this article.)

pH of interlayer OH and H₂O groups however, might be significantly lower than of the surrounding bulk solution. MAS-NMR experiments have been suggesting the internal pH to be 4–5.5 pH units more acidic than the surrounding bulk (Touillaux et al., 1968). Therefore, smaller oligocations or Ni(OH)₂ islands appear more likely to be the interlayer species. Even partial condensation with some uncondensed [Ni(H₂O)₆]²⁺ remaining cannot be safely excluded in the light of these NMR results.

(Partial) condensation was confirmed with UV/Vis-spectroscopy (Fig. 2). The absorption spectrum was obtained after transformation of the diffuse reflectance spectrum using the Kubelka-Munk-function (Yang and Kruse, 2004). As reference, commercially available β -Ni(OH)₂ was chosen. The spectrum of the Ni-Hec and the commercial β -Ni(OH)₂ were in agreement and confirmed the formation of condensed nickel hydroxide species during the cation-exchange process. The bands observed for β -Ni(OH)₂ have been assigned to Ni²⁺ in a crystal field of edge sharing octahedra (Table 1).

Additionally, X-ray photon spectroscopy (XPS) was used to analyze for the Ni-species present in dried Ni-Hec. In the survey spectrum, all expected core levels of the fluorohectorite were observed without any sign of side phases (Fig. S3). The respective peak positions observed for the Ni 2p_{3/2} core level (Fig. 3A and Table 2) do not correspond to pure NiO, Ni(OH)₂ or NiOOH with reported binding energies for Ni 2p_{3/2} of 853.7, 854.9 eV and 854.6 eV, respectively (Carley et al., 1999; Grosvenor et al., 2006; Matienzo et al., 1973). This indicates that the presence of an accessory phase adsorbed on the external surfaces as suggested previously (Michels et al., 2014) can be ruled out. The significant shift observed towards higher binding energies compared to the above cited values have previously been attributed to an electron poor

Table 1
Position of the UV/Vis-bands with the corresponding assigned transitions (Ikeda and Vedanand, 1999; Yu et al., 2011).

Wavelength [nm]	Transition
395	³ A _{2g} – ³ T _{1g} (P)
660	³ A _{2g} – ³ T _{1g} (F)
750	³ A _{2g} – ¹ E _g (D)
1150	³ A _{2g} – ³ T _{2g} (F)

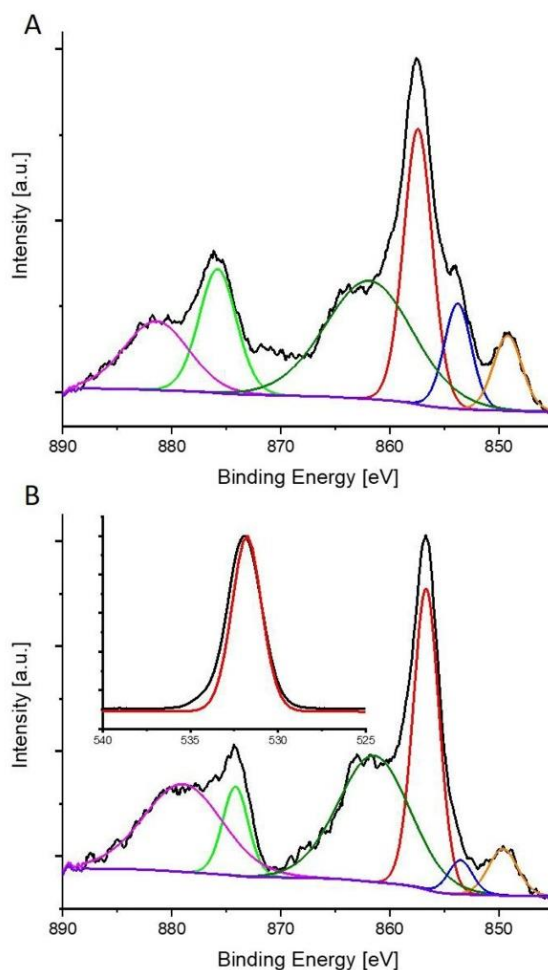


Fig. 3. XPS spectrum of Ni 2p peak of (A) Ni-Hec and annealed Ni-Hec at 600 °C, including the deconvolution of the spectrum and the comparison of the O 1s peak of Ni-Hec (black) and after annealing at 600 °C (red) as inset. (For interpretation of the references to colour in this figure legend, the reader is referred to the web version of this article.)

Table 2
Photoelectron binding energies of Ni-Hec determined with XPS.

Peak assignment	As prepared	600 °C
Fluorine-satellite	849.2	849.6
Fluorine-satellite	853.8	853.5
Ni 2p _{3/2}	857.4	856.7
Ni 2p _{3/2} -satellite	861.9	861.4
Ni 2p _{1/2}	875.8	874.2
Ni 2p _{1/2} -satellite	881.4	879.0

and positivated Ni-species (Davison et al., 1991; Stöcker et al., 1988).

Unfortunately, the resolution of the spectrum does not allow to assign all the different intercalated Ni-species, nor can the valence state of Ni be determined reliably. However, chrono amperometric measurements yield qualitative evidence that most of the Ni-species are present as Ni²⁺ (Supporting information Figs. S4–S7).

These experimental observations therefore consistently indicated

that charge compensation in Ni-Hec was assured by partial protonation of OH-groups of intercalated oligocations or extended Ni(OH)₂ islands. We postulate an interlayer species with a composition of [Ni(OH)_{2-y}(H₂O)_y]_x^{y+}, where x refers to the degree of condensation. This species will be stable at temperatures usually applied for drying smectites like applied here (150 °C, Ar flow). Consequently, if all interlayer spaces would be uniformly occupied by the same interlayer species [Ni(OH)_{2-y}(H₂O)_y]_x^{y+}, a basal spacing typically corresponding to chlorites (14–15 Å) would be expected but not the 11.4 Å phase observed for the dried state of Ni-Hec.

To probe the already mentioned hypothesis that this value would be related to interstratification of two types of interlayer species the samples equilibrated at 43% r. h. were analyzed by TGA. Non-bound interlayer water and water coordinated to interlayer cations like [Ni(H₂O)₆]²⁺ is expected to be released at significantly lower temperatures than water originating from condensed [Ni(OH)_{2-y}(H₂O)_y]_x^{y+} species.

Dehydration of interlayer water of Na-Hec commenced above 90 °C and is completed at 120 °C (Fig. 4A). The related weight loss of 9.9% corresponds to what is expected for the 1 WL (9.4%) (Kalo et al., 2012). Above the dehydration temperature, no significant weight loss is observed up to 700 °C reflecting the high thermal stability of fluorhectorites.

The thermal behavior of the Ni-Hec is complex compared to Na-Hec (Fig. 4B) and similar to what has been observed in literature (Altoé et al., 2016). Besides two peaks in the heat flow, related to the dehydration of the interlayer water at 100 °C and coordinated water at

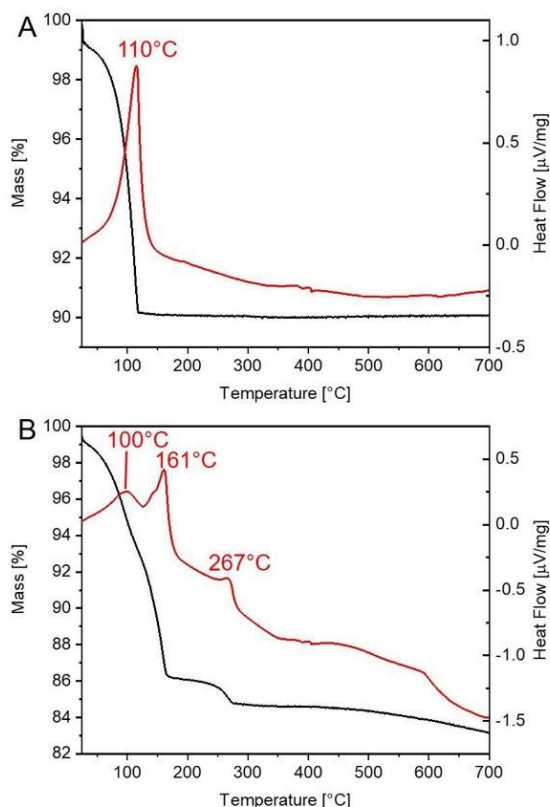


Fig. 4. TGA (black) and DSC curve (red) of (A) Na-Hec and (B) Ni-Hec after equilibration at 43% r. h. (For interpretation of the references to colour in this figure legend, the reader is referred to the web version of this article.)

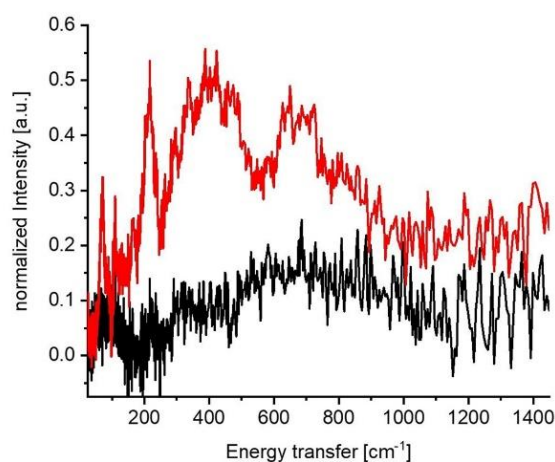


Fig. 5. INS spectra of Ni-Hec (red) and Na-Hec (black) dried at 150 °C in vacuum. (For interpretation of the references to colour in this figure legend, the reader is referred to the web version of this article.)

161 °C, another prominent signal was observed at 267 °C. The latter has been assigned to the dehydroxylation of β-Ni(OH)₂ to NiO, for which a temperature range of 200 °C - 300 °C was reported, depending on crystallinity, crystal size and pH during the synthesis (Horanyi, 1989; Sato et al., 1975; Song et al., 2002). The weight loss related to the interlayer and coordinated water (13.8%) is in the same range as reported for 2WL (15.4%) of Na-Hec (Kalo et al., 2012). Dehydroxylation of the nickel hydroxide species was, however, more sluggish and accumulated in an additional weight loss of around 3% up to 600 °C.

When drying Ni-Hec at 150 °C (Fig. 4B) in vacuum over night as done for preparing samples for Inelastic Neutron Scattering (INS), interlayer water and water coordinated to uncondensed interlayer cations is expected to be completely removed while [Ni(OH)_{2-y}(H₂O)_y]_x^{y+} will not yet be dehydroxylated. This was confirmed by the vibrational spectrum recorded applying INS spectroscopy (Fig. 5). Due to the 20 times larger incoherent scattering cross section of hydrogen as compared to other elements, the signal in INS is dominated by hydrogen species. The position of vibrations in the spectrum allows for conclusions on the hydrogen containing moieties, and changes in the intensity of the elastic INS line of the spectrum can be directly correlated to the quantity of the hydrogen species (Parker et al., 2011). As expected for a dehydrated, collapsed Na-Hec a spectrum with very small intensity (Fig. 5, black curve) was observed. Contrary to Na-Hec, the Ni-Hec sample showed a significant signal in the INS spectrum with a complex structure (Fig. 5, red curve). As indicated by TGA, interlayer and coordinated water had been completely removed during drying, so it can be assumed that the observed spectra is related to [Ni(OH)_{2-y}(H₂O)_y]_x^{y+}. Indeed, distinct vibrations at 109, 165, 300, 336 cm⁻¹ and broad distributions, centered around 400 and 670 cm⁻¹ with a shoulder around 810 cm⁻¹ were all previously assigned to Ni(OH)₂ (Baddour-Hadjean et al., 1995; Bantignies et al., 2008). The sharp vibrations at 70 and 215 cm⁻¹ are corresponding to coordinated H₂O of the [Ni(OH)_{2-y}(H₂O)_y]_x^{y+} species (Persson et al., 2017).

3.3. Identification of the ordered interstratification

Since both TGA and INS suggested two types of interlayer species in Ni-Hec, which according to the charged type of the 2:1 layer are expected to be segregated in separated interlayers (Möller et al., 2010a, 2010b; Stöter et al., 2014), an interstratified structure may be postulated. This interstratification might be random or ordered. For the first,

an irrational *00l*-series would be characteristic while the latter would require the observation of a superstructure reflection. This differentiation is, however, difficult:

By chance, both, the basal spacings for chlorites (14 Å -15 Å) (Brindley and de Souza, 1975; De Waal, 1970; Ohtsuka et al., 1987, 1990; Uehara et al., 1999; Yamanaka and Brindley, 1978) and of the 2 WL structure of a hectorite (15.1 Å) and the electron density in the interlayer space of the two are very similar. Both structures are built by distorted octahedral polyhedra of oxygen atoms surrounding the Ni²⁺ with condensation, leading to edge sharing and slightly flattened octahedra. Consequently, random or ordered interstratification will be hard to spot because Mering's rules will have little impact on FWHM and rationality of *00l* series of PXRD patterns (Moore and Reynolds, 1997). In the same line, the intensity of superstructure reflections of a potential ordered interstratification is expected to be weak, in particular if defects occur in the perfect R1 (Reichweite 1) ordering (Jagodźinski, 1949). Since the ordered interstratification involves one hydrated type of interlayer, the level of hydration of all these interlayers has to be the same. It turned out that this better realized with water activity levels where the 1WL structure rather than the 2 WL is thermodynamically preferred. At room temperature, for fluorohectorites exchanged with divalent cations the 1 WL regime extends all the way down to 0% r. h. When drying Ni-Hec over silica in a desiccator the smectite-like interlayers adopted uniformly the 1 WL state improving the order of the interstratification. At the same, the difference in the *d*-values of the two types of interlayer was enlarged. Both effects contributed to a much-increased intensity of the superstructure reflections (Fig. 6). The basal spacing of the superstructure of 26.2 Å was attributed to the sum of a 1 WL basal spacing (12.3 Å) and a chlorite-type interlayer with a basal spacing of 13.9 Å.

This might indicate, that the basal spacing of 11.4 Å observed for more harshly dried Ni-Hec is actually the *002* reflection of an ordered interstratification of dry, collapsed smectite-type interlayers and chlorite-type interlayers. In this line, a corrensite-type structure of chlorite and dried vermiculite was indeed found to have a basal spacing of 22.8 Å (Vivaldi and MacEwan, 1960).

Admittedly, intensity, rationality (CV = 0.89%) and FWHM of the *00l*-series of the ordered interstratification might not be fully convincing. This might be related to the control of hydration state of smectite-type interlayers. Two approaches were taken to gain better control of the *d*-spacing of these smectite-type interlayers.

Ion exchange with bulky organo cations will concomitantly change

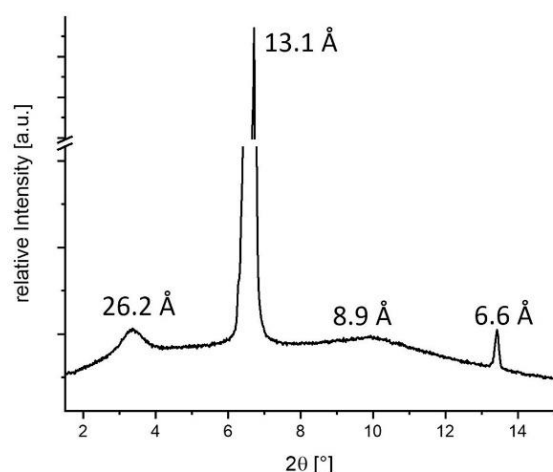


Fig. 6. Synchrotron PXRD pattern Ni-Hec, dried at 0% r. h. with marked reflections corresponding to a superstructure.

the *d*-spacing and the electron density distribution and thus enhance the contrast in an interstratified structure. After cation exchange with an excess of long chained and thus highly selective (Mermut and Lagaly, 2001) *n*-alkylammonium (C16, C₁₆H₃₃NH₃Cl) at 80 °C a clearly visible superstructure was observed by PXRD (Fig. 7A, bottom). The *00l*-series with a CV of 0.81% and a *d*₀₀₁-spacing of 40.4 Å was rational and the highest clearly observable odd *l* value was 11, indicating a highly crystalline order of this superstructure. The basal spacing can be explained with the formation of an ordered interstratification formed by two strictly alternating interlayer species: [Ni(OH)_{2-y}(H₂O)_y]_x^{y+} with a basal spacing of 14.5 Å and paraffin like arrangement of C16 cations with a basal spacing of 25.9 Å (Fig. 6A). The formation of such ordered interstratified heterostructures of organic or inorganic cations, using charge homogenous synthetic fluorohectorites, has been observed before (Möller et al., 2010a, 2010b; Stöter et al., 2014, 2015, 2016). The chemical composition after C16-exchange was determined with ICP-OES and CHN-analysis, giving a composition of {[Ni(OH)_{2-y}(H₂O)_y]_{0.37}^{y+}]_{int. 1}{C16_{0.72}]_{int. 2}[Mg₅Li] < Si₈ > O₂₀F₄ per unit cell. The high C16 content is in agreement with the paraffin like structure, forming an ordered interstratification with the non-exchangeable [Ni(OH)_{2-y}(H₂O)_y]_{0.37}^{y+} interlayers.

When assuming that alkylammonium exchange was selective for [Ni(H₂O)₆]²⁺ interlayers, comparing the Ni-content of the organophilized ordered interstratification with the total Ni-content of the parent Ni-Hec allowed to calculate the amount of exchangeable molecular [Ni(H₂O)₆]²⁺. Combining it with the charge density of the fluorohectorite, a structural formula of {[Ni(OH)_{0.83}(H₂O)_{1.17}]_{0.37}^{1.17+}]_{int. 1}{[Ni(H₂O)₆]_{0.28}²⁺]_{int. 2}[Mg₅Li] < Si₈ > O₂₀F₄ with a corrensite like structure is obtained (Fig. 7B). Since significantly more C16 had entered the interlayer space than [Ni(H₂O)₆]²⁺ had left, we have to postulate that the degree of protonation of [Ni(OH)_{0.83}(H₂O)_{1.17}]_{0.37}^{1.17+} was concomitantly lowered with alkylammonium exchange to assure charge neutrality. This makes sense, since the pH of the C16-Cl solution was 7.5, slightly higher than 6.9 during the Ni-exchange.

The Ni-content of the condensed [Ni(OH)_{0.83}(H₂O)_{1.17}]_{0.37}^{1.17+} species was, however, significantly lower than required for a continuous and defect free condensed nickel hydroxide interlayer as expected for a corrensite structure (4.88 Ni atoms per unit cell). Therefore, smaller islands of [Ni(OH)_{0.83}(H₂O)_{1.17}]_{0.37}^{1.17+} appear to be the actual interlayer species of the condensed interlayer.

The driving force for the segregation might be a higher selectivity of [Ni(OH)_{2-y}(H₂O)_y]_x^{y+} oligocations for the interlayer space. Because of the larger equivalent area of the oligocations as compared to [Ni(H₂O)₆]²⁺ the exchange is lower than required by the average CEC. To assure a local charge balance the adjacent interlayer consequently have to accommodate [Ni(H₂O)₆]²⁺ in excess of the average CEC. This resembles the mechanism suggested by Möller et al. for the spontaneous formation of rectorite type structures upon partial K⁺ exchange of Na-Hec (Möller et al., 2010a, 2010b).

Alternatively to ion exchange with alkylammonium cations, ordering of interstratified structures based on Ni-Hec could be greatly improved by annealing at 600 °C, followed by rehydration at 43% r. h. for 2 weeks at room temperature. Similar to alkylammonium exchange a clearly visible superstructure with a basal spacing of 22.5 Å (CV = 2.19%) appeared indicating a well ordered interstratification (Fig. 7C). The UV/VIS spectrum indicates that upon equilibration at 43% r. h. on one hand what was the condensed interlayer type was at least partially rehydrated (Fig. 2). On the other hand, the second type of interlayer, the not condensed individual Ni²⁺ cations, was not rehydrated as the PXRD pattern observed for pristine Ni-Hec equilibrated at 43% r. h., was not restored (Fig. 7B). This second type of interlayer rather remained collapsed.

The basal spacing of 22.5 Å of the ordered interstratification was interpreted to be composed of a 9.6 Å collapsed talc-like layer and a 12.9 Å layer of the rehydrated condensed [Ni(OH)_{2-y}(H₂O)_y]_x^{y+} (Fig. 7C).

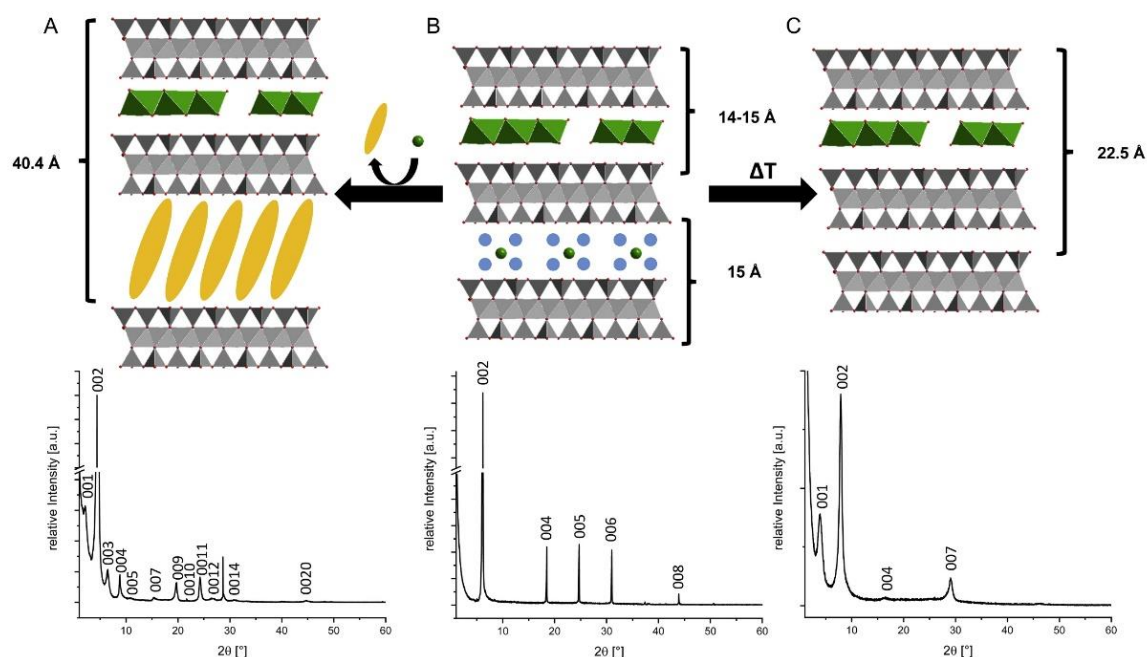


Fig. 7. Structural model (first row) and corresponding PXRD of textured samples of Ni-Hec (lower row): (A) C16 exchanged Ni-Hec, (B) initial structure from Ni-exchange at 43% r. h. and (C) annealed Ni-Hec at 600 °C after reequilibration at 43% r. h..

According to TGA, annealing at 600 °C will trigger complete dehydroxylation of $[\text{Ni}(\text{OH})_{2-y}(\text{H}_2\text{O})_y]_x^{y+}$ resulting in some form of 2-dimensional Ni-oxide that for charge compensation needs to carry a positive charge and which can be rehydrated at 43% r. h..

Comparing the XPS spectra of this material (Fig. 3B) with pristine Ni-Hec (Fig. 3A) reveal distinct differences resembling changes in the chemical environment. The Ni $2p_{3/2}$ core-level showed a significant shift of 0.7 eV towards lower binding energies (Table 2). Moreover, narrowing of the O 1s peak (Fig. 3B, inset) might be related to a reduction of the number of oxygen species after 600 °C treatment. As Ni is a complicated core level with a multiplet splitting, a reliable deconvolution and peak assignment, was unfortunately not possible.

As to the reason for the irreversible collapse of the second type, the $[\text{Ni}(\text{H}_2\text{O})_6]^{2+}$ interlayer, we can only speculate. Similar to what has been reported by Purnell and Yun for Ni-montmorillonite at 600 °C the mobility of Ni^{2+} interlayer cations was apparently sufficient to allow for a redistribution by a Hofman-Klemen-effect (Purnell and Yun, 1993). In the same line, a significant charge reduction was observed by annealing Mg-fluorohectorite commencing at 250 °C (Keenan et al., 2013). This reshuffling of Ni^{2+} could then have led to a collapse of alternating interlayers as Meier and Nüesch have shown for Li/Na-montmorillonites below a minimum CEC spontaneous segregation of collapsed and expanded interlayers occur leading to regularly interstratified structures (Meier and Nüesch, 1999). In line with this model of a irreversibly collapsed talc-type interlayer, the basal spacing of 22.5 Å observed for Ni-Hec annealed at 600 °C was slightly lower than the basal spacing of an ordered, corrensit-type interstratification of chlorite and dried vermiculite for which 22.8 Å was reported (Vivaldi and MacEwan, 1960).

4. Conclusion

Observed basal spacings of intercalation compounds, which cannot be related to the real sizes of atoms or molecules are artefacts and need

alternative explanations like random and ordered interstratifications of chemically meaningful real interlayer structures. To distinguish between both possibilities, the rationality of the $00l$ -series and the existence of superstructure reflections needs careful inspection. Since superstructure reflections in many cases will be weak, recording the $00l$ -series for textured samples in reflection mode might help. When hydrated interlayers are involved, uniform swelling is prerequisite for realizing a defined hydration state. Partial ion exchange may be considered as workaround as it concomitantly amplifies the contrast in alternating basal spacings and electron density variations of the two end-member types of interlayers. Ni-Hec is one particular problematic example for which ordered interstratification is easily overlooked because of similar d -spacings (at ambient r. h.) and electron densities of the two different interlayer types. Lorf et al. have presented evidence for $[\text{Fe}(\text{H}_2\text{O})_6]^{2+}$ residing in the interlayer space of Fe^{2+} exchanged vermiculite based on Mößbauer spectra recorded at 4.2 K (Lorf et al., 2011). In the light of the presented results on Ni^{2+} exchanged hectorites and since Fe^{2+} has a similarly high condensation tendency, the Fe-compounds should be reinvestigated and probed for interstratified structures.

Declaration of Competing Interest

The authors declare that they have no competing financial interest or personal relationship that could appeared to influence the work reported in this paper.

Acknowledgements

This work was supported by the Deutsche Forschungsgemeinschaft (SFB 840). The authors appreciate the support of the KeyLab for Optical and Electron Microscopy of the Bavarian Polymer Institute. We thank Lena Geiling for collecting EDX spectra and Marco Schwarzmann for the ICP-OES measurements. K.W.B.H, P.M.R, H.N.B, S.Ra, K.D.K. J.O-F

acknowledges the support by the Norwegian Research Council under the Frinatek Program, project number 250728. Experiments at the ISIS Pulsed Neutron and Muon Source were supported by a beamtime allocation from the Science and Technology Facilities Council (Fossum et al., 2019). The authors acknowledge the beamtime at the MSPD beamline at the ALBA Synchrotron. We acknowledge the support from Aleksandr Missiul. P.L. thanks Elite Network Bavaria in the framework of the Elite Study Program “Macromolecular Science” for support.

Appendix A. Supplementary data

Supplementary data to this article can be found online at <https://doi.org/10.1016/j.clay.2020.105831>.

References

- Altoé, M.A.S., Michels, L., Santos, E.C.d., Droppa, R., Grassi, G., Ribeiro, L., Knudsen, K.D., Bordallo, H.N., Fossum, J.O., da Silva, G.J., 2016. Continuous water adsorption states promoted by Ni^{2+} confined in a synthetic smectite. *Appl. Clay Sci.* 123, 83–91.
- Arnold, O., Bilheux, J.C., Borreguero, J.M., Buts, A., Campbell, S.I., Chapon, L., Doucet, M., Draper, N., Ferraz Leal, R., Gigg, M.A., Lynch, V.E., Markvardsen, A., Mikkelsen, D.J., Mikkelsen, R.L., Miller, R., Palmen, K., Parker, P., Passos, G., Perring, T.G., Peterson, P.F., Ren, S., Reuter, M.A., Savici, A.T., Taylor, J.W., Taylor, R.J., Tolchenov, R., Zhou, W., Zikovsky, J., 2014. Mantid-Data analysis and visualization package for neutron scattering and μ SR experiments. *Nucl. Instrum. Meth. A* 764, 156–166.
- Baddour-Hadjean, R., Fillaux, F., Tomkinson, J., 1995. Proton dynamics in $\beta\text{Ni}(\text{OH})_2$ and βNiOOH . *Physica B* 213, 637–639.
- Bailey, S.W., 1982. Nomenclature for regular interstratifications. *Am. Mineral.* 67, 394–398.
- Bantignies, J.L., Deabate, S., Righi, A., Rols, S., Hermet, P., Sauvajol, J.L., Henn, F., 2008. New insight into the vibrational behavior of nickel hydroxide and oxyhydroxide using inelastic neutron scattering, Far/Mid-infrared and Raman spectroscopies. *J. Phys. Chem. C* 112, 2193–2201.
- Breu, J., Seidl, W., Stoll, A.J., Lange, K.G., Probst, T.U., 2001. Charge homogeneity in synthetic fluorohectorite. *Chem. Mater.* 13, 4213–4220.
- Breu, J., Seidl, W., Stoll, A., 2003. Fehlordnung bei Smectiten in Abhängigkeit vom Zwischenschichtkation. *Z. Anorg. Allg. Chem.* 629, 503–515.
- Brindley, G.W., de Souza, J.V., 1975. Nickel-containing montmorillonites and chlorites from Brazil, with remarks on schuchardtite. *Mineral. Mag.* 40, 141–152.
- Busch, A., Bertier, P., Gensterblum, Y., Rother, G., Spiers, C.J., Zhang, M., Wentinck, H.M., 2016. On sorption and swelling of CO_2 in clays. *Geochem. Geophys. Geosyst.* 2, 111–130.
- Carley, A.F., Jackson, S.D., O’Shea, J.N., Roberts, M.W., 1999. The formation and characterization of Ni^{3+} – An X-ray photoelectron spectroscopic investigation of potassium-doped $\text{Ni}(\text{110})\text{-O}$. *Surf. Sci.* 440, L868–L874.
- Cavalcanti, L.P., Kalantzopoulos, G.N., Eckert, J., Knudsen, K.D., Fossum, J.O., 2018. A nano-silicate material with exceptional capacity for CO_2 capture and storage at room temperature. *Sci. Rep.* 8, 11827.
- Daab, M., Eichstaedt, N.J., Habel, C., Rosenfeldt, S., Kalo, H., Schießling, H., Förster, S., Breu, J., 2018. Onset of osmotic swelling in highly charged clay minerals. *Langmuir ACS J. Surf. Colloids* 34, 8215–8222.
- Davison, N., McWhinnie, W.R., Hooper, A., 1991. X-ray photoelectron spectroscopic study of cobalt(II) and nickel(II) sorbed on hectorite and montmorillonite. *Clay Clay Miner.* 39, 22–27.
- De Waal, S.A., 1970. Nickel minerals from Barberton, South Africa: II. Nimité, a nickel-rich chlorite. *Am. Mineral.* 55, 18–30.
- Devineau, K., Bihannic, I., Michot, L., Villiéras, F., Masroufi, F., Cuisinier, O., Fragneto, G., Michau, N., 2006. In situ neutron diffraction analysis of the influence of geometric confinement on crystalline swelling of montmorillonite. *Appl. Clay Sci.* 31, 76–84.
- Ferrage, E., Lanson, B., Sakharov, B.A., Drits, V.A., 2005. Investigation of smectite hydration by modeling experimental X-ray diffraction patterns: part I. Montmorillonite hydration properties. *Am. Mineral.* 90, 1358–1374.
- Ferrage, E., Lanson, B., Michot, L.J., Robert, J.-L., 2010. Hydration properties and interlayer organization of water and ions in synthetic na-smectites with tetrahedral layer charge. Part I. results from X-ray diffraction profile modelling. *J. Phys. Chem. C* 114, 4515–4526.
- Fossum, J.O., Knudsen, K., Rudic, S., Hunvik, K.W., Bordallo, H.N., Røren, P., 2019. Determining the interaction between water and carbon dioxide in smectite clay. STFC ISIS Neutron Muon Source.
- Giesting, P., Guggenheim, S., Koster van Groos, A.F., Busch, A., 2012a. Interaction of carbon dioxide with Na-exchanged montmorillonite at pressures to 640bars: implications for CO_2 sequestration. *Int. J. Greenh. Gas. Con.* 8, 73–81.
- Giesting, P., Guggenheim, S., Koster van Groos, A.F., Busch, A., 2012b. X-ray diffraction study of K- and Ca-exchanged montmorillonites in CO_2 atmospheres. *Environ. Sci. Technol.* 46, 5623–5630.
- Grosvenor, A.P., Biesinger, M.C., Smart, R.S.C., McIntyre, N.S., 2006. New interpretations of XPS spectra of nickel metal and oxides. *Surf. Sci.* 600, 1771–1779.
- Hemmen, H., Rolseth, E.G., Fonseca, D.M., Hansen, E.L., Fossum, J.O., Plivelic, T.S., 2012. X-ray studies of carbon dioxide intercalation in Na-fluorohectorite clay at near-ambient conditions. *Langmuir* 28, 1678–1682.
- Horanyi, T.S., 1989. The thermal stability of the beta-Ni(OH)2-beta-NiOOH system. *Thermochim. Acta* 137, 247–253.
- Ikeda, K., Vedanand, S., 1999. Optical spectrum of synthetic theophrastite, $\text{Ni}(\text{OH})_2$. *Neues Jb. Mineral. Abh.* 1, 21–26.
- Jagodzinski, H., 1949. Eindimensionale Fehlordnung in Kristallen und ihr Einfluss auf die Röntgeninterferenz. I. Berechnung des Fehlordnungsgrades aus den Röntgenintensitäten. *Acta Cryst* 2, 201–207.
- Kadoura, A., Narayanan Nair, A.K., Sun, S., 2016. Adsorption of carbon dioxide, methane, and their mixture by montmorillonite in the presence of water. *Microporous Mesoporous Mater.* 225, 331–341.
- Kalo, H., Milius, W., Breu, J., 2012. Single crystal structure refinement of one- and two-layer hydrates of sodium fluorohectorite. *RSC Adv.* 2, 8452.
- Keenan, C.D., Herling, M.M., Siegel, R., Petzold, N., Bowers, C.R., Rössler, E.A., Breu, J., Senker, J., 2013. Porosity of Pillared Clays Studied by Hyperpolarized ^{129}Xe NMR Spectroscopy and Xe Adsorption Isotherms. *Langmuir* 29, 643–652.
- Kosmulski, M., 2016. Isoelectric points and points of zero charge of metal (hydr)oxides: 50years after Parks’ review. *Adv. Colloid Interf. Sci.* 238, 1–61.
- Lerf, A., Wagner, F.E., Poyato, J., Pérez-Rodríguez, J.L., 2011. Intercalation and dynamics of hydrated Fe^{2+} in the vermiculites from Santa Olalla and Ojén. *J. Solid State Electrochem.* 15, 223–229.
- Matienzo, L.J., Yin, L.L., Swartz, W.E.J., 1973. X-ray photoelectron spectroscopy of Ni compounds. *Inorg. Chem.* 12, 2762–2769.
- Meier, L.P., Nüesch, R., 1999. The lower cation exchange capacity limit of montmorillonite. *J. Colloid Interface Sci.* 217, 77–85.
- Mermut, A.R., Lagaly, G., 2001. Baseline studies of the clay mineral society source clays: layer-charge determination and characteristics of those minerals containing 2:1-layers. *Clay Clay Miner.* 49, 393–397.
- Michels, L., Ribeiro, L., Mundim, M.S.P., Sousa, M.H., Droppa, R., Fossum, J.O., da Silva, G.J., Mundim, K.C., 2014. EXAFS and XRD studies in synthetic Ni-fluorohectorite. *Appl. Clay Sci.* 96, 60–66.
- Michels, L., Fossum, J.O., Rozynek, Z., Hemmen, H., Rustenberg, K., Sobas, P.A., Kalantzopoulos, G.N., Knudsen, K.D., Janek, M., Plivelic, T.S., da Silva, G.J., 2015. Intercalation and retention of carbon dioxide in a smectite clay promoted by inter-layer cations. *Sci. Rep.* 5, 8775.
- Möller, M.W., Handge, U.A., Kunz, D.A., Lunkenbein, T., Alstädt, V., Breu, J., 2010a. Tailoring shear-stiff, mica-like nanoplatelets. *ACS Nano* 4, 717–724.
- Möller, M.W., Hirsemann, D., Haarmann, F., Senker, J.R., Breu, J., 2010b. Facile scalable synthesis of rectorites. *Chem. Mater.* 22, 186–196.
- Moore, D.M., Reynolds, R.C.J., 1997. X-ray Diffraction and the Identification and Analysis of Clay Minerals, second ed. Oxford University Press, New York.
- Nam, K.-M., Kim, H.-J., Kang, D.-H., Kim, Y.-S., Song, S.-W., 2015. Ammonia-free co-precipitation synthesis of a Ni-Co-Mn hydroxide precursor for high-performance battery cathode materials. *Green Chem.* 17, 1127–1135.
- Ohtsuka, K., Suda, M., Ono, M., Takahashi, M., Sato, M., Ishio, S., 1987. Preparation of nickel(II)-hydroxide-(sodium fluoride tetrasilic mica) intercalation complexes and formation of ultra fine nickel particles by H₂ reduction. *Bull. Chem. Soc. Jpn.* 60, 871–876.
- Ohtsuka, K., Suda, M., Tsunoda, M., Ono, M., 1990. Synthesis of metal hydroxide-layer silicate intercalation compounds (Metal = Mg(II), Ca(II), Mn(II), Fe(II), Co(II), Ni(II), Zn(II), and Cd(II)). *Chem. Mater.* 2, 511–517.
- Parker, S.F., Lennon, D., Albers, P.W., 2011. Vibrational spectroscopy with neutrons: a review of new directions. *Appl. Spectrosc.* 65, 1325–1341.
- Parker, S.F., Fernandez-Alonso, F., Ramirez-Cuesta, A.J., Tomkinson, J., Rudic, S., Pinna, R.S., Gorini, G., Fernández Castañon, J., 2014. Recent and future developments on TOSCA at ISIS. *J. Phys. Conf. Ser.* 554.
- Persson, R.A.X., Pattni, V., Singh, A., Kast, S.M., Heyden, M., 2017. Signatures of solvation thermodynamics in spectra of intermolecular vibrations. *J. Chem. Theory Comput.* 13, 4467–4481.
- Purnell, J.H., Yun, L., 1993. Ionic migration and charge reduction in Ni^{2+} , Co^{2+} and Zn^{2+} -exchanged Texas montmorillonite. *Catal. Lett.* 18, 235–241.
- Rosenfeldt, S., Stöter, M., Schlenk, M., Martin, T., Albuquerque, R.Q., Förster, S., Breu, J., 2016. In-depth insights into the key steps of delamination of charged 2D nanomaterials. *Langmuir ACS J. Surf. Colloids* 32, 10582–10588.
- Rother, G., Ilton, E.S., Wallacher, D., Haubeta, T., Schaefer, H.T., Qafoku, O., Rosso, K.M., Felmy, A.R., Krukowski, E.G., Stack, A.G., Grimm, N., Bodnar, R.J., 2013. CO_2 sorption to subsingle hydration layer montmorillonite clay studied by excess sorption and neutron diffraction measurements. *Environ. Sci. Technol.* 47, 205–211.
- Sato, T., Nakamura, T., Ozawa, F., 1975. Thermal decomposition of nickel hydroxide. *J. Appl. Chem. Biotechn.* 25, 583–590.
- Song, Q., Tang, Z., Guo, H., Chan, S.L.L., 2002. Structural characteristics of nickel hydroxide synthesized by a chemical precipitation route under different pH values. *J. Power Sources* 112, 428–434.
- Stöcker, M., Jens, K.-J., Riis, T., Grepstad, J.K., 1988. Characterization of Ni-exchanged montmorillonites by X-ray photoelectron spectroscopy. *J. Chem. Soc. Faraday Trans.* 84, 1863–1870.
- Stöter, M., Kunz, D.A., Schmidt, M., Hirsemann, D., Kalo, H., Putz, B., Senker, J., Breu, J., 2013. Nanoplatelets of sodium hectorite showing aspect ratios of approximately 20,000 and superior purity. *Langmuir ACS J. Surf. Colloids* 29, 1280–1285.
- Stöter, M., Biersack, B., Reimer, N., Herling, M., Stock, N., Schobert, R., Breu, J., 2014. Ordered heterostructures of two strictly alternating types of nanoreactors. *Chem. Mater.* 26, 5412–5419.
- Stöter, M., Biersack, B., Rosenfeldt, S., Leitl, M.J., Kalo, H., Schobert, R., Yersin, H., Ozin, G.A., Förster, S., Breu, J., 2015. Encapsulation of functional organic compounds in nanoglass for optically anisotropic coatings. *Angew. Chem. Int. Ed.* 54, 4963–4967.
- Stöter, M., Godrich, S., Feicht, P., Rosenfeldt, S., Thurn, H., Neubauer, J.W., Seuss, M., Lindner, P., Kalo, H., Moller, M., Fery, A., Forster, S., Papastavrou, G., Breu, J., 2016.

P. Loch, et al.

Applied Clay Science 198 (2020) 105831

- Controlled exfoliation of layered silicate heterostructures into bilayers and their conversion into giant janus platelets. *Angew. Chem. Int. Ed. Eng.* 55, 7398–7402.
- Touillaux, R., Salvador, P., Vandermeersche, C., Fripiat, J.J., 1968. Study of water layers absorbed on Na- and Ca-montmorillonite by the pulsed nuclear magnetic resonance technique. *Isr. J. Chem.* 6, 337–348.
- Uehara, M., Yamzaki, A., Umezawa, T., Takahashi, K., Tsutsumi, S., 1999. A nickel-hydroxide-vermiculite complex: preparation and characterization. *Clays Clay Miner.* 47, 726–731.
- Vivaldi, J.L., MacEwan, D.M.C., 1960. Corrensite and swelling chlorite. *Clay Miner. Bull.* 4, 173–181.
- Yamanaka, S., Brindley, G.W., 1978. Hydroxy-nickel interlayering in montmorillonite by titration method. *Clay Clay Miner.* 26, 21–24.
- Yang, L., Kruse, B., 2004. Revised Kubelka-Munk theory. I. Theory and application. *J. Opt. Soc. Am.* 21, 1933–1941.
- Yu, J., Hai, Y., Cheng, B., 2011. Enhanced photocatalytic H₂-production activity of TiO₂ by Ni(OH)₂ cluster modification. *J. Phys. Chem. C* 115, 4953–4958.

Results

6.1.2. Supporting Information

Spontaneous Formation of an Ordered Interstratification upon Ni-exchange of Na-Fluorohectorite

Patrick Loch[†], Kristoffer William Bø Hunvik[‡], Florian Puchtler[†], Sebastian Weiß[†], Konstanse Kvaem Seljelid[‡], Paul Monceyron Røren[‡], Svemir Rudic[#], Steinar Raaen[‡], Kenneth Dahl Knudsen^{§, ‡}, Heloisa Nunes Bordallo^{¶, |, *}, Jon Otto Fossum^{‡, *} and Josef Breu^{†, *}

[†] *Bavarian Polymer Institute and Department of Chemistry, University of Bayreuth, Universitätsstraße 30, D-95440 Bayreuth, Germany*

[‡] *Department of Physics, Norwegian University of Science and Technology, Høgskoleringen 5, NO 7495 Trondheim, Norway*

[#] *ISIS Neutron and Muon Source, STFC Rutherford Appleton Laboratory, Chilton, Didcot OX11 0QX, United Kingdom*

[§] *Institute for Energy Technology (IFE), POB 40, N-2027 Kjeller, Norway*

[¶] *Niels Bohr Institute-University of Copenhagen, Universitetsparken 5, 2100 Copenhagen, Denmark*

[|] *European Spallation Source ESS ERIC, PO Box 176, SE-221 00 Lund, Sweden*

** Corresponding authors*

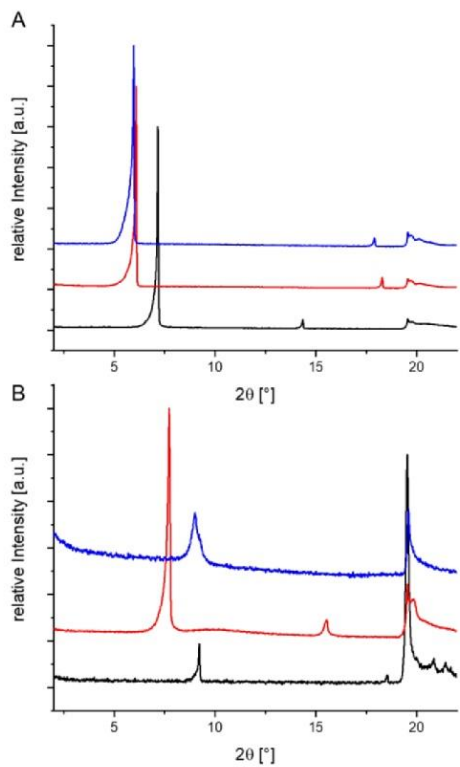


Figure S1: PXRD pattern recorded in transmission mode of Na-Hec (black), Ni-Hec (red) and Ca-Hec (blue) at 43 % r. h. and dried under Ar flow at 150°C (B).

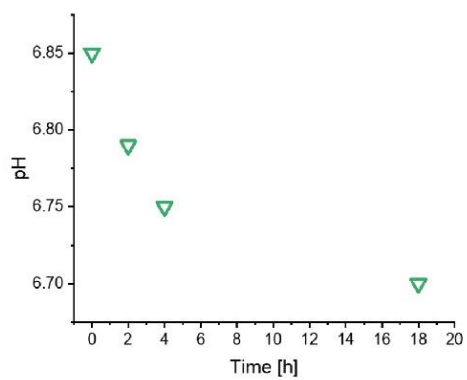


Figure S2: pH of the supernatant of the exchange solution during the Ni-exchange.

Results

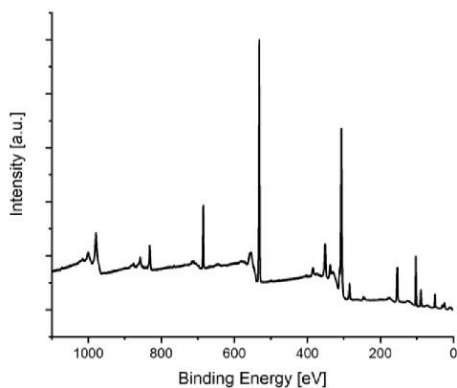


Figure S3: XPS survey spectrum of Ni-Hec with marked peaks assigned to the fluorohectorite.

Electrochemical experiments were performed using an Autolab Potentiostat/Galvanostat PGSTAT204 with an Autolab Rotating Disc Electrode (RDE). A modified Glassy Carbon (GC) electrode (\varnothing 3 mm) and a platinum plate were used as working and counter electrode, respectively. All measurements were performed using an Ag/AgCl (3 M KCl) double-junction reference electrode with 1 M KNO_3 in the outer filling. The GC electrode was modified by preparing a slurry (5 mg catalyst, 490 μl ethanol, 490 μl water and 20 μl Nafion® 117 solution) and exposing the dispersion to ultrasound for 10 s to achieve a homogeneous material distribution. All necessary chemicals were purchased from Sigma Aldrich and were used as received. The GC electrode was polished to a mirror finish and drop coated with the slurry to obtain a surface loading of roughly 12 mg/cm^2 . All the following electrochemical experiments were carried out at a rotation speed of 1600 rpm.

First, cyclic voltammetry was performed (Figure S4) to determine the corresponding oxidation and reduction potential of the $\text{Ni}^{2+}/\text{Ni}^{3+}$ pair in the material ($v = 100 \text{ mV/s}$). The position of the anodic and cathodic redox peaks are reasonably similar to literature reports on $\text{Ni}(\text{OH})_2$ and NiOOH under similar conditions and have been attributed to the oxidation and reduction of Ni^{2+} to Ni^{3+} and Ni^{3+} to Ni^{2+} , respectively. (Trafela et al., 2019) Note that the first scan is clearly different from the

consecutive scans which we attribute to a conditioning process involving the initial oxidation of Ni^{2+} to Ni^{3+} . In all subsequent cycles, a defined oxidation and reduction peak is observable which corresponds to Ni-species undergoing a reversible reaction.

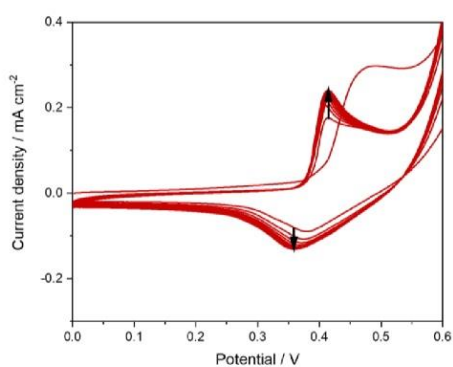


Figure S4: Cyclic voltammogram of Ni-Hec.

A freshly prepared sample was equilibrated by holding the voltage at the open circuit potential (OCP), which was determined to be 0.02 V, for 30s. Expectedly, no notable current was detected during this period. Subsequently, chrono amperometric measurements were performed employing a potential of 0.0 V for 120 s (Figure S5). The measured current was negligible during the whole experiment and did thus not exhibit any notable increase or decrease. After a rest period of 120 s, the Ni^{2+} species in the material were oxidised on purpose by applying 0.5 V over 120 s (Figure S6). An anodic current with notable current density was observed. Expectedly, as the oxidation of Ni^{2+} to Ni^{3+} progressed, the observed current decayed over time.

Results

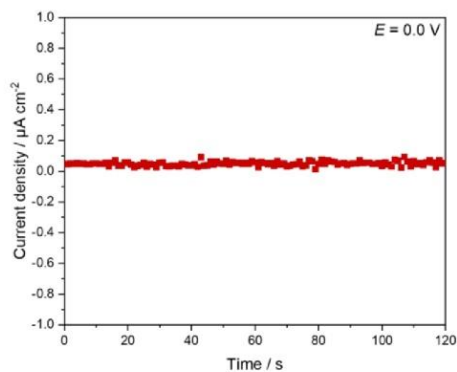


Figure S5: Chrono amperometric measurement of Ni-Hec at 0.0 V for 120 s.

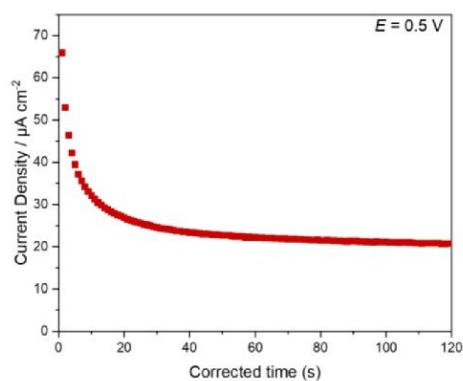


Figure S6: Chrono amperometric measurement of Ni-Hec at 0.5 V for 120 s.

The oxidised material was now subjected to the same treatment as the pristine material in the beginning (0.0 V for 120 s) (Figure S7). The measurement indicated a clearly observable cathodic current originating from the reduction of Ni^{3+} to Ni^{2+} , which was not detectable for the pristine material. Thus, we conclude that no notable amounts of Ni^{3+} were present in the pristine material and within experimental error the nickel-species were present in the Ni^{2+} oxidation state.

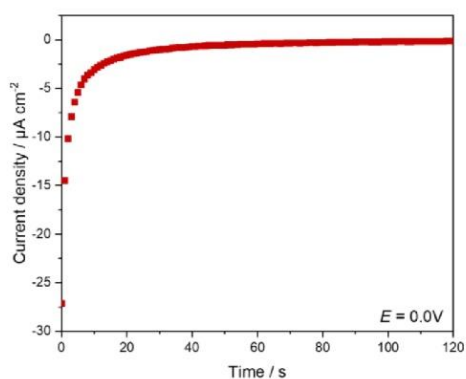


Figure S7: Chrono amperometric measurement of Ni-Hec at 0.0 V for 120 s after forced electrochemical oxidation.

Please note that the electrochemically induced oxidation and subsequent reduction did not match regarding charge flow as we cannot exclude material loss or guarantee a fully reversible reaction between the two Ni oxidation states.

REFERENCES

Trafela, Š., Zavašnik, J., Šturm, S., Rožman, K.Ž., 2019. Formation of a $\text{Ni}(\text{OH})_2/\text{NiOOH}$ active redox couple on nickel nanowires for formaldehyde detection in alkaline media. *Electrochim. Acta* 309, 346-353.

Results

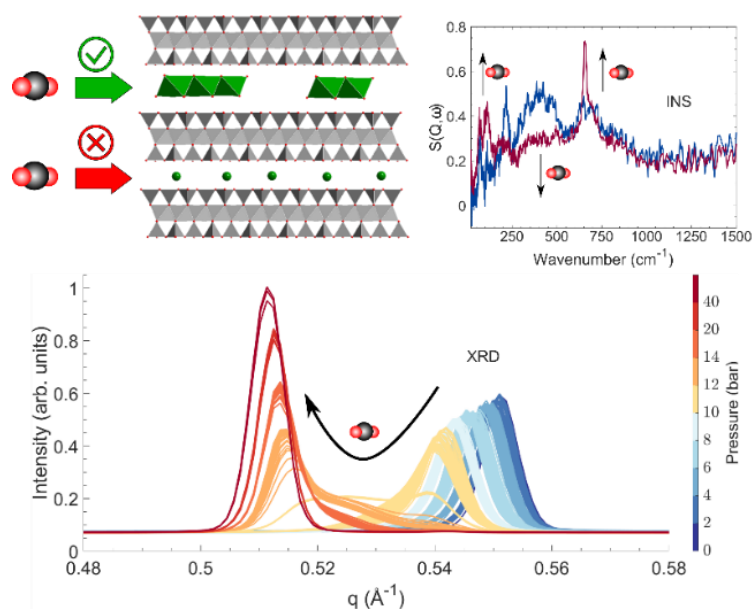
6.2. Insights into the CO₂ swelling mechanism of Ni-Hectorites

Kristoffer William Bø Hunvik^a, Patrick Loch^b, Leide P. Cavalcanti^{c, d}, Konstanse Kvaalem Seljelid^a, Paul Monceyron Røren^a, Svemir Rudić^d, Dirk Wallacher^b, Aleksandro Kirch^e, Kenneth Dahl Knudsen^{b, c}, Caetano Rodrigues Miranda^e, Josef Breu^{b, *}, Heloisa Nunes Bordallo^{f, g, *} and Jon Otto Fossum^{a, *}

CO₂ Capture by Nickel Hydroxide Interstratified in the Nanolayered Space of a Synthetic Clay Mineral

Published in: *The Journal of Physical Chemistry C* **2020**, 124, 2622-2631.

Reproduced under the terms of the CC-BY 4.0 license.



^a Department of Physics, Norwegian University of Science and Technology, Høgskoleringen 5, NO 7495 Trondheim, Norway

^b Bavarian Polymer Institute and Department of Chemistry, University of Bayreuth, Universitätsstraße 30, D-95440 Bayreuth, Germany

^c Institute for Energy Technology (IFE), POB 40, N-2027 Kjeller, Norway

^d ISIS Neutron and Muon Source, STFC Rutherford Appleton Laboratory, Chilton, Didcot OX11 0QX, United Kingdom

^e Departamento de Física dos Materiais e Mecânica, Instituto de Física, Universidade de São Paulo, 05508-090 São Paulo, Brazil

^f Niels Bohr Institute-University of Copenhagen, Universitetsparken 5, 2100 Copenhagen, Denmark

^g European Spallation Source ESS ERIC, PO Box 176, SE-221 00 Lund, Sweden

* Corresponding authors

Results

Individual Contribution:

This publication is the result of a cooperation with the NTNU. The publication was conceived by K.W.B. Hunvik, L P. Cavalcanti, Prof. K. D. Knudsen, Prof. J. Breu, Prof. J. O. Fossum and myself. K.W.B. Hunvik wrote the first draft of the manuscript. Together with K.W.B. Hunvik, Prof. J. O. Fossum and Prof. J. Breu, I developed the swelling model and contributed with corrections. I synthesized the material and provided the samples. K.W.B. Hunvik, L P. Cavalcanti, K.K. Seljelid, Prof. K. D. Knudsen and Prof. J. O. Fossum carried out the Raman and X-ray diffraction experiments at ESRF. K.W.B. Hunvik, S Rudić, P.M. Røren, Prof. K. D. Knudsen, Prof. H.N. Bordallo and Prof. J. O. Fossum carried out the INS measurements at the ISIS Neutron and Muon Source. D. Wallacher performed the adsorption measurements. A. Kirch and Prof. C. R. Rodrigues Miranda contributed with DFT simulations.

My contribution to the publication is approx. 25 %

6.2.1. CO₂ Capture by Nickel Hydroxide Interstratified in the Nanolayered Space of a Synthetic Clay Mineral

This is an open access article published under a Creative Commons Attribution (CC-BY) License, which permits unrestricted use, distribution and reproduction in any medium, provided the author and source are cited.



THE JOURNAL OF
PHYSICAL CHEMISTRY C

pubs.acs.org/JPC

Article

CO₂ Capture by Nickel Hydroxide Interstratified in the Nanolayered Space of a Synthetic Clay Mineral

Kristoffer W. Bø Hunvik, Patrick Loch, Leide P. Cavalcanti, Konstanse Kvalem Seljelid, Paul Monceyron Røren, Svemir Rudić, Dirk Wallacher, Alessandro Kirch, Kenneth Dahl Knudsen, Caetano Rodrigues Miranda, Josef Breu,* Heloisa N. Bordallo,* and Jon Otto Fossum*

Cite This: *J. Phys. Chem. C* 2020, 124, 26222–26231

Read Online

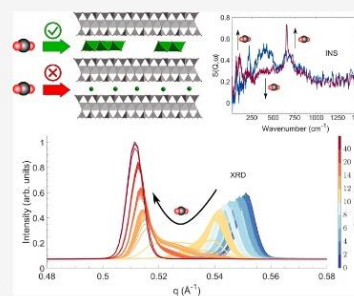
ACCESS

Metrics & More

Article Recommendations

Supporting Information

ABSTRACT: Clay minerals can adsorb large amounts of CO₂ and are present in anthropogenic storage sites for CO₂. Nanoscale functionalization of smectite clay minerals is essential for developing technologies for carbon sequestration based on these materials and for safe-guarding relevant long-term carbon storage sites. We investigate the adsorption mechanisms of CO₂ in dried and hydrated synthetic Ni-exchanged fluorohectorite clay—using a combination of powder X-ray diffraction, Raman spectroscopy, and inelastic neutron scattering. Both dried and hydrated Ni-exchanged fluorohectorite show crystalline swelling and spectroscopic changes in response to CO₂ exposure. These changes can be attributed to interactions with [Ni(OH)_{0.83}(H₂O)_{1.17}]_{0.37}^{1.17+}-interlayer species, and swelling occurs solely in the interlayers where this condensed species is present. The experimental conclusions are supported by density functional theory simulations. This work demonstrates a hitherto overlooked important mechanism, where a hydrogenous species present in the nanospace of a clay mineral creates sorption sites for CO₂.



Continuous and increasing release of greenhouse gases, in particular CO₂, to the atmosphere has a detrimental impact on our environment. In addition to emission reduction, it is imperative to establish effective ways of capturing these gases. Clay minerals have become an attractive alternative for investigating CO₂ capture because of their excellent behavior in adsorption and catalysis.¹ This is in addition to their abundance and stability, which make them potentially scalable for industrial processes.

Smectite clay minerals, such as hectorite and montmorillonite, are known to readily swell in response to water,^{2–4} CO₂^{5–10} and organic compounds.^{11,12} They consist of two-dimensional nanolayered stacks possessing a negative layer charge due to nonequivalent substitutions of atoms in the layers. The negative layer charge is typically counterbalanced by exchangeable interlayer cations, for example Na⁺, Ca²⁺, and K⁺.

The sorption of CO₂ in smectite clays at various hydration states as well as under gaseous and supercritical CO₂ conditions has been studied by a wide range of techniques, such as X-ray and neutron diffraction, infrared spectroscopy, nuclear magnetic resonance, quartz crystal microbalance, and volumetric/gravimetric gas adsorption.^{5–7,13–21} The sorption of CO₂ in smectite clays has been shown to largely depend on the initial hydration, the interlayer cation, and the specific clay type. For montmorillonite (Mt) and OH-hectorite (Hec), experiments and simulations at 323 K and 90 bar have shown

that for smaller interlayer cations with a high hydration energy (e.g. Na⁺, Ca²⁺, and Mg²⁺), a submonolayer of water is necessary to open up the interlayer to swell in response to CO₂.^{8–10} However, for larger interlayer cations with low hydration energy (e.g. Cs⁺, K⁺, and NH₄⁺), CO₂ is intercalated even in the absence of water.^{8–10}

Natural Hec has a varying composition of F[−] and OH[−] groups, whereas fluorohectorite is a synthetic Hec with only fluorine groups. Simulations²² have shown that by varying the F[−]/(F[−] + OH[−]) composition, the CO₂/(CO₂ + H₂O) ratio increases with increasing F[−] substitution. It has previously been demonstrated that a fluorinated Hec exchanged with Na⁺, Li⁺, and Ni²⁺ swells in response to CO₂ exposure^{5,6} and that Ni-Hec showed a much larger adsorption of CO₂ than Li-Hec and Na-Hec.⁷

Here, we report a hitherto overlooked mechanism for CO₂ sorption in Ni-Hec as studied with synchrotron X-ray diffraction, Raman spectroscopy, and inelastic neutron scattering (INS). The intercalation properties of Ni²⁺ in smectites have been shown to be substantially different from

Received: August 6, 2020

Revised: October 27, 2020

Published: November 16, 2020



ACS Publications

© 2020 American Chemical Society

26222

https://dx.doi.org/10.1021/acs.jpcc.0c07206
J. Phys. Chem. C 2020, 124, 26222–26231

other interlayer cations.^{6,23} As recently reported in Loch et al.,²⁴ Ni-Hec forms an ordered interstratification with a chlorite-like condensed $[\text{Ni}(\text{OH})_{0.83}(\text{H}_2\text{O})_{1.17}]_{0.37}^{1.17+}$ species in one interlayer and a smectite-like structure with hydrated Ni^{2+} cations in the adjacent interlayer. By employing powder X-ray diffraction (PXRD), we investigate the structural changes in response to CO_2 . We utilize *in situ* Raman scattering combined with PXRD, which allows studying how CO_2 adsorption changes the local structure. INS has no selection rules for the vibrational modes and a large cross section of the hydrogen atoms, making the signal from the water motions and other hydrogenous species, such as nickel hydroxide, prominent.²⁵ INS has previously been successfully employed to study how layer charge and cations influence the hydration properties of saponite, montmorillonite, and beidelitte.^{26,27}

By combining PXRD, Raman spectroscopy, and INS, we elucidate the active mechanisms of CO_2 sorption for Ni-Hec in the dried (at 150 °C under dynamic vacuum) and hydrated (equilibrated at 43% r.h.) states. To support our experimental conclusions, we have performed density functional theory calculations (DFT).

METHODS

Materials. Na-Hec with a stoichiometric composition of $\text{Na}(\text{Mg}_3\text{Li})\text{Si}_8\text{O}_{20}\text{F}_4$ was prepared via melt synthesis according to a published procedure,² followed by annealing (6 weeks, 1045 °C) to improve charge homogeneity and phase purity.²⁸ Ni-Hec was prepared by cation exchange of Na-Hec with 0.2 M nickel–acetate solution (>10 fold excess of the CEC, 5 times). The exchanged Ni-Hec was washed 5 times with Millipore water. The hydration and drying procedures are described below for each type of experiment.

In Situ Powder X-ray Diffraction and In Situ Raman Spectroscopy. For Ni-Hec, combined Raman and synchrotron X-ray powder diffraction data were collected at the Swiss-Norwegian Beamlines (SNBL, station BM01B) at ESRF, Grenoble, France. PXRD data were measured at a wavelength of 0.77495 Å using a 2D PILATUS2M detector.²⁹ The 2D diffractograms were integrated using the SNBL Bubble software to provide rebinned 1D diffraction patterns. The powdered samples were contained in borosilicate capillaries mounted in a custom made high-pressure sample cell based on the design by Jensen et al.³⁰ The temperature of the capillary was controlled by an Oxford Cryostream 700+ nitrogen blower. The cell was connected to a gas handling system providing vacuum (10^{-6} mbar) from a turbomolecular pump or pressurized CO_2 of quality 99.9995%. The dried Ni-Hec sample was prepared at 150 °C in the capillary sample cell for ~2 h and was considered sufficiently dried since the (00 l) Bragg reflections did not change position after reducing the temperature to 300 K. The hydrated sample was prepared in a desiccator prior to the measurements corresponding to 2 WL hydration. Raman spectra were collected on a Renishaw RA 100 Raman analyzer, using a 532 nm (green) excitation wavelength in backscattering mode. Spectra were recorded in the range 100–4000 cm^{-1} with a step size 1.2 cm^{-1} , and 5 scans per spectrum were recorded with an exposure of 60 s.

Included in the Supporting Information are PXRD data on a dried Na-Hec as a reference.

Inelastic Neutron Scattering. Inelastic neutron spectra were recorded using the TOSCA spectrometer^{31–33} at the ISIS facility, Rutherford Appleton Laboratory, UK. TOSCA is an indirect geometry time-of-flight spectrometer spanning an

energy-transfer range up to 4000 cm^{-1} in neutron energy loss (E_T) with a spectral resolution of 1.25% E_T .³¹ In order to minimize thermal effects, the spectra were recorded at $T < 20$ K.

Ni-Hec both in the hydrated and dried state was prepared for the INS experiment. Hydrated samples were equilibrated for 5 days at 43% relative humidity in a desiccator with saturated K_2CO_3 solution, while dried samples were prepared by heating the samples to 145 ± 15 °C under high vacuum (10^{-6} mbar) for 18 h (Ni-Hec sample). As a reference, included in the Supporting Information are data on dried Na-Hec (7 h at 145 ± 15 °C under high vacuum) with the same experimental procedure as dried Ni-Hec.

The samples were placed in an aluminum foil sachet and mounted in stainless steel cylinders. The sample holder was then mounted on a center stick connected to a gas handling system. Prior to measurements, the cell was leak tested with 50 bar helium which was pumped away in the case of dried samples and leaked slowly to atmospheric pressure in the case of the hydrated samples.

Dried Ni-Hec was measured under vacuum, at 5 bar of CO_2 , 44 bar of CO_2 , and after releasing CO_2 (~24 h under vacuum). The hydrated sample was measured at ambient pressure and 44 bar CO_2 pressure. Each pressure step was achieved by heating up the sample holder and center stick to room temperature, exposing the sample to CO_2 grade 99.9995% for 20 min, and subsequently cooling down to $T < 20$ K with CO_2 still inside the sample holder. Each INS measurement lasted around 6–8 h, depending on the amount of hydrogen in the sample.

The data were reduced using the software package Mantid.³⁴ After subtracting the signal from the empty cell, the spectra were scaled by the sample mass. After exposure to CO_2 , the signal was normalized to have the same area under the curve as the initial spectrum.

DFT Simulations. We performed *ab initio* investigations based on density functional theory calculations^{35,36} considering the generalized gradient approximation with the state-of-the-art van der Waals-corrected density functional developed by Berland and Hyldgaard,³⁷ as implemented in the Siesta package.³⁸ Norm-conserving pseudopotentials were used with double-zeta plus polarization and spin-polarized localized atomic orbital basis sets considering an energy cutoff of 400 Ry. The crystallographic structure reported by Breu et al.³⁹ was used for the Ni-Hec model with the unit cell containing 39 atoms. For $\beta\text{-Ni}(\text{OH})_2$, we took the structural model from the Aflowlib repository.⁴⁰ Adsorbents were allowed to relax during structural optimization using the conjugate gradient method under the self-consistent cycles considering a criteria of 0.01 eV/Å for the force minimization. The adsorption energy E_{Ads} was calculated following the equation

$$E_{\text{Ads}} = E_{\text{Total}} - E_{\text{Crystal}} - E_{\text{Molecule}} \quad (1)$$

where E_{Total} is the total energy for the adsorbed molecule in the most favorable adhesion site; E_{Crystal} and E_{Molecule} are the total energies for the isolated systems.

RESULTS AND DISCUSSION

Powder X-ray Diffraction. Dried Ni-Hec. In Figure 1, the swelling of Ni-Hec at 300 K with increasing CO_2 pressure is shown. After drying the sample in vacuum at 150 °C, an intense Bragg reflection is observed at 0.551 \AA^{-1} , corresponding to a d -value of 11.40 Å, which recently was identified as the

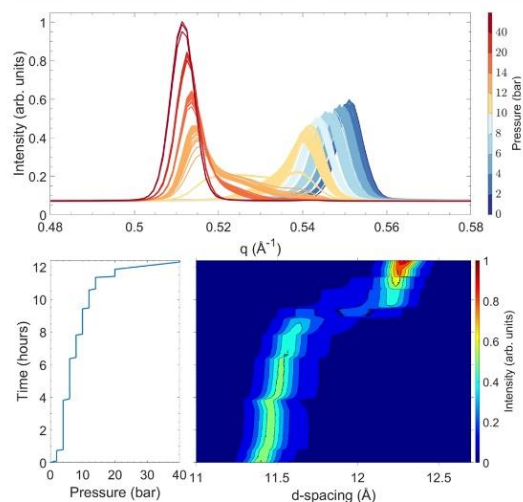


Figure 1. Evolution of the (002) Bragg reflection as a function of pressure at 300 K for dried Ni-Hec. In the top panel, the Bragg reflection is plotted with colors indicating pressure given by the color bar. The bottom left panel is the pressure of CO₂ applied to the sample as a function of time. The bottom right panel depicts a contour plot where the horizontal axis corresponds to d -spacing ($d = 2\pi/q$), the vertical axis corresponds to time, and the color represents the intensity.

(002) Bragg reflection of an ordered interstratification of a nonhydrated, collapsed interlayer and a chlorite-type interlayer of $[\text{Ni}(\text{OH})_{0.83}(\text{H}_2\text{O})_{1.17}]_{0.37}^{1.17+}$.²⁴

With increasing pressure of CO₂, transient interstratified domains are observed in addition to initial and final state domains, transferring the weight from one state to the other. Since swelling is an inherent two-dimensional process, reflections gradually move as the number of swollen interlayers increases and thus the weighting of the interstratified stacks becomes larger. For intermediate stages, the intensities are not proportional to the volumes of swollen and not yet swollen interlayers because of the weighting differing from the 1:1 ratio. The nonlinear transition of the educt to product intensities is an artifact that may be attributed to the effect of interstratification.

At pressures above 10 bar, the educt phase starts to vanish, while the product basal spacing continues to be shifted to larger d -spacings until around 12 bar, where the swelling reaches a plateau. At the final pressure of 40 bar CO₂, a symmetric peak with a maximum intensity centered at 0.511 Å⁻¹ corresponding to a d -value of 12.29 Å is observed. As the inspected Bragg reflection is (002), a total interlayer expansion of 1.78 Å is observed. While intermediate reflections, in line with Mering's rules, are broadened due to interstratification, the width of the Bragg reflection is unchanged when comparing the initial state and the final state, indicating completion of swelling. The observed swelling is clearly correlated with the gravimetric adsorption data presented in the Supporting Information, demonstrating that the swelling is caused by uptake of CO₂. As there is limited change above 20 bar, these results also provide valuable information on what could occur in a geological storage where the temperature and pressure can be >40 °C and >90 bar.⁴¹

Hydrated Ni-Hec. In Figure 2, the expansion upon CO₂ exposure of a Ni-Hec hydrated at 300 K is shown, adopting the

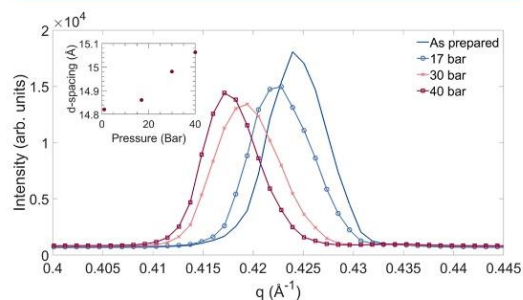


Figure 2. X-ray diffraction pattern of the (002) Bragg reflection for hydrated Ni-Hec at 300 K following the evolution with respect to pressure for the sample as-prepared at 1 bar up to 40 bar of CO₂. The inset shows the corresponding d -spacing evolution as a function of pressure.

2 WL hydrate state with a (002) Bragg reflection at 14.82 Å,²⁴ which gradually increases to 15.06 Å as the CO₂ pressure increases. Compared to the dried sample, a smaller increase is observed, that is 0.48 versus 1.78 Å. Again, the width of the Bragg reflection at the initial state and final CO₂ exposed state is comparable.

Interestingly, upon swelling in response to CO₂, the crystallinity was improved by reducing planar defects as indicated by cross-reflections in the region of the 11/02 band gaining significant intensity (Figure 3). While the starting material shows a λ -shaped band typical for turbostratic stacking, after CO₂ saturation, a 3D ordered stacking is observed with a refined unit cell of ($C2/m$, $a = 5.2504$ Å, $b = 9.0780$ Å, $c = 30.25$ Å, $\beta = 96.6280^\circ$, $\alpha/\gamma = 90^\circ$). Such a disorder/order transformation has previously been observed at the transition from 1 WL to 2 WL hydrate of Na-Hec^{4,28} and has been attributed to a strengthened interaction of interlayer species with the surface of the 2:1-silicate layers via hydrogen bonding. In the present case, this disorder/order transformation was reversible and was lost again as the CO₂ pressure was reduced, as shown in Figure S5.

In Situ Raman Spectroscopy. *In situ* Raman spectra corresponding to pristine (not yet exposed to CO₂) hydrated Ni-Hec (Figures 2 and 3) and exposed to 40 bar CO₂ pressure are shown in Figure 4. The assignment of the vibrations is given in Table 1. A very high fluorescent background did not allow us to record Raman spectra for dried Ni-Hec. Fluorescence is commonly observed in clay minerals;⁴² however, in this study, fluorescence also arises from the electronic structure of the Ni²⁺ cations, which have a 3d⁸ valence configuration.⁴³ Local distortion of octahedrally coordinated chlorite-type $[\text{Ni}(\text{OH})_{0.83}(\text{H}_2\text{O})_{1.17}]_{0.37}^{1.17+}$ greatly affects the associated orbitals also contributing to the observed fluorescence.⁴³

Modes associated to the Hec structure are assigned according to Rinaudo et al.⁴⁴ As recently shown in Loch et al.,²⁴ Ni-Hec contains both Ni²⁺ and $[\text{Ni}(\text{OH})_{0.83}(\text{H}_2\text{O})_{1.17}]_{0.37}^{1.17+}$ species segregated into adjacent interlayers. Thus, the vibrations at 319 cm⁻¹ (#4) and 467 cm⁻¹ (#7) can be associated to Ni-OH vibrations.⁴⁵ We also observe a third feature around 506 cm⁻¹ (#8) that can be

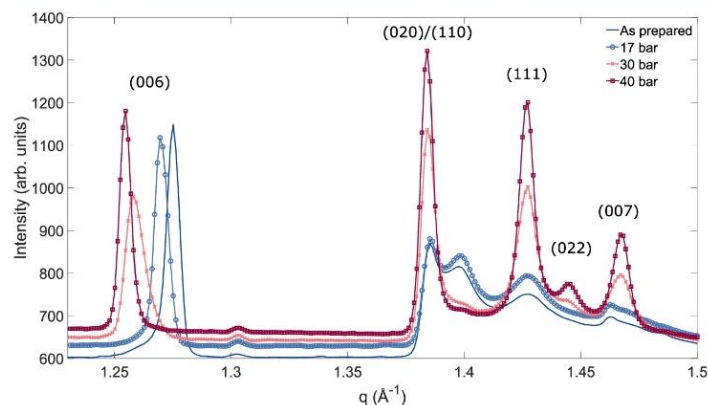


Figure 3. X-ray diffraction pattern of hydrated Ni-Hec as a function of CO₂ pressure at 300 K.

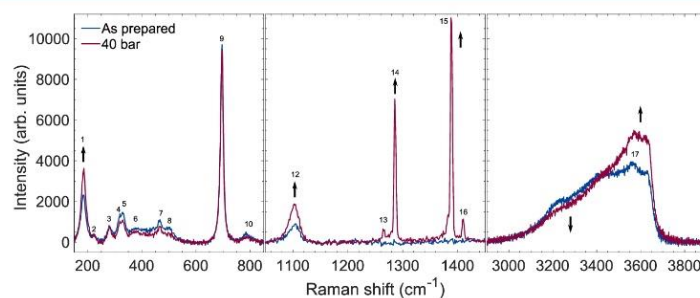


Figure 4. Raman spectra of hydrated Ni-Hec as prepared at 1 bar and exposed to 40 bar of CO₂ at 300 K. Numbering indicates the assigned vibrations, and arrows highlight prominent changes in the spectra. Mode assignment is summarized in Table 1.

Table 1. Raman Vibration Assignment of the Peaks Presented in Figure 4

feature number	position (cm ⁻¹)	suggested assignment
1	184	MgLiO ₆ octahedra ⁴⁴
2	222	(small vibration) unassigned
3	280	O–H–O vibrations ⁴⁵
4	319	A _{1g} (T), E _g (T) or E _g (R) Ni-(OH) ⁴⁵
5	330	bending SiO ₄ ⁴⁴
6	371	stretch Mg–O ⁵⁰
7	467	A _{1g} /E _u (LO)/A _{2u} (LO) Ni-(OH) ⁴⁵
8	506	A _{1g} (T) or E _g (T) Ni-(OH) ⁴⁵
9	696	ν _s SiO ₄ ⁴⁴
10	783	vibration SiO ₄ ⁵⁰
11	1006	vibration SiO ₄ ⁵⁰
12	1105	ν _{as} SiO ₄ ⁴⁴
13	1265	CO ₂ ; hot band ⁵¹
14	1286	CO ₂ ; 2ν ₂ ⁵¹
15	1388	CO ₂ ; ν ₁ ⁵¹
16	1410	CO ₂ ; hot band ⁵¹
17	3565	Ni-(OH) A _{1g} O–H ⁴⁵

assigned either to the presence of structural defects and/or to a E_g(R) mode for the Ni–OH structure.

In the range of OH-modes between 3000 and 3600 cm⁻¹, the sharp feature at 3565 cm⁻¹ (#17) is assigned to the A_{1g} O–H stretch of Ni–OH.⁴⁵ The remaining modes in this region

are assigned to water present in the clay. These can be divided into water bonded directly to the interlayer cations, interlayer water that does not directly interact with the cations, and water outside the interlayers.⁴⁶ The latter constitutes a tiny amount because of the large aspect ratio of the clay particles,^{2,8} which results in a relatively low external surface area. The water not directly coordinated to the interlayer cations can either be in the chlorite-like or the smectite-like layers. Given these possibilities, an unambiguous assignment of the modes in this region is difficult.

After exposure to 40 bar of CO₂ (Figure 4), the intensity of bands related to CO₂ at 1286 cm⁻¹ (#14) and 1388 cm⁻¹ (#15) increases. There is also a clear change in the intensity associated to OH-groups between 3000 and 3600 cm⁻¹ and an increase of intensity and sharpening of the vibration associated to the Mg, LiO₆ octahedra, and the asymmetric stretch of SiO₄.

Because the density ratio between intercalated and non-intercalated gaseous CO₂ in the probing volume of the Raman laser is low, the intensity of the CO₂ vibrations is most likely to be dominated by gaseous CO₂ in the capillary. The increase and sharpening of the modes associated to the octahedral and the tetrahedral sheet of the clay layers can be associated to the order–disorder transition observed by PXRD (Figures 2 and 3). Indeed, an increased long-range order in clays is known to enhance the signal to noise-ratio and sharpen the peaks.⁴⁷ The shape change in the H₂O/OH-region could indicate some local modification of the water population in the interlayers. In

addition, there are clear changes for the OH-stretching bands. The observed changes for the OH-stretching vibrations bear resemblance to previously observed changes when β -Ni(OH)₂ transforms to α -Ni(OH)₂,⁴⁸ which indicates that CO₂ has an effect on the intercalated [Ni(OH)_{0.83}(H₂O)_{1.17}]_{0.37}^{1.17+} species. The observed increase of intensity around 1100 cm⁻¹ (#12) can then, in addition to ordering of the clay crystal structure, be associated with introduced stress in the nickel hydroxide lattice.⁴⁸ The increased intensity at 1100 cm⁻¹ (#12) could also be due to carbonate (CO₃²⁻), which is known to form a strong symmetric stretch ν_1 mode in this region for Raman spectroscopy.⁴⁹ The remaining modes for carbonate, which would be located around 880, 1400, and 680 cm⁻¹, are weaker⁴⁹ and, in this case, located in regions where other modes due to the clay and CO₂ gas phase are dominating.

Inelastic Neutron Spectroscopy. INS spectra of pristine Ni-Hec, both in dried and equilibrated at 43% r.h. states, are presented in Figure 5.

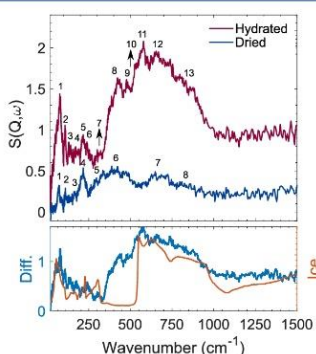


Figure 5. INS experimental spectra of Ni-Hec in dried (145 °C under vacuum) and hydrated states (equilibrated at 43% r.h.). The difference spectrum below is compared with the INS spectrum of ice Ih as a standard reference (in orange and scaled by the right axis). As a result of an ordered H-bond network, amorphous Ih is characterized by a pronounced librational edge. Numbers and arrows highlight important modes summarized in Tables S1 and S2. The spectra were recorded at $T < 20$ K.

Dried Ni-Hec before CO₂ Exposure. In the spectrum for the dried Ni-Hec sample (Figure 5), we observe peaks at 70, 109, 165, 215, and 300 cm⁻¹ (#1, #2, #3, #4, and #5), a broad distribution centered around 400 cm⁻¹ (#6), a broad distribution centered around 670 cm⁻¹ (#7), and a broad shoulder centered at 810 cm⁻¹ (#8). Previous INS measurements on β -Ni(OH)₂ have shown peaks at 90, 115, 294/313, 358, 394, 421/452, 680, and 880 cm⁻¹.^{45,52} In agreement with the findings by Loch et al.,²⁴ where the structure was identified as [Ni(OH)_{0.83}(H₂O)_{1.17}]_{0.37}^{1.17+}, the sharp peaks at 70 and 215 cm⁻¹ (#1, #4) are correlated with the confined water coordinated to the nickel hydroxide species.⁵³ One could question whether the peaks might be related to partial hydrolysis of Mg₃F-moieties giving rise to a structure Mg₃OH. This is, however, unlikely as the Ni-Hec was obtained by ion exchange of melt-synthesized Na-Hec (Figure S3), which lacks bands in this region. Modes and tentative assignment are summarized in Table S1.

Hydrated Ni-Hec before CO₂ Exposure. For hydrated Ni-Hec equilibrated at 43% r.h., corresponding to a 2 WL hydration as in the PXRD/Raman spectroscopy measurements (Figure 5), which contains both [Ni(H₂O₆)]²⁺ and [Ni(OH)_{0.83}(H₂O)_{1.17}]_{0.37}^{1.17+}, we observe a sharp peak on a broad distribution at 76 cm⁻¹ (#1), in addition to sharp peaks at 109, 215, and 237 cm⁻¹ (#2, #5, and #6), and minor vibrations centered around 130 and 165 cm⁻¹ (#3 and #4). From 335 to 1000 cm⁻¹, a broad distribution is found, with sharper features at 430, 480, 575, 650, and 800 cm⁻¹ (#8, #9, #11, #12, and #13). The hydrated Ni-Hec shows the same modes as the dried sample associated to the Ni-OH moieties as well as new modes associated to water (see further discussion below). Modes and the assignment are summarized in Table S2.

In the difference spectrum in Figure 5, since we have removed the contribution from the clay and the condensed [Ni(OH)_{0.83}(H₂O)_{1.17}]_{0.37}^{1.17+}, we are left only with the contribution from different types of water present in this sample. Considering that INS is in particular sensitive to intramolecular water librational modes located between 300 and 1100 cm⁻¹, we can argue that the sharp librational edge at 336 cm⁻¹, previously observed in beidellite and montmorillonite²⁶ and shown to have a clear dependence on the interlayer cation, here originates from water coordinated to Ni²⁺. The second onset around 510 cm⁻¹ with a significant peak at 580 cm⁻¹ suggests the presence of less confined interlayer water, which is the noncoordinated interlayer water and responsible for the water loss below 100 °C observed in the TGA data (Figure S6). The absence of a clear librational edge similar to ice confirms the absence of a significant amount of noninterlayer water. The presence of these assigned water populations is further confirmed by analyzing the low energy region of the spectra. Free bulk water⁵⁴ is characterized with an excitation around 50 cm⁻¹, while confined water molecules are characterized by a vibrational mode centered at about 80 cm⁻¹.^{54,55} Thus, the observation of the sharp peak at 76 cm⁻¹ is indicative of interlayer water coordinated to the Ni²⁺ cation, while the observation of a broad shoulder toward 50 cm⁻¹, also observed recently by Larsen et al.,⁵⁵ is consistent with the presence of water that is not coordinated with cations.

Dried Ni-Hec after CO₂ Exposure. Pronounced changes in the INS spectra are observed for the dried Ni-Hec (Figure 6a,b) upon CO₂ exposure. For the dried sample exposed to 5 bars of CO₂ at low energy transfer, a gain of intensity at 50 cm⁻¹, followed by an intensity loss at 72 cm⁻¹, and broad intensity gain between 80 and 160 cm⁻¹ and at 176 cm⁻¹ are observed. At 44 bar of CO₂, the signal in this region is more pronounced. Both at 5 and 44 bar, with the broad peaks centered around 215 and 400 cm⁻¹, a significant intensity loss was recorded. At 5 bar, there are still visible peaks left associated to the Ni-OH moieties at 336, 420, and 470 cm⁻¹, which are quite suppressed at 44 bar. Furthermore, at 5 bar, we observe an excess in energy at 675 cm⁻¹ that transforms into a sharp peak at 655 cm⁻¹ when increasing the CO₂ pressure to 44 bar.

For dried Ni-Hec after removing CO₂ by applying vacuum (Figure 6c), we observe at low wavenumbers a small increase of intensity at 50, 70, and 101 cm⁻¹, whereas at higher energy transfers, the broad peaks centered at 215 and 400 cm⁻¹ have not reached their full initial prominence. The onset of the peak centered at 680 cm⁻¹ has a shift to 530 cm⁻¹ from 610 cm⁻¹. The signal seems to a large degree to return the initial signal, however, not to full prominence.

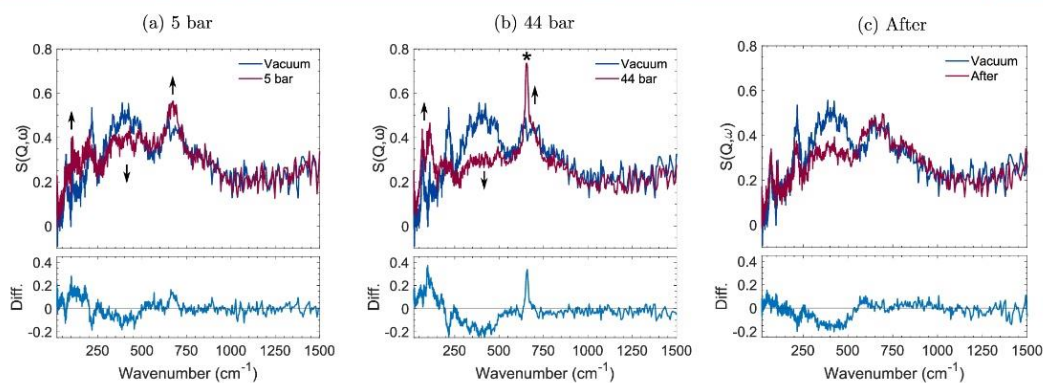


Figure 6. INS experimental spectra of the dried Ni-Hec initial state and that exposed to (a) 5 bar of CO₂, (b) 44 bar of CO₂ and (c) after cycling (loading and pumping) with the corresponding difference spectra given below. Loading of CO₂ was performed at room temperature, and the spectra were recorded at $T < 20$ K. Arrows and asterisk (*) highlight important changes in the spectra.

For dried Ni-Hec, the modes associated to the [Ni(OH)_{0.83}(H₂O)_{1.17}]_{0.37}^{1.17+} interlayer species are severely attenuated (Figure 6b) and considerable crystalline swelling due to CO₂ exposure is observed (Figure 1). INS, gravimetric adsorption, and PXRD data on dried Na-Hec are presented in the Supporting Information, where neither uptake, swelling, nor spectroscopic changes are observed. As no changes are found when dried Na-Hec is exposed to CO₂ and, in addition, previous observations on cations with high hydration enthalpy^{8,10,22} show no swelling, this suggests that the smectite-like interlayer does not play a role for the CO₂ capture in the dried case. Thus, the [Ni(OH)_{0.83}(H₂O)_{1.17}]_{0.37}^{1.17+} species plays the important role in the adsorption of CO₂ by dried Ni-Hec. This then means that the smectite layers remain unchanged with a d-spacing of about 10 Å and that the chlorite-like layers swell from about 13–14 to 15–16 Å. This reaction must be reversible since our PXRD experiments with repeated exposure to CO₂, a long (>24 h) evacuation of the sample or moderate heating (>50 °C) is sufficient to return the Bragg reflection to the same initial position. This suggests that the observed state by INS after releasing the CO₂ (Figure 6c) is a transient step during the return to the initial structure and that there is still some CO₂ adsorbed to the structure. However, based on the present data, we cannot completely rule out the possibility that the reaction between CO₂ and nickel hydroxide contained within the clay produces permanent structural changes to nickel hydroxide islands.

Hydrated Ni-Hec after CO₂ Exposure. After being exposed to CO₂ at room temperature and cooled down to $T < 20$ K, for the hydrated Ni-Hec (Figure 7), the changes are evident in the difference spectrum, and new modes are observed at 64, 95, and 117 cm⁻¹. There is also a slight increase of intensity around 315 cm⁻¹ and a small general loss of intensity between 400 and 900 cm⁻¹. In addition, a new vibration is observed at 655 cm⁻¹.

As various different hydrogenated species (coordinated and non-coordinated interlayer water, and [Ni(OH)_{0.83}(H₂O)_{1.17}]_{0.37}^{1.17+}) coexist for hydrated Ni-Hec, it is less obvious whether the changes observed by INS upon CO₂ exposure are a consequence of changes in the librational modes associated to one or more of the water species or by direct

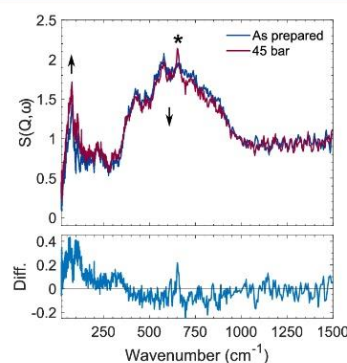


Figure 7. INS experimental spectra of hydrated Ni-Hec (equilibrated 43% r.h.) in the initial state and exposed to 44 bar of CO₂ at room temperature. Arrows and asterisk (*) highlight important changes in the spectra. The spectra were recorded at $T < 20$ K.

association to the [Ni(OH)_{0.83}(H₂O)_{1.17}]_{0.37}^{1.17+}. The negligible changes along the librational edge agree with a strong coordination of water with Ni²⁺, which is not disrupted by CO₂ exposure. However, we observe changes in the modes of the interlayer water by Raman spectroscopy (Figure 4), which together with the INS observations may be indicative of influence on the non-coordinated interlayer water by CO₂. The general loss of INS intensity, similar to the dried case, suggests a similar interaction between CO₂ and interlayer [Ni(OH)_{0.83}(H₂O)_{1.17}]_{0.37}^{1.17+} both for dried and hydrated Ni-Hec. In addition, by Raman spectroscopy, we observe clear changes in what we identify as the OH-stretching modes of the intercalated nickel hydroxide, indicating an interaction with CO₂. The smaller crystalline swelling of hydrated Ni-Hec compared to the dried case (Figure 2) is due to the layers being more similar to one another for hydrated Ni-Hec. We can assume that the smectite-like interlayer remains unchanged at about 15 Å, which is evidenced by the observed stability of the H-bonding by INS. Then, the chlorite-like layer swells from about 14–15 Å, and the chlorite-like layer could adopt a similar structure to what is observed for the dried state. The observed improved ordering is similar to what has previously

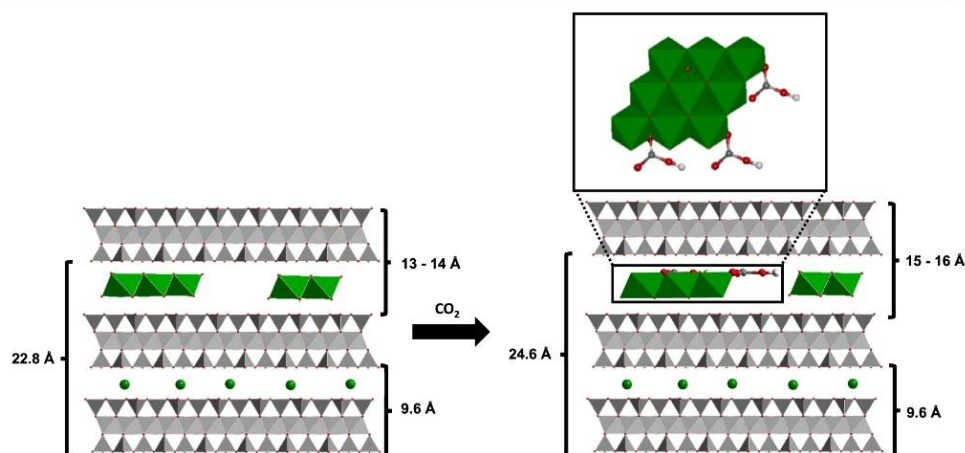


Figure 8. Hypothesized model for crystalline swelling in Ni-Hec clay in response to CO_2 exposure. The CO_2 interacts only with and causes swelling only of chlorite-like layers.

been observed upon hydration of Na-Hec and¹ suggests that the incorporation of CO_2 in the interlayer strengthens the interaction between the interlayer species and 2:1 clay layers.

Further Discussion. For both the dried and the hydrated sample, a peak is forming at 655 cm^{-1} , (marked by an asterisk in Figure 6b), accompanied with vibrations at 64, 95, and 117 cm^{-1} . For the vibration at 655 cm^{-1} , we may suggest three possibilities based on the literature: Librational modes for water are observed in this region, bending modes for CO_2 are also observed at 640 cm^{-1} ⁵⁶ as well as modes associated to bicarbonates.⁵⁷ As this peak is not observed in the spectra of the dried Na-Hec (see Supporting Information), formation of solid CO_2 on the external surfaces of the Hec samples or in the remaining probing volume of the neutrons in the sample cell is unlikely. Notably the cross section of CO_2 is 20 times lower than that of hydrogen; thus, the observation of this peak is unlikely to be due to the bending mode of CO_2 . It is possible that these changes also are associated with local changes of the water population. Following this reasoning, the peak that gains intensity at 64 cm^{-1} could suggest a more ordered water population.⁵⁴ The sharp vibration at 655 cm^{-1} could also originate from a specific librational mode associated to this ordered water state, possibly through segregation of some water molecules to monomers and dimers.⁵⁸ Water confinement in UO_2F_2 displays a peak at 778 cm^{-1} , that simulations attribute to a librational phonon mode along the a/b-axis at 712 cm^{-1} , due to confined water within the van der Waals gap of that material.⁵⁹ The incorporation of CO_2 in the interlayer may then force some of the H_2O associated with the hydroxide species into a more confined situation. If we consider that the hydrogen bonds in HCO_3^- are weak, we may assign the present INS modes to HCO_3^- based on the study of Fillaux et al. on potassium bicarbonate.⁵⁷ However, there are no observed bicarbonate modes by Raman spectroscopy (Figure 4).

From the current experiments, it still is unclear what is the reaction between CO_2 and the $[\text{Ni}(\text{OH})_{0.83}(\text{H}_2\text{O})_{1.17}]_{0.37}^{1.17+}$ species. A possible mechanism that can be suggested has been observed on goethite under anhydrous conditions,⁶⁰ where CO_2 is chemisorbed according to $\text{Ni}-\text{OH} + \text{CO}_2 \rightarrow \text{Ni}-\text{O}(\text{HCO}_2)$. By this reaction, hydroxide groups are converted into

bicarbonate and this would significantly reduce the intensity associated to the corresponding modes. The chemisorbed CO_2 may then be grafted as a bicarbonate to the condensed nickel hydroxide species, causing the swelling by adopting a structure as illustrated in Figure 8. However, as no bicarbonate modes are unambiguously observed by Raman spectroscopy, this is not evident from the present data.

Nevertheless, our experimental data show clear evidence that the intercalated $[\text{Ni}(\text{OH})_{0.83}(\text{H}_2\text{O})_{1.17}]_{0.37}^{1.17+}$ species play a crucial role in the incorporation of CO_2 in the interlayers, both for the dried and hydrated cases. This is corroborated by DFT simulations (Figure 9), which are consistent with the

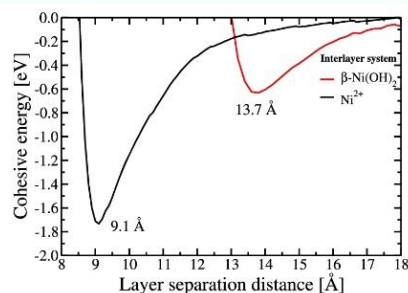


Figure 9. Basal spacing and energy per unit cell cohesive energy obtained by computational studies based on DFT calculations for the dehydrated smectite layers with Ni^{2+} and chlorite-like layers with a confined $\beta\text{-Ni}(\text{OH})_2$.

experimentally observed d -spacing of the dehydrated system here and in the study by Loch et al.²⁴ In addition, the simulations (Figure 9) show that the cohesion energy of the chlorite-like layers (-0.63 eV) is significantly lower than that for the smectite-like layers (-1.73 eV). This strengthens our arguments that the chlorite-like layers are responsible for the CO_2 uptake and swelling in this system. Based on these calculations, we can argue that CO_2 in the chlorite-like layers may attach to the edge of the nickel hydroxide islands and bind

to not fully coordinated nickel atoms forming a strong bond (E_{Ads}), see Supporting Information.

CONCLUSIONS

Developing new sorbent materials for CO_2 is of key importance to solve issues related to greenhouse gas emissions. By PXRD, Raman spectroscopy, and INS, we identified a hitherto overlooked mechanism for CO_2 adsorption in hectorite clay. With these techniques, we took a new approach, where we study the mechanism for CO_2 adsorption from the perspective of interlayer hydrogeneous species, that is hydroxides and water. Phase pure and charge homogeneous synthetic fluorohectorite provides a unique template for studying such interactions as it has no structural hydrogen incorporated in the 2:1 clay layer structure. For Ni-exchanged hectorite, an ordered interstratification of chlorite-like layers and smectite-like layers, we found that the intercalated nickel hydroxide promotes incorporation of CO_2 in the clay interlayers. Our results suggest that the CO_2 binds to the $[\text{Ni}(\text{OH})_{0.83}(\text{H}_2\text{O})_{1.17}]_{0.37}^{1.17+}$ species, both in the dried and the hydrated case, and is responsible for swelling in response to CO_2 . No incorporation of CO_2 was found in the smectite-like layers for the dried case. Furthermore, CO_2 has limited impact on the water coordinated to the interlayer cations for the hydrated case.

In future work, we will perform ion exchange with a variety of transition metal elements known for their condensation tendency at slightly elevated pH (>8). As shown in the literature,^{61–63} this will produce condensed chlorite-type interlayers only and therefore should increase the adsorption capacity for CO_2 , rendering Ni-exchanged hectorite technologically competitive to other adsorption materials.

ASSOCIATED CONTENT

Supporting Information

The Supporting Information is available free of charge at <https://pubs.acs.org/doi/10.1021/acs.jpcc.0c07206>.

Supporting INS and PXRD measurements of dried Na-Hec; diffractograms of hydrated Ni-Hec; gravimetric adsorption measurements on Ni-Hec and Na-Hec; thermogravimetric analysis of Ni-Hec and Na-Hec; and tables of assigned modes for INS (PDF)

AUTHOR INFORMATION

Corresponding Authors

Josef Breu – Bavarian Polymer Institute and Department of Chemistry, University of Bayreuth, D-95440 Bayreuth, Germany; orcid.org/0000-0002-2547-3950; Phone: +49 (0)921 / 55-2530; Email: josef.breu@uni-bayreuth.de

Heloisa N. Bordallo – Niels Bohr Institute-University of Copenhagen, 2100 Copenhagen, Denmark; European Spallation Source ESS ERIC, SE-221 00 Lund, Sweden; orcid.org/0000-0003-0750-0553; Phone: +45 21 30 88 29; Email: bordallo@nbi.ku.dk

Jon Otto Fossum – Department of Physics, Norwegian University of Science and Technology, 7491 Trondheim, Norway; orcid.org/0000-0002-8952-303X; Phone: +47 911 39 194; Email: jon.fossum@ntnu.no

Authors

Kristoffer W. Bo Hunvik – Department of Physics, Norwegian University of Science and Technology, 7491 Trondheim, Norway

Patrick Loch – Bavarian Polymer Institute and Department of Chemistry, University of Bayreuth, D-95440 Bayreuth, Germany

Leide P. Cavalcanti – Institute for Energy Technology (IFE), N-2027 Kjeller, Norway; ISIS Neutron and Muon Source, STFC Rutherford Appleton Laboratory, OX11 0QX Didcot, U.K.; orcid.org/0000-0002-0408-0058

Konstane Kvaalem Seljelid – Department of Physics, Norwegian University of Science and Technology, 7491 Trondheim, Norway

Paul Monceyron Røren – Department of Physics, Norwegian University of Science and Technology, 7491 Trondheim, Norway

Svemir Rudić – ISIS Neutron and Muon Source, STFC Rutherford Appleton Laboratory, OX11 0QX Didcot, U.K.

Dirk Wallacher – Department Sample Environments, Helmholtz-Zentrum Berlin für Materialien und Energie, 14109 Berlin, Germany

Alexandro Kirch – Departamento de Física dos Materiais e Mecânica, Instituto de Física, Universidade de São Paulo, 05508-090 São Paulo, São Paulo, Brazil

Kenneth Dahl Knudsen – Institute for Energy Technology (IFE), N-2027 Kjeller, Norway; Department of Physics, Norwegian University of Science and Technology, 7491 Trondheim, Norway

Caetano Rodrigues Miranda – Departamento de Física dos Materiais e Mecânica, Instituto de Física, Universidade de São Paulo, 05508-090 São Paulo, São Paulo, Brazil

Complete contact information is available at: <https://pubs.acs.org/10.1021/acs.jpcc.0c07206>

Notes

The authors declare no competing financial interest.

ACKNOWLEDGMENTS

This work was supported by the Research Council of Norway under the Frinatek Program, project number 250728. This work was supported by the Deutsche Forschungsgemeinschaft (SFB 840). P.L. thanks Elite Network Bavaria in the framework of the Elite Study Program “Macromolecular Science” for support. A.K. and C.R.M. gratefully acknowledge the Research Centre for Gas Innovation (RCGI) and support from the Brazilian agencies FAPESP (2017/02317–2) and CNPq. We acknowledge the European Synchrotron Radiation Facility for provision of synchrotron radiation facilities and we would like to thank Wouter van Beek, Vadim Diadkin, and Dmitry Chernyshov for excellent assistance in using beamline SNBL BM01. Experiments at the ISIS Pulsed Neutron and Muon Source were supported by a beamtime allocation from the Science and Technology Facilities Council.⁶⁴ Paulo Henrique Michels-Brito, Koiti Araki, and Leander Michels are acknowledged for helpful discussions.

REFERENCES

- Bergaya, F.; Lalagay, G. *Handbook of clay science*; Newnes, 2013.
- Daab, M.; Eichstaedt, N. J.; Habel, C.; Rosenfeldt, S.; Kalo, H.; Schießling, H.; Förster, S.; Breu, J. Onset of Osmotic Swelling in Highly Charged Clay Minerals. *Langmuir* **2018**, *34*, 8215–8222.

- (3) Dazas, B.; Lanson, B.; Breu, J.; Robert, J.-L.; Pelletier, M.; Ferrage, E. Smectite fluorination and its impact on interlayer water content and structure: A way to fine tune the hydrophilicity of clay surfaces? *Microporous Mesoporous Mater.* **2013**, *181*, 233–247.
- (4) Kalo, H.; Milius, W.; Breu, J. Single crystal structure refinement of one- and two-layer hydrates of sodium fluorohectorite. *RSC Adv.* **2012**, *2*, 8452–8459.
- (5) Hemmen, H.; Rolseth, E. G.; Fonseca, D. M.; Hansen, E. L.; Fossum, J. O.; Plivelic, T. S. X-ray studies of carbon dioxide intercalation in Na-fluorohectorite clay at near-ambient conditions. *Langmuir* **2012**, *28*, 1678–1682.
- (6) Michels, L.; Fossum, J. O.; Rozynek, Z.; Hemmen, H.; Rustenberg, K.; Sobas, P. A.; Kalantzopoulos, G. N.; Knudsen, K. D.; Janek, M.; Plivelic, T. S.; et al. Intercalation and retention of carbon dioxide in a smectite clay promoted by interlayer cations. *Sci. Rep.* **2015**, *5*, 8775.
- (7) Cavalcanti, L. P.; Kalantzopoulos, G. N.; Eckert, J.; Knudsen, K. D.; Fossum, J. O. A nano-silicate material with exceptional capacity for CO₂ capture and storage at room temperature. *Sci. Rep.* **2018**, *8*, 11827.
- (8) Schaeff, H. T.; Loganathan, N.; Bowers, G. M.; Kirkpatrick, R. J.; Yazaydin, A. O.; Burton, S. D.; Hoyt, D. W.; Thanthirawatte, K. S.; Dixon, D. A.; McGrail, B. P.; et al. Tipping point for expansion of layered aluminosilicates in weakly polar solvents: supercritical CO₂. *ACS Appl. Mater. Interfaces* **2017**, *9*, 36783–36791.
- (9) Loganathan, N.; Bowers, G. M.; Yazaydin, A. O.; Schaeff, H. T.; Loring, J. S.; Kalinichev, A. G.; Kirkpatrick, R. J. Clay swelling in dry supercritical carbon dioxide: effects of interlayer cations on the structure, dynamics, and energetics of CO₂ intercalation probed by XRD, NMR, and GCMC simulations. *J. Phys. Chem. C* **2018**, *122*, 4391–4402.
- (10) Loganathan, N.; Bowers, G. M.; Yazaydin, A. O.; Kalinichev, A. G.; Kirkpatrick, R. J. Competitive Adsorption of H₂O and CO₂ in 2-Dimensional Nanoconfinement: GCMC Simulations of Cs-and Ca-Hectorites. *J. Phys. Chem. C* **2018**, *122*, 23460–23469.
- (11) dos Santos, E. C.; Gates, W. P.; Michels, L.; Juranyi, F.; Mikkelsen, A.; da Silva, G. J.; Fossum, J. O.; Bordallo, H. N. The pH influence on the intercalation of the bioactive agent ciprofloxacin in fluorohectorite. *Appl. Clay Sci.* **2018**, *166*, 288–298.
- (12) Herling, M. M.; Rieß, M.; Sato, H.; Li, L.; Martin, T.; Kalo, H.; Matsuda, R.; Kitagawa, S.; Breu, J. Purely Physisorption-Based CO₂-Selective Gate-Opening in Microporous Organically Pillared Layered Silicates. *Angew. Chem.* **2018**, *130*, 573–577.
- (13) Schaeff, H. T.; Ilton, E. S.; Qafoku, O.; Martin, P. F.; Felmy, A. R.; Rosso, K. M. In situ XRD study of Ca²⁺ saturated montmorillonite (STX-1) exposed to anhydrous and wet supercritical carbon dioxide. *Int. J. Greenhouse Gas Control* **2012**, *6*, 220–229.
- (14) Schaeff, H. T.; Loring, J. S.; Glezakou, V.-A.; Miller, Q. R. S.; Chen, J.; Owen, A. T.; Lee, M.-S.; Ilton, E. S.; Felmy, A. R.; McGrail, B. P.; et al. Competitive sorption of CO₂ and H₂O in 2: 1 layer phyllosilicates. *Geochim. Cosmochim. Acta* **2015**, *161*, 248–257.
- (15) Loring, J. S.; Schaeff, H. T.; Turcu, R. V. F.; Thompson, C. J.; Miller, Q. R. S.; Martin, P. F.; Hu, J.; Hoyt, D. W.; Qafoku, O.; Ilton, E. S.; et al. In situ molecular spectroscopic evidence for CO₂ intercalation into montmorillonite in supercritical carbon dioxide. *Langmuir* **2012**, *28*, 7125–7128.
- (16) Loring, J. S.; Ilton, E. S.; Chen, J.; Thompson, C. J.; Martin, P. F.; Bénézech, P.; Rosso, K. M.; Felmy, A. R.; Schaeff, H. T. In situ study of CO₂ and H₂O partitioning between Na–montmorillonite and variably wet supercritical carbon dioxide. *Langmuir* **2014**, *30*, 6120–6128.
- (17) Loring, J. S.; Schaeff, H. T.; Thompson, C. J.; Turcu, R. V.; Miller, Q. R.; Chen, J.; Hu, J.; Hoyt, D. W.; Martin, P. F.; Ilton, E. S.; et al. Clay hydration/dehydration in dry to water-saturated supercritical CO₂: implications for caprock integrity. *Energy Procedia* **2013**, *37*, 5443–5448.
- (18) Giesting, P.; Guggenheim, S.; Koster van Groos, A. F.; Busch, A. Interaction of carbon dioxide with Na-exchanged montmorillonite at pressures to 640 bars: Implications for CO₂ sequestration. *Int. J. Greenhouse Gas Control* **2012**, *8*, 73–81.
- (19) Hwang, J.; Joss, L.; Pini, R. Measuring and modelling supercritical adsorption of CO₂ and CH₄ on montmorillonite source clay. *Microporous Mesoporous Mater.* **2019**, *273*, 107–121.
- (20) Rother, G.; Ilton, E. S.; Wallacher, D.; Hauß, T.; Schaeff, H. T.; Qafoku, O.; Rosso, K. M.; Felmy, A. R.; Krukowski, E. G.; Stack, A. G.; et al. CO₂ sorption to subsingle hydration layer montmorillonite clay studied by excess sorption and neutron diffraction measurements. *Environ. Sci. Technol.* **2013**, *47*, 205–211.
- (21) Botan, A.; Rotenberg, B.; Marry, V.; Turq, P.; Noetinger, B. Carbon dioxide in montmorillonite clay hydrates: thermodynamics, structure, and transport from molecular simulation. *J. Phys. Chem. C* **2010**, *114*, 14962–14969.
- (22) Loganathan, N.; Yazaydin, A. O.; Kirkpatrick, R. J.; Bowers, G. M. Tuning the Hydrophobicity of Layer-Structure Silicates To Promote Adsorption of Nonaqueous Fluids: Effects of F–for OH–Substitution on CO₂ Partitioning into Smectite Interlayers. *J. Phys. Chem. C* **2019**, *123*, 4848–4855.
- (23) Altoé, M. A. S.; Michels, L.; Santos, E. C. d.; Droppa, R. Jr; Grassi, G.; Ribeiro, L.; Knudsen, K. D.; Bordallo, H. N.; Fossum, J. O.; da Silva, G. J. Continuous water adsorption states promoted by Ni²⁺ confined in a synthetic smectite. *Appl. Clay Sci.* **2016**, *123*, 83–91.
- (24) Loch, P.; Hunvik, K. W. B.; Puchtl, F.; Weiß, S.; Seljelid, K. K.; Røren, P. M.; Rudic, S.; Raen, S.; Knudsen, K. D.; Bordallo, H. N.; et al. Spontaneous formation of an ordered interstratification upon Ni-exchange of Na-fluorohectorite. *Appl. Clay Sci.* **2020**, *198*, 105831.
- (25) Martins, M. L.; Gates, W. P.; Michot, L.; Ferrage, E.; Marry, V.; Bordallo, H. N. Neutron scattering, a powerful tool to study clay minerals. *Appl. Clay Sci.* **2014**, *96*, 22–35.
- (26) Cygan, R. T.; Daemen, L. L.; Ilgen, A. G.; Krumhansl, J. L.; Nenoff, T. M. Inelastic neutron scattering and molecular simulation of the dynamics of interlayer water in smectite clay minerals. *J. Phys. Chem. C* **2015**, *119*, 28005–28019.
- (27) Jiménez-Ruiz, M.; Ferrage, E.; Blanchard, M.; Fernandez-Castanon, J.; Delville, A.; Johnson, M. R.; Michot, L. J. Combination of inelastic neutron scattering experiments and ab Initio quantum calculations for the study of the hydration properties of oriented Saponites. *J. Phys. Chem. C* **2017**, *121*, 5029–5040.
- (28) Stöter, M.; Kunz, D. A.; Schmidt, M.; Hirsemann, D.; Kalo, H.; Putz, B.; Senker, J.; Breu, J. Nanoplatelets of sodium hectorite showing aspect ratios of 20 000 and superior purity. *Langmuir* **2013**, *29*, 1280–1285.
- (29) Dyadkin, V.; Pattison, P.; Dmitriev, V.; Chernyshov, D. A new multipurpose diffractometer PILATUS@ SNBL. *J. Synchrotron Radiat.* **2016**, *23*, 825–829.
- (30) Jensen, T. R.; Nielsen, T. K.; Filinchuk, Y.; Jørgensen, J.-E.; Cerenius, Y.; Gray, E. M.; Webb, C. J. Versatile in situ powder X-ray diffraction cells for solid–gas investigations. *J. Appl. Crystallogr.* **2010**, *43*, 1456–1463.
- (31) Pinna, R. S.; Rudić, S.; Parker, S. F.; Armstrong, J.; Zanetti, M.; Škor, G.; Waller, S. P.; Zacek, D.; Smith, C. A.; Capstick, M. J.; et al. The neutron guide upgrade of the TOSCA spectrometer. *Nucl. Instrum. Methods Phys. Res. Sect. A Accel. Spectrom. Detect. Assoc. Equip.* **2018**, *896*, 68–74.
- (32) Parker, S. F.; Fernandez-Alonso, F.; Ramirez-Cuesta, A. J.; Tomkinson, J.; Rudić, S.; Pinna, R. S.; Gorini, G.; Fernández Castañón, J. Recent and future developments on TOSCA at ISIS. *J. Phys.: Conf. Ser.* **2014**, *554*, 012003.
- (33) Mitchell, P. C. H. *Vibrational Spectroscopy with Neutrons: with Applications in Chemistry, Biology, Materials Science and Catalysis*; World Scientific, 2005; Vol. 3.
- (34) Arnold, O.; Bilheux, J. C.; Borreguero, J. M.; Buts, A.; Campbell, S. I.; Chapon, L.; Doucet, M.; Draper, N.; Ferraz Leal, R.; Gigg, M. A.; et al. Mantid—Data analysis and visualization package for neutron scattering and μ SR experiments. *Nucl. Instrum. Methods Phys. Res. Sect. A Accel. Spectrom. Detect. Assoc. Equip.* **2014**, *764*, 156–166.

- (35) Hohenberg, P.; Kohn, W. Inhomogeneous electron gas. *Phys. Rev.* **1964**, *136*, B864.
- (36) Kohn, W.; Sham, L. J. Self-consistent equations including exchange and correlation effects. *Phys. Rev.* **1965**, *140*, A1133.
- (37) Berland, K.; Hyldgaard, P. Exchange functional that tests the robustness of the plasmon description of the van der Waals density functional. *Phys. Rev. B: Condens. Matter Mater. Phys.* **2014**, *89*, 035412.
- (38) Soler, J. M.; Artacho, E.; Gale, J. D.; García, A.; Junquera, J.; Ordejón, P.; Sánchez-Portal, D. The SIESTA method for ab initio order-N materials simulation. *J. Phys.: Condens. Matter* **2002**, *14*, 2745.
- (39) Breu, J.; Seidl, W.; Stoll, A. Fehlordnung bei smectiten in abhängigkeit vom zwischenschichtkation. *Z. Anorg. Allg. Chem.* **2003**, *629*, 503–515.
- (40) Curtarolo, S.; Setyawan, W.; Wang, S.; Xue, J.; Yang, K.; Taylor, R. H.; Nelson, L. J.; Hart, G. L. W.; Sanvito, S.; Buongiorno-Nardelli, M.; et al. AFLOWLIB.ORG: A distributed materials properties repository from high-throughput ab initio calculations. *Comput. Mater. Sci.* **2012**, *58*, 227–235.
- (41) Busch, A.; Bertier, P.; Gensterblum, Y.; Rother, G.; Spiers, C. J.; Zhang, M.; Wentinck, H. M. On sorption and swelling of CO₂ in clays. *Geomech. Geophys. Geo-Energy Geo-Resour.* **2016**, *2*, 111–130.
- (42) Klopogge, J. *Developments in Clay Science*; Elsevier, 2017; Vol. 8; pp 150–199.
- (43) Hall, D. S.; Lockwood, D. J.; Poirier, S.; Bock, C.; MacDougall, B. R. Raman and infrared spectroscopy of α and β phases of thin nickel hydroxide films electrochemically formed on nickel. *J. Phys. Chem. A* **2012**, *116*, 6771–6784.
- (44) Rinaudo, C.; Roz, M.; Boero, V.; Franchini-Angela, M. FT-Raman spectroscopy on several di- and trioctahedral T–O–T phyllosilicates. *Neues Jahrbuch Mineral. Monatsh.* **2004**, *2004*, 537–554.
- (45) Bantignies, J. L.; Deabate, S.; Righi, A.; Rols, S.; Hermet, P.; Sauvajol, J. L.; Henn, F. New insight into the vibrational behavior of nickel hydroxide and oxyhydroxide using inelastic neutron scattering, far/mid-infrared and Raman spectroscopies. *J. Phys. Chem. C* **2008**, *112*, 2193–2201.
- (46) Gates, W. P.; Bordallo, H. N.; Aldridge, L. P.; Seydel, T.; Jacobsen, H.; Marry, V.; Churchman, G. J. Neutron time-of-flight quantification of water desorption isotherms of montmorillonite. *J. Phys. Chem. C* **2012**, *116*, 5558–5570.
- (47) Frost, R. L.; Rintoul, L. Lattice vibrations of montmorillonite: an FT Raman and X-ray diffraction study. *Appl. Clay Sci.* **1996**, *11*, 171–183.
- (48) Hall, D. S.; Lockwood, D. J.; Poirier, S.; Bock, C.; MacDougall, B. R. Applications of in situ Raman spectroscopy for identifying nickel hydroxide materials and surface layers during chemical aging. *ACS Appl. Mater. Interfaces* **2014**, *6*, 3141–3149.
- (49) Frost, R. L.; Dickfos, M. J.; Jagannadha Reddy, B. Raman spectroscopy of hydroxy nickel carbonate minerals nullaginite and zaraitite. *J. Raman Spectrosc.* **2008**, *39*, 1250–1256.
- (50) Arab, M.; Bougeard, D.; Smirnov, K. S. Experimental and computer simulation study of the vibrational spectra of vermiculite. *Phys. Chem. Chem. Phys.* **2002**, *4*, 1957–1963.
- (51) Anderson, G. R. The Raman spectra of carbon dioxide in liquid water and water-d₂. *J. Phys. Chem.* **1977**, *81*, 273–276.
- (52) Baddour-Hadjean, R.; Fillaux, F.; Tomkinson, J. Proton dynamics in β Ni(OH)₂ and β NiOOH. *Phys. B* **1995**, *213*–214, 637–639.
- (53) Persson, R. A. X.; Pattni, V.; Singh, A.; Kast, S. M.; Heyden, M. Signatures of solvation thermodynamics in spectra of intermolecular vibrations. *J. Chem. Theory Comput.* **2017**, *13*, 4467–4481.
- (54) Berg, M. C.; Dalby, K. N.; Tsapatsaris, N.; Okhrimenko, D. V.; Sørensen, H. O.; Jha, D.; Embs, J. P.; Stipp, S. L. S.; Bordallo, H. N. Water Mobility in Chalk: A Quasielastic Neutron Scattering Study. *J. Phys. Chem. C* **2017**, *121*, 14088–14095.
- (55) Larsen, S. R.; Michels, L.; dos Santos, E. C.; Berg, M. C.; Gates, W. P.; Aldridge, L. P.; Seydel, T.; Ollivier, J.; Telling, M. T. F.; Fossum, J. O.; et al. Physicochemical characterisation of fluorohectorite: Water dynamics and nanocarrier properties. *Microporous Mesoporous Mater.* **2020**, *306*, 110512.
- (56) Bandosz, T. J.; Seredych, M.; Rodríguez-Castellón, E.; Cheng, Y.; Daemen, L. L.; Ramírez-Cuesta, A. J. Evidence for CO₂ reactive adsorption on nanoporous S- and N-doped carbon at ambient conditions. *Carbon* **2016**, *96*, 856–863.
- (57) Fillaux, F.; Tomkinson, J.; Penfold, J. Proton dynamics in the hydrogen bond. The inelastic neutron scattering spectrum of potassium hydrogen carbonate at 5 K. *Chem. Phys.* **1988**, *124*, 425–437.
- (58) Öberg, K. I.; Fraser, H. J.; Boogert, A. C. A.; Bisschop, S. E.; Fuchs, G. W.; van Dishoeck, E. F.; Linnartz, H. Effects of CO₂ on H₂O band profiles and band strengths in mixed H₂O: CO₂ ices. *Astron. Astrophys.* **2007**, *462*, 1187–1198.
- (59) Miskowicz, A.; Niedziela, J. L.; Kirkegaard, M. C.; Shields, A. E. Analysis of Water Coupling in Inelastic Neutron Spectra of Uranyl Fluoride. *Sci. Rep.* **2019**, *9*, 10476.
- (60) Yeşilbaş, M.; Song, X.; Boily, J.-F. Carbon Dioxide Binding in Supercooled Water Nanofilms on Nanominerals. *Environ. Sci.: Nano* **2020**, *7*, 437.
- (61) Ohtsuka, K.; Suda, M.; Tsunoda, M.; Ono, M. Synthesis of metal hydroxide-layer silicate intercalation compounds (metal= Mg (II), Ca (II), Mn (II), Fe (II), Co (II), Ni (II), Zn (II), and Cd (II)). *Chem. Mater.* **1990**, *2*, 511–517.
- (62) Uehara, M.; Yamzaki, A.; Umezawa, T.; Takahashi, K.; Tsutsumi, S. A nickel hydroxide-vermiculite complex: Preparation and characterization. *Clays Clay Miner.* **1999**, *47*, 726–731.
- (63) Yamanaka, S.; Brindley, G. Hydroxy-nickel interlayering in montmorillonite by titration method. *Clays Clay Miner.* **1978**, *26*, 21–24.
- (64) Fossum, J. O.; Knudsen, K. D.; Rudic, S.; Hunvik, K. W. B.; Bordallo, H. N.; Røren, P. M., *Determining the Interaction between Water and Carbon Dioxide in Smectite Clay (INS)*; STFC ISIS Neutron and Muon Source, 2019.

6.2.2. Supporting Information

Supporting Information: CO₂ Capture by Nickel Hydroxide Interstratified in the Nanolayered Space of a Synthetic Clay Mineral

Kristoffer W. Bø Hunvik,[†] Patrick Loch,[‡] Leide P. Cavalcanti,^{¶,§} Konstanse
Kvalem Seljelid,[†] Paul Monceyron Røren,[†] Svemir Rudić,[§] Dirk Wallacher,^{||}
Alexandro Kirch,[⊥] Kenneth Dahl Knudsen,^{¶,†} Caetano Rodrigues Miranda,[⊥]
Josef Breu,^{*,‡} Heloisa N. Bordallo,^{*,#,Ⓜ} and Jon Otto Fossum^{*,†}

[†]*Department of Physics, Norwegian University of Science and Technology, Høgskoleringen
5, 7491 Trondheim, Norway*

[‡]*Bavarian Polymer Institute and Department of Chemistry, University of Bayreuth,
Universitätsstraße 30, D-95440 Bayreuth, Germany*

[¶]*Institute for Energy Technology (IFE), POB 40, N-2027 Kjeller, Norway*

[§]*ISIS Neutron and Muon Source, STFC Rutherford Appleton Laboratory, Chilton, Didcot
OX11 0QX, United Kingdom*

^{||}*Department Sample Environments, Helmholtz-Zentrum Berlin für Materialien und
Energie, Hahn-Meitner-Platz 1, Berlin, 14109, Germany*

[⊥]*Departamento de Física dos Materiais e Mecânica, Instituto de Física, Universidade de
São Paulo, 05508-090 São Paulo, SP, Brasil*

[#]*Niels Bohr Institute-University of Copenhagen, Universitetsparken 5, 2100 Copenhagen,
Denmark*

[Ⓜ]*European Spallation Source ESS ERIC, PO Box 176, SE-221 00 Lund, Sweden*

E-mail: josef.breu@uni-bayreuth.de; bordallo@nbi.ku.dk; jon.fossum@ntnu.no

Results

Dried Na-Hec

PXRD

For dried Na-Hec PXRD measurements were carried out at NTNU (Trondheim, Norway) using an in-house X-ray scattering instrument, attached to a Xenox stationary electron impact source with a copper anode, producing K_{α} radiation. The scattered intensity was recorded by a two-dimensional Dectris Pilatus3 R 200K detector. The samples were mounted in the same high-pressure sample cell^{S1} in contact with a temperature regulated copper plate. Temperature control was provided by heat cartridges and a circulation bath. The sample cell was connected to a gas handling system providing vacuum from a rotary vane pump (10^{-2} mbar) or pressurized CO_2 of quality 99.9992%. Na-Hec was dried under vacuum at $150\text{ }^{\circ}\text{C}$ for 2h.

In Figure S1 the response of the Bragg reflection for the dried and hydrated Na-Hec is shown upon CO_2 exposure. Initially, the (001) Bragg reflection for the dried Na-Hec is found at $q = 0.65\text{ \AA}^{-1}$, corresponding to a basal spacing of $9.6 \pm 0.1\text{ \AA}$, which indicates complete collapse to 0 WL.^{S2,S3} When exposed to CO_2 there is no appreciable change in the pattern. The intensity change is due powder compacting and potentially texture being increased. This is validated by the 2D diffractograms (Figure S2). No crystalline swelling was observed for this sample, even under the same conditions as in ref.^{S4,S5} with $-20\text{ }^{\circ}\text{C}$ and 20 bar of CO_2 , nor after 13 days of CO_2 exposure. The samples in the present work are different from the ones studied in ref.^{S4,S5} both with respect to origin, preparation, charge and phase purity. This observation is in line with other previous experiment and simulations on montmorillonite and hectorite.^{S6,S7}

INS

For dried Na-Hec ($150\text{ }^{\circ}\text{C}$ under dynamic vacuum) (Figure S3) only a low intensity is observed before CO_2 exposure, as expected as there is next to no hydrogen left in the sample.

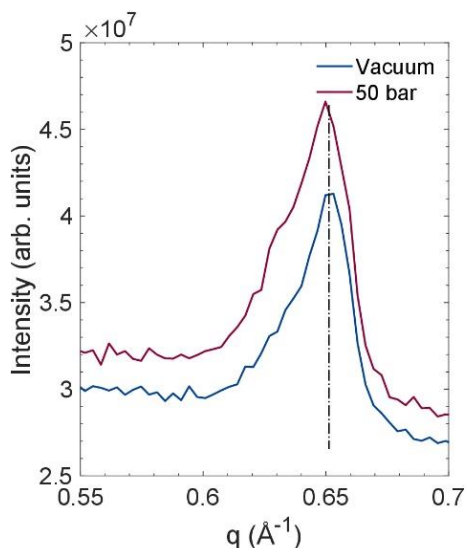


Figure S1: X-ray diffraction pattern of the (001) Bragg reflection for dried Na-Hec at 300 K for the initial and CO₂ exposed states. The horizontal line indicates the center of the reflection.

However, the presence of a tiny broad structure around 80 cm⁻¹, and a tiny broad hump between 500 and 1000 cm⁻¹, suggests that minor amount of residual water was trapped in the sample. After exposing dried Na-Hec to 5 bar (Figure S3a) and 44 bar CO₂ (Figure S3b), only insignificant changes are observed in the spectrum. This is in full agreement with *in situ* PXRD data (Figure S1), that showed that CO₂ does not intercalate in dried Na-Hec, suggesting that collapsed clay interlayers are incapable of swelling in the response to CO₂ in agreement with simulations.^{S6}

Gravimetric adsorption

CO₂ adsorption measurements were conducted with an IsoSORP gravimetric sorption analyzer from Rubotherm. Each sample was prepared by degassing them at 120±5 °C overnight under high vacuum, and was considered as dry when no more mass loss occurred. For each

Results

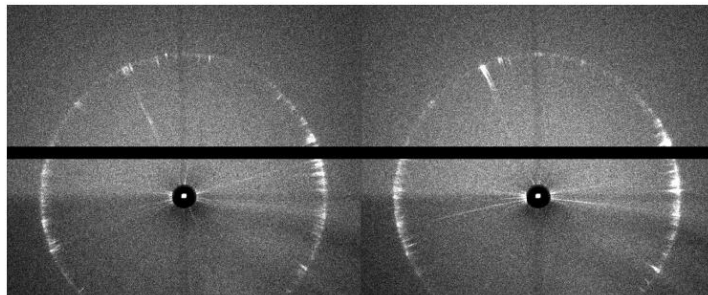


Figure S2: 2D detector image of a) dried NaFht under vacuum and b) dried NaFht with 50 bar CO₂ pressure.

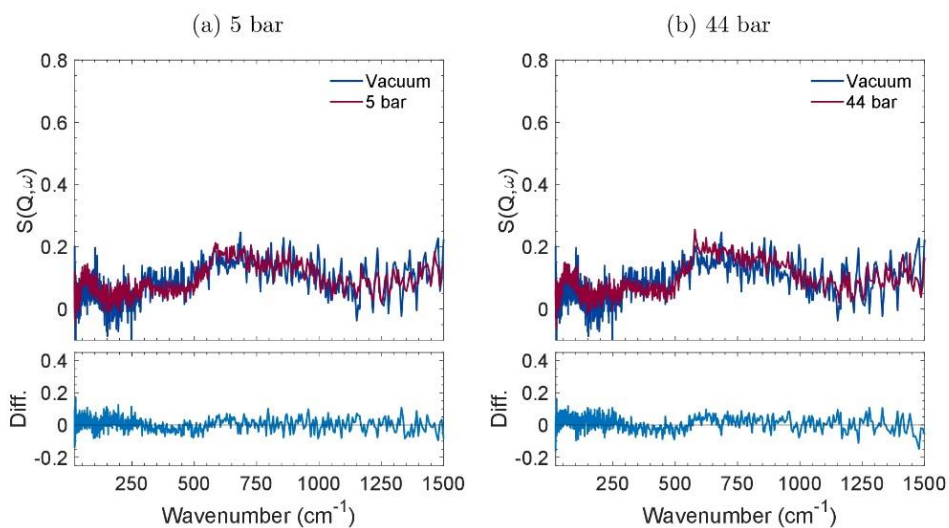


Figure S3: INS spectra of dried Na-Hec initial state and exposed to a) 5 bar of CO₂ and b) 44 bar of CO₂ with the corresponding difference spectra given below. Loading of CO₂ was performed at room temperature, and the spectra were recorded at $T < 20$ K.

sample two measurements were conducted with equilibration times of 4 h at each pressure step from high vacuum to 35 bar. The temperature was measured with a Pt-100 temperature sensor placed directly underneath the sample crucible surrounded by a double walled thermostat controlled by a circulating water bath CC-K6 from Huber. Temperature stability of the sample was within 22.5 ± 1 °C. The suspension balance has a resolution of 0.01 mg and reproducibility < 0.002 % rdg (≈ 0.002 mg). The data for pressure, temperature, and sample

weight were continuously recorded. The measured quantity is the excess adsorbed amount, which is obtained by correcting for buoyancy of the skeletal volume of the sample material and the suspended metal parts (including the sample holder). The skeletal volume of the samples was determined by individual helium isotherms. The buoyancy of the suspended metal parts was obtained by a blank measurement with CO₂. The density of helium and CO₂ for the given pressure and temperature conditions were obtained from the equation of state data provided by NIST.^{S8}

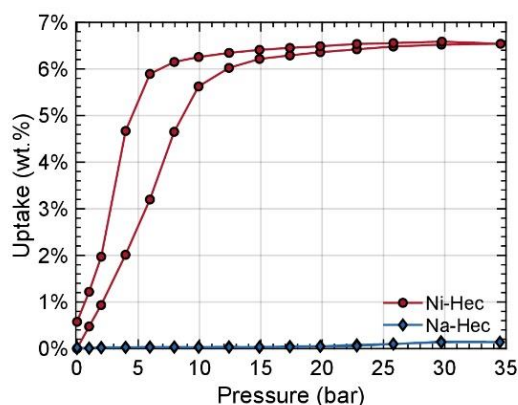


Figure S4: Gravimetric CO₂ adsorption measurements of Na-Hec and Ni-Hec equilibrated at each pressure step for 4 h.

The gravimetric adsorption measurements were carried out for dehydrated Ni-Hec and Na-Hec, and is shown in Figure S4. He-isotherms were obtained over the same pressure range giving a density of 2.35 g/ml and 2.59 g/ml for Ni-Hec and Na-Hec, respectively. This is somewhat lower than the theoretical density of 2.8 g/ml for Na-Hec,^{S2} and suggest that some cavities in the sample are inaccessible for He. The result clearly demonstrate that there is no adsorption within the pressure range for dehydrated Na-Hec, thus confirming the XRD and INS results of no response to CO₂. For Ni-Hec the uptake initiates already at low pressures and reaches a plateau at around 15 - 20 bar. Finally, at 35 bar an uptake of 6.5 wt.% (1.59 mmol/g) is observed for Ni-Hec. Upon desorption most of the CO₂ released, and at the final stage there is still about 0.5 wt.% CO₂ left in the sample. A detailed analysis will

Results

be presented in a future publication. The observed d-spacing follows closely the gravimetric uptake, which confirms that the swelling is correlated with sorption. Therefore it is very unlikely that CO₂ can adsorb in the interlayer without causing swelling.

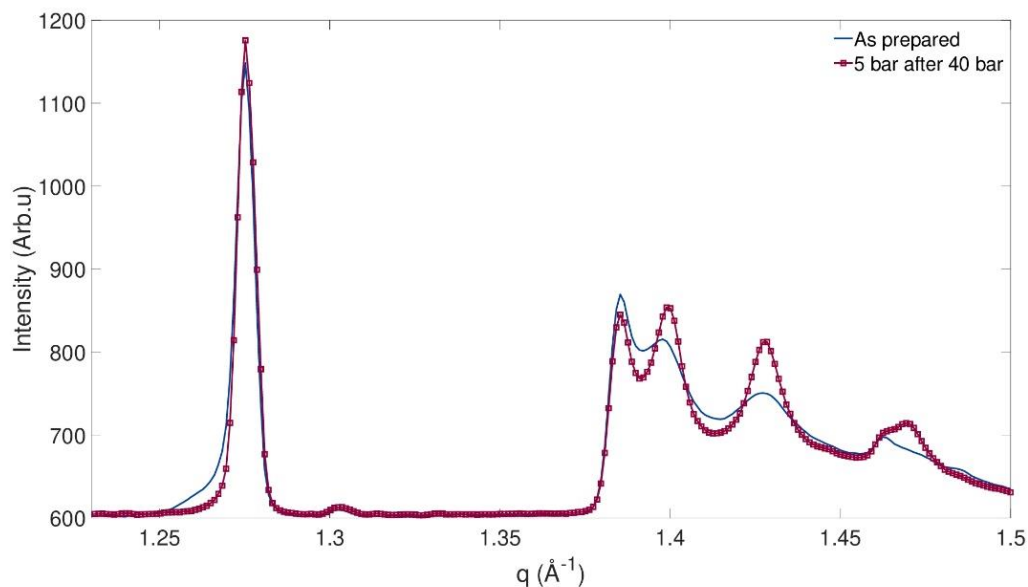


Figure S5: X-ray diffraction pattern of hydrated Ni-Hec as-prepared at 1 bar, and after exposure to a maximum of 40 bar and followed by a reduction to 5 bar CO₂ at 300 K.

Thermogravimetric analysis

Thermogravimetric analysis (TGA) were recorded on Na-Hec and Ni-Hec equilibrated at 43% r.h. in a desiccator with K₂CO₃ salt solution. Data recorded on a NETZSCH STA F3 449 Jupiter from 25 °C to 900 °C with a heating rate of 10 K/s under N₂ flow (20 ml/min purge, 10 ml/min protective).

TGA of hydrated Na-Hec and Ni-Hec is shown in Figure S6. The single decomposition at 110 °C observed in the dm/dT curves of Na-Hec (Figure S6b) is assigned to a highly uniform interlayer water population, in agreement with Larsen *et al.*^{S9}

For Ni-Hec we observe a more complex mass loss in agreement with previous observa-

tions.^{S10,S11} The first at about 100 °C can be identified as the loosely bound interlayer water, the second at about 160 °C can be related to the strongly bound interlayer water that is coordinated to the Ni²⁺ cations. The last signal at about 270 °C is identified as dehydroxilation of the nickel hydroxide interlayer species.

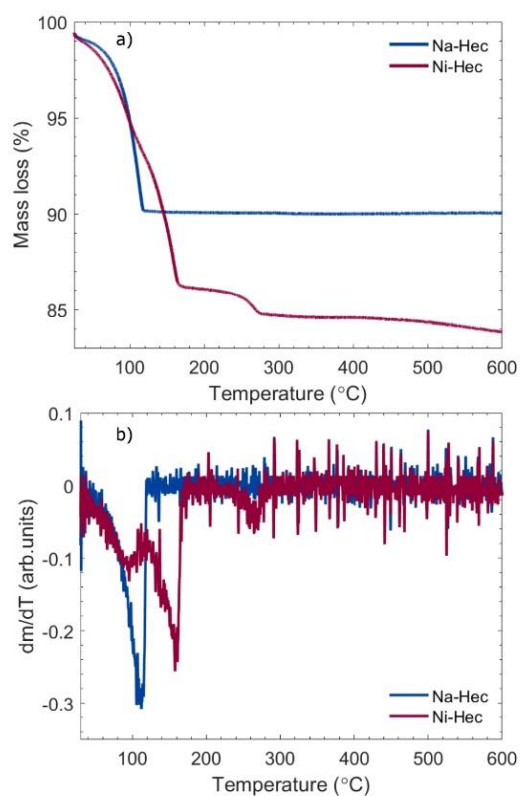


Figure S6: a) TGA and b) dTGA of Na-Hec and Ni-Hec equilibrated at 43% r.h. in a dessicator with K₂CO₃ salt solution.

Results

Table S1: An Assignment of the Vibrational Modes Associated with Nickel Hydroxide $[\text{Ni}(\text{OH})_{0.83}(\text{H}_2\text{O})_{1.17}]_{0.37}^{1.17+}$ observed using INS for Dried Ni-Hec with Numbering given in Figure 5

Feature number	Position (cm^{-1})	Suggested assignment
1	70	Ni-(H ₂ O); acoustic
2	109	Ni-(OH) acoustic ^{S12,S13}
3	165	Ni-(OH)
4	215	Ni-(H ₂ O)
5	300	Ni-(OH); A _{1g} (T) ^{S13} or E _g ^{S12}
6	400 (broad)	Ni-(OH); E _u (T), A _{2u} , E _g (T), A _{1g} ^{S12,S13}
7	670 (broad)	Ni-(OH); E _u (R) ^{S13} or 2E _g ^{S12}
8	810 (broad shoulder)	Ni-(OH); E _g ^{S12,S13}

Table S2: An Assignment of the Vibrational Modes observed using INS for Hydrated Ni-Hec with Numbering given in Figure 5

Feature number	Position (cm^{-1})	Suggested assignment
1	76 (broad)	H ₂ O/Ni-(H ₂ O); acoustic
2	109	Ni-(OH); acoustic ^{S12,S13}
3	130	H ₂ O
4	165	Ni-(OH)
5	215	Ni-(H ₂ O)
6	237	H ₂ O
7	335 (rise)	librational edge cation coordinated H ₂ O
8	430	Ni-(OH); A _{1g} (T) ^{S13} or E _g ^{S12}
9	480	H ₂ O
10	510 (rise)	librational edge loosely bound interlayer H ₂ O
11	575	H ₂ O
12	650	Ni-(OH); E _u (R) ^{S13} or 2E _g ^{S12}
13	800	Ni-(OH); E _g ^{S12,S13}

DFT simulations

With the computational approach based on the DFT, we evaluated the CO₂ and H₂O adsorption energies on the Hec surface (Hec interfaced with the vacuum). Both CO₂/Hec and H₂O/Hec systems display low adsorption energies indicating a physisorption interaction with the clay surface oxygen atoms (see Figure S7). The water molecules exhibit more stable configurations for carbon dioxide due to the hydrogen bonds (see Table S3). Both molecules

may adsorb also on the interlayer Ni^{2+} cation, resulting in more negative adsorption energies, especially for the water case. In the confinement context, the CO_2 and H_2O insertion in the Hec interlayer region results in larger d-spacing depending on the molecule kinetic diameter. The corresponding interaction energies for the most favored adsorption sites and the resulting d-spacings are shown in Table S3.

Table S3: CO_2 and H_2O Adsorption Energies (eV) and d-spacing for the Most Favorable Hec Adhesion Site.

	Adsorption site	H_2O	CO_2
Surface	Surface oxygen	-0.32	-0.20
	Ni^{2+} cation	-0.99	-0.53
Interlayer	Ni^{2+} cation	-1.40	-0.81
d-spacing	Ni^{2+} cation	10.3 Å	11.7 Å

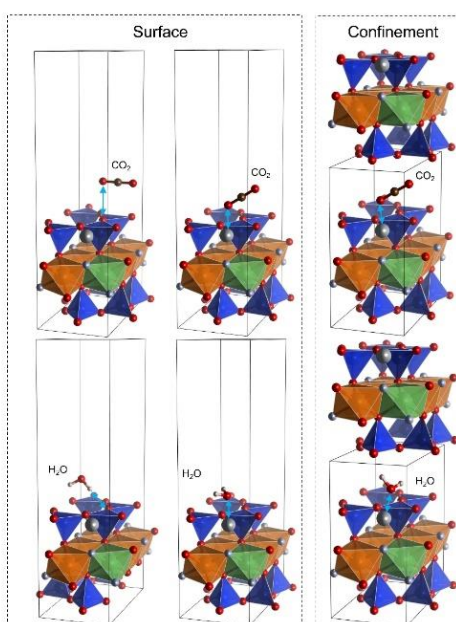


Figure S7: Most favorable CO_2 and H_2O adsorption sites on a Hec surface interfaced with vacuum or under confinement.

We also evaluated the CO_2 adsorption on the $\beta\text{-Ni}(\text{OH})_2$ phase (see Figures S8 a-d). Among the adsorption sites, the CO_2 interacts weakly with the surface OH terminations

Results

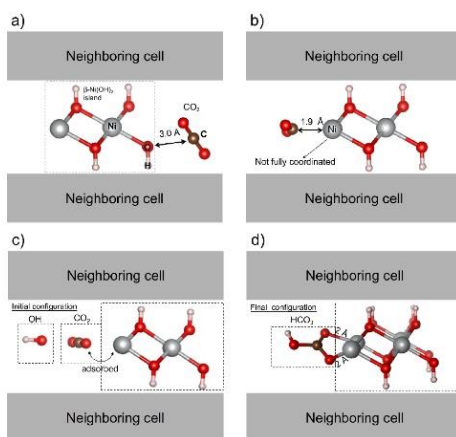


Figure S8: Side adsorption sites with the CO₂ interacting with the a) surface OH and b) a not fully coordinated nickel atom in the β -Ni(OH)₂ island. c) Our calculations indicate the proximity of a OH molecule may result in d) the HCO₃⁻ molecule adsorbed in the crystalline phase.

(E_{ads} between -0.15 to -0.30 eV, see Figure S8 a). However, the scenario changes in the case where the adsorption site is a not fully coordinated nickel atom in the edge of the crystal islands, therefore displaying a more negative adsorption energy $E_{\text{ads}}=-1.85$ eV (Figure S8 b). In this situation, the adsorbed CO₂ may attract free surrounding OH ions, resulting in the HCO₃⁻ molecule adsorbed on the β -Ni(OH)₂ phase (see Figures S8 c-d). We stress the HCO₃⁻ formation from CO₂+OH interaction is not a spontaneous process if the molecules are isolated, but it is favorable when the CO₂ is firstly adsorbed on that not-fully coordinated nickel atom. These calculations may indicate the existence of a bicarbonate structure as we suggest in the main text.

References

- (S1) Jensen, T. R.; Nielsen, T. K.; Filinchuk, Y.; Jørgensen, J.-E.; Cerenius, Y.; Gray, E. M.; Webb, C. J. Versatile in situ powder X-ray diffraction cells for solid–gas investigations. *Journal of applied crystallography* **2010**, *43*, 1456–1463.
- (S2) Kalo, H.; Milius, W.; Breu, J. Single crystal structure refinement of one-and two-layer hydrates of sodium fluorohectorite. *Rsc Advances* **2012**, *2*, 8452–8459.
- (S3) Stöter, M.; Kunz, D. A.; Schmidt, M.; Hirsemann, D.; Kalo, H.; Putz, B.; Senker, J.; Breu, J. Nanoplatelets of sodium hectorite showing aspect ratios of 20 000 and superior purity. *Langmuir* **2013**, *29*, 1280–1285.
- (S4) Michels, L.; Fossum, J. O.; Rozynek, Z.; Hemmen, H.; Rustenberg, K.; Sobas, P. A.; Kalantzopoulos, G. N.; Knudsen, K. D.; Janek, M.; Plivelic, T. S., et al. Intercalation and retention of carbon dioxide in a smectite clay promoted by interlayer cations. *Scientific reports* **2015**, *5*, 8775.
- (S5) Hemmen, H.; Rolseth, E. G.; Fonseca, D. M.; Hansen, E. L.; Fossum, J. O.; Plivelic, T. S. X-ray studies of carbon dioxide intercalation in Na-fluorohectorite clay at near-ambient conditions. *Langmuir* **2012**, *28*, 1678–1682.
- (S6) Loganathan, N.; Yazaydin, A. O.; Kirkpatrick, R. J.; Bowers, G. M. Tuning the Hydrophobicity of Layer-Structure Silicates To Promote Adsorption of Nonaqueous Fluids: Effects of F–for OH–Substitution on CO₂ Partitioning into Smectite Interlayers. *The Journal of Physical Chemistry C* **2019**, *123*, 4848–4855.
- (S7) Schaef, H. T.; Loganathan, N.; Bowers, G. M.; Kirkpatrick, R. J.; Yazaydin, A. O.; Burton, S. D.; Hoyt, D. W.; Thanthiriwatte, K. S.; Dixon, D. A.; McGrail, B. P., et al. Tipping point for expansion of layered aluminosilicates in weakly polar solvents: supercritical CO₂. *ACS applied materials & interfaces* **2017**, *9*, 36783–36791.

Results

- (S8) Lemmon, E. W.; McLinden, M. O.; Friend, D. G. *Thermophysical Properties of Fluid Systems*; Retrieved June 22, 2020; NIST Standard Reference Database Number 69.
- (S9) Larsen, S. R.; Michels, L.; dos Santos, É. C.; Berg, M. C.; Gates, W. P.; Aldridge, L. P.; Seydel, T.; Ollivier, J.; Telling, M. T.; Fossum, J. O., et al. Physicochemical characterisation of fluorohectorite: Water dynamics and nanocarrier properties. *Microporous and Mesoporous Materials* **2020**, *306*, 110512.
- (S10) Altoé, M. A. S.; Michels, L.; dos Santos, E.; Droppa Jr, R.; Grassi, G.; Ribeiro, L.; Knudsen, K.; Bordallo, H. N.; Fossum, J. O.; da Silva, G. J. Continuous water adsorption states promoted by Ni²⁺ confined in a synthetic smectite. *Applied Clay Science* **2016**, *123*, 83–91.
- (S11) Loch, P.; Hunvik, K. W.; Puchtler, F.; Weiss, S.; Røren, P. M.; Rudic, S.; Knudsen, K. D.; Bordallo, H. N.; Fossum, J. O.; Breu, J. Nickel Intercalated Smectites capable for CO₂ swelling. *To be submitted*
- (S12) Bantignies, J.; Deabate, S.; Righi, A.; Rols, S.; Hermet, P.; Sauvajol, J.; Henn, F. New insight into the vibrational behavior of nickel hydroxide and oxyhydroxide using inelastic neutron scattering, far/mid-infrared and Raman spectroscopies. *The Journal of Physical Chemistry C* **2008**, *112*, 2193–2201.
- (S13) Baddour-Hadjean, R.; Fillaux, F.; Tomkinson, J. Proton dynamics in β Ni(OH)₂ and β NiOOH. *Physica B: Condensed Matter* **1995**, *213*, 637–639.

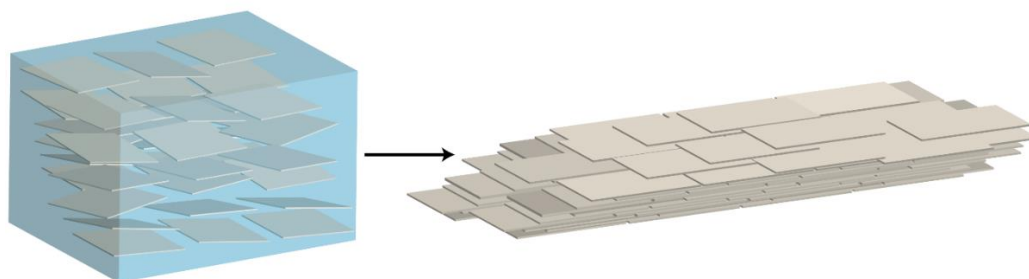
6.3. Delamination of layered zeolites into aqueous dispersions of nanosheets

Patrick Loch^a, Dominik Schuchardt,^a Gerardo Algara-Siller,^{b,c} Paul Markus,^a Katharina Ottermann,^a Sabine Rosenfeldt,^a Thomas Lunkenbein,^b Wilhelm Schwieger^d Georg Papastavrou^a and Josef Breu^{a,*}

Nematic suspension of a microporous layered silicate obtained by forceless spontaneous delamination via repulsive osmotic swelling for casting high-barrier all Inorganic Films

Published in: *Science Advances* **2022**, 8, eabn9084.

Reproduced under the terms of the CC-BY-NC 4.0 license.



^a Bavarian Polymer Institute and Department of Chemistry, University of Bayreuth, Universitätsstraße 30, D-95447 Bayreuth, Germany

^b Department of Inorganic Chemistry, Fritz-Haber-Institut der Max-Planck-Gesellschaft, Faradayweg 4-6, D-14195 Berlin, Germany

^c Institute of Physics & IRIS Adlershof, Humboldt-Universität zu Berlin, D-12489 Berlin, Germany

^d Institute of Chemical Reaction Engineering, Friedrich-Alexander University Erlangen-Nürnberg, Egerlandstraße 3, 91058 Erlangen, Germany

* Corresponding author

Individual Contribution:

The concept of this publication was developed by Prof. J. Breu and me. Prof. J. Breu and I wrote the manuscript. I designed the experiments, synthesized the materials and did most of the characterization. G. Algara-Siller, S. Rosenfeldt and D. Schuchardt commented on the manuscript. G. Algara-Siller and T. Lunkenbein performed the electron diffraction analysis. D. Schuchardt helped with SAXS measurements, film casting and gas permeation tests. P. Markus, K. Ottermann and Prof. G. Papastavrou conducted AFM imaging. S. Rosenfeldt helped with SAXS measurements and fitted the SAXS data. Prof. W. Schwieger helped with the Ilerite synthesis. All authors contributed to scientific discussion. Parts of this publication were provided for a patent application.

My contribution to the publication is approx. 75 %

6.3.1. Nematic suspension of a microporous layered silicate obtained by forceless spontaneous delamination via repulsive osmotic swelling for casting high-barrier all Inorganic Films

SCIENCE ADVANCES | RESEARCH ARTICLE

MATERIALS SCIENCE

Nematic suspension of a microporous layered silicate obtained by forceless spontaneous delamination via repulsive osmotic swelling for casting high-barrier all-inorganic films

Patrick Loch¹, Dominik Schuchardt¹, Gerardo Algara-Siller^{2,3}, Paul Markus¹, Katharina Ottermann¹, Sabine Rosenfeldt¹, Thomas Lunkenbein², Wilhelm Schwieger⁴, Georg Papastavrou¹, Josef Breu^{1*}

Copyright © 2022
The Authors, some
rights reserved;
exclusive licensee
American Association
for the Advancement
of Science. No claim to
original U.S. Government
Works. Distributed
under a Creative
Commons Attribution
NonCommercial
License 4.0 (CC BY-NC).

Exploiting the full potential of layered materials for a broad range of applications requires delamination into functional nanosheets. Delamination via repulsive osmotic swelling is driven by thermodynamics and represents the most gentle route to obtain nematic liquid crystals consisting exclusively of single-layer nanosheets. This mechanism was, however, long limited to very few compounds, including 2:1-type clay minerals, layered titanates, or niobates. Despite the great potential of zeolites and their microporous layered counterparts, nanosheet production is challenging and troublesome, and published procedures implied the use of some shearing forces. Here, we present a scalable, eco-friendly, and utter delamination of the microporous layered silicate ilerite into single-layer nanosheets that extends repulsive delamination to the class of layered zeolites. As the sheet diameter is preserved, nematic suspensions with cofacial nanosheets of ≈ 9000 aspect ratio are obtained that can be cast into oriented films, e.g., for barrier applications.

INTRODUCTION

Layered or two-dimensional (2D) materials represent a versatile tool with a variety of properties. The pronounced anisotropy in bonding strength of layered solids like graphite (1), clay minerals (2), transition metal dichalcogenides (3), lepidocrite-type titanates (4), perovskite-type niobates (5, 6), or NaFeO₂-type cathode materials (7) leads to a platy morphology and, in many cases, to intracrystalline reactivity. The latter is frequently taken advantage of to increase the basal spacing and thus weaken the adhesion between layers. This then sets the stage for liquid-phase exfoliation by ultrasonic (US) treatment, which nowadays is established as the standard approach to produce nanosheets that are applied in a plethora of applications (8–10). Some applications like the formation of heterostructures (11), permselective microporous membranes (12), textured (barrier) films, or composites (13) require a uniform nanosheet thickness and a large aspect ratio (ratio of nanosheet diameter to thickness). US treatment clearly does not offer this degree of control as it inevitably leads to broad distribution of thicknesses and platelet breakage, thus the maximum aspect ratio inherent to the pristine platelet diameter will not be achieved (8, 9).

Contrary to brute-force liquid-phase exfoliation, nanosheets of some charged layered materials may alternatively be obtained by thermodynamically allowed delamination via so-called repulsive osmotic swelling [see (14) for a definition of exfoliation versus delamination]. This was, however, long limited to a handful of layered compounds such as titanates (15, 16), niobates (5, 6), antimonates

(17), manganese oxides (18), tungsten oxides (19), and clay minerals (20, 21). The process resembles the dissolution of ionic crystals while being limited to one dimension because of the anisotropic bonding situation. In summary, osmotic swelling requires separation above a certain threshold value where entropic contributions of interlayer species convert the initial adhesion into repulsion. While this repulsive swelling is rare, many cases are known where solvation of pristine or exchanged interlayer cations leads to so-called crystalline swelling. In this swelling regime, uptake of solvent resembles a first-order phase transition and is limited to distinct values even in excess of swelling agent because the interaction of adjacent layers remains attractive (21). Although crystalline swelling weakens the adhesion in the ionic crystal, exfoliation is not a spontaneous process and requires external (shearing) forces. Exfoliation gives a broad distribution of multilayers aside of monolayers and because of the forces applied bears the risk of breaking platelets and thus reducing the aspect ratio. The ultimate defining signature for repulsive swelling is the formation of a liquid crystalline, nematic suspension of nanosheets, which is indicated by the presence of sharp reflections in its X-ray scattering patterns at small scattering angles, corresponding to large periodicities (22). The occurrence of a homogeneous and single liquid crystalline phase critically depends on the complete, thermodynamically driven delamination of the pristine crystallites in the solvent.

If the pristine platelets have appreciable diameters, even dilute suspensions obtained by repulsive osmotic swelling will not be isotropic. Rather, nematic liquid crystalline phases are formed because the rotation of nanosheets, which are separated to large distances (>10 nm) by swelling at low concentrations, is hindered (21, 23, 24). As no mechanical input is required for repulsive osmotic swelling, the process is most gentle and preserves the lateral extension of the parent crystal in the nanosheets, and hence, the aspect ratio is maximized. For (synthetic) clay minerals, spontaneous delamination into high-aspect ratio nanosheets has recently been extended to high-charge

¹Bavarian Polymer Institute, Department of Chemistry, University of Bayreuth, Universitätsstraße 30, D-95447 Bayreuth, Germany. ²Department of Inorganic Chemistry, Fritz-Haber-Institut der Max-Planck-Gesellschaft, Faradayweg 4-6, D-14195 Berlin, Germany. ³Institute of Physics and IRIS Adlershof, Humboldt-Universität zu Berlin, D-12489 Berlin, Germany. ⁴Institute of Chemical Reaction Engineering, Friedrich-Alexander University Erlangen-Nürnberg, Egerlandstraße 3, D-91058 Erlangen, Germany.

*Corresponding author. Email: josef.breu@uni-bayreuth.de

density vermiculite-type materials, and it was realized that bulky interlayer cations induce separation above the threshold separation distances and trigger delamination (23, 25).

Compared to clay minerals, layered zeolites carry reactive silanol groups at the microporous basal surface, which renders zeolite nanosheets highly attractive for fabricating functional films and membranes (26–29). RUB-15 nanosheets, for example, were exfoliated by shear forces in a polymer melt and then used to cast into thin permselective membranes for hydrogen separation with a H_2/CO_2 selectivity of up to 100 (12). Alternatively, MCM-22P was already exfoliated following ion exchange with tetrapropylammonium hydroxide in water. The monolayer yield was 15 to 20%, and typical aspect ratios of ≈ 20 were observed (30). More recently, by ion exchange with tetrabutylammonium hydroxide (TBAOH) of MCM-56 and ZSM-55, aqueous dispersions of nanosheets were obtained with 40 and 70% yield, respectively, and typical aspect ratios of < 200 . Films of zeolite nanosheets could be casted following this approach (27, 31).

Here, we present a scalable, eco-friendly, and utter delamination of ilerite (RUB-18) into nanosheets by repulsive osmotic swelling (Fig. 1A). As ilerite can easily be crystallized in quadratic plates of $> 6 \mu\text{m}$ diameter, upon its gentle delamination, nanosheets with exceptional aspect ratios (≈ 9000) are obtained. As a first example of its application potential, all-inorganic high-barrier films were fabricated by simply doctor-blading the nematic suspension.

RESULTS AND DISCUSSION

To trigger osmotic swelling, adjacent layers in a layered ionic crystal need to be separated by incorporation of solvent to a certain threshold value (21, 23). At this stage, the translational entropy of the interlayer species (solvent and interlayer cations) becomes dominating over the electrostatic attraction of the negatively charged layers, and the interlayer cations and adjacent layers in the crystal repel each other. The threshold separation may be achieved only through the solvation enthalpy of interlayer cations, as is the case with clay minerals of low charge density like hectorite (32). For higher charge density, the threshold separation may still be achieved by supplementing hydration forces with a steric pressure exerted by bulky interlayer cations (20, 23). The steric pressure arises once the equivalent area of the interlayer cation exceeds the charge density of the underlying anionic layer. While, for 2:1-type clay minerals like montmorillonite or hectorite, this charge density is permanent and independent of pH, for compounds like layered titanates (33, 34) or zeolites (35, 36), acidic OH groups are exposed at the basal surfaces and thus the charge density will alter with pH. For ilerite ($\text{Na}_8[\text{Si}_{32}\text{O}_{64}(\text{OH})_8] \cdot 32 \text{H}_2\text{O}$), only half of the acidic protons are replaced by Na^+ during crystallization. These interlayer cations can be readily exchanged by a hydrophilic and sterically demanding cationic amino sugar *N*-methyl-*D*-glucosamine (meglumine). As the organocation is a base, the charge density is modified concomitantly with the ion exchange.

Ilerite is a 2D microporous silica-based material with a layered structure built from $[5^4]$ cages resembling the building units of zeolites. While each layer has a polar structure, the stacking is centrosymmetric. The layer charge originates from half of terminal silanol bonds being deprotonated at the pH of synthesis (pH 13) and is balanced by chains of edge sharing $[\text{Na}(\text{H}_2\text{O})_6]$ octahedra in the interlayer space (37). The single layer exhibits a network of four- and six-membered rings, making ilerite nanosheets potentially interesting for the fabrication of permselective hydrogen membranes (Fig. 1B).

Ilerite grows as characteristic square-shaped platelets (Fig. 1C) with appreciable lateral extension ($> 6 \mu\text{m}$).

Contrary to common layered zeolites [e.g., MFI (29), MCM-56 (38), or MCM-22 (39)], the synthesis of the microporous layered silicate ilerite requires no structural directing agent and can be performed under mild conditions (40–42). Phase-pure ilerite was obtained in a water-based sol-gel route by the simple mixing of NaOH pellets with H_2O and a colloidal SiO_2 dispersion in a defined molar ratio ($\text{Na}_2\text{O}:\text{SiO}_2:\text{H}_2\text{O}$ ratio of 1:4:37) followed by annealing (4 weeks) at 100°C in a closed vessel. Upscaling of layered sodium silicates, in general, is straightforward and has been established in industry (Chemiekombinat Bitterfeld, CWK Bad Köstritz, and Hoechst AG). The moderate synthesis temperature of 100°C requires no high-pressure autoclaves; rather, the synthesis can be conducted in low-cost, closed, glassy carbon crucibles or stainless steel vessels. Phase purity of the synthesized ilerite was checked with powder X-ray diffraction (PXRD; Fig. 1D). The PXRD pattern could be completely indexed in space group $I4_1/amd$ (no. 141), indicating phase purity, and refinement of lattice parameters yielded $a = b = 7.333(3) \text{ \AA}$ and $c = 44.31(4) \text{ \AA}$ in accordance with Vortman *et al.* (37). The particle size was determined with static light scattering, resulting in a narrow particle size distribution and a median particle size of $6.7 \mu\text{m}$ (fig. S1).

As previously mentioned, quantitative delamination via repulsive delamination requires cation exchange with a bulky organocation like meglumine. The ternary amine is a strong base, allowing the exchange to be performed at high pH where the zeolite is perfectly stable and the base is still protonated. Simple ion exchange of interlayer Na^+ of the as-synthesized material with an aqueous solution of meglumine at pH 9 and subsequent reduction of the ionic strength gave nematic dispersions of ilerite monolayers (Fig. 1A).

In a typical procedure, the synthesized ilerite was repeatedly treated with a 1 M solution of meglumine in water to ensure a complete ion exchange of interlayer Na^+ with meglumine to obtain meglu-ilerite. The pH of the meglumine solution was adjusted to 9 by addition of HCl. Upon ion exchange, the basal spacing increased from 11.0 to approximately 14.9 \AA (fig. S2). Ion exchange was complete and no residual interlayer Na^+ could be detected by energy-dispersive X-ray (EDX) spectroscopy (table S1). CHN analysis confirmed the intercalation of meglumine and was also used to calculate the amount of intercalated meglumine. Meglu-ilerite was found to contain 2.16 mmol/g of the organocation, which is notable less than the Na^+ content of the pristine ilerite (2.83 mmol/g). This indicates that, as expected at the lower pH of ion exchange, some silanol groups get protonated, resulting in a lowering of the charge density of the silicate layers. Nevertheless, the remaining charge density of meglu-ilerite is still high enough to generate steric pressure to assist expansion of the interlayer space beyond the threshold separation, as clarified when considering the charge equivalent areas. Meglumine has an equivalent area of 77 \AA^2 per charge, which is larger than the charge density of the ilerite at pH 9 of 70 \AA^2 per charge (for details of the calculation, see the Supplementary Materials). Neither the pristine ilerite nor other hydrophilic organocations like TBAOH, 2-ammonium-2-(hydroxymethyl)-1,3-propanediol, cyclohexylammonium, piperidine, 2-ammonium-3-(1H-imidazol-4-yl)propanoic acid (histidine), 2-(trimethylammonium)ethyl methacrylate, or 4-(dimethylammonium)pyridine allow for osmotic swelling because the hydration enthalpy is too low and the equivalent areas (table S2) are too small to take the basal spacing beyond the threshold separation.

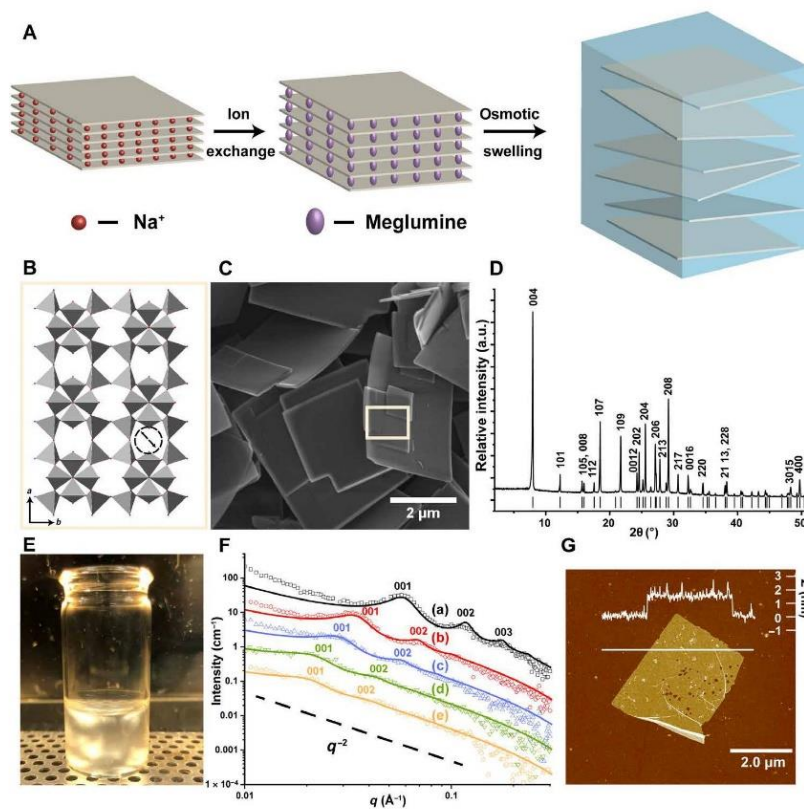


Fig. 1. Characterization and delamination of ilerite into nanosheets. (A) Schematic illustration of the delamination process by cation exchange of interlayer Na⁺ against a bulky organocation meglumine and subsequent reduction of the ionic strength triggering osmotic swelling. (B) Structure of ilerite nanosheets. (C) Scanning electron microscopy (SEM) images of the pristine ilerite. Inset: The selected area of the structure. (D) Completely indexed PXRD pattern of ilerite indicating a phase pure material. Ticks indicate the theoretical reflections of ilerite. a.u., arbitrary units. (E) Nematic phase with characteristic birefringes formed upon delamination into nanosheets (0.5 volume %). (F) SAXS pattern proving complete delamination. Observed swelling upon addition of water to a highly concentrated gel with a solid content of 7.04 wt % (A) to 3.47 wt % (B), 2.81 wt % (C), 1.67 wt % (D), and 1.42 wt % (E), respectively. The corresponding *d*-spacings of 10.6, 18.0, 21.5, 28.5, and 30.0 nm, respectively, were obtained applying a simplified disc model. (G) Only single ilerite nanosheets could be found in the AFM with a characteristic square shape of the parent compound.

Because repulsive osmotic delamination is based on electrostatic repulsion, which is screened in ionic backgrounds, it tolerates only low ionic strengths (typically <0.02 M) (21). The ionic background was therefore lowered by repeated washing/centrifugation cycles or alternatively by dialysis. Both eventually triggered delamination of meglu-ilerite, and birefringent, nematic, aqueous suspensions consisting of zeolite-like silica-based monolayers could be obtained (Fig. 1E). Please note that, during washing/centrifugation, no coarse-grained, not delaminated material was discarded. The single-phase nature of the liquid crystal can easily be inspected by eye via a homogeneous birefringent appearance of the suspensions. The nanosheets in the nematic domains are separated to large distances, which are determined by the solid content of the suspensions. The separation of single nanosheets in a concentrated gel of 7.04 weight % (wt %) was determined by small-angle X-ray scattering (SAXS). Because of strong electrostatic repulsion, the negatively charged ilerite nanosheets adopt a cofacial arrangement (21, 24) leading to a rational 00 *l* series in the SAXS pattern with a periodicity of 10.6 nm

(Fig. 1F). The separation of 10.6 nm was obtained by fitting the scattering curve with a simplified disc model (for details, see fig. S3). Moreover, the observed q^{-2} scaling of the scattering intensity is typical for thin, platy scattering objects (21). The lack of basal reflections in the range of 1° to 10° 2θ, where ilerite and meglu-ilerite basal reflections would be expected, indicates complete delamination into monolayers (fig. S4).

Upon dilution of the highly concentrated gel, a continuous shift to lower *q* values was observed, indicating an increasing separation of the layers (Fig. 1F). The shift in the *d*-spacing from 10.7 to 30.0 nm corroborates the delamination mechanism that is based on repulsive osmotic swelling, because additional water is used to increase the distance between adjacent layers, minimizing the repulsive interactions of the negatively charged zeolite layers (15, 25). While, for the highly concentrated gel, an intense 00 *l* series is clearly visible, the intensity decreases after further dilution. As previously observed for hectorite suspensions, upon increasing the separation distance, the thin and flexible nanosheets gradually lose the coplanarity by local undulations, etc. (21).

Quantitative conversion into high-aspect ratio monolayers was further confirmed with atomic force microscopy (AFM). For imaging, a highly diluted aqueous dispersion of ilerite was drop-casted on an ammonium modified Si wafer. For a single layer of ilerite, a height of 0.74 nm was calculated on the basis of the crystal structure of the parent compound. Because delaminated meglu-ilerite nanosheets have bulky, hydrated meglumine attached at the external surfaces, the height of 1.5 nm observed in AFM (fig. S5) is in good agreement with expectations and in line with the basal spacing of meglu-ilerite (Fig. 1G). Meglumine is slightly elliptical with an estimated diameter of 0.7 to 0.8 nm, adding to the nanosheet thickness of 0.74 nm. The nanosheet height of 1.5 nm observed with AFM (fig. S5) would therefore indicate a meglumine monolayer to be adsorbed only on the upper basal surface. On closer inspection of the AFM image, rectangular, nanoscopic holes become apparent. It is unclear whether they are inherited from defects in the pristine ilerite or whether they are etched into the nanosheets during the delamination. In any case, these represent pinholes that are expected to be detrimental to the barrier performance, as discussed later. Figure 1G and fig. S5 reveal another interesting feature: While crystalline ilerite is centrosymmetric, individual ilerite single-layer nanosheets have a polar structure meaning that the two basal surfaces are different. Ilerite nanosheets thus represent patchy platelets and consequently tend to roll up at the edges when cast on a planar support. This behavior tends to make preparation of AFM samples difficult and requires positively charged groups to be attached to the substrate surface by silylation.

To confirm the integrity of the structure of the ilerite monolayers, the nanosheets (fig. S6) were characterized with electron diffraction (ED) analysis. The experimentally observed diffraction pattern is in good agreement with simulated patterns of a single-layer ilerite, showing reflections at d -spacings of 7.32 and 5.18 Å [i.e., (100) and (110)]. These reflections are systematically absent in the ED pattern of the 3D bulk material (Fig. 2) because of the centrosymmetric stacking. Comparison of the ED pattern of a single-layer and a few-layer-thick bulk material, obtained by increasing the concentration, proves the sensitivity of ED to detect incomplete delamination or restacking. In particular, as the layer stacking in the bulk ilerite is centrosymmetric, reflection conditions imposed by the center of symmetry (i.e., $hk0: h,k = 2n$) are lifted for a single-layer nanosheet and reflections like 110 are observed (Fig. 2D). While the ED pattern of

a single ilerite layer shows only discrete reflections, higher concentration of ilerite suspensions lead to a turbostratic restacking of monolayers resulting in an overlay of misoriented diffraction patterns from single layers, corroborating the successful delamination (fig. S7, A to C).

The obtained nanosheets are purely electrostatically stabilized without any steric contribution. Small molecular counter cations on the surface of the nanosheets can be easily replaced. Meglumine desorbs, for example, upon deposition of the nanosheets on the positively charged Si wafer from the bottom side of the surface. Moreover, because of the gentle delamination driven by thermodynamics, the large particle diameter of the parent ilerite may be transformed into an exceptional aspect ratio. Assuming the diameter of the parent ilerite as determined by light scattering to be preserved, the aspect ratio can be estimated (32). The height of the bare monolayers as found in the crystal structure is 0.74 nm, resulting in an estimated aspect ratio of more than 9000. Given this large aspect ratio, any type of casting on a planar substrate will inevitably result in textured, monodomain films with band-like structures formed because of partial overlap of adjacent nanosheets (Fig. 3A, inset). This renders ilerite most appropriate for applications such as barrier coatings. Liquid dispersions of the layered zeolite can easily be processed into highly oriented thin films applying common fabrication techniques like filtration, doctor blading, slot-die, or spray coating. In the following, we exemplify their high value in the field of barrier coatings. As the barrier improvement factor scales with the square of the aspect ratio, the gentle nature of repulsive osmotic delamination assuring maximum aspect ratios is key. The full potential inherent to the large diameter of the pristine ilerite crystals can be completely used because nanosheets are seldom broken during the delamination process.

Defect-free, thin ilerite films were obtained with doctor blading of a nematic nanosheet dispersion onto polyethylene terephthalate (PET) substrates (Fig. 3A). The casted film is optically clear, rendering it suitable for packaging of optoelectronic devices. EDX mapping of a film cross section shows the ilerite coating of $\approx 1.5 \mu\text{m}$ on the PET substrate (Fig. 3B and fig. S8). The high stacking order along the c axis of the nanosheets of the textured films is confirmed in the PXRD pattern, giving a basal spacing of 13.8 Å (Fig. 3C and fig. S9). Barrier performance of the coating was tested for H_2O , O_2 , and He gases at a high relative humidity (r.h.) of 75% and 23°C for an ilerite

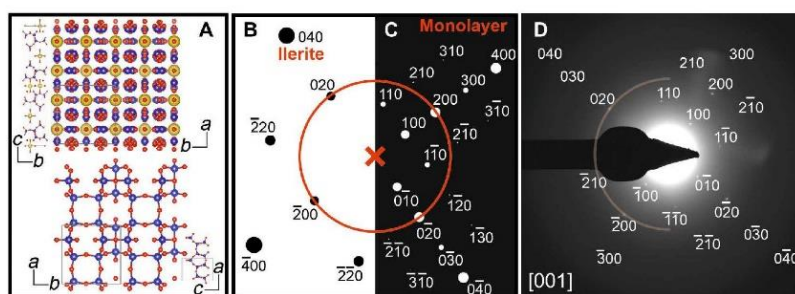


Fig. 2. ED analysis of ilerite nanosheets. (A) Structure of crystalline ilerite (top) and of a single layer (bottom) each displayed in two different orientations. (B) Simulated diffraction pattern of 3D crystalline ilerite compared to (C) a simulated diffraction pattern of a single-layer nanosheet of ilerite without Na⁺ counter cations, both viewed perpendicular to the layer(s). Red circle marks the (200) reflection (i.e., 3.66-Å d -spacing) for comparison. (D) Experimental nanobeam ED pattern, with observed reflections, i.e., at 7.32 and 5.18 Å, corresponding to the reflections (100) and (110) in the simulated pattern of a single-layer ilerite. These reflections are absent with the centrosymmetric stacking of bulk ilerite. Width of diffraction patterns (B to D) is 10.17 nm^{-1} at 200 kV.

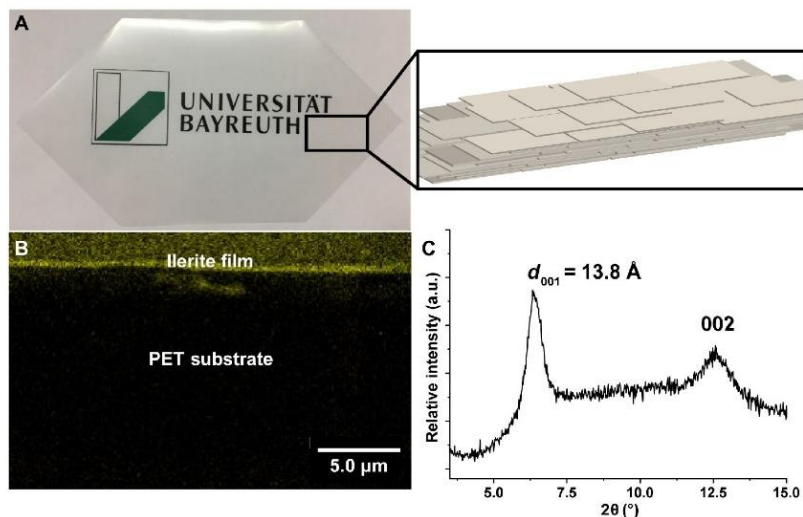


Fig. 3. Casting of thin zeolite films. (A) Doctor-bladed thin and clear ilerite film on a PET substrate, formed by overlapping, self-assembled coplanar ilerite nanosheets as schematically shown in the inset. (B) SEM image of a cross section of the film (1.5-µm thickness) with element mapping of Si. (C) Upon self-assembly, a 1D crystalline monodomain is obtained with a basal spacing of 13.8 Å as determined by PXRD.

film dried at 100°C. The water vapor transmission rate was below the detection limit ($<0.05 \text{ g m}^{-2} \text{ day}^{-1}$). For O_2 and He, transmission rates of 0.017 and $3.1 \text{ cm}^3 \text{ m}^{-2} \text{ day}^{-1} \text{ atm}^{-1}$, respectively, were observed. Compared to the ilerite-coated substrate, the neat PET substrate shows a water vapor transmission rate of $4.42 \text{ g m}^{-2} \text{ day}^{-1}$ and O_2 and He transmission rates of 31.9 and $1740 \text{ cm}^3 \text{ m}^{-2} \text{ day}^{-1} \text{ atm}^{-1}$ (below 10% r.h.), respectively, confirming an excellent barrier performance of the inorganic film.

In conclusion, by establishing appropriate conditions for repulsive osmotic swelling, an environmentally friendly, water-born, and scalable process is introduced, producing functional zeolite-like nanosheets with 100% yield and a huge aspect ratio of ≈ 9000 . By simple ion exchange of the layered parent zeolite-like layered silicate ilerite with an affordable, bulky amino sugar meglumine, nanosheets can be obtained quantitatively. The gentle nature of repulsive osmotic swelling preserves the lateral extensions of the parent crystal, as well as the crystal structure of single layers. Microporous, high-aspect ratio nanosheets are obtained that carry silanol groups on the basal surface allowing for further functionalization in future work. This makes ilerite nanosheets a highly promising material for various applications ranging from gas barrier applications to materials for permselective hydrogen membranes.

The process of repulsive osmotic swelling should generally work for charged layered compounds. Onset of repulsive osmotic swelling is triggered by the contribution of interlayer species to translational entropy and requires the interlayer gallery to be enlarged beyond a sufficient threshold. In most cases, solvation enthalpy is not sufficient to achieve this but needs to be supplemented by steric stress exerted by bulky interlayer cations. As layered zeolites carry acidic groups on the basal surfaces, the charge density is, however, dependent on the pH of the dispersion medium. The lower the pH, the lower the charge density will be and the bulkier the interlayer cation has to be to exert internal pressure. If amines are applied as interlayer cations, then the pH moreover is coupled to the pK_a value. As

zeolites have a stability window in respect to low and high pH, identification of appropriate conditions for repulsive delamination might, in practice, turn out to be troublesome and require adjustment for every zeolite candidate. Last, materials to be delaminated must be truly 2D. Intergrown or self-intercalated structures will not work.

MATERIALS AND METHODS

Synthesis methods

Synthesis of ilerite

Ilerite was synthesized by applying a published procedure (40, 41). Briefly, NaOH pellets ($\geq 98\%$, Sigma-Aldrich) were dissolved in deionized water and added to colloidal SiO_2 (30 wt %, Köstrosol 1030 KD) under vigorous stirring, giving a molar $\text{Na}_2\text{O}:\text{SiO}_2:\text{H}_2\text{O}$ ratio of 1:4:37. Typically, 99.85-g NaOH pellets ($\geq 98\%$, Sigma Aldrich) were dissolved in 131.95-g deionized water and then added to 1000-g colloidal SiO_2 . The layered zeolite was obtained after synthesis under hydrothermal conditions at 100°C for 4 weeks in a closed crucible. Ilerite was obtained in the form of a gel, washed with deionized water, and lastly dried in air.

Preparation of the colloidal dispersion

For preparation of the colloidal dispersion, ilerite was treated with an aqueous solution of meglumine (*N*-methyl-*D*-glucamine, $>99.0\%$, Sigma-Aldrich). Before the treatment, meglumine was dissolved in deionized water, titrated to a pH of approximately 9 using HCl (32 wt %), and dissolved with purified water to yield a 1 M solution. Typically, 500 mg of the dried ilerite was suspended in 40 ml of a 1 M solution of meglumine, corresponding to a 28-fold excess of the cation exchange capacity (theoretically 284 meq/100 g). This treatment was repeated five times. The treated ilerite was separated from the liquid by centrifugation (10,000g, 10 min), and the supernatant solution was discarded and replaced by fresh 1 M solution of meglumine. Separation during the washing was performed by centrifugation (12,000g, 30 min). The obtained treated ilerite was washed with

deionized water to reduce the ionic strength, allowing the delamination into a delaminated layered zeolite dispersion as a gel.

Preparation of zeolite thin films

A layered zeolite dispersion, prepared as described above, was diluted to a concentration of approximately 2 wt %. Thin films of layered zeolite nanosheets were prepared by doctor blading on a PET foil using an automated device (Zehntner ZAA 2300, Zehntner GmbH Testing Instruments, Switzerland), followed by drying at 100°C in air.

Characterization

Powder X-ray diffraction

PXRD patterns were recorded in sealed glass capillaries on a STOE Stadi P powder diffractometer equipped with a MYTHENIK detector using Cu K α_1 radiation (1.5406 Å). Textured samples were measured in Bragg-Brentano geometry on a PANalytical Empyrean diffractometer with Cu K α_1 radiation ($\lambda = 1.5406$ Å) equipped with a PixCellD-Medipix3 detector.

Small-angle X-ray scattering

SAXS data of the gels were measured using a “Double Ganesha AIR” (SAXSLAB, Denmark). The X-ray source of this laboratory-based system is a rotating copper anode (MicroMax 007HF, Rigaku Corporation, Japan) providing a microfocussed beam. The data were recorded by a position sensitive detector (PILATUS 300 K, Dectris). Samples of the treated layered zeolite were prepared by washing the meglumine-treated ilerite with a diluted aqueous solution of meglumine (0.05 M, pH 9) three times. The swelling experiment was conducted upon addition of a defined amount of ultrapure water to the highly concentrated gel. SAXS pattern is recorded after equilibration for 1 day in 1-mm glass capillaries. The circularly averaged data are normalized to incident beam, sample thickness, and measurement time. Background subtraction was performed by using the SAXS pattern of a water-filled capillary. Fitting of the scattering curve was performed by using the program scatter (version 2.5).

Atomic force microscopy

AFM was performed on a Bruker Dimension Icon, equipped with a NanoScope V controller. A ScanAsyst-Air silicon nitride tip (Bruker) was used in PeakForce mode. Samples were prepared by dropping a dilute aqueous dispersion (5 mg/liter) in Millipore water onto silicon wafers. The silicon wafers were cleaned with a snow jet, silylated with 3-(ethoxydimethylsilyl)propylamine via gas phase overnight and rinsed with ultrapure water prior application of the samples. The images were analyzed with a NanoScope Analysis 1.8 software.

Transmission electron microscopy

The samples for the electron microscopic characterization were prepared by dissolution in water, mixed thoroughly, and deposited on holey-carbon gold grids (Quantifoil Au 1.2-1.3). The prepared samples were then characterized in a transmission electron microscope (TEM) Titan 80-300 operated at 200 kV. The model structure of ilerite (37) was delaminated manually using the VESTA software (43). ED simulation was made using the software ReciPro taking kinematical and excitation error for intensity calculation.

Scanning electron microscopy and EDX spectroscopy

Scanning electron microscope images were recorded on a Zeiss 1530. Completeness of the ion exchange was checked with EDX on a Zeiss 1530 equipped with an EDX INCA 400 unit (Oxford) and a detection limit of 1 atomic %.

CHN analysis

An Elementar Unicode equipped with a combustion tube filled with tungsten (VI) oxide granules was used at a combustion temperature

of 1050°C. Before the measurement, the delaminated gel of ilerite was freeze-dried, followed by drying at 80°C.

Gas permeation test

Oxygen transmission rates were determined applying a Mocon OX-TRAN 2/21 M10x instrument with a lower detection limit of 0.0005 cm³ m⁻² day⁻¹ atm⁻¹. A mixture of 95% N₂ and 5% H₂ was used as carrier gas, and pure O₂ (>99.95%, Linde Sauerstoff 3.5) was used as permeate gas. The measurement was conducted at 23°C and 75% r.h. Water vapor transmission rates were measured on a Mocon PERMATRAN-W Model 3/33 with a lower detection limit of 0.05 g m⁻² day⁻¹ at 23°C and 75% r.h. Helium transmission rates were measured applying the pressure difference method with a gas transmission tester of Brügger Feinmechanik GmbH and a measurement limit of 0.5 cm³ m⁻² day⁻¹ atm⁻¹.

SUPPLEMENTARY MATERIALS

Supplementary material for this article is available at <https://science.org/doi/10.1126/sciadv.abn9084>

REFERENCES AND NOTES

- D. D. L. Chung, Review graphite. *J. Mater. Sci.* **37**, 1475–1489 (2002).
- E. Paineau, I. Bihannic, C. Baravian, A.-M. Philippe, P. Davidson, P. Levitz, S. S. Funari, C. Rochas, L. J. Michot, Aqueous suspensions of natural swelling clay minerals. 1. Structure and electrostatic interactions. *Langmuir* **27**, 5562–5573 (2011).
- M. Chhowalla, H. S. Shin, G. Eda, L. J. Li, K. P. Loh, H. Zhang, The chemistry of two-dimensional layered transition metal dichalcogenide nanosheets. *Nat. Chem.* **5**, 263–275 (2013).
- T. Tanaka, Y. Ebina, K. Takada, K. Kurashima, T. Sasaki, Oversized titania nanosheet crystallites derived from flux-grown layered titanate single crystals. *Chem. Mater.* **15**, 3564–3568 (2003).
- W. Yang, S. Yamamoto, K. Sueyoshi, T. Inadomi, R. Kato, N. Miyamoto, Perovskite nanosheet hydrogels with mechanochromic structural color. *Angew. Chem. Int. Ed.* **60**, 8466–8471 (2021).
- Y. Song, N. Iyi, T. Hoshide, T. C. Ozawa, Y. Ebina, R. Ma, S. Yamamoto, N. Miyamoto, T. Sasaki, Massive hydration-driven swelling of layered perovskite niobate crystals in aqueous solutions of organo-ammonium bases. *Dalton Trans.* **47**, 3022–3028 (2018).
- J. Zhao, L. Zhao, N. Dimov, S. Okada, T. Nishida, Electrochemical and thermal properties of α -NaFeO₂ Cathode for Na-Ion batteries. *J. Electrochem. Soc.* **160**, A3077–A3081 (2013).
- J. N. Coleman, M. Lotya, A. O'Neill, S. D. Bergin, P. J. King, U. Khan, K. Young, A. Gaucher, S. De, R. J. Smith, I. V. Shvets, S. K. Arora, G. Stanton, H.-Y. Kim, K. Lee, G. T. Kim, G. S. Duesberg, T. Hallam, J. J. Boland, J. J. Wang, J. F. Donegan, J. C. Grunlan, G. Moriarty, A. Shmeliov, R. J. Nicholls, J. M. Perkins, E. M. Grieveson, K. Theuvsissen, D. W. McComb, P. D. Nellist, V. Nicolosi, Two-dimensional nanosheets produced by liquid exfoliation of layered materials. *Science* **331**, 568–571 (2011).
- V. Nicolosi, M. Chhowalla, M. G. Kanatzidis, M. S. Strano, J. N. Coleman, Liquid exfoliation of layered materials. *Science* **340**, 1226419 (2013).
- R. J. Smith, P. J. King, M. Lotya, C. Wirtz, U. Khan, S. De, A. O'Neill, G. S. Duesberg, J. C. Grunlan, G. Moriarty, J. Chen, J. Wang, A. I. Minett, V. Nicolosi, J. N. Coleman, Large-scale exfoliation of inorganic layered compounds in aqueous surfactant solutions. *Adv. Mater.* **23**, 3944–3948 (2011).
- A. K. Geim, I. V. Grigorieva, Van der Waals heterostructures. *Nature* **499**, 419–425 (2013).
- M. Dakhchoune, L. F. Villalobos, R. Semino, L. Liu, M. Rezaei, P. Schouwink, C. E. Avalos, P. Baade, V. Wood, Y. Han, M. Ceriotti, K. V. Agrawal, Gas-sieving zeolitic membranes fabricated by condensation of precursor nanosheets. *Nat. Mater.* **20**, 362–369 (2020).
- F. Ding, J. Liu, S. Zeng, Y. Xia, K. M. Wells, M.-P. Nieh, L. Sun, Biomimetic nanocoatings with exceptional mechanical, barrier, and flame-retardant properties from large-scale one-step coassembly. *Sci. Adv.* **3**, e1701212 (2017).
- J. E. F. C. Gardolinski, G. Lagaly, Grafted organic derivatives of kaolinite: II. Intercalation of primary n-alkylamines and delamination. *Clay Miner.* **40**, 547–556 (2005).
- T. Sasaki, M. Watanabe, Osmotic swelling to exfoliation. Exceptionally high degrees of hydration of a layered titanate. *J. Am. Chem. Soc.* **120**, 4682–4689 (1998).
- F. Geng, R. Ma, Y. Ebina, Y. Yamauchi, N. Miyamoto, T. Sasaki, Gigantic swelling of inorganic layered materials: A bridge to molecularly thin two-dimensional nanosheets. *J. Am. Chem. Soc.* **136**, 5491–5500 (2014).
- J.-C. P. Gabriel, F. Cemerel, B. J. Lemaire, H. Desvaux, P. Davidson, P. Batall, Swollen liquid-crystalline lamellar phase based on extended solid-like sheets. *Nature* **413**, 504–508 (2001).

18. Y. Omomo, T. Sasaki, L. Wang, M. Watanabe, Redoxable nanosheet crystallites of MnO₂ derived via delamination of a layered manganese oxide. *J. Am. Chem. Soc.* **125**, 3568–3575 (2003).
19. K. Fukuda, K. Akatsuka, Y. Ebina, R. Ma, K. Takada, I. Nakai, T. Sasaki, Exfoliated nanosheet crystallite of cesium tungstate with 2D pyrochlore structure: Synthesis, characterization, and photochromic properties. *ACS Nano* **2**, 1689–1695 (2008).
20. G. F. Walker, Macroscopic swelling of vermiculite crystals in water. *Nature* **187**, 312–313 (1960).
21. S. Rosenfeldt, M. Stöter, M. Schlenk, T. Martin, R. Q. Albuquerque, S. Förster, J. Breu, In-depth insights into the key steps of delamination of charged 2D nanomaterials. *Langmuir* **32**, 10582–10588 (2016).
22. P. Davidson, C. Penisson, D. Constantin, J. P. Gabriel, Isotropic, nematic, and lamellar phases in colloidal suspensions of nanosheets. *Proc. Natl. Acad. Sci. U.S.A.* **115**, 6662–6667 (2018).
23. M. Daab, N. J. Eichstaedt, C. Habel, S. Rosenfeldt, H. Kalo, H. Schießling, S. Förster, J. Breu, Onset of osmotic swelling in highly charged clay minerals. *Langmuir* **34**, 8215–8222 (2018).
24. K. Sano, Y. S. Kim, Y. Ishida, Y. Ebina, T. Sasaki, T. Hikima, T. Aida, Photonic water dynamically responsive to external stimuli. *Nat. Commun.* **7**, 12559 (2016).
25. M. Daab, N. J. Eichstaedt, A. Edenharter, S. Rosenfeldt, J. Breu, Layer charge robust delamination of organo-clays. *RSC Adv.* **8**, 28797–28803 (2018).
26. K. Varoon, X. Zhang, B. Elyassi, D. D. Brewer, M. Gettel, S. Kumar, J. A. Lee, S. Maheshwari, A. Mittal, C.-y. Sung, M. Cococcioni, L. F. Francis, A. V. McCormick, K. A. Mkhoyan, M. Tsapatsis, Dispersible exfoliated zeolite nanosheets and their application as a selective membrane. *Science* **334**, 72–75 (2011).
27. W. J. Roth, T. Sasaki, K. Wolski, Y. Song, D.-M. Tang, Y. Ebina, R. Ma, J. Grzybek, K. Kalahurska, B. Gil, M. Mazur, S. Zapotoczny, J. Cejka, Liquid dispersions of zeolite monolayers with catalytic activity prepared by soft-chemical exfoliation. *Sci. Adv.* **6**, eaay8163 (2020).
28. K. V. Agrawal, B. Topuz, T. C. Pham, T. H. Nguyen, N. Sauer, N. Rangnekar, H. Zhang, K. Narasimharao, S. N. Basahel, L. F. Francis, C. W. Macosko, S. Al-Thabaiti, M. Tsapatsis, K. B. Yoon, Oriented MFI membranes by Gel-Less secondary growth of sub-100 nm MFI-nanosheet seed layers. *Adv. Mater.* **27**, 3243–3249 (2015).
29. M. Choi, K. Na, J. Kim, Y. Sakamoto, O. Terasaki, R. Ryoo, Stable single-unit-cell nanosheets of zeolite MFI as active and long-lived catalysts. *Nature* **461**, 246–249 (2009).
30. T. Maluangnont, Y. Yamauchi, T. Sasaki, W. J. Roth, J. Cejka, M. Kubu, The aqueous colloidal suspension of ultrathin 2D MCM-22P crystallites. *Chem. Commun.* **50**, 7378–7381 (2014).
31. W. J. Roth, T. Sasaki, K. Wolski, Y. Ebina, D. M. Tang, Y. Michiue, N. Sakai, R. Ma, O. Cretu, J. Kikkawa, K. Kimoto, K. Kalahurska, B. Gil, M. Mazur, S. Zapotoczny, J. Cejka, J. Grzybek, A. Kowalczyk, Exfoliated ferrierite-related unilamellar nanosheets in solution and their use for preparation of mixed zeolite hierarchical structures. *J. Am. Chem. Soc.* **143**, 11052–11062 (2021).
32. M. Stöter, D. A. Kunz, M. Schmidt, D. Hirsemann, H. Kalo, B. Putz, J. Senker, J. Breu, Nanoplatelets of sodium hectorite showing aspect ratios of $\approx 20,000$ and superior purity. *Langmuir* **29**, 1280–1285 (2013).
33. R. Ma, T. Sasaki, Nanosheets of oxides and hydroxides: Ultimate 2D charge-bearing functional crystallites. *Adv. Mater.* **22**, 5082–5104 (2010).
34. L. Wang, T. Sasaki, Titanium oxide nanosheets: Graphene analogues with versatile functionalities. *Chem. Rev.* **114**, 9455–9486 (2014).
35. W. J. Roth, O. V. Shvets, M. Shamzhy, P. Chlubná, M. Kubu, P. Nachtigall, J. Cejka, Postsynthesis transformation of three-dimensional framework into a lamellar zeolite with modifiable architecture. *J. Am. Chem. Soc.* **133**, 6130–6133 (2011).
36. W. J. Roth, B. Gil, W. Makowski, B. Marszałek, P. Eliášová, Layer like porous materials with hierarchical structure. *Chem. Soc. Rev.* **45**, 3400–3438 (2016).
37. S. Vortmann, J. Rius, S. Siegmann, H. Gies, Ab initio structure solution from X-ray powder data at moderate resolution: Crystal structure of a microporous layer silicate. *J. Phys. Chem. B* **101**, 1292–1297 (1997).
38. B. Gil, W. Makowski, B. Marszałek, W. J. Roth, M. Kubu, J. Cejka, Z. Olejniczak, High acidity unilamellar zeolite MCM-56 and its pillared and delaminated derivatives. *Dalton Trans.* **43**, 10501–10511 (2014).
39. V. V. Narkhede, H. Gies, Crystal structure of MCM-22 (MWW) and its delaminated zeolite ITQ-2 from high-resolution powder x-ray diffraction data: An analysis using rietveld technique and atomic pair distribution function. *Chem. Mater.* **21**, 4339–4346 (2009).
40. G. Borbély, H. K. Beyer, H. G. Karge, W. Schwieger, A. Brandt, K. H. Bergk, Chemical characterization, structural features, and thermal behavior of sodium and hydrogen octosilicate. *Clays Clay Miner.* **39**, 490–497 (1991).
41. W. Schwieger, K.-H. Bergk, Dehydrierung und hydrogenolyse an Metallpolysilicathydraten. *Z. Chem.* **25**, 228–230 (1985).
42. P. Loch, T. Martin, M. Grüner, G. Kaupp, W. Schwieger, J. Breu, Synthesis of large platelets of egyptian blue via pseudomorphosis after NaRUB-18. *Z. anorg. allg. Chem.* **646**, 1570–1574 (2020).
43. K. Momma, F. Izumi, VESTA 3 for three-dimensional visualization of crystal, volumetric and morphology data. *J. Appl. Cryst.* **44**, 1272–1276 (2011).

Acknowledgments: We appreciate the support of the Keylab for Optical and Electron Microscopy of the Bavarian Polymer Institute and for providing access to SAXS facilities within the Keylab Mesoscale Characterization: Scattering Techniques. We thank M. Schwarzmann and U. Mansfeld for collecting EDX spectra and SEM images. O. Khoruzhenko is acknowledged for the graphic design and R. Timmins for English proofreading. We thank X. Duan and K.-V. Agrawal for fruitful discussion on membranes. **Funding:** G.A.-S. acknowledges funding support of the Deutsche Forschungsgemeinschaft (DFG; German Research Foundation) (Projektnummer: 451037016) (PREGRAM). P.L. thanks Elite Network Bavaria in the framework of the Elite Study Program “Macromolecular Science” for support. This work was funded by the Deutsche Forschungsgemeinschaft (DFG; German Research Foundation) (491183248) and by the Open Access Publishing Fund of the University of Bayreuth. **Author contributions:** J.B. conceived and supervised the research. P.L. conceived the research and established the synthesis and delamination. W.S. gave valuable assistance with synthesis. D.S. casted barrier films and measured transmission rates. G.A.-S. and T.L. took TEM images and ED patterns. P.M., K.O., and G.P. performed and interpreted AFM images. S.R. measured and fitted the SAXS data. P.L., D.S., G.A.-S., and J.B. wrote the manuscript. All authors discussed the results and commented on the manuscript. **Competing interests:** P.L. and J.B. have applied for a patent (application number EP20205796.4) entitled “Process for delamination of layered zeolite, a delaminated layered zeolite dispersion and use thereof.” The authors declare that they have no other competing interests. **Data and materials availability:** All data needed to evaluate the conclusions in the paper are present in the paper and/or the Supplementary Materials.

Submitted 29 December 2021

Accepted 1 April 2022

Published 18 May 2022

10.1126/sciadv.abn9084

6.3.2. Supporting Information

Science Advances
AAAS

Supplementary Materials for

Nematic suspension of a microporous layered silicate obtained by forceless spontaneous delamination via repulsive osmotic swelling for casting high-barrier all-inorganic films

Patrick Loch, Dominik Schuchardt, Gerardo Algara-Siller, Paul Markus, Katharina Ottermann, Sabine Rosenfeldt, Thomas Lunkenbein, Wilhelm Schwieger, Georg Papastavrou, Josef Breu*

*Corresponding author. Email: josef.breu@uni-bayreuth.de

Published 18 May 2022, *Sci. Adv.* **8**, eabn9084 (2022)
DOI: 10.1126/sciadv.abn9084

This PDF file includes:

Figs. S1 to S9
Tables S1 and S2

Results

Supplementary Materials

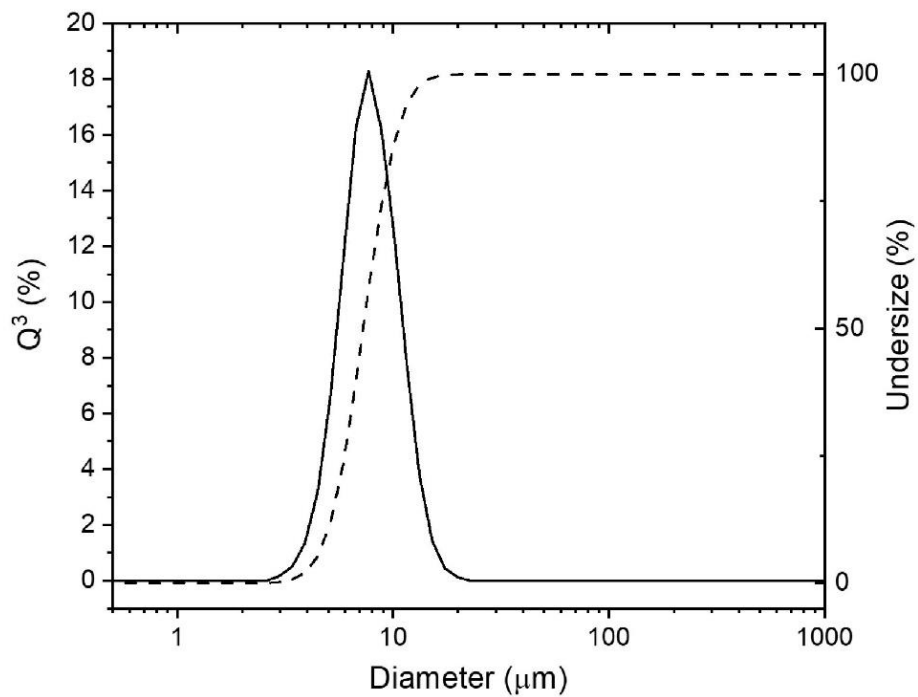


Fig. S1. Particle size distribution of as synthesized Ilerrite, determined with static light scattering (SLS).

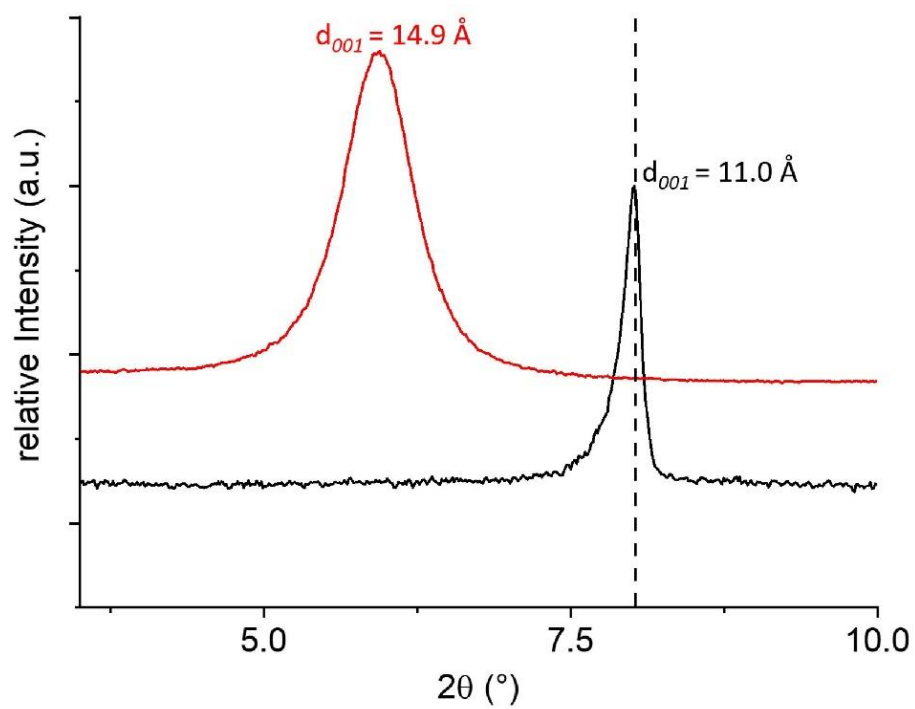


Fig. S2. Powder X-ray diffraction pattern of textured samples of as synthesized Ilerite (black) and meglu-Ilerite (red), dried over night at 80°C.

Results

Table S1: EDX analysis of meglu-Ilerite to confirm completeness of Na⁺-exchange.

Point	O (atom%)	Na (atom%)	Si (atom%)
1	63.6	0.0	23.6
2	53.8	0.0	39.4
3	57.9	0.0	35.2
4	50.8	0.0	40.4
5	54.2	0.0	39.5

Calculation of equivalent area at pH 9:

The charge equivalent area of Ilerite was calculated, using the carbon content determined with CHN-analysis. At pH 9 of the exchange solution, 18.2 wt% carbon was found for dried meglu-Ilerite. The carbon content was converted into the CEC (cation exchange capacity) in mmol/g using the molar mass of carbon (12.011 g/mol), the number of carbon atoms in meglumine ($n = 7$), and the mass of dried meglu-Ilerite used for CHN-analysis ($m = 1.86$ mg):

$$CEC_{megl\text{-}Ilerite} = \frac{wt\% \text{ carbon}}{n \cdot 12.011 \text{ g/mol} \cdot 100}$$

This gives a CEC for intercalated meglumine of 2.16 mmol/g. For pristine Ilerite with a well-known chemical composition and crystal structure, a CEC of 2.83 mmol/g and a charge equivalent $A_{Ilerite}$ area of $54 \text{ \AA}^2/\text{charge}$ can be found, calculated from the unit cell and composition of Ilerite. Using the known parameter of pristine Ilerite, the charge equivalent area of meglu-Ilerite $A_{megl\text{-}Ilerite}$ can be calculated:

$$A_{megl\text{-}Ilerite} = \frac{CEC_{megl\text{-}Ilerite}}{CEC_{Ilerite}} \cdot A_{Ilerite}$$

This results in a charge equivalent area for meglu-Ilerite at pH 9 of $70 \text{ \AA}^2/\text{charge}$, which is higher compared to pristine Ilerite.

Results

Table S2: Charge equivalent areas of selected organo cations.

Organo cation	$A_{\text{organo cation}} (\text{\AA}^2/\text{charge})$
tetrabutylammonium hydroxide (TBAOH)	90
2-ammonium-2-(hydroxymethyl)-1,3-propanediol (TRIS)	37
cyclohexylammonium	40
piperidine	34
2-(trimethylammonium)ethyl methacrylate (TMAEMA)	60
4-(dimethylammonium)pyridine (DMAP)	47
meglumine	77

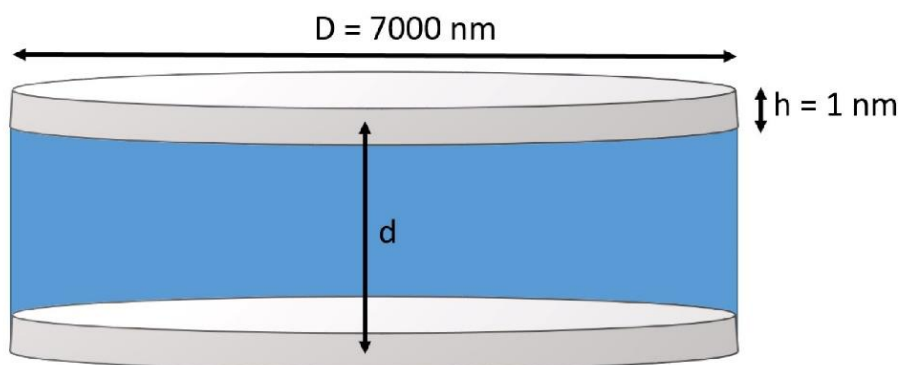


Fig. S3. Fitting model used to calculate the basal spacing d from the SAXS pattern, assuming a layer thickness of 1 nm and a nanosheet diameter of 7000 nm.

Results

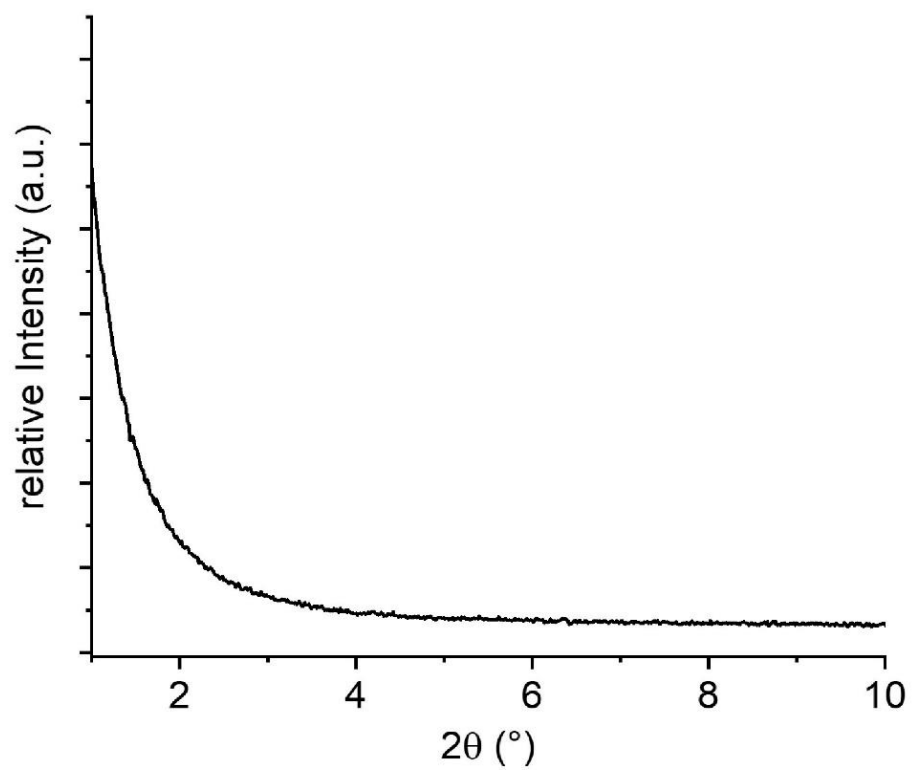


Fig. S4. PXRD pattern in transmission mode of a highly concentrated nanosheet dispersion.

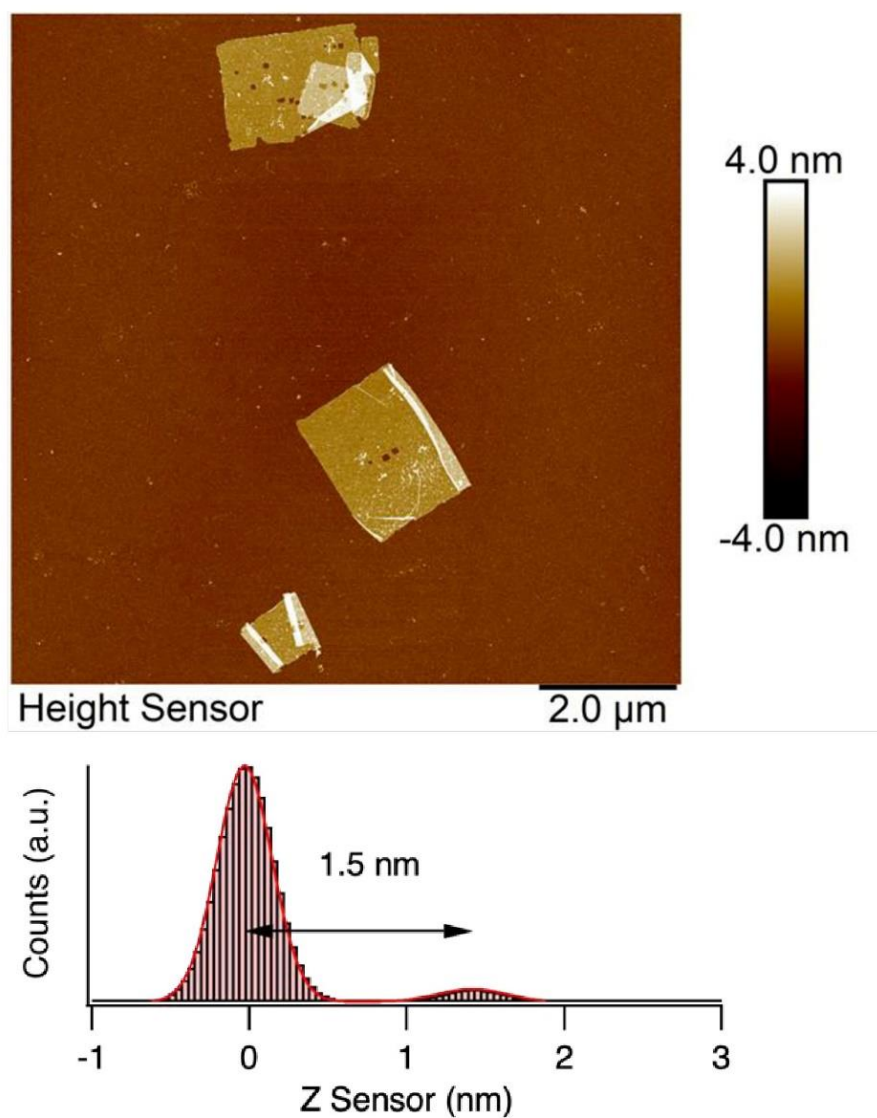


Fig. S5. AFM overview of delaminated Ilerite nanosheets. Overview of a large area showing only single Ilerite nanosheets of 1.5 nm thickness. The histogram below provides a bimodal Gaussian distribution with two distinct heights and the resulting thickness of the nanosheets is highlighted.

Results

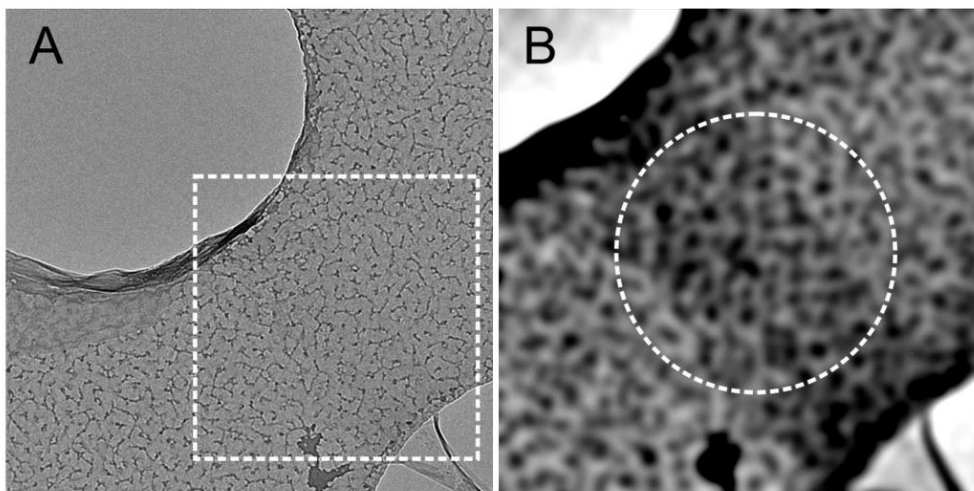


Fig. S6. TEM image of the single layer on a holey carbon mesh. (A) Original image showing the spot where the single layer is located. Due to the very low contrast of a single layer Ierite nanosheet on top of the holey carbon mesh the area marked by a white rectangle in the original image was cropped and the contrast was enhanced to be able to visualize the nanosheet (B). The dashed circle marks the approximate size of nanobeam applied to obtain the electron diffraction pattern shown in Fig. 2D.

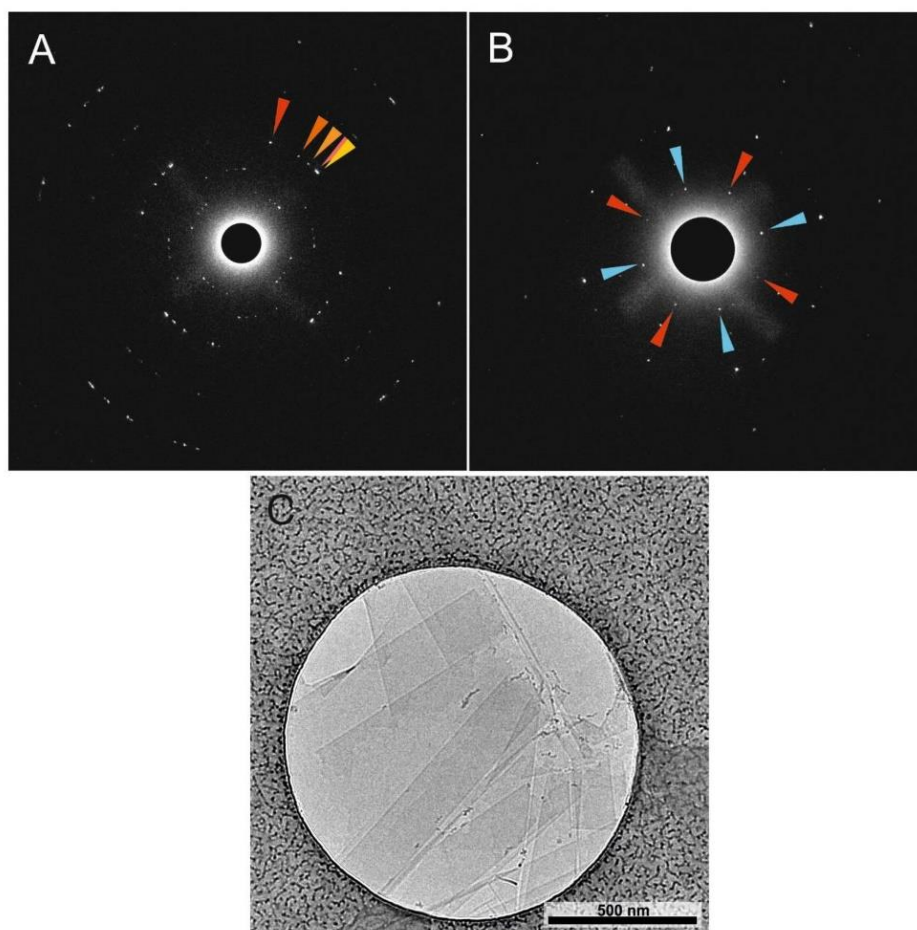


Fig. S7. Electron diffraction analysis of turbostratic restacked Ilerrite nanosheets. (A) Electron diffraction patterns of turbostratic stacked single layer Ilerrite of 5 different stacking orientations and (B) of 2 stacked layers misoriented by 41.4 degrees. Marked reflections in (A) correspond to a d-spacing of 3.6 Å, while marked reflections in (B) correspond to a d-spacing of 7.3 Å (C) TEM image of stacked single layers. Contrast increment makes the disordered layer-by-layer stacking of single layers visible.

Results

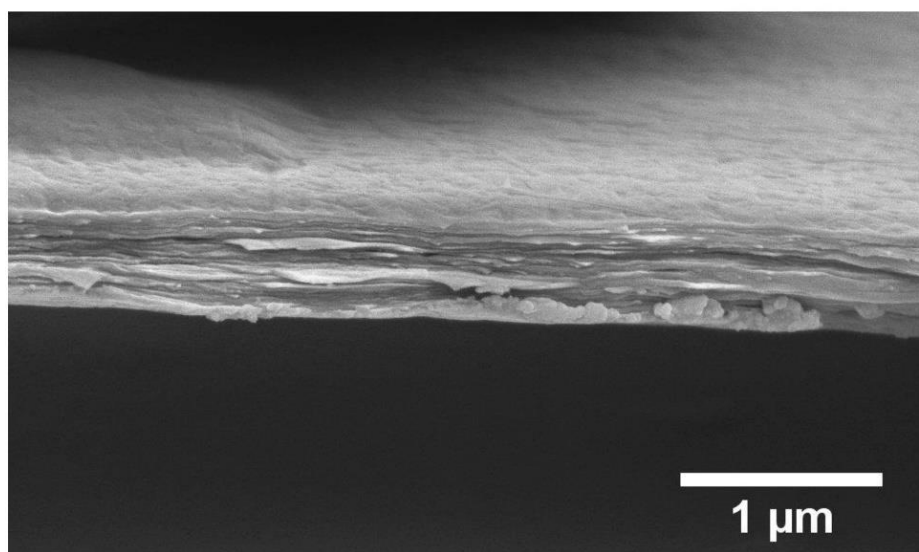


Fig. S8. SEM cross section of a casted Ilerite film.

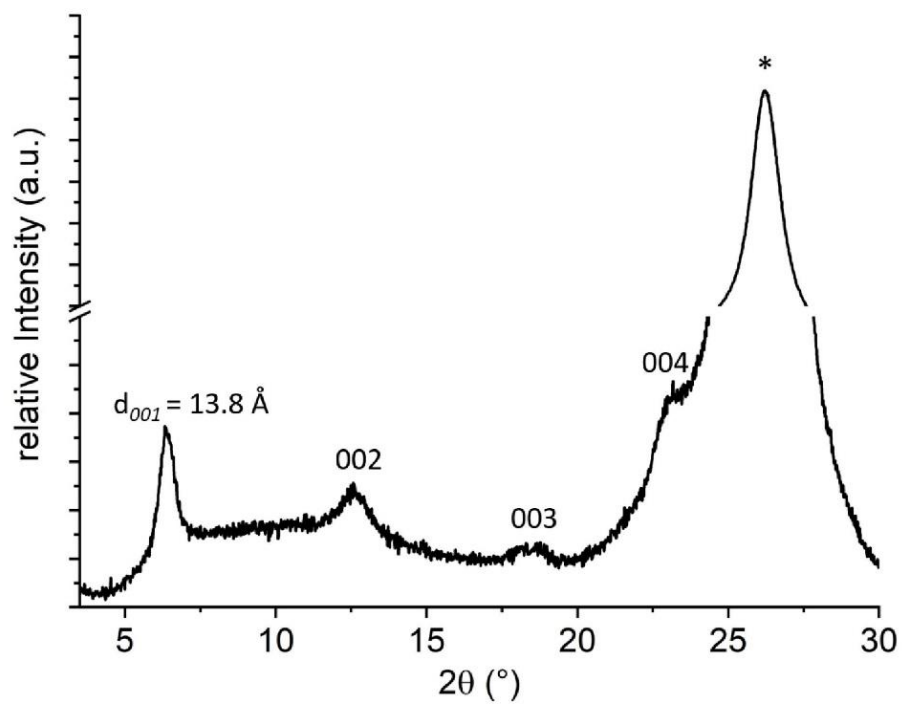


Fig. S9. PXRD pattern of casted ordered 1D crystalline Ilerite films. Doctor bladed of Ilerite nanosheets results in a 1D crystalline monodomain Ilerite film with a $00l$ series and a basal spacing of 13.8 \AA . The asterisk marks the reflection of the PET substrate.

Results

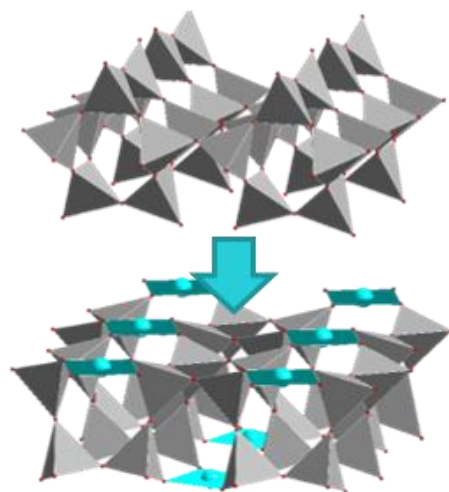
6.4. Egyptian blue as colored substrates for pearlescent pigments

Patrick Loch^a, Thomas Martin^a, Michael Grüner^b, Günther Kaupp^b, Wilhelm Schwieger^c and Josef Brey^{a, *}

Synthesis of Large Platelets of Egyptian Blue via Pseudomorphosis after NaRUB-18

Published in: *Zeitschrift für anorganische und allgemeine Chemie* **2020**, 646, 1570-1574.

Reproduced under the terms of the CC-BY 4.0 license.



^a Bavarian Polymer Institute and Department of Chemistry, University of Bayreuth, Universitätsstraße 30, 95440 Bayreuth, Germany

^b Eckart GmbH ALTANA AG, Günthersthal 4, 91235, Germany

^c Institute of Chemical Reaction Engineering, Friedrich-Alexander University Erlangen-Nürnberg, Egerlandstraße 3, 91058 Erlangen, Germany

* Corresponding author

Individual Contribution:

This publication was a result of a collaboration with the Eckart GmbH, a member of the ALTANA AG. Prof. J. Brey and I developed the concept of this publication. I did all the experimental work and analyzed the material (except Rietveld refinement). T. Martin conducted the Rietveld refinement. All authors contributed to scientific discussion. Prof. J. Brey and I wrote the manuscript.

My contribution to the publication is approx. 90 %

6.4.1. Synthesis of Large Platelets of Egyptian Blue via Pseudomorphosis after NaRUB-18

Journal of Inorganic and General Chemistry

ZAAC

Zeitschrift für anorganische und allgemeine Chemie

DOI: 10.1002/zaac.202000203

ARTICLE

Synthesis of Large Platelets of Egyptian Blue via Pseudomorphosis after NaRUB-18

Patrick Loch,^[a] Thomas Martin,^[a] Michael Grüner,^[b] Günther Kaupp,^[b] Wilhelm Schwieger,^[c] and Josef Breu^{*[a]}*Dedicated to Prof. Dr. Bernd Harbrecht on Occasion of his 70th Birthday*

Abstract. A colored platy substrate with appreciable aspect ratio can improve the hiding power while extending the color range of pearlescent pigments. One of the oldest synthetic pigments, Egyptian blue, possesses a layered structure and a platy morphology, making it a promising colored substrate for pearlescent pigments, which derives its blue color from Cu^{II} . Unfortunately, existing synthesis routes are

either not technically benign or lack the natural platy morphology. Here, we introduce a new synthesis route starting with large, square-shaped platelets of a synthetic layered sodium silicate (NaRUB-18). As evidenced by Rietveld refinement and scanning electron microscopy, NaRUB-18 can be converted with conservation of this attractive morphology (pseudomorphosis) into Egyptian blue.

Introduction

Pearlescent pigments draw their attractiveness from a combination of lustrous appearance and color, leading to their widespread application ranging from automotive paints to cosmetics. The colors originate from interference of a strongly refractive coating on top of a weakly refractive layered substrate. The aspect ratio of the platy substrate is responsible for the texture, which is essential for the pearlescent effect and the glossy appearance.^[1] The accessible color range is limited and may be extended by applying colorants on top of the coating, which, however, reduces the pearlescent effect. Colored substrates, in particular bright blue platelets, represent a technically interesting alternative and are therefore highly sought after. Thus, this work focuses on a particular platy pigment and not on blue pigments as Cu phthalocyanine in general.

One of the first synthetic blue pigments, Egyptian blue, has been fabricated in Egypt as early as in 3600 B.C.^[2] The structure of Egyptian blue ($\text{CaCuSi}_4\text{O}_{10}$) has been solved by *Pabst* in 1959^[3] and was later refined using neutron scattering.^[4] The structure consists of corner sharing Si_4O_{10} rings, which in turn

are connected to corrugated layers (Figure 1B). Cu^{II} resides in a square-planar coordination provided by non-bridging oxygen atoms of the SiO_4 tetrahedra and is responsible for the blue color. The silicate layers carry a negative charge, which is compensated by Ca^{II} in the interlayer space.^[3,4] The layered structure is reflected in a platy morphology with atomically flat surfaces, rendering Egyptian blue a potentially interesting colored substrate for pearlescent pigments.^[1a]

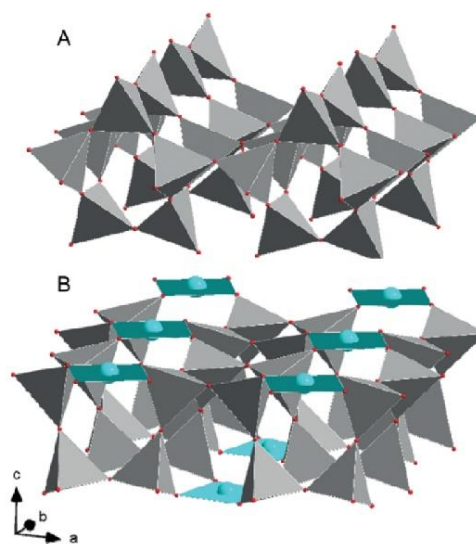


Figure 1. Comparison of NaRUB-18 layers (A) with SiO_4 tetrahedra building a layered structure formed by channels formed with $[\text{Si}_4]^{4-}$ cages, linked through a four-membered ring, whereas the Egyptian blue layers (B) shows corrugated layers of corner shared SiO_4 -tetrahedra, Cu^{II} is located in square-planar coordination, formed by unsaturated Si–O bonds.

* Prof. Dr. J. Breu

E-Mail: Josef.Breu@uni-bayreuth.de

[a] Bavarian Polymer Institute and Department of Chemistry
University of Bayreuth
Universitätsstraße 30
95440 Bayreuth, Germany[b] Eckart GmbH, ALTANA AG
Günthersthal 4
91235, Germany[c] Institute of Chemical Reaction Engineering
Friedrich-Alexander University Erlangen-Nürnberg
Egerlandstraße 3
91058 Erlangen, GermanySupporting information for this article is available on the WWW under <http://dx.doi.org/10.1002/zaac.202000203> or from the author.

© 2020 The Authors published by Wiley-VCH GmbH · This is an open access article under the terms of the Creative Commons Attribution License, which permits use, distribution and reproduction in any medium, provided the original work is properly cited.

Aside of the pigment issue, Egyptian blue has recently attracted interest for its strong NIR luminescence,^[5] which has potential as luminescence marker in tissue^[5a] or as fingerprint dusting powder.^[6] The physical properties of exfoliated monolayers of Egyptian blue were explored in detail by density functional calculations.^[7]

As indicated by its pre-industrial invention in Egypt, the synthesis of Egyptian blue is simple and only requires control of stoichiometry and heat for mass transport. The Egyptians applied a salt-flux procedure at temperatures of 800–900 °C providing large (typically 60 µm), platy single crystals.^[2a,3,8] The only commercial product (Kremer Pigmente GmbH) still follows this ancient route. The saline waste water incurring with this production route, however, result in a price of > 2000 \$ per kg. Classical solid state synthesis on the other hand needs higher temperatures (ca. 1000 °C) and provides only microcrystalline material being inadequate for pearlescent pigments.^[4,9] Hydrothermal synthesis requires harsh conditions and yields only spherulitic aggregates, which are also useless for pearlescent pigments.^[10]

The biggest obstacle in obtaining morphologies appropriate for pearlescent pigments via a technically benign synthesis is the reduction sensitivity of Cu^{II}. At ambient oxygen fugacity and at thermodynamic equilibrium (Figure S1, Supporting Information) Cu^{II} is reduced to Cu^I at 1150 °C. This is close too close to the melting point (1045 °C), to allow crystal growth from the melt, which would offer sufficient crystal growth kinetics. The partial pressure of O₂ therefore has to be increased to > 5 bar.

Herein we present the fabrication of large platy crystals of Egyptian blue at 1000 °C by a pseudomorphosis after NaRUB-18, a long known phyllosilicate.^[11]

Results and Discussion

Crystalline layered sodium silicates like Kanemite, Magadiite, and NaRUB-18 are known for some time.^[11] The conversion of these two-dimensional (2D) silicates into 3D zeolites has been intensively explored.^[12] For some of them, a conversion via topotactic reaction has been suggested.^[12c,12f,12h,12i] Of the above mentioned phyllosilicates, NaRUB-18^[13] (Na₈[Si₃₂O₆₄(OH)₈]·32H₂O) possess a O:Si-ratio of 2.25, which among the above mentioned compounds is most similar to the ratio of 2.5 found in Egyptian blue.

Most pleasing, applying a mild published sol-gel route (90–130 °C), phase pure (Figure 1) large platelets (median 6.7 µm, Figure 3C) with appreciable aspect ratio (> 20) of NaRUB-18 could be obtained.^[14] The powder X-ray diffraction (PXRD, Figure 2A) could be completely indexed in space group *I*₄¹/*amd* (no. 141) and lattice parameters [*a* = *b* = 7.333(3) Å and *c* = 44.31(4) Å] in good agreement with literature data could be refined.^[13]

The structure of NaRUB-18 (Figure 1A) has been solved by Vortman et al. and is built from [5⁴] cages connected to layers.^[13] Charge balance is accomplished by chains of edge sharing [Na(H₂O)₆] octahedra in the interlayer space. Individual silicate layers are polar but are stacked in a centrosymmetric

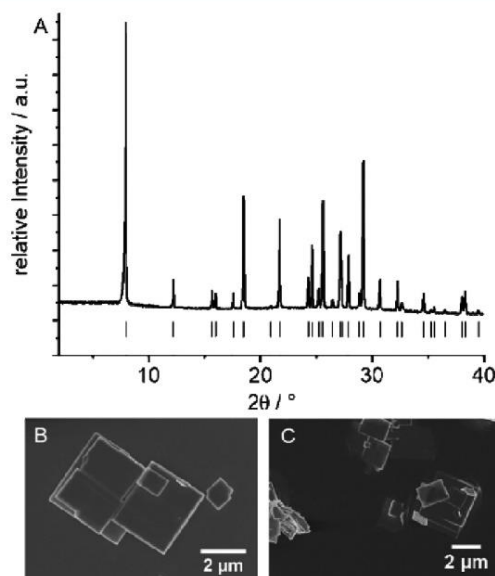


Figure 2. PXRD Pattern of the as synthesized NaRUB-18 (A), ticks indicate the ideal position of the theoretical reflections obtained from simulation using the crystal data from Vortman et al.^[12] and representative SEM images of the synthesized particles of NaRUB-18 (B) and CuRUB-18 after Cu^{II} exchange (C).

fashion, which has been suggested to reduce strain and allowing for an extended lateral growth. The Q³:Q⁴ ratio of NaRUB-18 is 1 with half of the terminal Si–O groups being protonated. In contrast to NaRUB-18, Egyptian blue is completely condensed and contains only symmetrically equivalent Q³X tetrahedra. Clearly, the two structures of NaRUB-18 and Egyptian blue have little in common but the 2D nature. Although both structures are comprised by “Einerdoppelketten” running along the *b* axis, the connectivity is quite different. The conversion of NaRUB-18 to Egyptian blue not only requires adjustments in composition and thus diffusion of atoms, but also reconstructions in the silicate framework to provide the coordination sites for Cu^{II}. These changes are expected to come along with correspondingly high activation energies. The conversion of NaRUB-18 to Egyptian blue was nevertheless attempted.

To adjust the composition of NaRUB-18 to that of Egyptian blue, first NaRUB-18 was ion exchanged with Cu-acetate until free of Na⁺ as evidenced by energy dispersive X-ray spectroscopy (EDX). Due to the high basicity of the unsaturated Si–O-bonds in the RUB-18 layers with a p*K*_a value of 9.5,^[15] part of the interlayer Na⁺ might actually be replaced by protons upon the ion exchange with Cu-acetate (pH = 5.3). This ion exchange is prerequisite for the conversion to Egyptian blue. If omitted a black glass is obtained upon heating instead of Egyptian blue.

The PXRD pattern of CuRUB-18 (not shown) could be indexed in space group *I*₄212 (no. 92), which has been sug-

gested for CaRUB-18,^[16] with lattice parameters of $a = b = 7.363(8)$ Å and $c = 29.88(5)$ Å. The considerable shift in the basal spacing is due to different degrees of solvation. For instance, for CaRUB-18, α -HRUB-18 and β -HRUB-18 basal spacings of 36.81, 29.76, and 26.0 Å were reported respectively.^[16] As expected, no morphological changes were observed upon ion exchange (Figure 1C).

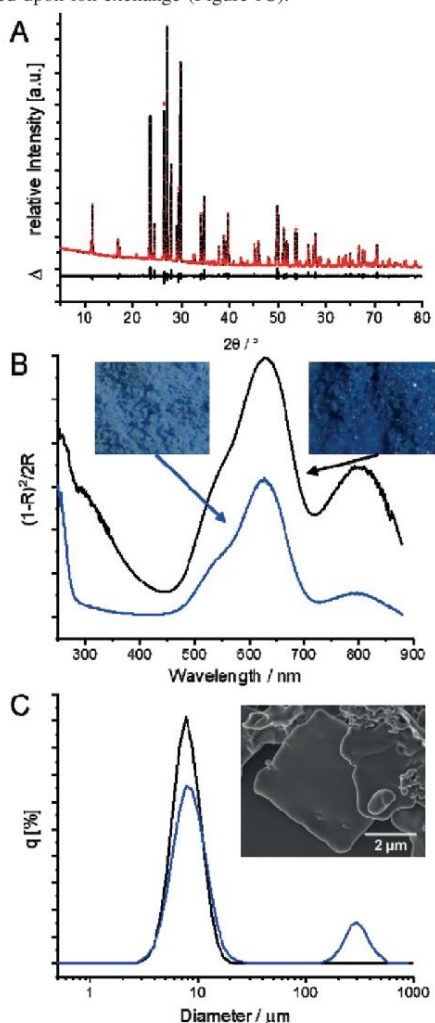


Figure 3. Rietveld refinement of the synthesized Egyptian blue (A), the refinement shows a good agreement between the observed and calculated pattern, – marks the observed pattern, o the profile of the Rietveld-fit, and Δ the difference plot between calculated and observed pattern. (B) Transformed diffuse reflectance spectrum of the commercial Egyptian blue from Kremer Pigmente GmbH (black) in comparison with synthesized Egyptian blue. The lower color strength of the synthesized material is shown in the optical microscope images. (C) SLS measurements of the as synthesized NaRUB-18 (black) in comparison with the synthesized Egyptian blue (blue), the inset shows a representative SEM image of the synthesized Egyptian blue particles.

With Cu:Si ratios of 1:8 and 1:4, respectively, the total exchange capacity of NaRUB-18 is sub-stoichiometric in respect to Cu-content for Egyptian blue. To make up for the missing amounts of Cu^{II} and Ca^{II} , needed to match the stoichiometry of Egyptian blue (Ca:Cu:Si = 1:1:4), ground CaCO_3 and the powder of CuRUB-18 were suspended in the corresponding volume of aqueous solution of CuSO_4 (0.1 M). Upon evaporation of the solvent a gel is formed.

When heating the gel at 900 °C no formation of Egyptian blue could be observed. Heating the gel at 1000 °C overnight, however, gave a complete conversion of CuRUB-18 to Egyptian blue as evidenced by PXRD. To safely avoid reduction of Cu^{II} to Cu^{I} , annealing was done in pure oxygen atmosphere.

Aside of Egyptian blue, the PXRD pattern of the raw product showed traces of cupric oxide, which could not be removed by additional annealing cycles (Figure S2, Supporting Information). For whatever reason, a complete and stoichiometric incorporation of Cu^{II} proved impossible. Accessory cupric oxide, however, can easily be removed post synthesis by washing with concentrated hydrochloric acid.

The Rietveld refinement of the purified Egyptian blue showed a good agreement of calculated and observed diffraction pattern (Figure 3A). Crystallographic data and details of the refinement are listed in Table 1 and Table 2. Unit cell and structural parameters were in good agreement with literature data (see Tables S1 and S2, Supporting Information).^[41] Unfortunately, attempting to refine the occupation factors for the Cu and Ca sites, did not lead to convergence.

Table 1. Crystallographic data of the synthesized Egyptian blue resulting from Rietveld refinement.

	Egyptian blue
Formula	$\text{CaCuSi}_4\text{O}_{10}$
MW / $\text{g}\cdot\text{mol}^{-1}$	375.96
Crystal system	tetragonal
Space group	$P4/ncc$
$a = b$ /Å	7.3025(4)
c /Å	15.131(3)
$a = b = \gamma$ /°	90
Z	4
V /Å ³	806.917(9)
ρ / $\text{g}\cdot\text{cm}^{-3}$	3.09473(4)
T /K	295
R_p	0.0269
R_{wp}	0.0403
R_{exp}	0.0080
R_{Bragg}	0.0206

The Cu content of the purified Egyptian blue was therefore determined by atomic absorption spectroscopy and was found to be $1.69 \text{ mmol}\cdot\text{g}^{-1}$, which is significantly lower than the content of $2.26 \text{ mmol}\cdot\text{g}^{-1}$ for the commercial material of Kremer Pigmente GmbH. The latter is still lower than what is expected from the ideal composition of Egyptian blue ($\text{CaCuSi}_4\text{O}_{10}$, $2.66 \text{ mmol}\cdot\text{g}^{-1}$).

The optical spectrum of the synthesized material corresponds to the spectrum of the commercial material (Figure 3B). Diffuse reflectance spectra, measured with an Ulbricht sphere, were transformed into absorption spectra applying the Kubelka-Munk equation.^[17] Both spectra showed the charac-

Table 2. Fractional atomic coordinates in space group $P4/mcc$ obtained from Rietveld refinement.

Atom	Wyckoff Position	x/a	y/b	z/c
Ca	4b	1/4	3/4	0
Cu	4c	1/4	1/4	0.08191(5)
Si	16g	0.50375(12)	0.92666(12)	0.14741(7)
O1	8f	0.4616(2)	0.9616(2)	1/4
O2	16g	0.7089(2)	0.0009(2)	0.12786(11)
O3	16g	0.3568(2)	0.0054(2)	0.08455(10)

teristic d-d transitions for a square planar ligand field of Cu^{II}. The transitions around 540, 630, and 800 nm can be assigned to the ²B_{1g}-²A_{1g}, ²B_{1g}-²E_g, and ²B_{1g}-²B_{2g} transitions, respectively.^[9,18] Although the used sample holder does not assure a defined thickness and thus does not allow a quantitative interpretation of the absorbance, it was obvious that the commercial material showed a higher absorption than the synthesized material. Although color saturation is influenced by particle size and scattering, the more intense blue color of the commercial Egyptian blue as compared to the pale blue of the synthesized sample (Figure 3B inset) most likely is due to the lower absorbance, which in turn is related to the lower Cu^{II} content.

Fortunately, and despite the required reconstruction of the silicate network, the morphology of NaRUB-18 was by large conserved upon conversion to Egyptian blue. SLS and SEM images indicate that particle size distribution and morphology of starting material and product are similar (compare Figure 2B and Figure 3C inset). Given the extended heat treatment at 1000 °C, the partial agglomeration and the rounding of crystal edges is not surprising. The pseudomorphosis of Egyptian blue after CuRUB-18 delivers rectangular shaped platelets of Egyptian blue with appreciable aspect ratio. The surface, however, appears rougher as compared to NaRUB-18.

Conclusions

Controlling the morphology is the key for pearlescent pigments. In particular, when the synthesis temperature is limited by reduction sensitivity like with Egyptian blue that owes its color to square planar Cu^{II}, classical solid state synthesis routes may prove inappropriate. In these cases, pseudomorphosis may be an option. In particular, since as shown here, it allows both changes in composition and reconstructive phase transitions while providing apparent “crystal growth” kinetics much faster than for classical routes to the same product. At the same time, the desired morphology is inherited from the starting material. Following such a pseudomorphosis route we were able to fabricate large square rectangular platelets of Egyptian blue in two steps starting with a layered silicate, NaRUB-18.

Experimental Section

Synthesis of Egyptian Blue: In a first step, NaRUB-18 was synthesized applying a published procedure.^[14] In brief, NaOH pellets ($\geq 98\%$, Sigma Aldrich) were dissolved in deionized water and then added to colloidal SiO₂ (30 wt.-%, Köstrosol 1030 KD) under vigorous stirring, giving a molar Na₂O:SiO₂:H₂O-ratio of 1:4:37. NaRUB-18 was obtained after synthesis at 100 °C for 4 weeks. Next a cation

exchange of sodium against Cu^{II} with Cu-acetate (p.a., Grüsing 0.2 M, 10 fold excess of the CEC, 3 times) was carried out and the resulting CuRUB-18 was dried at 45 °C. Residues of sodium could be excluded by energy dispersive X-ray spectroscopy (EDX) using an EDX INCA 400 unit (Oxford). For the synthesis of Egyptian blue, typically, 348.4 mg grounded CaCO₃ (99%, Suprapur) and 1.5 g of the synthesized CuRUB-18 powder were dispersed in 17.40 mL of an aqueous CuSO₄ solution (0.1 M, Grüsing) under vigorous stirring to match the nominal composition of Egyptian blue (Ca:Cu:Si of 1:1:4). Evaporation of the dispersion (115 °C) yielded a gel, which was transferred to a corundum crucible. The final synthesis was conducted for 16 h under pure oxygen at 1000 °C and the resulting Egyptian blue was washed once with HCl (32%, Grüsing).

Powder X-ray Diffraction: Powder X-ray diffraction (PXRD) patterns were recorded in sealed glass capillaries on a STOE Stadi P powder diffractometer equipped with a MYTHEN1K detector using Cu-K_{α1} radiation (1.54056 Å). Rietveld refinement was done starting with a published structural model^[4] applying TOPAS Academic^[19] and a fundamental parameters approach for describing the peak profiles.^[20]

Scanning Electron Microscopy and Energy Dispersive X-ray Spectroscopy: Scanning electron microscope (SEM) images were recorded on a Zeiss 1530.

UV/Vis-Spectroscopy: The diffuse reflectance UV/Vis spectra were measured using a Varian Cary 5000 UV/Vis/NIR-Spectrophotometer (Agilent) with attached Diffuse Reflectance Accessory between 250 and 900 nm. The obtained reflectance spectra were transformed into an absorption spectrum with the Kubelka-Munk function.^[17] Teflon was used as a white standard.

Atom Absorption Spectroscopy: The copper content of the final product has been determined with atom absorption spectroscopy. About 20 mg of the samples were weighted into clean Teflon-flasks of 15 mL volume. After addition of 1.5 mL 30 wt % HCl (Merck), 0.5 mL of 85 wt % H₃PO₄ (Merck), 0.5 mL of 65 % HNO₃ (Merck) and 1 mL of 48 % HBF₄ (Merck), the samples was digested in a MLS 1200 Mega microwave digestion apparatus for 6.5 min and heated at 600 W (MLS GmbH, Mikrowellen-Labor-Systeme, Leutkirch, Germany). The closed sample container was cooled to room temperature, the clear solution was diluted to 100 mL in a volumetric flask and analyzed on a Varian AA100-spectrometer.

Static Light Scattering: The particle size has been determined with static light scattering (SLS) in a flow cell setup on a Retsch LA-950 (Horiba) assuming a refractive index of 1.5 in a preinstalled measurement routine.

Supporting Information (see footnote on the first page of this article): Phase barogram of CuO-Cu₂O-system, PXRD patterns of Egyptian blue, crystallographic data and fractional atom coordinates obtained from neutron scattering.

Acknowledgements

We thank *Lena Geiling* for taking the SEM images, collecting EDX spectra, and *Sonja Lutschinger* for the AAS measurement. We appreciate the support of the Keylab for Optical and Electron Microscopy of the Bavarian Polymer Institute (BPI). P. L. thanks Elite Network Bavaria in the framework of the Elite Study Program "Macromolecular Science" for support. Open access funding enabled and organized by Projekt DEAL.

Keywords: Egyptian blue; Solid state synthesis; Pseudo-morphosis; NaRUB-18; Layered silicic acid

References

- [1] a) G. Buxbaum, G. Pfaff, *Industrial Inorganic Pigments*, Wiley, **2006**; b) F. J. Mailic, G. Pfaff, P. Reynders, *Prog. Org. Coat.* **2005**, *54*, 150–163.
- [2] a) H. Berke, *Angew. Chem. Int. Ed.* **2002**, *41*, 2483–2487; b) H. Berke, *Chem. Soc. Rev.* **2007**, *36*, 15–30; c) H. Jaksch, W. Seipel, K. L. Weiner, A. El Goresy, *Sci. Nat.* **1983**, *70*, 525–535.
- [3] A. Pabst, *Acta Crystallogr.* **1959**, *12*, 733–739.
- [4] B. C. Chakoumakos, J. A. Fernandez-Baca, L. A. Boatner, *J. Solid State Chem.* **1993**, *103*, 105–113.
- [5] a) G. Accorsi, G. Verri, M. Bolognesi, N. Armaroli, C. Clementi, C. Miliani, A. Romani, *Chem. Commun.* **2009**, 3392–3394; b) D. Johnson-McDaniel, C. A. Barrett, A. Sharafi, T. T. Salguero, *J. Am. Chem. Soc.* **2013**, *135*, 1677–1679; c) D. Johnson-McDaniel, T. T. Salguero, *J. Viso. Exp.* **2014**, *10*; d) S. M. Borisov, C. Wurth, U. Resch-Genger, I. Klimant, *Anal. Chem.* **2013**, *85*, 9371–9377.
- [6] B. Errington, G. Lawson, S. W. Lewis, G. D. Smith, *Dyes Pigm.* **2016**, *132*, 310–315.
- [7] Y. Chen, M. Kan, Q. Sun, P. Jena, *J. Phys. Chem.* **2016**, *120*, 399–405.
- [8] A. Bloise, S. Abd El Salam, R. De Luca, G. M. Crisci, D. Miriello, *Appl. Phys. A* **2016**, *122*.
- [9] E. Kendrick, C. J. Kirk, S. E. Dann, *Dyes Pigm.* **2007**, *73*, 13–18.
- [10] D. Johnson-McDaniel, S. Comer, J. W. Kolis, T. T. Salguero, *Chem. Eur. J.* **2015**, *21*, 17560–17564.
- [11] T. Selvam, A. Inayat, W. Schwieger, *Dalton Trans.* **2014**, *43*, 10365–10387.
- [12] a) S. M. Ciocilteu, M. Salou, Y. Kiyozumi, S.-i. Niwa, F. Mizukami, M. Haneda, *J. Mater. Chem.* **2003**, *13*, 602–607; b) M. Salou, F. Kooli, Y. Kiyozumi, F. Mikamizu, *J. Mater. Chem.* **2001**, *11*, 1476–1481; c) R. M. Mihályi, F. Lónyí, H. K. Beyer, Á. Szegedi, M. Kollár, G. Pál-Borbély, J. Valyon, *J. Mol. Catal. Chem.* **2013**, *367*, 77–88; d) T. Selvam, G. T. P. Mabandé, W. Schwieger, Y. Sugi, I. Toyama, Y. Kubota, H.-S. Lee, J.-H. Kim, *Catal. Lett.* **2004**, *94*, 17–24; e) B. Marler, N. Ströter, H. Gies, *Microporous Mesoporous Mater.* **2005**, *83*, 201–211; f) T. Ikeda, Y. Oumi, T. Takeoka, T. Yokoyama, T. Sano, T. Hanaoka, *Microporous Mesoporous Mater.* **2008**, *110*, 488–500; g) Z. Zhao, W. Zhang, P. Ren, X. Han, U. Müller, B. Yilmaz, M. Feyen, H. Gies, F.-S. Xiao, D. De Vos, T. Tatsumi, X. Bao, *Chem. Mater.* **2013**, *25*, 840–847; h) B. Marler, H. Gies, *Eur. J. Mineral.* **2012**, *24*, 405–428; i) Y. Oumi, T. Takeoka, T. Ikeda, T. Yokoyama, T. Sano, *New J. Chem.* **2007**, *31*.
- [13] S. Vortmann, J. Rius, S. Siegmann, H. Gies, *J. Phys. Chem. B* **1997**, *101*, 1292–1297.
- [14] a) G. Borbély, H. K. Beyer, H. G. Karge, W. Schwieger, A. Brandt, K. H. Bergk, *Clays Clay Miner.* **1991**, *39*, 490–497; b) W. Schwieger, K.-H. Bergk, *Z. Chem.* **1985**, *25*, 228–230.
- [15] K.-H. Bergk, W. Schwieger, M. Porsch, *Chem. Tech.-Leipzig* **1987**, *39*, 508–514.
- [16] M. Borowski, O. Kovalev, H. Gies, *Microporous Mesoporous Mater.* **2008**, *107*, 71–80.
- [17] L. Yang, B. Kruse, *J. Opt. Soc. Am.* **2004**, *21*, 1933–1941.
- [18] G. Pozza, D. Ajò, G. Chiari, F. Zuane, M. Favaro, *J. Cult. Herit.* **2000**, *1*, 393–398.
- [19] TOPAS Academic v5, Coelho Software, Brisbane, Australia, 2012.
- [20] R. W. Cheary, A. Coelho, *J. Appl. Crystallogr.* **1992**, *25*, 109–121.

Received: May 7, 2020

Published Online: September 4, 2020

6.4.2. Supporting Information

Z. Anorg. Allg. Chem. **2020** · ISSN 0044–2313

SUPPORTING INFORMATION

Title: Synthesis of Large Platelets of Egyptian Blue via Pseudomorphosis after NaRUB-18

Author(s): P. Loch, T. Martin, M. Grüner, G. Kaupp, W. Schwieger, J. Breu*

Ref. No.: z202000203

Synthesis of Large Platelets of Egyptian Blue via Pseudomorphosis after NaRUB-18

Patrick Loch^[a], Thomas Martin^[a], Michael Grüner^[b], Günther Kaupp^[b], Wilhelm Schwieger^[c] and Josef Breu^{*[a]}

Dedicated to Prof. Dr. Bernd Harbrecht on Occasion of his 70th Birthday

Supporting Information

Content:

- Figure S1: Phase barogram of CuO-Cu₂O-system
- Figure S2: PXRD of Egyptian blue
- Table S1: Crystallographic Data obtained from neutron scattering
- Table S2: Fractional atom coordinates obtained from neutron scattering
- Supporting References

* Prof. Dr. J. Breu
E-Mail: Josef.Breu@uni-bayreuth.de

[a] Bavarian Polymer Institute and Department of Chemistry
University of Bayreuth
Universitätsstraße 30
D-95440 Bayreuth, Germany

[b] Eckart GmbH, ALTANA AG
Günthersthal 4
D-91235, Germany

[c] Institute of Chemical Reaction Engineering
Friedrich-Alexander University Erlangen-Nürnberg
Egerlandstraße 3
D-91058 Erlangen, Germany

Supporting information for this article is given via a link at the end of the document.

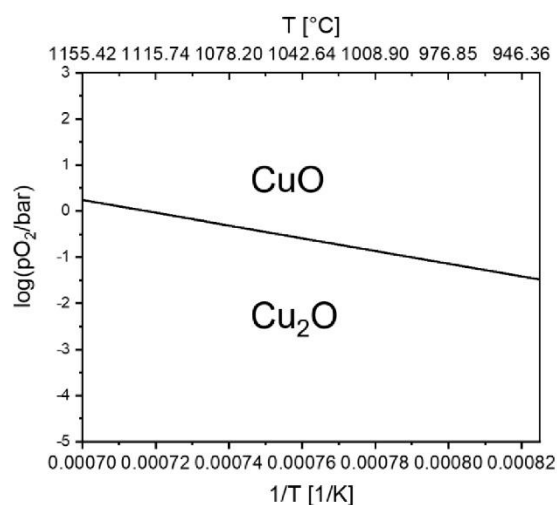


Figure S1. Phase-barogram showing the temperature depending oxygen fugacity of the system CuO-Cu₂O. The oxygen fugacity ($\log\left(\frac{pO_2}{\text{bar}}\right) = A - \frac{B}{T}$ with $A = \frac{\Delta S_R(T)}{2.303 \cdot R}$ and $B = \frac{\Delta S_R(T)}{2.303 \cdot R} \cdot [K]$) were calculated using selected thermodynamic data of reference [1].

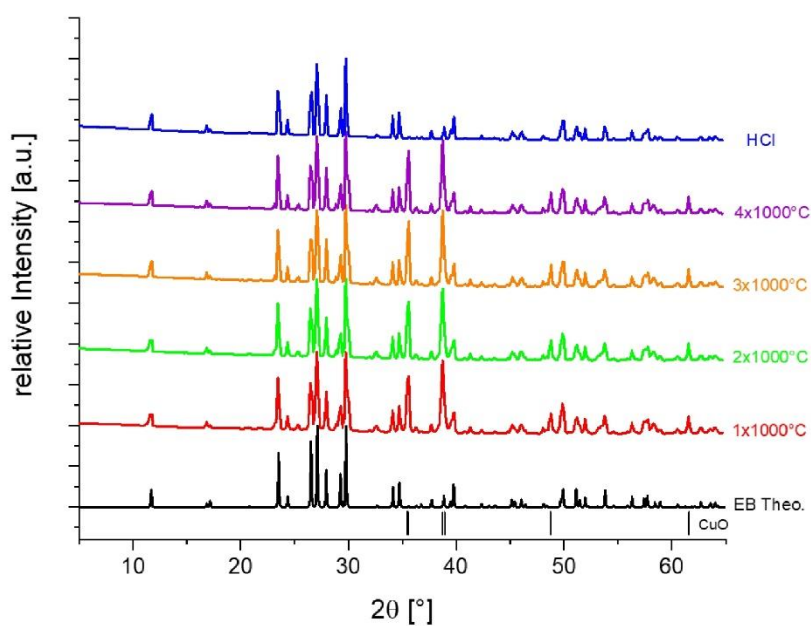


Figure S2. PXRD patterns after different annealing cycles at 1000°C in comparison with the theoretical diffraction pattern, calculated with WinXPOW using single crystal data from literature^[2]. Ticks indicate the accessory CuO phase.

Results

Table S1. Crystallographic data from Rietveld refinement using neutron scattering.^[3]

Egyptian blue	
Formula	CaCuSi ₄ O ₁₀
MW [g·mol ⁻¹]	375.96
Crystal system	tetragonal
Space group	P4/ncc
$a = b / \text{Å}$	7.3017(3)
$c / \text{Å}$	15.1303(6)
$\alpha = \beta = \gamma / ^\circ$	90
Z	4
$V / [\text{Å}^3]$	806.66(9)
$\rho / \text{g cm}^{-3}$	3.095
T / K	295
R _p	0.0448
R _{wp}	0.0515
R _{exp}	0.0453

Table S2. Fractional atomic coordinates in space group P4/ncc obtained from Rietveld refinement using neutron scattering.^[3]

Atom	Wyckoff Position	x/a	y/b	z/c
Ca	4b	1/4	3/4	0
Cu	4c	1/4	1/4	0.0819(1)
Si	16g	0.5036(3)	0.9267(2)	0.1475(1)
O1	8f	0.4608(2)	0.9608	1/4
O2	16g	0.7076(2)	1.0025(2)	0.1268(1)
O3	16g	0.3533(2)	0.0068(2)	0.0821(1)

Supporting References

- [1] P. Schmidt, *Thermodynamische Analyse der Existenzbereiche fester Phasen-Prinzipien der Syntheseplanung in der Anorganischen Festkörperchemie: Habilitation*, **2007**.
- [2] A. Pabst, *Acta Cryst.* **1959**, *12*, 733–739.
- [3] B. C. Chakoumakos, J. A. fernandez-Baca, L. A. Boatner, *J. Solid State Chem.* **1993**, *103*, 105–113.

7. List of Publications and Patents

7.1. Publications included in this thesis

Loch P., Algara-Siller G.; Schuchardt D., Markus P., Ottermann K., Rosenfeldt, S., Lunkenbein T., Schwieger, W., Papastavrou, G., Breu J.: Nematic suspension of a microporous layered silicate obtained by forceless spontaneous delamination via repulsive osmotic swelling for casting high-barrier all inorganic films. *Sci. Adv.* **2022**, *8*, eabn9084.

Hunvik K. W. B., Loch P., Cavalcanti L. P., Seljelid K. K., Røren P. M., Rudić S., Wallacher D., Kirch A., Knudsen K. D., Rodrigues Miranda C., Breu J., Bordallo H. N., Fossum J. O.: CO₂ Capture by Nickel Hydroxide Interstratified in the Nanolayered Space of a Synthetic Clay Mineral. *J. Phys. Chem. C* **2020**, *124*, 2622-2631.

Loch P., Hunvik K. W. B., Puchtler F., Weiß S., Seljelid K. K., Røren P. M., Rudic S., Raaen S., Knudsen K. D., Bordallo H. N., Fossum J. O., Breu J.: Spontaneous formation of an ordered interstratification upon Ni-exchange of Na-fluorohectorite. *Appl. Clay Sci.* **2020**, *198*, 105831.

Loch P., Martin T., Grüner M., Kaupp G., Schwieger W., Breu, J.: Synthesis of Large Platelets of Egyptian Blue via Pseudomorphosis after NaRUB-18. *Z. anorg. allg. Chem.* **2020**, *646*, 1570-1574.

7.2. Additional publications

Hunvik K. W. B., da Silva Lima R. J., Loch P., Røren P. M., Petersen M. H., Rudić S., Sakai V. G., Knudsen K. D., Breu J., Fossum J. O., Bordallo H. N.: Influence of CO₂ on Nanoconfined Water in a Clay Mineral. *J. Phys. Chem. C.* **2022**, Accepted. (DOI: 10.1021/acs.jpcc.2c03310)

Göbel C., Marquardt K., Baabe D., Drechsler M., Loch P., Breu J., Greiner A., Schmalz H., Weber B.: Realizing shape and size control for the synthesis of coordination polymer nanoparticles template by diblock copolymer micelles. *Nanoscale.* **2022**, *14*, 3131-3147.

Hunvik K. W. B., Loch P., Wallacher D., Kirch A., Cavalcanti L. P., Rieß M., Daab M., Josvanger V., Grätz S., Yokaichiya F., Knudsen K. D., Rodrigues Miranda C., Breu J., Fossum J. O.: CO₂ Adsorption Enhanced by Tuning the Layer Charge in a Clay Mineral. *Langmuir*. **2021**, 37, 14491-1449.

Hiebl C., Loch P., Brinek M., Gombotz M., Gadermaier B., Heitjans P., Breu J., Wilkening H. M. R.: Rapid Low-Dimensional Li⁺ Ion Hopping Processes in Synthetic Hectorite-Type Li_{0.5}[Mg_{2.5}Li_{0.5}]Si₄O₁₀F₂. *Chem. Mater.* **2020**, 32, 7445-7457.

Kuznetsov V., Ottermann K., Helfricht N., Kunz D., Loch P., Kalo H., Breu J., Papastavrou G.: Surface charge density and diffuse layer properties of highly defined 2:1 layered silicate platelets. *Colloid Polym. Sci.* **2020**, 298, 907-920.

Daab M., Loch P., Milius W., Schönauer-Kamin D., Schubert M., Wunder A., Moos R., Wagner F. E., Breu J.: Single-Crystal Structure and Electronic Conductivity of Melt Synthesized Fe-rich, near End-Member Ferro-Kinoshitalite. *Z. anorg. allg. Chem.* **2017**, 643, 1661–1667.

7.3. Patents

P. Loch, J. Breu; EP20205796.4: Process for delamination of layered zeolite, a delaminated layered zeolite dispersion and use thereof (2020)

8. Acknowledgements

Mein besonderer Dank gilt meinem Doktorvater Prof. Josef Breu. Ich möchte mich für die Möglichkeit meine Promotion an seinem Lehrstuhl durchführen zu können bedanken. Die vielfältigen Themenstellungen, die lehrreichen Diskussionen, die vielen Kooperationen, sowie die hervorragende Infrastruktur und die großen gewährten Freiheiten während der Promotion halfen mich stets selbst weiterzuentwickeln. Lieber Josef, vielen Dank für die Zeit an deinem Lehrstuhl!

Allen Kooperationspartnern im In- und Ausland gilt ein großer Dank, ohne die diese Arbeit nicht möglich gewesen wäre. Besonders Dr. Kristoffer William Bø Hunvik und Prof. Jon-Otto Fossum der NTNU Trondheim, die mir die Möglichkeit gaben auf Messzeit am ALBA Synchrotron teilzunehmen und zusammen die Problematik der Ni-Hectorite angegangen sind. Ich bedanke mich bei Dr. Günther Kaupp und Michael Grüner von ECKART GmbH für die gute Zusammenarbeit und die zahlreichen Diskussionen. Für die Unterstützung der Chemielehrstühle und Keylabs der Universität Bayreuth und des Bayrischen Polymer Instituts bedanke ich mich bei P. Markus, K. Ottermann, Prof. Dr. G. Papastavrou, Dr. Sabine Rosenfeldt und Dr. U. Mansfeldt. Darüber hinaus möchte ich mich bei Dr. Gerardo Algara-Siller, Dr. T. Lunkenbein, Prof. Dr. Wilhelm Schwieger und allen weiteren Kooperationspartnern bedanken.

Ich danke dem Elitenetzwerk Bayern, für die Aufnahme in das Elitestudienprogramm „Macromolecular Science“, das vielfältige Weiterbildungsmöglichkeiten ermöglichte.

Allen Mitgliedern Lehrstühlen AC1 und AC3 danke ich für die gut Arbeitsatmosphäre und die Hilfsbereitschaft. Petra, Iris und Sieglinde danke für eure organisatorischen Leistungen, die den Arbeitsalltag rund ablaufen ließen. Bedanken möchte ich mich bei all meinen Laborkollegen über die Jahre, besonders bei Marco, Florian, Martin, Natalie, Kevin und Matthias für die vielen hilfreichen Diskussionen, die entspannte Atmosphäre und die ständige Unterstützung. Meinen Bachelor Studenten Jannik, meinen Hiwis und Praktikanten danke ich für ihr präparatives Geschick und dem Einsatz im Labor.

Acknowledgements

Ich bedanke mich bei all meinen Freunden in der Uni, außerhalb und in der Heimat. Ohne euch wäre alles nur halb so witzig gewesen. Besonders die Kaffeepausen mit Kevin, Simon, Daniel und Dominik werde ich lange in Erinnerung behalten. Vielen Dank an Kevin für die Korrektur der Arbeit und den hilfreichen Anmerkungen.

Ohne die Unterstützung meiner Familie wäre ich nie so weit gekommen. Danke, dass ihr mich immer unterstützt habt und mir zur Seite gestanden seid. Besonderer Dank gilt Lena, die mir immer zur Seite gestanden ist und ohne die diese Arbeit nicht möglich gewesen wäre.

Danke!!!

9. Erklärung des Verfassers

(Eidesstattliche) Versicherungen und Erklärungen

(§ 8 Satz 2 Nr. 3 PromO Fakultät)

Hiermit versichere ich eidesstattlich, dass ich die Arbeit selbstständig verfasst und keine anderen als die von mir angegebenen Quellen und Hilfsmittel benutzt habe (vgl. Art. 64 Abs. 1 Satz 6 BayHSchG).

(§ 8 Satz 2 Nr. 3 PromO Fakultät)

Hiermit erkläre ich, dass ich die Dissertation nicht bereits zur Erlangung eines akademischen Grades eingereicht habe und dass ich nicht bereits diese oder eine gleichartige Doktorprüfung endgültig nicht bestanden habe.

(§ 8 Satz 2 Nr. 4 PromO Fakultät)

Hiermit erkläre ich, dass ich Hilfe von gewerblichen Promotionsberatern bzw. –vermittlern oder ähnlichen Dienstleistern weder bisher in Anspruch genommen habe noch künftig in Anspruch nehmen werde.

(§ 8 Satz 2 Nr. 7 PromO Fakultät)

Hiermit erkläre ich mein Einverständnis, dass die elektronische Fassung der Dissertation unter Wahrung meiner Urheberrechte und des Datenschutzes einer gesonderten Überprüfung unterzogen werden kann.

(§ 8 Satz 2 Nr. 8 PromO Fakultät)

Hiermit erkläre ich mein Einverständnis, dass bei Verdacht wissenschaftlichen Fehlverhaltens Ermittlungen durch universitätsinterne Organe der wissenschaftlichen Selbstkontrolle stattfinden können.

.....
Ort, Datum, Unterschrift